![COPPE UFRJ logo - Instituto Alberto Luiz Coimbra de Pós-Graduação e Pesquisa de Engenharia]

HETEROGENEIDADE PULMONAR E LESÃO INDUZIDA PELA VENTILAÇÃO MECÂNICA

Gabriel Casulari da Motta Ribeiro

Tese de Doutorado apresentada ao Programa de Pós-graduação em Engenharia Biomédica, COPPE, da Universidade Federal do Rio de Janeiro, como parte dos requisitos necessários à obtenção do título de Doutor em Engenharia Biomédica.

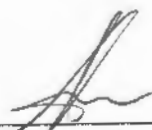Orientadores: Alysson Roncally Silva Carvalho
Alessandro Beda

Rio de Janeiro
Junho de 2018

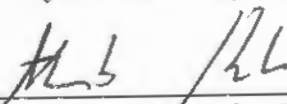# HETEROGENEIDADE PULMONAR E LESÃO INDUZIDA PELA VENTILAÇÃO MECÂNICA

Gabriel Casulari da Motta Ribeiro

TESE SUBMETIDA AO CORPO DOCENTE DO INSTITUTO ALBERTO LUIZ COIMBRA DE PÓS-GRADUAÇÃO E PESQUISA DE ENGENHARIA (COPPE) DA UNIVERSIDADE FEDERAL DO RIO DE JANEIRO COMO PARTE DOS REQUISITOS NECESSÁRIOS PARA A OBTENÇÃO DO GRAU DE DOUTOR EM CIÊNCIAS EM ENGENHARIA BIOMÉDICA.
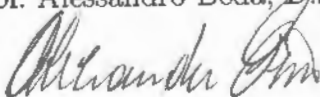
Examinada por:

_____
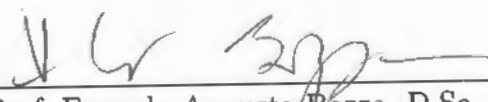Prof. Alysson Roncally Silva Carvalho, D.Sc.

_____
Prof. Alessandro Beda, D.Sc.

_____
Prof. Alexandre Visintaner Pino, D.Sc.

_____
Prof. Eduardo Leite Vieira Costa, D.Sc

_____
Prof. Fernado Augusto Bozza, D.Sc.

RIO DE JANEIRO, RJ – BRASIL
JUNHO DE 2018

Agradecimentos

Agradeço a minha família. Aos meus pais e minha irmã que me apoiaram nas minhas decisões (que são sempre difíceis) e ajudaram a enfrentar a mudança, não só geográfica, inerente a um doutorado sanduíche. E aos primos, tios e avôs que serviram de exemplo com sua dedicação aos seus trabalhos e ideais.

Agradeço aos meus orientadores, Alysson Roncally e Alessandro Beda, pelo apoio desde o início do doutorado. Ambos foram essenciais para esta tese, mesmo que não sejam coautores dos trabalhos diretamente apresentados no texto.

Aos professores Frederico Jandre e Antonio Giannela Neto que me receberam no Laboratório de Engenharia Pulmonar (LEP) como um aluno de graduação e tem grande importância na minha formação como engenheiro e pesquisador. Ao Giannela devo ainda agradecer pelo apoio durante os dois periodos em que estive como visitante na Leipzig Universtät, agradecimento que é estendido a sua família: Ivanir, Beatriz e Theo.

Falando em Leipzig, agradeço a Hermann Wrigge e Andreas Reske em nome de todos que me receberam no hospital universitário. *Danke schön.*

Ao povo do LEP, os alunos representados por Alan, Leonardo, Marcelo, Neto, Niedja e Rhenan que ajudaram no período de doutorado no Brasil, e o engenheiro Luciano que sempre manteve o laboratório funcionando. Aqui incluo também o Daniel, que se juntou a turma pela proximidade física do local de trabalho.

Do período de sanduíche no Massachusetts General Hospital agradeço aos membros do Pulmonary Imaging and Biomedical Engineering Laboratory em especial ao Marcos Vidal Melo que me recebeu como supervisor do sanduíche e apresentou uma nova perspectiva de pesquisa, e ao Tilo Winkler. *Thank you Tilo, more than what I learned about imaging processing, our discussions were very pleasant. I have also to thanks Tilo's wife, Tila, for the talk and the food.* Muito obrigado as andorinhas do PUBBoston representados por Alexandre, Diego, Dirson, George e Getúlio.

Agradeço à FAPERJ pelo apoio financeiro durante o período no Brasil e a CAPES pelo apoio no estágio no exterior.

A todos, e aqueles que não consegui listar, muito obrigado!

Mit dem Wissen wächst der
Zweifel.
(Com o conhecimento cresce a
dúvida.)
Johann Wolfgang von Goethe

iv

Resumo da Tese apresentada à COPPE/UFRJ como parte dos requisitos necessários para a obtenção do grau de Doutor em Ciências (D.Sc.)

HETEROGENEIDADE PULMONAR E LESÃO INDUZIDA PELA VENTILAÇÃO MECÂNICA

Gabriel Casulari da Motta Ribeiro

Junho/2018

Orientadores: Alysson Roncally Silva Carvalho
                Alessandro Beda

Programa: Engenharia Biomédica

A expansão pulmonar regional durante um ciclo respiratório é heterogênea, com possíveis consequências para o resultado da ventilação mecânica. Essa tese estudou essa heterogeneidade em um modelo animal nas primeiras 24 h de ventilação mecânica de pulmões inicialmente normais e em um modelo teórico da manobra de lavagem de N_2 em múltiplos ciclos. Os experimentos em animais compararam duas condições iniciais de expansão pulmonar, posição prona (homogênea) ou posição supina (heterogênea). O parâmetros ventilatórios seguiram a prática clínica, aumentando a relevância translacional. Imagens de tomografia computadorizada e por emissão de pósitrons foram utilizadas para quantificar a expansão estática (aeração) e dinâmica (strain) em cada voxel e a atividade metabólica (ligada a inflamação) regional. Animais em supino apresentaram deterioração progressiva da mecânica regional, com heterogeneidade espacial na (leve) inflamação e lesão, bem como na expressão gênica, do tecido pulmonar. Em contraste, a posição prona resultou em inflamação e perda de aeração leves, sem alteração na distribuição espacial. Um novo modelo para explicar a manobra de lavagem de N_2 foi proposto. Este considera o pulmão como compartimentos em paralelo e um espaço morto em série. Comparado ao modelo clássico, o novo modelo impõe menos restrições aos ciclos respiratórios durante a manobra, sendo mais adequado ao uso durante ventilação mecânica. Simulações numéricas e experimentos em bancada mostraram que o modelo proposto tem melhor desempenho que o clássico na reconstrução de distribuições de ventilação específica (ligada a expansão dinâmica). Os resultados obtidos auxiliarão a definição de estratégias ventilatórias em pacientes sem lesão pulmonar inicial e o avanço da monitorização à beira do leito, com potencial impacto na prática clínica.

LUNG HETEROGENEITY AND VENTILATION INDUCED LUNG INJURY

Gabriel Casulari da Motta Ribeiro

June/2018

Advisors: Alysson Roncally Silva Carvalho
Alessandro Beda

Department: Biomedical Engineering

Lung expansion during a respiratory cycle is spatially heterogeneous with possible consequences for the outcome of mechanical ventilation. This thesis studied this heterogeneity in a large animal model of the first 24 h of mechanical ventilation of initially normal lungs, and in a theoretical model of gas mixing during a multiple-breath N_2 washout maneuver. The animal experiments compared two initial states of lung expansion, prone position (homogeneous) and supine position (heterogeneous). The ventilator settings were in accordance to current clinical practice, increasing the translational relevance. Computed and positron emission tomography were used to asses voxel-level distribution of static (aeration) and dynamic (strain) lung expansion, and regional metabolic activity (marker of inflammation). Supine animals showed progressive deterioration of regional lung mechanics resulting in spatially distinct mild tissue injury and inflammation, as well as gene expression. In contrast, the prone position had mild inflammation and loss in aeration without increase in heterogeneity. A new model to explain the N_2 washout maneuver was proposed. This considers the lungs as parallel compartments with a series dead space. Compared to the classical model, the new model imposes fewer restrictions on the ventilatory cycles during the maneuver, potentially allowing its application in mechanically ventilated patients. Computational simulations and bench experiments demonstrated that the proposed model outperforms the classical in the reconstruction of distributions of specific ventilation (linked to dynamic expansion). The current findings will help to define mechanical ventilation strategies for patients without initial lung injury and advance bedside monitoring, with potential impact on clinical practice.

Contents

List of Figures

xiii

List of Tables

List of Symbols

J	index of alveolar unit, p. 68
$F_{N_2}^{et}$	end-tidal N_2 concentration, p. 69
$F_{N_2}^{I,A}$	alveolar unit inspired N_2 concentration, p. 69
F_b	blood fraction, p. 49
F_e	distribution volume, p. 49
F_{es}	tissue-normalized distribution volume, p. 49
F_{GAS}	gas fraction, p. 48
F_{TIS}	tissue fraction, p. 49
V_T	tidal volume, p. 2
V_{T0}	reference tidal volume, p. 70
V_T^E	expiratory tidal volume, p. 70
V_T^I	inspiratory tidal volume, p. 70
N	number of modeled alveolar units, p. 67
k	index of breath cycle, p. 69
k_3	phosphorylation rate, p. 49
Ki	uptake rate, p. 48
Kis	tissue-normalized uptake rate, p. 49
K_1	transport rate from blood to tissue, p. 49
k_2	transport rate from tissue to blood, p. 49
γ	alveolar unit fraction of tidal volume, p. 68

List of Abbreviations

ARDS   Acute Respiratory Distress Syndrome, p. 3

CT   Computed Tomography, p. 5

EELV   End-Expiratory Lung Volume, p. 5

EIT   Electrical Impedance Tomography, p. 5

PET   Positron Emission Tomography, p. 3

RMS   respiratory mass spectrometers, p. 66

VILI   Ventilator Induced Lung Injury, p. 2

^{18}F-FDG   2-deoxy-2-[(18)F]fluoro-d-glucose, p. 3

MBN_2W Multiple-Breath Nitrogen Washout, p. 5

Chapter 1

Introduction

Lung static (aeration) and dynamic (ventilation) expansions are spatially heterogeneous. In a macroscopic view, the elastic characteristic (relationship between pressure and volume) of lung tissue is homogeneous, i.e. large random samples of tissue in an individual lung would show the same characteristic if tested *ex vivo*. However, even with slow breaths (flow rate $<0.5\,\mathrm{L\,s^{-1}}$), when airway pressure could be considered equally distributed in the lungs, healthy humans present differences in aeration between apex and basal lung regions in upright position [1]. This difference in aeration can be interpreted as difference in alveolar sizes and are explained by the vertical gradient in the pressure in the pleural space (between parenchyma and chest wall), as the alveolar pressure = airway - pleural. This difference in pleural pressures depends on the shape of the chest-wall [2] and the lungs [3, 4], and the lung weight [5]. Aeration can also be influenced by the alveolar surfactant layer, which changes the tissue surface tension and consequently the lung elastic recoil [6]. The distribution in ventilation is a consequence of the non-linear elastic characteristic of the lung tissue. Without alveolar collapse or airway closure, the lung regional pressure-volume relationship can be modeled by an exponential function [7]. For the same variation in pressure, the change in volume of regions with higher initial volume are smallest. Therefore, the initial aeration determines the regional stiffness and the less aerated dependent (i.e. lower in the direction of gravity) regions of normal lungs expand more than non-dependent regions during tidal breathing [1]. In addition, the pattern of bifurcations of the airway tree [8] and regional differences in airway caliber due to airway-parenchyma interdependence [9] influence flow distribution. Of note, in a microscopic view, the composition of the extra cellular matrix generates heterogeneity in lung parenchyma mechanics [6].

In mechanically ventilated lungs, the spatial heterogeneity of expansion increases. Patients are generally lying supine (or semi-supine with the torso tilted upward) on the bed. Consequently, the diaphragm and the heart are compressing the dorsal regions of the lung [10, 11]. Intubation for invasive mechanical ventilation is ac-

1

companied by sedation and often muscle paralysis that decrease the stiffness of the chest wall and diaphragm, reducing their elastic recoil and thus the lung volume [12]. The reduction in lung volume aggravates the regional differences in aeration [1] and decreases the diameter of airways, potentially leading even to airway closure [13]. Because during mechanical ventilation most of the work of breathing comes from the positive pressure delivered by the ventilator, the relaxed diaphragm counteracts the expansion of dorsal regions [10].

Cells sense and respond to mechanical forces and deformation in a process called mechanotrasduction [14]. This mechanism is extremely relevant to the lungs, where the air movement and lung change in size at each breath are constantly providing mechanical stimuli to the cells. Mechanotransduction is known to regulate lung development [15], epithelial cell differentiation and apoptosis [16], alveolar fluid clearance [17], and surfactant [18] and inflammatory cytokines [19] release. Lung cells respond to both high and low deformation, for example, surfactant release is decreased if not enough or excessive stretch is applied to epithelial cells [20]. The lung cells are also sensible to the peak, tidal amplitude, and frequency of deformation [21].

Mechanical ventilation can induce lung injury or aggravate a primary injury, what is known as Ventilator Induced Lung Injury (VILI). VILI is an inflammatory process that causes and is affected by systemic dysfunctions [22–25]. Mechanotransduction seems to play an important role in the development of VILI. Reducing the amplitude of lung tissue cyclic stretch through a reduction in tidal volume (V_T), which should decrease the release of inflammatory cytokines, improve outcomes for mechanically ventilated patients with both injured [26, 27] and normal lungs [28–34]. The injured lungs can have a highly heterogeneous distribution of aeration, characterized by an affected non-aerated region and an aerated region with normal elastic characteristics [35]. In this condition, choosing V_T without taking into account the size of the actually ventilated lung may result in excessive cell stretch, even if the V_T is within the range of normal spontaneous (physiological) breath. This lung-size dependence for setting of V_T can be enclosed in the concept of strain. Strain is a measure of deformation relative to a reference state. In the lungs, it is the ratio of volume change to a rest volume [36].

As highlighted in the beginning of this chapter, pressure and volume are partially related trough the elastic properties in the lung, similar to the stress-strain relationships studied in solid materials. The lung injury could be a consequence of one or both the stress or the strain on lung tissue. In this thesis, strain will be considered as the injurious variable because it is more practical to be assessed in a regional level, mechanical ventilation to the same peak pressure with different V_T result in different degrees of injury [37], and surface strain is the input used in most isolated cell mechanotransduction experiments [15–19]. In some places plateau pressure (the

pressure measured during a breath hold at end-inspiration) will be used as a marker of overall peak lung stretch, and driving pressure (plateau – end-expiratory pressure) will be considered as a rough surrogate of strain [38]. This is because driving pressure represents V_T normalized by lung compliance, which is correlated to the aerated lung volume [39].

The magnitude of global strains required to generate lung injury in experimental studies is unlikely to happen during mechanical ventilation of patients with normal lungs [40]. PROTTI *et al.* [41] observed that healthy-lung pigs would not develop lung injury during 54 h of mechanical ventilation if the global strain (V_T/functional residual capacity) was below 1.5. Yet, strains above 2.0 would always result in injury (mostly lethal) within the same 54 h. Therefore, they determined the existence of a strain threshold between 1.5 and 2.0 leading to injury exclusively by excessive tissue stretch. These strain levels correspond to a unphysiological lung inflation, requiring V_Ts of $(22 \pm 8)\,mL\,kg^{-1}$. In fact, experimental studies on the effects of V_T in normal lungs usually employed very large global strains ($V_T > 15\,mL\,kg^{-1}$) [23, 37, 41–43]. This setting is far from the recommended for clinical mechanical ventilation and rare in the actual practice [44]. In consequence, the translation of those studies to interpret VILI in patients is limited. This is evidenced by the observation of VILI in patients with V_T lower than the experimental [28]. The assumption invoked to reconcile the experimental results and clinical observation is that due to the spatially heterogeneous expansion of the lungs, regional strain can be markedly different from the mean (determined by V_T). Thus, the exaggerated experimental V_T tries to model the injurious processes that develops in lung regions present in the tail of lung expansion distribution, where strain is unphysiological.

The relationship between aeration and strain heterogeneities and VILI has been previously studied using positron emission tomography (PET) scans with the tracer 2-deoxy-2-[(18)F]fluoro-d-glucose (^{18}F-FDG) to measure regional metabolic activity, an index of inflammation [45–48] and early biomarker of acute respiratory distress syndrome (ARDS) [49]. Briefly, this technique quantifies the glucose uptake of tissue as a combination of a volume of distribution (non-metabolized ^{18}F-FDG inside cells) and the rate of the phosphorylation of ^{18}F-FDG (the first step for the conversion of glucose in energy). COSTA *et al.* [50] ventilated endotoxemic sheep (intravenous infusion of lipopolysaccharide, LPS) for 2 h using high V_T (plateau pressure of $30\,cm\,H_2O$ and zero pressure at end-expiration) and found increased ^{18}F-FDG uptake rate compared with a non-endotoxemic group. The regional uptake rate in the LPS group was linked to the local aeration and perfusion, without assessment of dynamic expansion. WELLMAN *et al.* [51] studied the influence of regional strain on local inflammation in six regions-of-interest (three equal-height regions along the ventro-dorsal axis divided in two in the cephalo-caudal axis) and

3

three different experimental conditions: high V_T with and without endotoxemia (same settings as above), and low V_T with endotoxemia. After 3 h of ventilation, in both high V_T groups, ^{18}F-FDG phosphorylation rate was correlated to regional strain and presence of endotoxin increased the slope of this relationship.

The magnitude of strain heterogeneity and its consequence to inflammation during mechanical ventilation with clinical settings are unknown. The two previously described studies demonstrated that regional mechanical and functional parameters are relevant for the development of VILI. Nevertheless, the applicability of the results for determining a preventive mechanical ventilation strategy is limited. While the ventilator settings used resulted in clinically acceptable plateau pressures, the high V_T (average ~ 18 mL kg^{-1}) was higher than current practice [44]. In addition, driving pressures of 30 cm H_2O are normally avoided, especially after the recent works linking high driving pressure to worse outcomes in patients with ARDS [38] or normal lungs [52]. The low-V_T group in WELLMAN *et al.* [51] suggests that at small magnitudes, the strains measured in the 6 regions-of-interest are not correlated with local inflammation. However, this group used high positive end-expiratory pressures (PEEP) of (17 ± 3) cm H_2O, uncommon in patients with normal lungs [44, 53]. This PEEP may have influenced the results by homogenizing the distributions of aeration and strain. Moreover, due to limitations of the imaging technique and device, the authors could not determine strain in smaller regions-of-interest. The size of structures (length-scale) determining the tissue strain heterogeneity is unknown, but as mentioned before it can decrease down to the cellular level. Therefore, it is undefined if the absence of direct relationship between local strain and inflammation in the low-V_T group was because this association occurs in regions smaller than the assessed by the authors (median volume 89 mL). The range of strains resulting from the combination of high PEEP and low V_T was small compared to the variability in inflammation, reducing the power for measuring correlation. Thus, the study of WELLMAN *et al.* [51], does not answer if despite a global "safe" value of tidal strain, lung heterogeneity could result in high injurious local tidal strains sufficient to start the inflammatory process leading to ARDS. Additionally, the duration of those experiments may have been short to observe significant effects of small mechanical stimuli [54], even in the presence of endotoxemia that sensitizes the lung to stretch [22] (and the results of the high V_T + LPS group in [51]). If the mechanical lung injury or the effect of systemic inflammation over the lungs have a cumulative characteristic, or lung heterogeneity increases along time, longer experiments would be required.

The heterogeneity of dynamic lung expansion has been little explored so far in clinical practice. Experimentally, such heterogeneity was assessed using different variables and imaging techniques: specific ventilation (ratio of volume of fresh

4

gas entering a region to the regional end-expiratory gas volume) derived from PET [55–57], computed tomography (CT) [58, 59] and magnetic resonance [60, 61]; ventilation distribution using Electrical Impedance Tomography (EIT) [62]; and strain using PET transmission scans [51, 63] or CT [58, 64–67]. However, only EIT, which is relatively new as a commercially available technology, can be applied at the bedside. Also, the non-imaging technique of Multiple-Breath N_2 Washout (MBN$_2$W) maneuvers allows for bedside estimation of the heterogeneity of regional specific ventilation. This maneuver consists in measuring the inspired and expired concentrations of N_2 (or other inert gas, i.e. a gas not participating in gas exchange with blood) after a step change in the inspired concentration. From a MBN$_2$W it is possible to estimate the End-Expiratory Lung Volume (EELV) [68–70], several indexes of specific ventilation heterogeneity [70, 71], and the distribution of specific ventilation [72]. However, despite the promising initial studies [73–76], this last technique has been almost forgotten. One reason could be that the classical equation used to identify specific ventilation during MBN$_2$W requires constant V_T, equal inspired and expired volumes, and a perfect step in the concentration of N_2 to start the washout. These three conditions are almost impossible to obtain in a clinical scenario. Additionally, the classical model considers all ventilation units, including the dead space (conducing airways), to be positioned in parallel [73]. This inconsistency with the existence of a non-negligible series dead space can lead to deviations from the real specific ventilation distribution [77].

1.1 Objectives

Mechanical ventilation is needed in a large number of patients in critical care without a primary lung disease [78] and for the millions of major surgery procedures executed annually worldwide [79]. We hypothesize that in these patients with normal lungs the regional deformation (characterized by the tidal strain) plays an important role in the development of VILI even with low (i.e. "protective") V_Ts. Even if the local expansion is not large enough to cause physical injury, the regional mechanotransduction may activate inflammatory pathways and act synergistically with systemic stimuli. Yet, the experimental studies performed so far on this matter used ventilatory settings not compatible with clinical practice, limiting the clinical applicability of the results. Additionally, characterization of the heterogeneity of dynamic expansion at bedside is currently limited to EIT or single parameters trying to summarize the local phenomena [71], while a simple maneuver of MBN$_2$W could provide a good surrogate for tidal strain distribution [58]. The main objectives of this thesis were:

5

1. to investigate the effects of regional mechanotransduction in the early phase of VILI development during mechanical ventilation with clinically relevant settings, and specifically

   (a) to apply high-resolution CT analysis in order to quantify the spatial distribution of aeration and tidal strain in mechanically ventilated normal lungs, and to determine how these spatial distributions change in the early stages of lung injury;

   (b) to establish topographical relationships between mechanical and functional parameters of the lung with biological processes of injury through analyses of PET scans and gene expression;

2. to improve the current mathematical models of the MBN_2W maneuver for estimation of specific ventilation distribution, by introducing less stringent requirements for their use, allowing for example automated and unsupervised tracking of lung dynamic expansion heterogeneity of patients under assisted ventilation, and specifically:

   (a) to formulate and test *in silico* a generalized mathematical model of the maneuver as well as a data-fitting algorithm;

   (b) to compare *in vitro* the proposed and the classical washout mathematical models.

1.2   Thesis overview

The remaining of the thesis manuscript is organized in six chapters. The first chapter (Chapter 2) is an overview about compartmental modeling for PET and image registration. The text of each of the next four chapters corresponds to a paper submitted for publication during the Doctorate period. The last chapter (Chapter 7) presents a final discussion considering practical implications of the main results. Following, an overview of the thesis is presented, highlighting its original contributions and my specific contribution in each one of the reported works.

Chapter 3 There is a common assumption that the spatially heterogeneous lung expansion during mechanical ventilation allows for regional strains significantly larger than the global strain, which is controllable by mechanical ventilator settings. However, there is no measurement of the distribution of lung expansion during mechanical ventilation using clinically relevant settings, and how this distribution changes with development of lung injury in the time periods observed in clinical practice. Hence, it is unknown if that assumption about the heterogeneity holds true or if other factors are necessary to explain the observed VILI in healthy lung patients. Because mechanotransduction produces

an inflammatory response during VILI, its development can be monitored *in vivo* by PET scan. Image analysis can be applied to obtain high-resolution aeration and strain from CT scans. In this chapter, these imaging techniques were combined to compare the effects of supine (heterogeneous aeration) and prone (homogeneous aeration) positions in the development of lung injury. The dependence of the regional tissue inflammation on regional aeration, strain and blood volume was assessed making use of a new technique to define regions-of-interest for PET analysis. This technique consistently samples the lung in small volumes while keeping reliable fitting of ^{18}F-FDG compartmental model, increasing the resolution of the analysis. The regional aspects of VILI were further assessed with analysis of tissue expression of selected genes. The use of PET/CT allowed for longitudinal measurements revealing new information about deterioration of lung mechanics and early tissue injury in a mechanical ventilation strategy considered protective with implications to the clinical practice. Published as [80] and reproduced with editors authorization. (Objective 1)

Specific contributions: I participated in two of the ten experiments reported in the manuscript. I was responsible for all the image analysis, including the proposition and implementation of the new method to define regions-of-interest, and also statistical analysis and interpretation of all results. I created the figures and wrote the drafts and final version of the manuscript.

Chapter 4 The different sources of aeration and strain heterogeneity specified before indicate the presence of different physical scales for these heterogeneities. However, there is no quantification of aeration and strain heterogeneity at different length-scales in normal lungs, neither during the initial stages of VILI. This knowledge contributes to the understanding of the spatial progress of injury and may suggest anatomical structures relevant to the injury process. In this chapter, high-resolution aeration and strain derived from CT images were analyzed with the low-pass filtering technique [81] comparing heterogeneity in length-scales from 5 mm to 90 mm in supine and prone positions. The injury caused by different regional mechanical forces due to the heterogeneous lung expansion potentially results in different biological processes. The kinetic analysis of dynamic ^{18}F-FDG PET scans gives parameters related to different aspects of the tissue metabolic activity (linked to inflammation), which were explored to help in pathway identification from data of transcriptome wide microarray gene expression. This combination of functional parameters and gene expression allows for comparisons between regions known to be different, avoiding the reduction of the heterogeneous biological process to a

7

single sample. Additionally, it helps to interpret the complex multifactorial gene expression possibly narrowing the different causes/consequences of single pathways. Accepted for publication in Academic Radiology and reproduce in the pre-print version according to the editor rules. (Objective 1)

Specific contributions: the data for this chapter is from a previously published paper [49] and the first eight animals of Chapter 3. I was responsible for all the analysis, including the proposition of the method for pathway identification using topographical correlation with ^{18}F-FDG-PET kinetics parameters. I interpreted the results, created all figures and wrote the drafts and final version of the manuscript.

Chapter 5 The classical multicompartmental model for the MBN$_2$W maneuver considers all lung units in parallel with mixing of their contents only in the expired gas. This is fundamentally different from the anatomical characteristics of the lung where the alveolar gases mix in the conducing airway with the mix being partially re-inhaled in the next cycle. That classical model assumes constant V_T that is equal during expiration and inspiration. Reaching such conditions on V_T requires the active control of breath by the patient or anesthetized and paralyzed patients under monotonous controlled ventilation modes. Finally, in the classical model the inspired N$_2$ concentration should change as an instantaneous step at the beginning of the maneuver. This is not achievable in the current mechanical ventilators where the inspiratory gases need do move from the machine through the inspiratory limb of the respiratory circuit. In this chapter, a new generalized model for the MBN$_2$W was proposed. This new model allows for variable V_T and differences between inspired and expired volumes (variable EELV), does not assumes an ideal step change in the tracer gas and includes a common dead space in series with the parallel lung compartments. The model equations were derived in incremental complexity steps ending in a general description of individual compartments and measured gas at the mouth (compartments and dead space mixing) that reduces to the classical model if its assumptions are applied. The new model was evaluated in simulations of uni- and bimodal distributions of specific ventilation considering measurement noise. The simulations also explored different parameters for the reconstruction algorithm, including constraints that are made possible by the consideration of the series dead space. The simulated results show adequate recovery of specific ventilation distributions with noisy data and indicate the settings to be adopted in the reconstruction algorithm

in real measurements. Published as [82] and reproduced under the Creative Commons Attribution 4.0 International License.[1] (Objective 2-a)

Specific contributions: part of the proposed model was published before by two of the co-authors [83]. The theoretical concept of the complete model was developed together by the authors, and I proposed the solution for tracking the changes in EELV and formulated the final set of equations. I created all the simulations and final figures, helped to interpret the results and wrote the drafts and final version of the manuscript.

Chapter 6 The generalized model for MBN_2W proposed in Chapter 5 has less restrictions over the maneuver than the classical model [72, 74, 84] and restores the dead space to its anatomical position, i.e. in series with the ventilation compartments. The location of the series dead space has direct impact on the estimated distribution even in the ideal maneuver considered by the classical model. Using the equations describing the generalized and all-parallel models it can be analytically demonstrated that for a single compartment lung, ignoring the mixing in the dead space results in the estimation of a compartment with a lower specific ventilation. As shown in this chapter, this shift is not equal for all compartments resulting in a change in the breadth of the distribution. This difference of estimated distributions by the generalized and classical models was experimentally observed using physical single- and four-compartments models with known specific ventilations. The results demonstrate for the first time the theoretical predictions for the effect of ignoring dead space in the classical model and the practical applicability of the generalized model. Published as [85] and reproduced under the Creative Commons Attribution 4.0 International License.[1] (Objective 2-b)

Specific contributions: the experiments were planned and executed together with one co-author. I developed the analytical results, performed all the data analysis, created the figures and wrote the drafts and final version of the manuscript.

The texts of Chapters 3 to 6 are composed by the papers' main text[2] with minimal edition to comply with formatting rules. In general, the abstracts were omitted and each section of the chapters corresponds to a section in the paper (introduction, methods, results, discussion and conclusion[3]). Figures and tables numbers, and references were altered to be consistent and continuous along the text. Abbreviations were also uniquely defined (and nomenclature was unified) at

---

[1] https://creativecommons.org/licenses/by/4.0/

[2] i.e. sections as Funding Sources, Conflict of Interest, Data Availability, etc. were omitted

[3] In Chapter 3 Conclusion is merged in the Discussion

the first appearance in the thesis. For completeness, the supplementary digital contents accompanying the papers were reproduced as appendix with the same type of modifications.

Chapter 2

PET Compartmental Model and Image Registration

The results about regional tissue expansion and the consequences of regional mechanotransduction to lung injury, presented in Chapters 3 and 4, are based primarily in image processing of PET/CT scans. The two main methods applied are compartmental modeling for kinetic analysis of dynamic PET data, and image registration for voxel level estimation of lung tissue deformation. Both methods are briefly described here.

2.1 PET compartmental model

The PET is a functional image, i.e. provides spatial localization and quantification of biological processes. The function being quantified depends of the radioactive tracer used [86]. Here the focus will be the ^{18}F-FDG that is widely used in oncology [87] and was established as a marker of lung neutrophilic inflammation [47, 48].

2.1.1 The ^{18}F-FDG

The ^{18}F-FDG is a molecule analogous to the glucose where the hydroxyl of the carbon 2 is substituted by an ^{18}F (Fig. 2.1). Hence, ^{18}F-FDG follows a similar metabolic path to glucose while emitting protons from the decay of the fluorine, which allow its imaging with PET. Glucose is the main source of energy to a cell and will be uptake faster during high metabolic states (e.g. tumor cell proliferation, inflammation). The glucose uptake can be simplified in two steps, the transport to the cell and the phosphorylation. The transport is active trough membrane proteins (GLUT 1–7) activated by insulin and that function in both ways from the highest to the lowest concentration of glucose [87]. Once inside the cell, the glucose can be phosphorylated by the hexokinase (Fig. 2.1). The glucose-6-phosphate that results

11

from the phosphorylation will no more interact with the GLUT, staying inside the cell and continuing the glycolysis (or the pentose phosphate) pathway. Because the ^{18}F-FDG lacks the hydroxyl in the carbon 2, the new molecule resulting from phosphorylation (2-deoxy-2-F-glucose-6-P) cannot be further metabolized and the ^{18}F will remain trapped inside the cell. Of note, the 2-deoxy-2-F-glucose-6-P can be dephosphorylated returning to ^{18}F-FDG, which could leave the cell. In the lungs, the expression of the enzyme promoting the dephosphorylation is very low and this process is negligible.
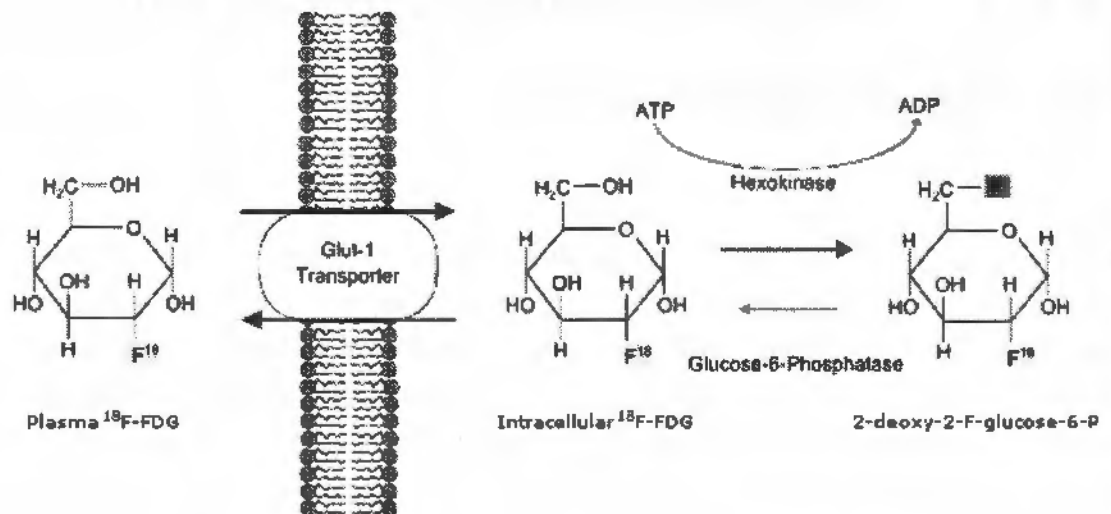
Figure 2.1: Representation of the cellular uptake of the ^{18}F-FDG. The molecule is actively transported through membrane proteins (GLUT) and the phosphorylated by hexokinase. Adapted from [87] with permission.

The described metabolism of ^{18}F-FDG in the cellular level is then controlled by the expression and activity of both GLUT and hexokinase. As said before, the transport of glucose through the cell membrane depends on a gradient, so ^{18}F-FDG uptake depends of the availability of this molecule to the tissue. Because ^{18}F-FDG is transported in the plasma, availability is proportional to perfusion and the permeability of the vessels.

2.1.2 The models

Compartmental model is a modeling technique used, among other fields, in pharmacokinetics. The objective is to describe the dynamics of a substance inside functional units of the body. Functional units are not restricted by anatomical structures, representing different states of the substance. Each compartment, models a pool of the original substance or the byproducts of its metabolism. The kinetics is given by the chemical reaction (or series of reactions) that transform the tracer between this compartments. Therefore, it is parameterized by transport rates in the forward and

backward reaction directions. The number of compartments and interpretation of the transport rates depends of the tracer and organ being modeled.

The most common model for the kinetics of ^{18}F-FDG is the three-compartment model proposed by SOKOLOFF *et al.* [88] for study brain metabolism with ^{14}C-deoxyclucose. This is the minimal model to represent the two main processes of facilitated transport and phosphorylation. The three compartments are the plasma (C_p), the extravascular compartment (C_E), i.e. tissue cells, and a metabolized compartment (C_m) representing the phosphorylated ^{18}F-FDG (Fig. 2.2A). The exchange between these compartments is given by four rate constants: K_1 and k_2 representing the transport from the plasma to the tissue, and the inverse direction; and k_3 and k_4 representing the phosphorylation and dephosphorylation rates (k_4 is normally not considered). The net uptake rate ($Ki = F_e \cdot k_3$) is given by the product of the ^{18}F-FDG available for phosphorylation (inside cells) and k_3. The amount of tracer available for phosphorylation (F_e) is the fractional volume of C_e, which is given by the balance of tracer flowing in and out ($F_e = K_1/(k_2+k_3)$). The fifth parameter of the model is the fraction of the region-of-interest occupied by blood (volume of C_p) represented as F_b.

Because advanced stages of lung injury are characterized by interstitial or alveolar edema, the ^{18}F-FDG may leave the plasma but not be available for phosphorylation. To model this condition a new compartment must be added [46]. The exchange of ^{18}F-FDG between this new extra vascular-extra cellular compartment (C_{ee}) and Ce is modeled by the rates k_5 (to C_{ee}) and k_6 (from C_{ee}) (Fig. 2.2B). The fractional volume of the cellular compartment remains equal Fe in the three-compartment model. The fractional volume of Cee is given by $F_{ee} = F_e \cdots k_5/k_6$.

These three- and four-compartment models consider that the input function (see below) and the tracer kinetics in the region-of-interest are synchronized in time. This is normally not the case and exist a delay between these curves due to the physical distance between the sample sites (Fig. 2.2C). Modeling this delay may have a significant effect in the estimated F_b and early kinetic parameters (K_1 and k_2) [89]. Moreover, because regional perfusion is a function of the local volume and transit time, the estimated delay and F_b allow for calculation of relative perfusion to the region-of-interest [89]. This three-compartment model with delayed input function was used in his thesis due to the expectation of mild injury (no significant edema) in the experimental model. Importantly, the lack of edema was confirmed with histology and wet-to-dry lung weight ratios (see Chapter 3), and the appropriateness of this model was assessed comparing the Akaike information criteria resulting from non-delayed three- and four-compartment models [46, 89].
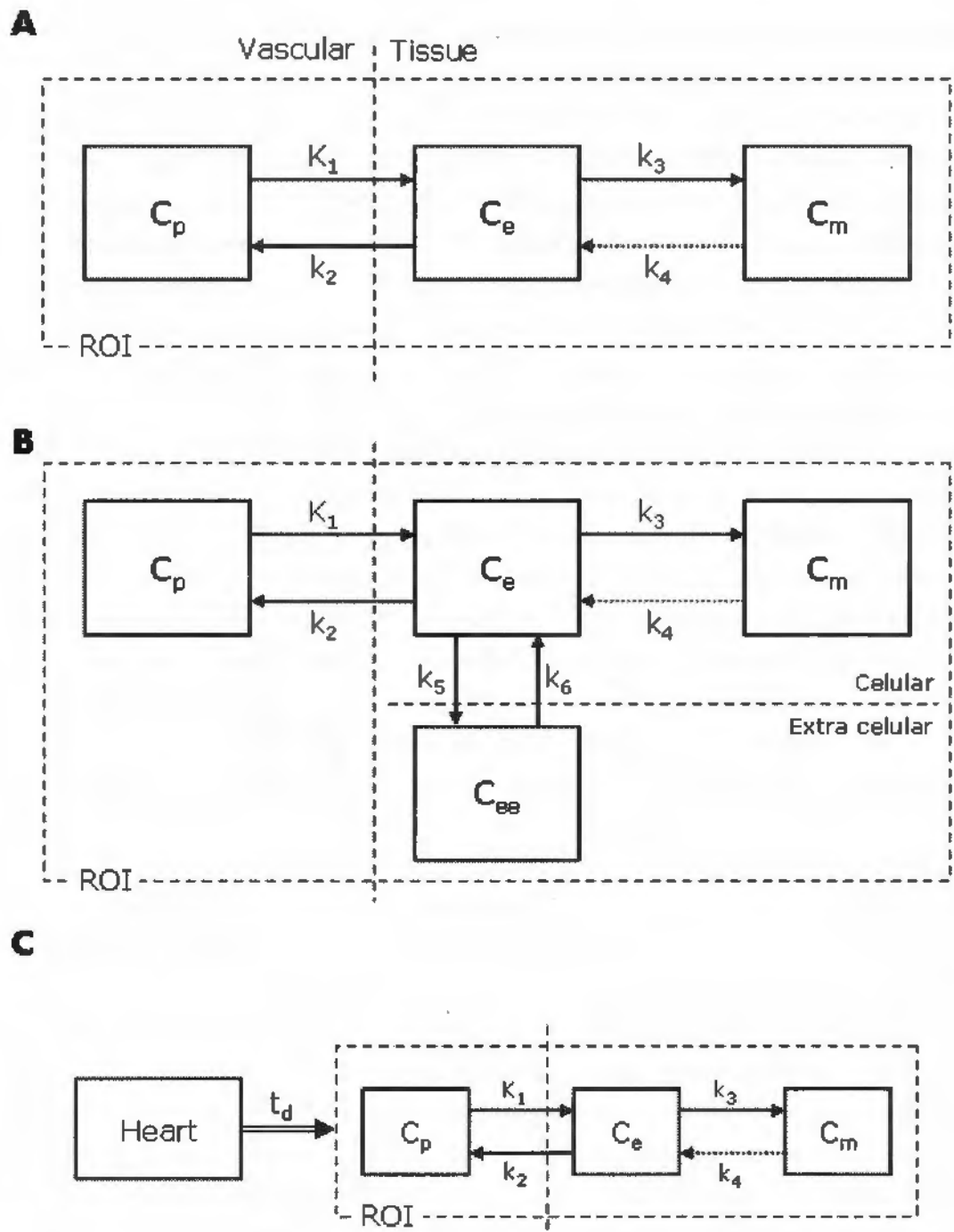
Figure 2.2: Block diagrams representing three possible compartmental models for the ^{18}F-FDG kinetics in the lungs. (2.2A) Classic three compartments (Sokoloff) model; (2.2B) four compartments model; and (2.2C) three compartments with delayed input function. C_p = plasma compartment; C_e = extravascular compartment where ^{18}F-FDG is available for phosphorylation; C_{ee} = extra vascular- extra cellular compartment (^{18}F-FDG cannot be phosphorylated); and C_m = metabolized compartment (after phosphorylation). K_1 = facilitated transport rate from blood to tissue; k_2 = transport rate from tissue to blood; k_3 = phosphorylation rate; k_4 = dephosphorylation rate; k_5 = transport rate from the cellular to the extra-cellular compartment; k_6 = transport rate from the extra-cellular to the cellular compartment; and t_d = blood travel time between the right heart and the region-of-interest (ROI).

14

Input function

The compartmental model is an input-output model; therefore, it is necessary to know the input function for data analysis. The compartmental model does not include the mixing of the injected ^{18}F-FDG in the blood, nor the uptake of tracer in regions outside the region-of-interest. These effects vary among subjects and within a subject according to their metabolic condition, avoiding an *a priori* description of the input function. Thus, to estimate this input, sequential arterial blood samples are drawn and their tracer concentration is determined [45, 90]. Normally, a large number of samples must be used to have a correct description of the shape of the curve for interpolation, especially at the first minutes when the changes are faster (Fig. 2.3). In order to reduce the number of samples, image derived methods were proposed [91, 92].
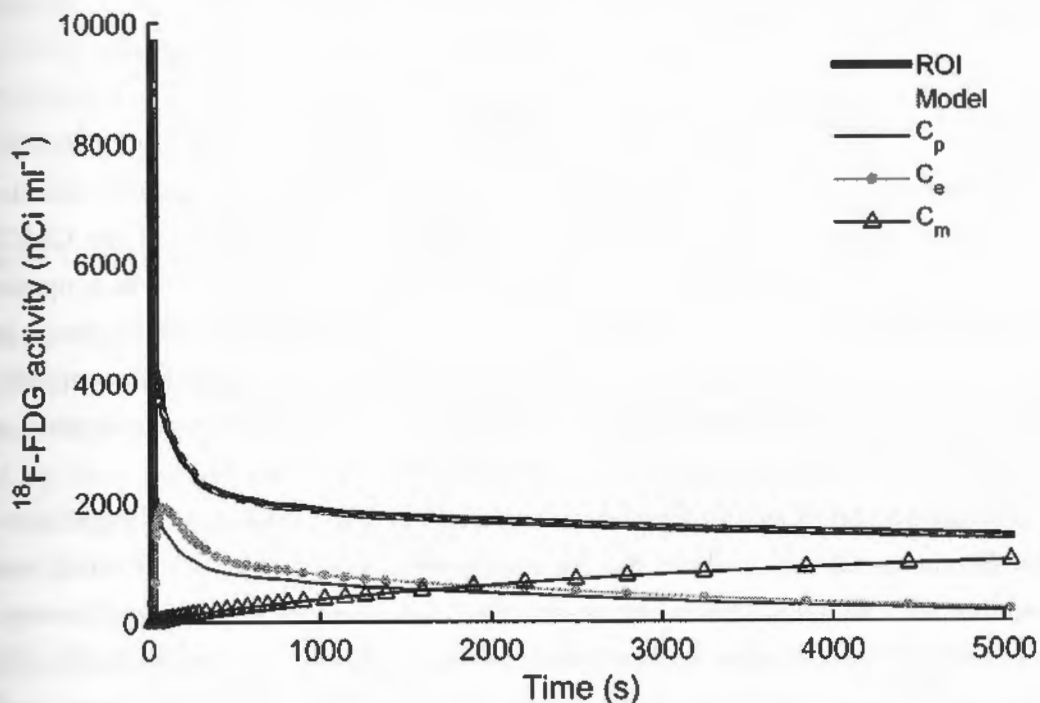
Figure 2.3: Representation of the lung ^{18}F-FDG kinetics after a pulse injection of the tracer. The curve measured in a region-of-interest within a PET image (ROI, thick black) may be fitted (Model, light gray dashed) to a sum of three compartments: the plasma (C_p, dark gray), a pool of ^{18}F-FDG available for phosphorylation (C_e, light gray continuous) and the phosphorylated tracer (C_m, black with triangles).

In such imaging guided approaches, the activity in a region-of-interest representing a blood poll before the analyzed region (for the lung it is commonly the right heart) is used to determine the shape to the input curve. The magnitude is then calibrated using the tracer concentration in a few blood samples. Three PET image characteristics should be considered during the calibration: the signal to noise ratio, the partial-volume effect, and the spillover between neighbor regions. This imposes

somewhat conflicting constraints. The signal to noise ratio increases for large number of voxels (volume), which will normally lead to regions-of-interest close to the anatomical boundaries of the blood pool. This in turn, increases the partial-volume and spillover. To mitigate these last two effects, SCHROEDER et al. [91] proposed to calibrate the input function magnitude using a two-compartment model

$$C_{blood-pool} = RC C_p(t) + SC \int C_p(t)\, dt$$

where $C_{blood\text{-}pool}$ is the tracer activity measured in the image and C_p the activity in the plasma samples. The constants RC and SC represent, respectively, the recovery coefficient that quantifies the geometrical partial-volume, and spillover coefficient. RC and SC are adjusted to the data in an iterative search to approximate the integral term, initially assuming that the C_p kinetics is equal C_{ROI} [91]. This was the method used in this thesis.

2.1.3 Experimental interpretation

The constant rate K_1 models the transport of ^{18}F-FDG from the blood to the tissue, than should be correlated with perfusion and tissue expression of the GLUT proteins. Indeed, measurements of ^{18}F-FDG kinetics and ^{15}O-water (which uptake is proportional to local perfusion [93]) show that K_1 is correlated with perfusion in breast cancer [94, 95]. This was true at baseline and in treatment follow-up [94]. Measurements in patients with cancer showed that the K_1 from tracer kinetics is correlated with GLUT gene expression of tumor cells samples [96].

The association of k_3 and hexokinase activity was also demonstrated experimentally. Similar to the result about K_1, the k_3 measured in PET kinetics of cancer was correlated with hexokinase activity in samples of the tumor cells [96, 97]. Moreover, k_3 is shown to be a marker for tumor staging and response to treatment [97, 98], reinforcing its importance to characterize metabolic activity. The other component of the net uptake rate, the F_e, was shown to correlate to neutrophils counts in histology slides of lung tissue [47], indicating that an increase in the number of this highly metabolic cells is associated with increased volume of distribution of ^{18}F-FDG.

In the context of lung injury, the metabolic activity measured with ^{18}F-FDG-PET is associated with the level of inflammation, especially neutrophilic inflammation. Ki is shown to be increased in different models of VILI [47, 49, 50], differentiating lung regions and cause of injury. High levels of ^{18}F-FDG uptake are also present in lungs of patients before and after established ARDS [99, 100]. The regional k_3 was shown to be correlated with gene expression of inflammatory markers in lung tissue [47]. The association between ^{18}F-FDG uptake and neutrophilic inflammation

was proposed by CHEN e SCHUSTER [45]. Different lung injuries show correlation of ^{18}F-FDG uptake and neutrophil migration into the lungs [45, 47, 101, 102]. Direct association of ^{18}F-FDG uptake and neutrophil activity was demonstrated in an experiment with autoradiography. It showed that in tissue slides of inflamed rats' lungs, neutrophils were the cells with the highest accumulation of ^{18}F-FDG [103]. Another rat experiment showed a parallel of increased ^{18}F-FDG and myeloperoxidase (an enzyme mostly expressed in neutrophils) activity in the lungs after systemic administration of LPS [48]. In this same paper, *in vitro* activated human neutrophil showed increased accumulation of glucose, and elevated expression of GLUT and hexokinase proteins and genes when compared to non-activated neutrophils [48]. From these findings, the measure ^{18}F-FDG uptake is considered to reflect a combination of the neutrophil infiltration (F_e) and activation (k_3), although not strictly specific. Of note, the number of cells in a region-of-interest of a PET image can be large because of more neutrophil infiltration of increase in tissue density (derecruitment), thus it is important to account for differences in tissue content when comparing regions with different levels of aeration.

2.2 Image registration

Image registration is the process of transforming the data in an image to a new coordinate system. More specifically, the goal is to match spatial features between two images. As an example, consider the use case of this thesis: register an image of the same lung at two different phases of the respiratory cycle.

In Fig. 2.4 one slice of an end-expiratory CT scan and one of an end-inspiratory scan are shown. The later was visually matched to the first. In consequence, there is a good agreement of the large vessels and airways present in the dorsal regions of both images, although their shapes and positions are noticeably different. Differences that more remarkable are observed in the overall shape of the lungs. In the end-inspiratory image the lungs (and the chest wall) are more round and have a larger area. In the ventral regions the dense structures (light colors) are clearly different between both slices and the end-inspiratory lung is located in a more apical region of the heart. These differences are captured when the end-inspiratory image is subtracted from the end-expiratory generating large positive and negative errors (light and dark gray in Fig. 2.4).

The application of image registration (to the whole images as a 3D procedure) will estimate a transformation applied to each voxel of the end-inspiratory image in order to revert the described differences. The resulting transformed image is notably closer to the end-expiratory CT, generating a blunted difference image (Fig. 2.4).
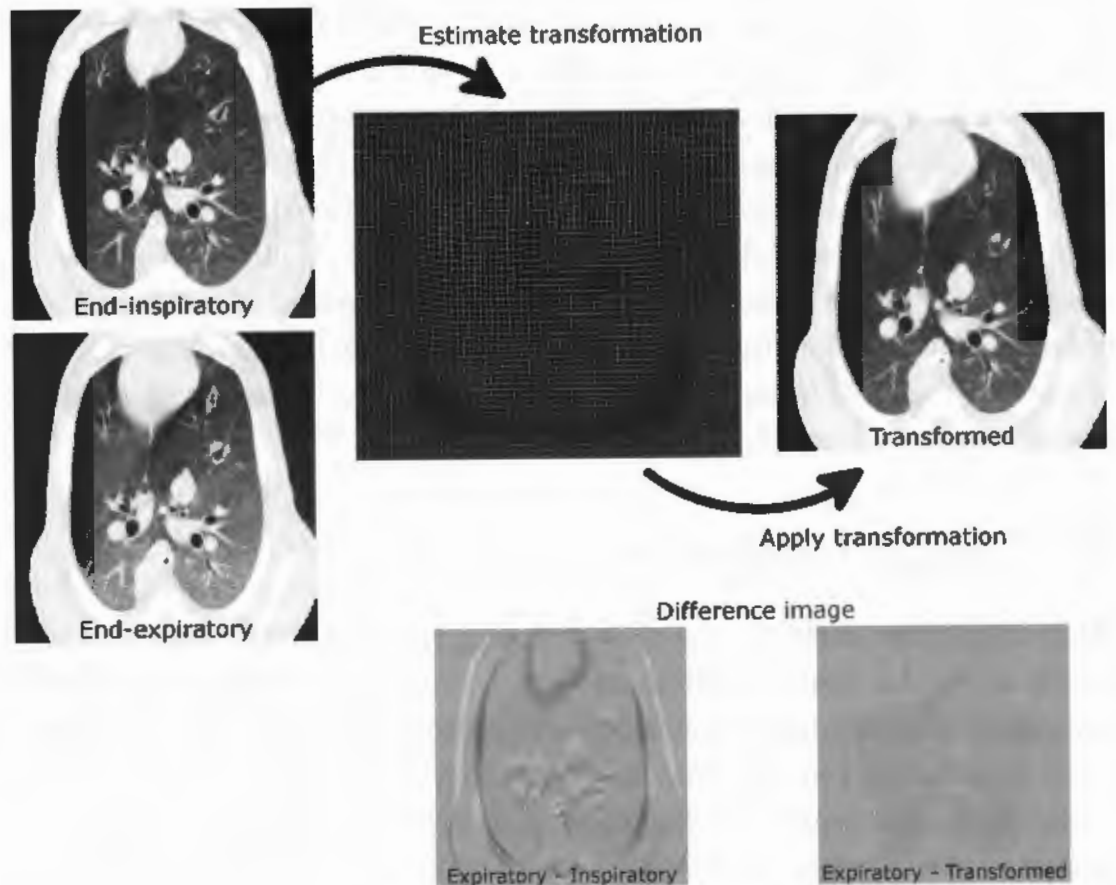
Figure 2.4: Schematic example of image registration applied to lung computed tomography (CT). The objective of image registration is to find a transformation that matches the spatial data of the end-inspiratory to the end-expiratory CT scan. The inspiratory slice before registration was visually matched to the expiratory slice. Some difference are clearly noticed, at inspiration: the area of the lungs is larger, the lungs and chest wall are more round, the lungs is positioned closer to the heart apex, and the anatomical structures (vessels and airways) in the ventral region are different from expiratory image. The two difference images at the bottom of the figure are in the same color scale.

Importantly, on top of the registration errors and noise, the difference in aeration between both lung states prevents a zero difference.

2.2.1 Applications

Image registration is applied in the medical field in order to provide spatially comparable images in longitudinal studies, and between different subjects and image modalities. In the field of neuroimaging, for example, the evaluation of brain degeneration can be performed by comparison of the patient magnetic resonance image to a template with annotated anatomical regions [104]. In the pulmonary field; this direct spatial comparison is normally performed through parametric response maps of aeration.

Parametric response maps are scatter plots of CT voxels in two different levels of lung inflation. They summarize the distribution of aeration in both lung sates, as well as the regional changes in aeration. As they are derived from CT scans, the voxels identified as having special characteristics can be mapped to the original image providing anatomical information about the observed mechanisms [105]. Parametric response maps are used primarily in chronic obstructive pulmonary disease (COPD) where it can identify functional small airway disease (fSAD, voxels' Hounsfield units (HU)< -856 at end-expiration and > -950 at full inspiration) and emphysema (voxels' HU< -950 in both lung inflations), the two main components of COPD [105]. A recent application of prametric response maps is for identification of areas in risk of VILI (injury defined irreversible low gas content regions, voxels' HU> -300 during the whole breath cycle) after a injury insult with acid aspiration [106]. In experimental measurements in rats such areas in risk of injury were determined as having large tidal changes in density, from $-600 < \text{HU} < 0$ at end-expiration to $-700 < \text{HU} < -300$ at end-inspiration [106].

To study mechanotransduction, more relevant than spatially matched images, is the estimated transformation by itself. The output of an image registration procedure is a vector field $(T(x))$ that maps the location of each voxel from one image to the other. When generating the transformed image, the voxels are moved to their new positions and the intensity values are interpolated in a new image with the same voxel grid than the original CT. When considering a voxel together with its neighbors, the final transformed voxel has an effective shape and volume that are potentially different from the grid in the CT scan (Fig. 2.5). The $T(x)$ provides information about deformation, and hence strain, in the resolution of voxels.

Voxel level strain can be calculated from the determinant of the Jacobian matrix of $T(x)$, which is an infinitesimal local approximation of the vector function [58]. Importantly, the strain calculated from the Jacobian is referred to the total voxel
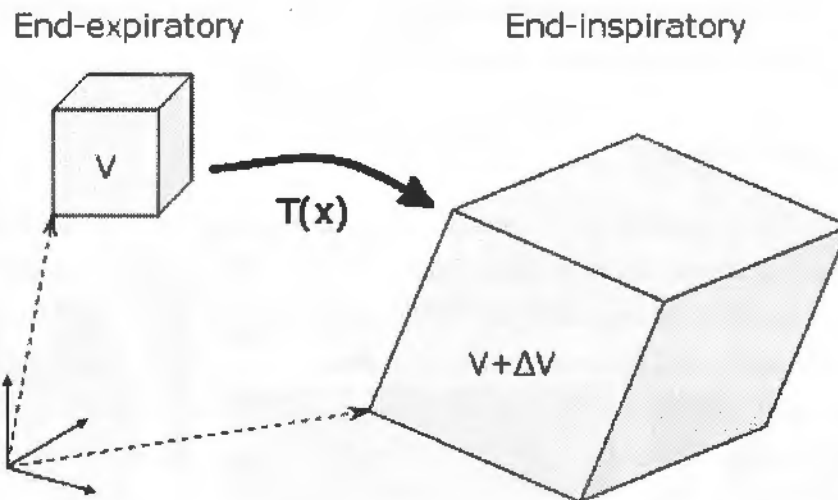
Figure 2.5: Representation of the volumetric deformation assessed by image registration. From end-expiration to end-inspiration, each voxel can be translated to a new location by a transformation $T(x)$ and the movement of neighbor voxels may result in rotation and change in volume.

volume (tissue+air), differing from other strain estimations based on changes in gas content [51, 67]. It is possible to calculate a gas based voxel level strain as the image registration gives spatially matched expiratory and inspiratory images. However, this measure is more sensitive to noise than the Jacobian, resulting in poor reproducibility [107].

2.2.2 Methods

As shown in the example in Fig. 2.4, the lung expansion during inspiration results not only in movement in the cephalo-caudal axis and expansion of the rib cage, but also in out-of-plane movements (ventral and dorsal regions do not match in the same slice between both inflation states). Consequentially, registering two lung images requires an elastic registration, which allow for local deformations. There is a variety of such methods proposed in the literature. These methods are mainly differentiated by the type of transformation (e.g. diffeomorphic, thin-plate), the regularization (e.g. B-spline, greedy symmetric) and cost function (e.g. tissue preserving, voxel intensity, cross-correlation). One list of methods in the perspective of pulmonary imaging is found in [108].

In this thesis, all the image registrations were performed using the open-source Advanced Normalization Tools (ANTs)[1]. It provides a set of choices for the three characteristics listed above, from which was chosen a diffeomorphic transform with

---

[1]Available at `stnava.github.io/ANTs/` in May/2018

B-spline regularization minimizing the cross-correlation between neighbor voxels. By definition, diffeomorphic transforms are smooth with smooth inverse, presumable characteristics of elastic tissue deformation. B-spline regularization guarantee continuity of the deformation field and are computationally efficient for problems requiring high amount of regularization [104]. The cross-correlation is not affects by multiplication by a constant, being more robust to expected changes in voxels intensity due to differences in lung aeration at expiration and inspiration.

2.2.3 Validation

The primary method for evaluation of the results of the image registration is the landmark distances. A set of landmarks (characteristic points that are present in both images) is defined in both end-inspiratory and end-expiratory images in a paired way. After image registration, $T(x)$ is applied to one of these sets of points generating the transformed landmarks. In a perfect registration this transformed set is exactly superimposed to the one in the reference image, than the distance between transformed and reference landmark positions is a figure of merit of the registration procedure.

Two methods were previously proposed for defining the paired landmarks in lung images: bifurcations of the airways and vessels trees [109], and a semiautomatic visual matching [110]. Here the second was used because the performance of airways and vessels segmentation is poor for large slice thickness [111]. The semiautomatic landmark definition was performed using the public available software isiMatch[2]. First, the reference landmark set is automatically generated as distinctive points, i.e. points in sharp intensity transitions that can be differentiated from its neighbors within a given sphere [110], in one of the images (Fig. 2.6, left). Then, each landmark is sequentially displayed in axial, sagittal and coronal views and using the same views of the other image, the user can manually select the point corresponding to the landmark (Fig. 2.6, right). During the matching process the isiMatch generates a thin-plate transformation to try to predict the location of the next points, after a user defined threshold of consecutive confirmed guesses, it automatically defines the rest of the matches in the landmark set. The final matched landmarks should be verified by the user. Results for landmark analysis applied to the set of images of this thesis are shown in Appendices A and B.

Other methods to validate the results of lung image registration include measures of the superposition of lung masks [112] and the positioning of lung fissures [108]. In 2010, an image registration challenge was proposed [108]. It compared 34 methods of image registration in a common set of lung images. Of note, the ANTs registration

---

[2]Available at http://isimatch.isi.uu.nl in May/2018
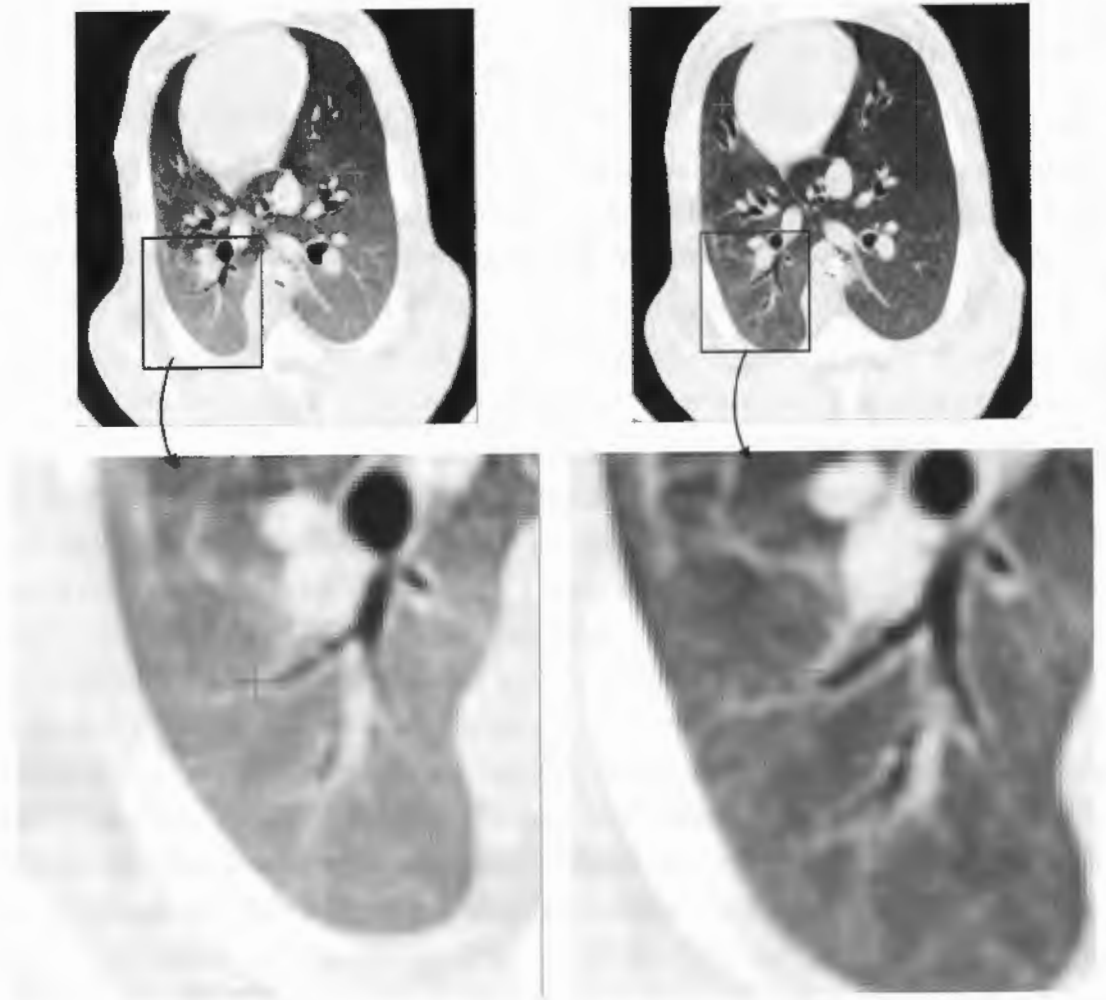
Figure 2.6: Example of matched landmarks in the expiratory (left) and inspiratory (right) images.

algorithm adopted here was later included in the analysis and positioned in 3rd at the time the data processing for the thesis was initiated.

The three methods commented above (landmark, Dice distance and fissure location) provide a metric for the spatial matching between the reference and transformed images globally and in sparse points. Therefore, they are only an indirect measurement of the accuracy in estimation of local volume changes. As these regional volumes are the variable of interest when studding mechanotransduction, here a directed assessment of average regional expansion was proposed. The volumetric deformation calculated from image registration was compared to references derived from using the same images: the whole lung inspiratory and expiratory masks; large regions-of-interest comprising $1/15^{th}$ of the total lung tissue at end-expiration and end-inspiration either in the ventro-drosal (Fig. 2.7, left) or latero-lateral (Fig. 2.7, center) axis; and in tetrahedra defined between the landmarks (Fig. 2.7, right). In all cases, the image registration derived deformation (Jacobian = final/initial volume) was the mean of voxels within the region-of-interest (for the tetrahedra the center of the voxel was considered). The data was from eight animals mechanically ventilated with low V_T ($\sim$8 mL kg^{-1}) and PEEP (5 cm H$_2$O) in supine (n=5) and prone (n=3) positions from the experiment described in Chapters 3 and 4. In all animals, there was three pairs of CT scans: at baseline, and after 6 h and 24 h of mechanical ventilation. Landmarks where available for three animals (2 supine and 1 prone) at baseline and 24 h, and one supine animal at 6 h (chosen because presented the largest change in volume).
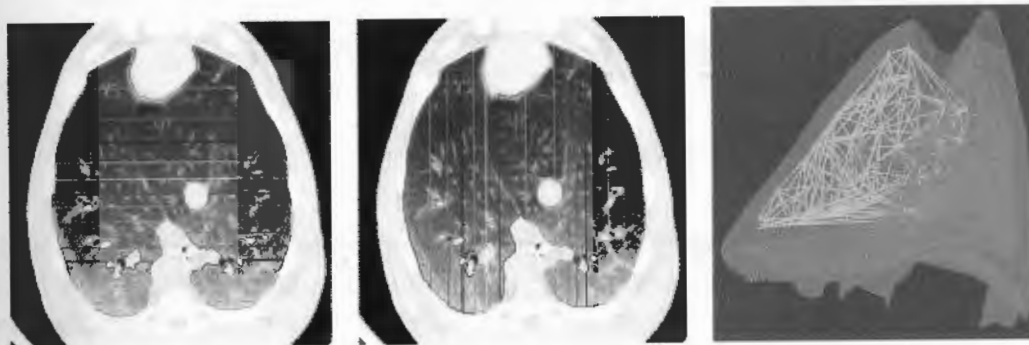
Figure 2.7: Reference regions-of-interest for evaluation of regional deformation estimation by image registration. The recovery of spatial distributions of relative deformations by image registration was validated in 15 large regions-of-interest with equal mass defined in the ventro-dorsal (left) and latero-lateral (central) axis. For smaller length-scales, tetrahedra (right) were defined between landmarks semi-automatically matched in the expiratory and inspiratory images.

Whole lung

For the whole lung, the reference was the ratio of the number of voxels in the inspiratory to the number of voxel in the expiratory mask. The comparison showed that the average deformation estimated with image registration represented the different expansions in the 24 images, although with a systematic lower magnitude (difference $= -0.90 \pm 0.04$, (-7 ± 2) %, Fig. 2.8). Additionally to an error in the registration, this difference in magnitude also reflects uncertainty in lung segmentation. There was a proportional bias, with the difference between the Jacobian and the mask deformation increasing for the largest differences between expiratory and inspiratory volumes. A decrease in performance (assessed by landmark distances) of image registration with increasing lung volume variation was reported before with a different registration method [113], being inherent of the current available registration techniques. For the cases in this thesis, a factor that may have contributed to this proportional error is that the field-of-view of the CT did not include the whole lung with a possible movement of tissue to outside the image during inspiration.
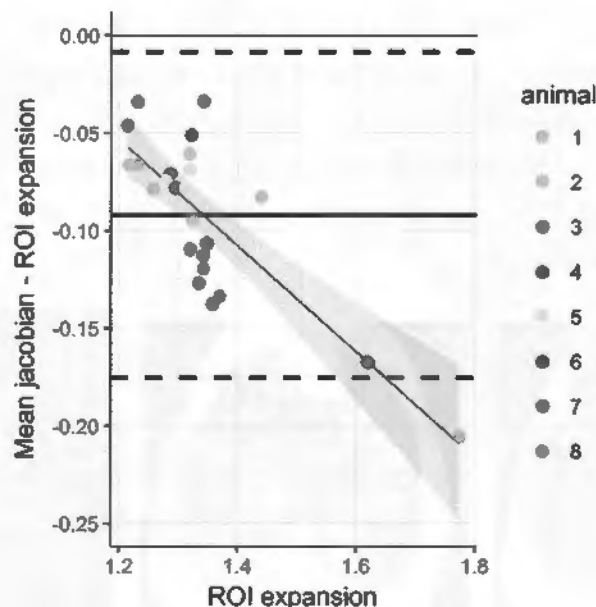
Figure 2.8: Bland-Altman plot for the comparison of the whole lung average expansion estimated with image registration and the volume change between expiratory and inspiratory masks. The image registration is sensible to difference in expansions between animals. However, the accuracy decreases for larger deformations.

Iso-tissue regions-of-interest

The goal with the iso-tissue regions-of-interest was to identify if the image registration could represent the spatial profiles of lung expansion. To generate the references, the tissue content of each row or column of voxels within the lung masks

was calculated and lines or columns were grouped to account to as close as possible $1/15^{th}$ of total tissue, without superposition and including the whole masks. Because the resolution of the reconstructed image was low in the cephalo-caudal axis (slice thickness = 2.5 mm) the variability of tissue between regions-of-interest would be large and this direction was not considered. The reference expansions were the ratio of corresponding regions-of-interest in both lung states.

The Jacobian provided regional deformations that followed the heterogeneous spatial distribution in supine and the homogeneous distribution in prone. This was true for both vertical and lateral directions in the three time points (Fig. 2.9). Again, the magnitude of the deformation from image registration was lower than the direct obtained from the regions-of-interest. Furthermore, it seemed to increase for larger deformations.
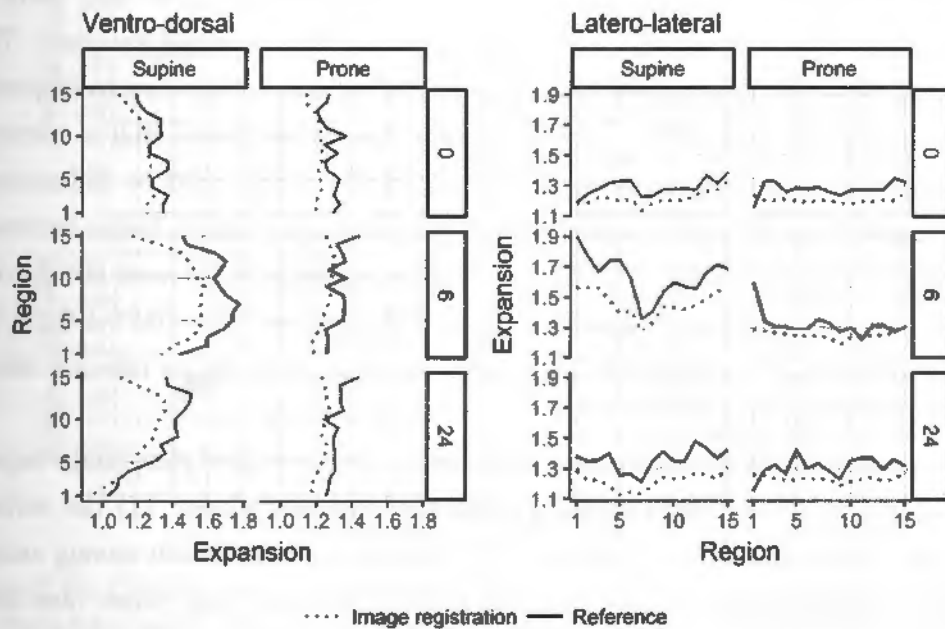
Figure 2.9: Examples of lung expansion profiles along the ventro-dorsal and latero-lateral axis during mechanical ventilation in supine and prone positions. The curves represent the deformation of 15 equal tissue regions-of-interest in each axis. Note that despite the difference in magnitude, average voxel level deformation (dashed lines) followed the spatial pattern of the reference regions-of-interest (solid lines). Data is for one supine and one prone animal at baseline (0), and after 6 h and 24 h of mechanical ventilation.

Tetrahedra

The tetrahedra were used to assess deformations in length-scales smaller than in the iso-tissue references. The vertices were automatically defined using Delaunay triangulation constrained to the left and right lung boundaries to avoid tetrahedra

25

partially outside the lung. The vertices defined in the expiratory landmarks were repeated for the inspiratory to reassure matching. Tetrahedra with height lower than 2.5 mm were excluded. The reference expansion was the ratio between the volume of the inspiratory and expiratory tetrahedra.

In a first moment, the small length-scale deformation assessed with the tetrahedra pointed to low agreement between image registration and the reference (Fig. 2.10, Pearson correlation r=(0.24 ± 0.12) [range 0.09 to 0.46]). This result did not seem to be compatible to the landmark distance ((1.6 ± 1.4) mm, below the slice thickness of 2.5 mm). The apparent disagreement in the data leads to a close examination of the tetrahedra that showed a difference in the tissue amount represented by the corresponding expiratory and inspiratory tetrahedra. The correction for this tissue difference clearly increased the correlation (r=(0.51 ± 0.17) [0.19 to 0.66, Fig. 2.10 lower panel). This improvement indicates that there was an important contribution of tissue warping to regional lung deformation. Thus, the planar faces of the tetrahedra were not preserved from expiration to inspiration as imposed in uncorrected data. Interestingly, in the iso-tissue ROI a correction for differences in tissue content at both lung states (there could be differences in the lung inside the field-of-view and variations due to the discrete tissue increments restricted to one row/column) also improved the agreement between the Jacobian and the reference (r=(0.54 ± 0.34) [−0.43 to 0.95] before and r=(0.75 ± 0.23) [0.14 to 0.98] after tissue correction). Therefore, warping seems to be relevant also for large regions-of-interest.

Overall the results of this internal comparison demonstrated that image registration estimation of lung deformation provides information about: (1) the variation in regional expansion within the lungs; (2) differences in expansion among animals; and (3) changes in expansion for the same lungs at different time points (and degree of injury). Hence, this is an adequate method to be applied in the investigation of progression of spatial distribution of tidal strain during development of VILI.
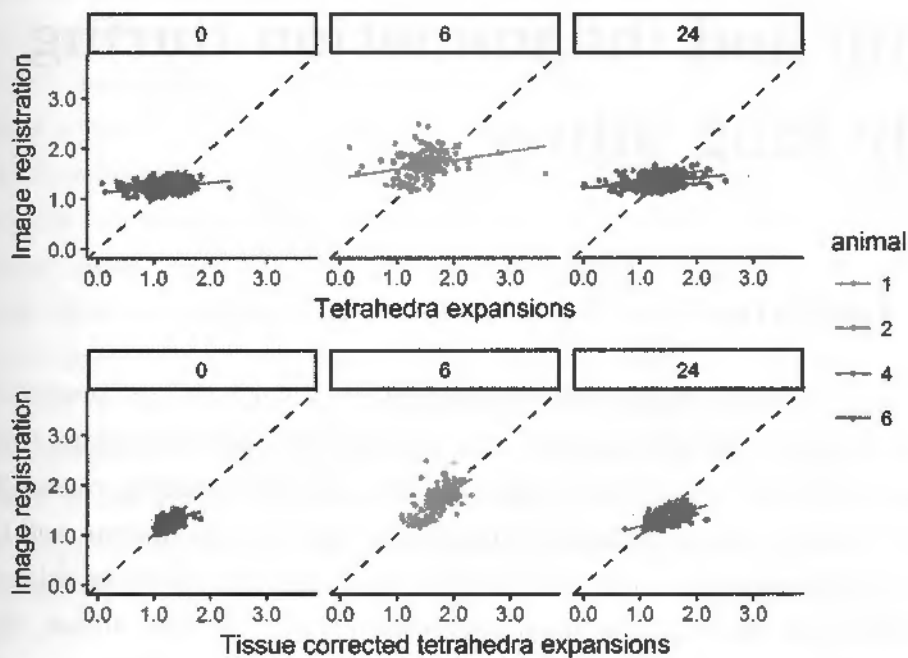
Figure 2.10: Correlation of local lung deformation estimated from image registration and from tetrahedra between matched landmarks. Correction of reference values by the ratio of end-expiratory and end-inspiratory lung tissue within the tetrahedra improved the correlations. This indicates the presence of significant warping of the planar faces of the tetrahedra. The dashed line represents the identity. Data is from three animals at baseline (0) and 24 h and one animal at 6 h.

Chapter 3

Deterioration of regional lung strain and inflammation during early lung injury

3.1 Introduction

Recent clinical trials and large registry studies have shown benefits of protective ventilatory strategies in patients without lung injury at the onset of mechanical ventilation both in intensive care units [28, 30, 31, 114, 115] and operating rooms [29, 32–34, 116]. However, the mechanisms causing lung injury remain unclear, and there is no known optimal strategy to prevent injury in these patients. Limiting tidal volume (V_T) has been proposed as the main intervention [117, 118]. In contrast, data are conflicting for strategies aiming at homogenizing lung aeration such as prone position and higher positive end-expiratory pressure (PEEP). In critically ill patients, these interventions are predominantly directed to severe cases of the ARDS despite calls for early use [119, 120] and adverse results of aggressive PEEP strategies [121]. In surgical patients, while intraoperative low PEEP is still prevalent worldwide [53], intermediate levels have been associated with better pulmonary outcomes [122].

At least three factors could contribute to the injurious effect of heterogeneous lung aeration in initially uninjured lungs. First, regional parenchymal stretch could exceed the global strain (change in total lung volume/resting volume) during tidal breathing because of atelectasis, airway closure or heterogeneity in regional ventilation. Data are scant in this field, and it has been argued that experimental global strain thresholds for lung injury (=1.5 to 2.0 applying $V_T \geq 20\,\mathrm{mL\,kg^{-1}}$ for $(28 \pm 17)\,\mathrm{h}$) [41] would not occur in human healthy lungs even with moderate V_T [40]. Second, sepsis, surgical inflammatory response, and other injurious insults could increase the susceptibility of lung parenchyma to mechanical stretch (two-hit

mechanism). Third, a mechanism linked to regional blood volume or flow could affect susceptibility to injury or its progression [123]. Knowledge on such factors is essential to guide early management and prevent ARDS in those patients. Although animal experiments provided information on the first two factors [22, 51], a combination of exaggerated V_T, short experimental times and use of small animals limit their extrapolation to conditions comparable to those present in humans.

Computed Tomography allows for high resolution assessment of regional lung deformation [58, 64–66]. Neutrophilic inflammation is a major process in early lung injury quantifiable with PET [45, 47–50]. Using hybrid PET/CT methods, we tested the hypotheses that (1) mechanical ventilation strategies consistent with clinical practice do not protect from worsening in regional lung strains during early lung injury, and (2) local neutrophilic inflammation is associated with local strain and blood volume at global strains below an injurious threshold [41]. We investigated these hypotheses in a large animal model comparable to human lung inflation pursuing the following goals: 1) to quantify the spatial distribution of aeration and tidal strain during the first 24 h of mild endotoxemia and mechanical ventilation. To study the effect of aeration heterogeneity on strain distribution, we compared the usual heterogeneous lung aeration (supine) with a standard homogeneous condition (prone); and 2) to establish the topographical relationship between regional neutrophilic inflammation as well as gene expression markers of lung inflammation and injury with strain and blood volume. Our results, reinforced by data in critically ill patients, support the concept of applying lung homogenization strategies before the onset of ARDS.

3.2 Methods

The Subcommittee on Research Animal Care at the Massachusetts General Hospital approved the experimental protocol. Ten female sheep ((15.7 ± 2.6) kg) were anesthetized, paralyzed, intubated and mechanically ventilated for 24 h using the ARDSNet lower PEEP table [27] and low V_T adjusted to reach an alveolar plateau in the volumetric capnogram. After prone lung recruitment, animals were divided into: supine (N=5) or prone (N=5) positions. Intravenous endotoxin was started after baseline data collection ($2.5 \, \text{ng} \, \text{kg}^{-1} \, \text{min}^{-1}$, Escherichia coli O55:B5, List Biologic Laboratories Inc, Campbell, CA). Methods are detailed in Appendix A.

3.2.1 CT Imaging

At baseline, 6 h and 24 h, CT images were acquired during end-inspiratory and end-expiratory breath holds for aeration and strain analysis; and at mean lung

29

volume (tidal breathing, 2 min) for PET attenuation correction and delineation of regions-of-interest. Voxel gas fraction was quantified considering air Hounsfield units (HU)= − 1000 and tissue HU=0 as Fgas = voxelHU/ − 1000.

We used image registration of the end-inspiratory to the end-expiratory CT images to calculate voxel level tidal strain (voxel volume change/end-expiratory volume including lung tissue+air) [58, 64–66]. Registration accuracy was validated using landmarks (Appendix A Fig. A.2). To compare animals and time points, strains were normalized by CT-measured global inspired air volume. Heterogeneity of aeration and tidal strain were assessed by the variance normalized by the squared mean.

3.2.2 PET Imaging

At baseline and 24 h, we acquired dynamic PET images of ^{18}F-FDG to measure tissue glucose metabolism, a biomarker of early ARDS [49]. Kinetics parameters reflective of net uptake, phosphorylation rate, and volume of distribution and blood volume [124] were calculated for the whole lung and multiple small cylindrical regions-of-interest ($\sim$1.4 mL).

3.2.3 Tissue Samples

At 24 h, lung tissue was sampled from ventral, mid and dorsal regions. From the left lung we assessed histological lung injury score [125] and from the right lung, wet-to-dry ratios and gene expression.

Gene Expression Analysis

Using real-time reverse transcription quantitative PCR (RT-qPCR), we measured tissue expression of genes related to inflammatory cytokines (IL-1β, IL-6, CXCL-8), neutrophilic inflammation (ICAM-1, CD11B) and epithelial (RAGE) and endothelial (amphiregulin, PAI-1) cell injury.

3.2.4 Human Data

PET/CT images were acquired for two septic patients after informed consent from their surrogates. Both were mechanically ventilated (<96 h) in supine position with low V_T (5.0 mL kg^{-1} and 7.0 mL kg^{-1}) and moderate PEEP (8 cm H$_2$O and 13 cm H$_2$O).

3.2.5 Statistical Analysis

Data are mean±SD or median [25th-75th percentile] as appropriate. Two-way repeated measures ANOVA was used for comparisons within and between groups, applying aligned rank transformation if needed. Multiple comparisons p-values were calculated from a multivariate t-distribution or adjusted by Benjamini-Hochberg. Determinants of change in 18F-FDG phosphorylation rate from baseline to 24 h were assessed through mixed-effects linear regression. Tests were two-tailed and performed in R 3.3.1(R Foundation for Statistical Computing, Vienna, Austria). Significance was set at p<0.05.

3.3 Results

Mechanical Ventilation and Mild Endotoxemia Produced Mild ARDS in 24 h

P_aO_2/F_IO_2 ratios decreased in supine animals with gas exchange criteria for mild ARDS reached at 6 h and worsening despite increased F_IO_2 (Fig. 3.1A, Appendix A Tables A.3 and A.4). Supine animals presented lower systemic blood pressure than prone despite their higher cardiac output (Appendix A Table A.5).

Histology showed mild-moderate injury scores in both groups, with more marked ventral-dorsal score gradients in supine animals (Fig. 3.1F). The main factor for those scores was neutrophilic infiltration (interstitium¿air spaces, Fig. 3.1G, Appendix A Table A.6). Hyaline membranes while infrequent, were more prevalent in dorsal areas of supine sheep. Wet-to-dry ratios showed no group effect (supine 5.9 [5.7 to 6.1] and prone 5.6 [5.4 to 5.8]).

Transpulmonary Pressures were Higher in Heterogeneously Aerated Supine Lungs in the first 24 h of Lung Injury

Transpulmonary and driving pressures increased continuously during the 24 h. Transpulmonary pressures were higher in supine (heterogeneously aerated) than prone (homogeneously aerated) sheep (Fig. 3.1C). In contrast, no difference was observed for driving pressures (Fig. 3.1C). This was explained by the higher lung elastance in supine while prone sheep with supported abdomen had higher chest wall elastance (Fig. 3.1D-E). Only after 6 h lung elastance in prone ((48.7 ± 24.8) cm H_2O L^{-1}) deteriorated to values comparable to those present at baseline in supine animals ((44.2 ± 7.9) cm H_2O L^{-1}). Resistances were comparable between groups (Appendix A Table A.7).
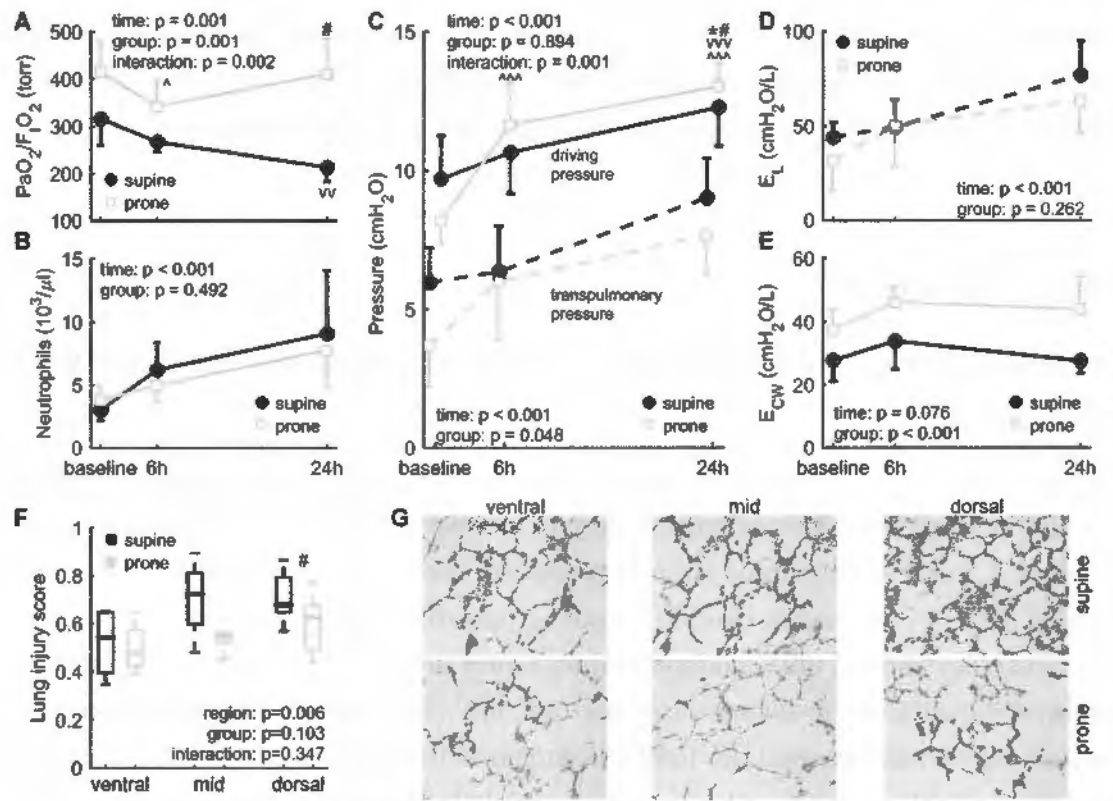
Figure 3.1: Ratios of arterial oxygen tension to inspired oxygen fraction (P_aO_2/F_IO_2, 3.1A) and peripheral blood neutrophils counts (3.1B) at baseline, and after 6 h and 24 h of low tidal volume mechanical ventilation and mild endotoxemia. (3.1C) Driving pressure ($E_{RS} \cdot V_T$, solid line) and delta transpulmonary pressure ($E_L \cdot V_T$, dashed line). The equal driving pressure with different transpulmonary pressure in supine and prone positions was explained by the difference in lung (E_L, 3.1D) and chest wall elastances (E_{CW}, 3.1E). ^ prone and 'v' supine vs baseline. # prone and * supine vs 6 h. One symbol $p<0.05$ and three symbols $p<0.001$. Gray square = prone; black circle = supine. Histological findings showed regional differences in lung injury. (3.1F) Boxplot of lung injury score evaluated in three regions from ventral to dorsal in supine (black) and prone (gray) animals. # vs ventral region, $p<0.05$. (3.1G) Examples of H&E staining in high-power (400X) fields for each one of the regions in one supine and one prone animal.
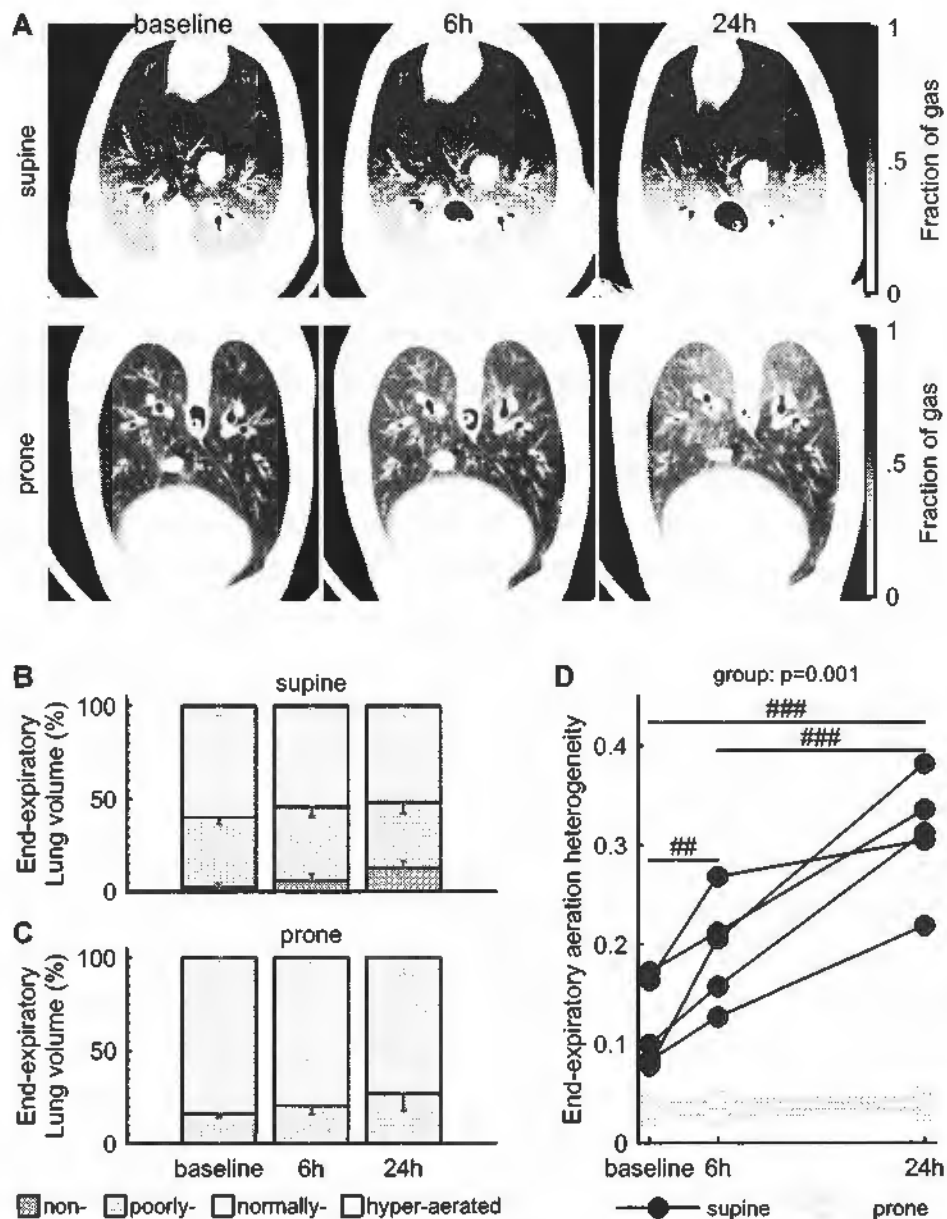
Figure 3.2: Lung aeration decreased faster in supine than prone conditions when a mechanical ventilation strategy compatible with clinical practice using low positive end-expiratory pressure and tidal volume was applied for 24 h to mild endotoxemic animals (3.2A). In the supine lung, on average 48 % of regions are either non- or poorly aerated at the end of 24 h of mechanical ventilation and endotoxemia (3.2B) while in prone animals 27 % of the lung is poorly aerated and none nonaerated (3.2C). Non-aerated = $F_{GAS} < 0.1$, poorly-aerated = $0.1 \leq F_{GAS} < 0.5$, normally-aerated = $0.5 \leq F_{GAS} < 0.9$ and hyper-aerated = $0.9 \leq F_{GAS}$. (3.2D) Aeration heterogeneity, measured as the variance normalized by the squared mean along time. There is marked contrast between the progressions of aeration heterogeneity in supine versus prone animals, with increase significantly only in supine. Values computed at end-expiration. Group effect is indicated in the figure. # represents comparison among time points, ## $p < 0.01$ and ### $p < 0.001$. Prone animals had no difference between time points. Gray squares = prone; black circles = supine. All data refer to the whole lung.

34
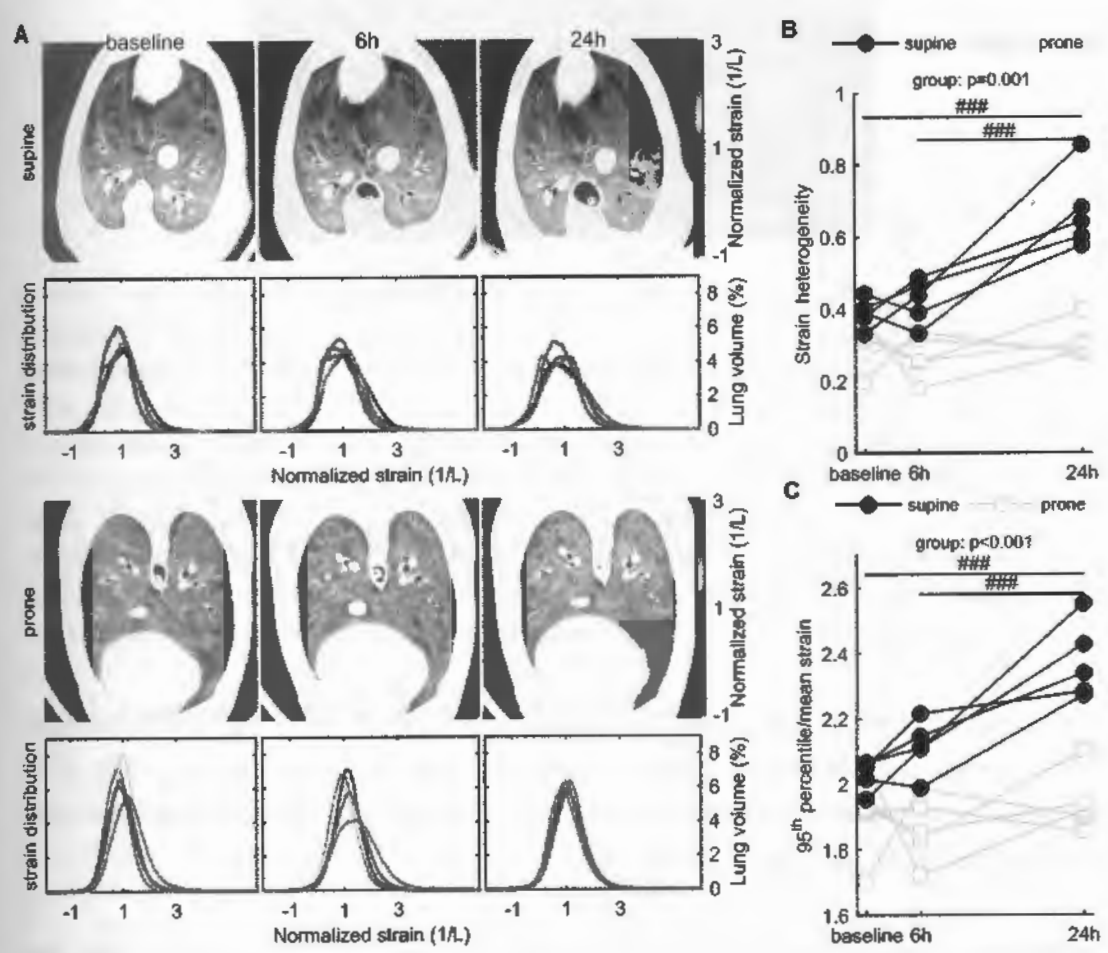
Figure 3.3: Normalized strain computed from measurements at the voxel level in supine and prone animals at baseline and after 6 h and 24 h of low tidal volume mechanical ventilation and mild endotoxemia. (3.3A) A transverse slice at approximately 2/3 of the cephalo-caudal axis is presented along time showing voxel level strain in a cold to hot color scale (dark blue=compression/no strain, red=higher strain value within the image) superimposed on the CT. Note the heterogeneous spatial distribution of strains in supine animals, in contrast to the more homogeneous distribution in prone sheep, also shown in the normalized strain distribution presented for each animal (different colors). Heterogeneity (variance normalized by squared mean strain) increased in the supine position (3.3B), leading to an increase in the ratio of maximum (95th percentile) to mean strain in this group (3.3C).
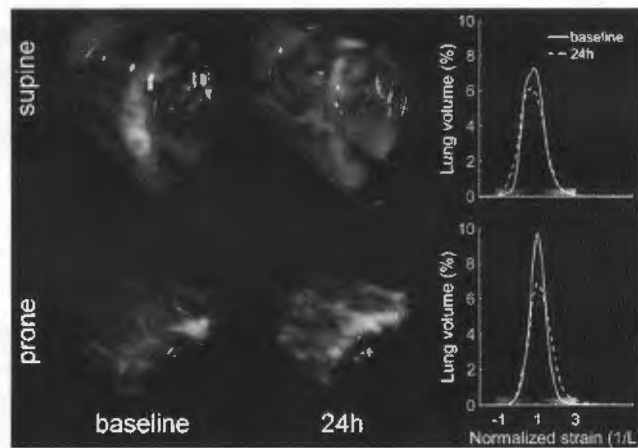
Figure 3.4: Normalized strain in one supine (upper panels) and one prone (lower panels) animal at baseline and after 24 h of low tidal volume mechanical ventilation and mild endotoxemia. Strains are color coded from low and slight compression $-1\,L^{-1}$ (blue) to expansion $3\,L^{-1}$ (yellow). Values at the ends of the scale were highlighted making the center $(1\,L^{-1})$ transparent with a gradual increase in opacity for both sides, as shown in the color bars associated with the strain histograms in the right panels. In both groups, there was heterogeneity in isogravitational levels. Note the larger heterogeneity in the spatial distribution of strains in the supine position, with more extreme values seen in subdiaphragmatic (dark blue) and nondependent (yellow) regions, while a more homogeneous pattern is observed in prone conditions.

normal-high aeration. In contrast, prone animals displayed a markedly homogeneous spatial distribution of strain vs aeration, slightly spread at 24 h (Fig. 3.5). Parametric response maps showed irreversibly low gas content regions present only in supine animals (Appendix A Fig. A.6).

Increased Lung Tissue ^{18}F-FDG Uptake at 24 h of Lung Injury was Associated with Regional High-Aeration, Blood Volume and Tidal Strain

Whole lung metabolic activity estimated from ^{18}F-FDG uptake increased significantly at 24 h in both groups $((0.23 \pm 0.04) \times 10^{-2}\,min^{-1}$ to $(0.34 \pm 0.09) \times 10^2\,min^{-1}$, Fig. 3.6A). This increase was due mostly to an increased phosphorylation rate $((1.9 \pm 0.2) \times 10^{-2}\,min^{-1}$ to $(2.6 \pm 0.5) \times 10^{-2}\,min^{-1}$, Fig. 3.6B), indicating more cellular activation than increased ^{18}F-FDG volume of distribution (Fig. 3.6C). The circulating neutrophil counts increased in both groups (Fig. 3.1B).

Spatial distribution of ^{18}F-FDG uptake rate was homogeneous for both groups at baseline. At 24 h, it remained homogenous in prone, but showed a vertical gradient for supine sheep (Fig. 3.6D, Appendix A Fig. A.7). This gradient was not only due to higher density in dependent atelectasis, as tissue-normalized uptake increased more in atelectatic than in continuously normally aerated regions (F_{GAS}=0.5 to
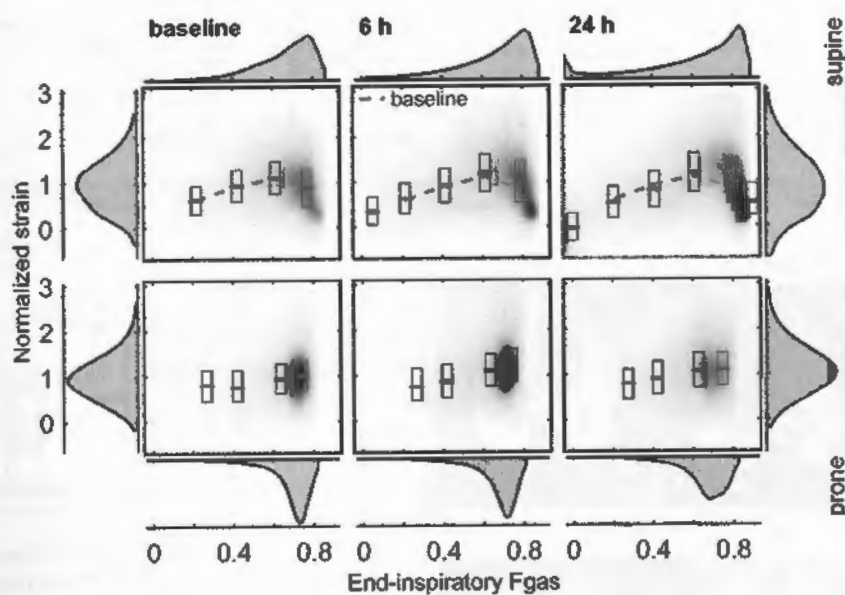
Figure 3.5: Voxel level normalized strain versus end-inspiratory aeration (fraction of gas, F_{GAS}) at baseline and after 6 h and 24 h of mild endotoxemia and low tidal volume mechanical ventilation. Data refers to all animals in supine (upper panels) and prone (lower panels). The boxes represent median (red) and interquartile range of strains for voxels in the aeration intervals: <0.1; 0.1 to 0.3; 0.3 to 0.5; 0.5 to 0.7; 0.7 to 0.9; >0.9, centered in the mean aeration within each aeration interval. Voxels between the 5th and 95th strain percentiles are depicted in a two-dimensional histogram, with the gray scale indicating the fraction of total lung volume represented by a pair of strain and aeration (black is highest). Gray scale is the same within groups. In the supine animals (upper panels), strain-aeration relationships showed an inverted U-shaped pattern. Strain increased with aeration up to an $F_{GAS}\sim0.6$ followed by a decrease with aeration for F_{GAS} above that value. This pattern was consistent across time points, with progressive decrease in median strain at low aerations and increase at high aerations when compared to median strain at baseline (dashed line). The decrease in gray scale for prone (lower panels) at 24 h indicate a slight spread of the distribution.
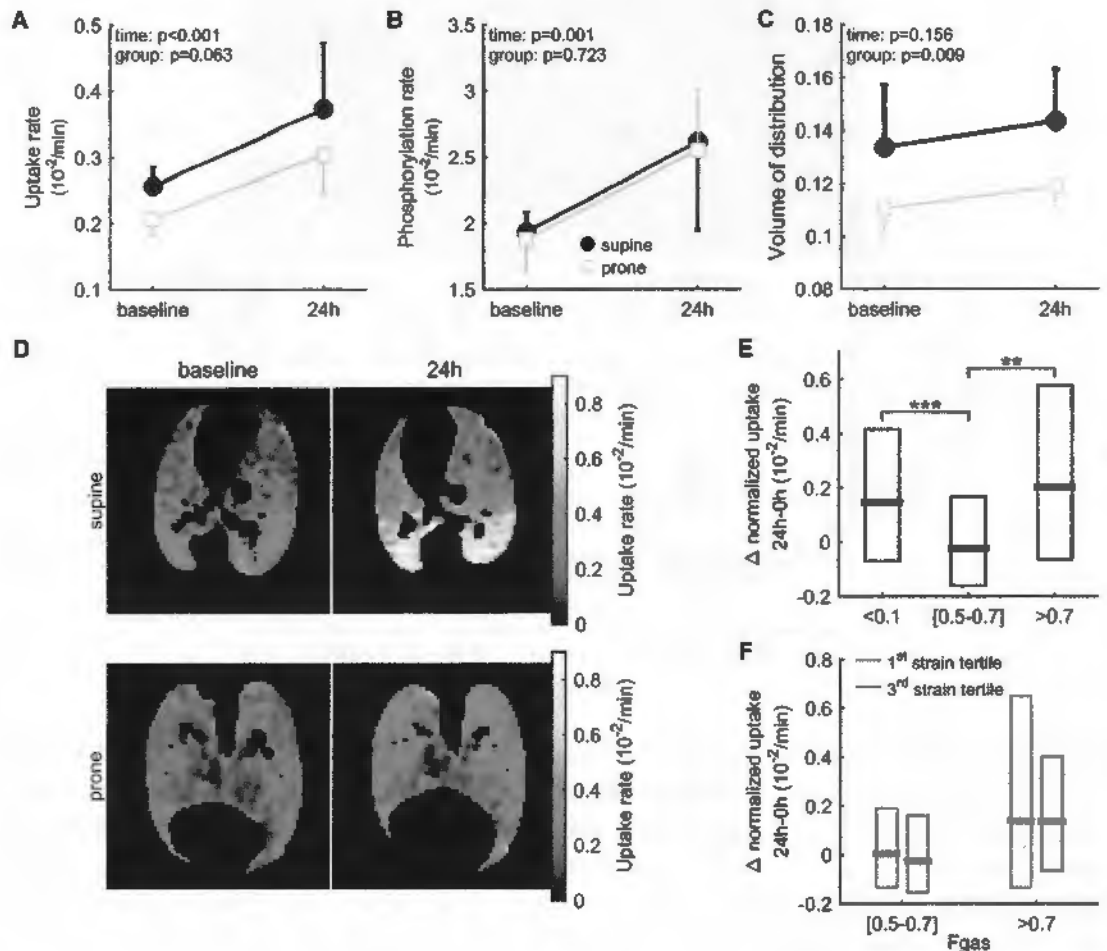
Figure 3.6: After 24 h of low tidal volume mechanical ventilation and mild endotoxemia, ^{18}F-FDG uptake rate, a marker of inflammation, was increased relative to baseline both in animals in supine and prone positions (3.6A). This increase was due more to an increase in the phosphorylation rate (3.6B) than to volume of distribution (3.6C), indicating predominance of cellular metabolic activation. At baseline, ^{18}F-FDG uptake rate spatial distribution was mostly homogeneous in both groups. After 24 h, it remained homogeneous in prone, but showed a vertical gradient in supine (3.6D). Not only the tissue density increased, but regions that became atelectatic (3.6E, <0.1) had higher increase in tissue-normalized uptake when compared to regions of constant normal (6E, [0.5, 0.7]) aeration. Within aerated regions, 1st (light blue) and 3rd (dark blue) tertile of strain had no difference in normalized uptake increase (3.6F). ** (p<0.01) and *** (p<0.001) vs normally-aerated region.

0.7, Fig. 3.6E). Interestingly, the high aerated regions ($F_{GAS} > 0.7$) also had higher normalized uptake increase (Fig. 3.6E). In both aerated regions, normalized uptake increased equally for the high and low tertile of tidal strains (average of baseline and 24 h) (Fig. 3.6F).

To study the determinants of regional inflammation in aerated areas ($F_{GAS} > 0.1$) we tested the effect of regional aeration, strain (mean and standard deviation, SD_{strain}) and blood volume on the change in phosphorylation rate from baseline to 24 h. The interaction between blood volume and strain (blood volume×strain, p=0.010), strain (p<0.001), and SD_{strain} (p<0.001) were related to phosphorylation rate change. Such finding suggests that higher regional blood volume increased tissue metabolic response to strain. Details in Appendix A.2 - Determinants of Inflammation.

Regional Gene Expression at 24 h was Heterogeneously Distributed in The Lungs and Consistent with Activation of Locally Distinct Inflammatory Pathways

Regional lung tissue gene expression of a subset of markers relevant to lung injury was heterogeneous and consistent with heterogeneous local mechanical forces and blood volume. ICAM-1 (adhesion molecule) gene expression was larger in dorsal than ventral regions in supine animals and not in prone (region-group interaction p=0.028, Fig. 3.7). This pattern was also present in the expression of the leukocyte adhesion mediator CD11b (p=0.274), which was upregulated in all animals (Fig. 3.7). CXCL8 (encodes neutrophil chemokine IL-8) expression was consistently lower in prone than supine animals, and largest in ventral and dorsal regions. PAI-1 (secreted by the endothelium and thought to promote inflammation-mediated tissue thrombosis) expression was highest in ventral regions (=high aeration, moderate strain, low blood volume, Appendix A Fig. A.8). The RAGE (felt to partake in barrier disruption in lung injury) gene, although in general downregulated, was more expressed also in ventral and dorsal regions, with a trend to higher expression in ventral than dorsal regions of supine sheep (4 of 5 animals, p=0.073). IL-6 was upregulated in ventral and dorsal supine regions. IL-1β(pro-inflammatory cytokine) was upregulated nearly two-fold though appeared to have lower expression in prone animals. In contrast, amphiregulin (modulator that might dampen the inflammatory response) expression was downregulated.
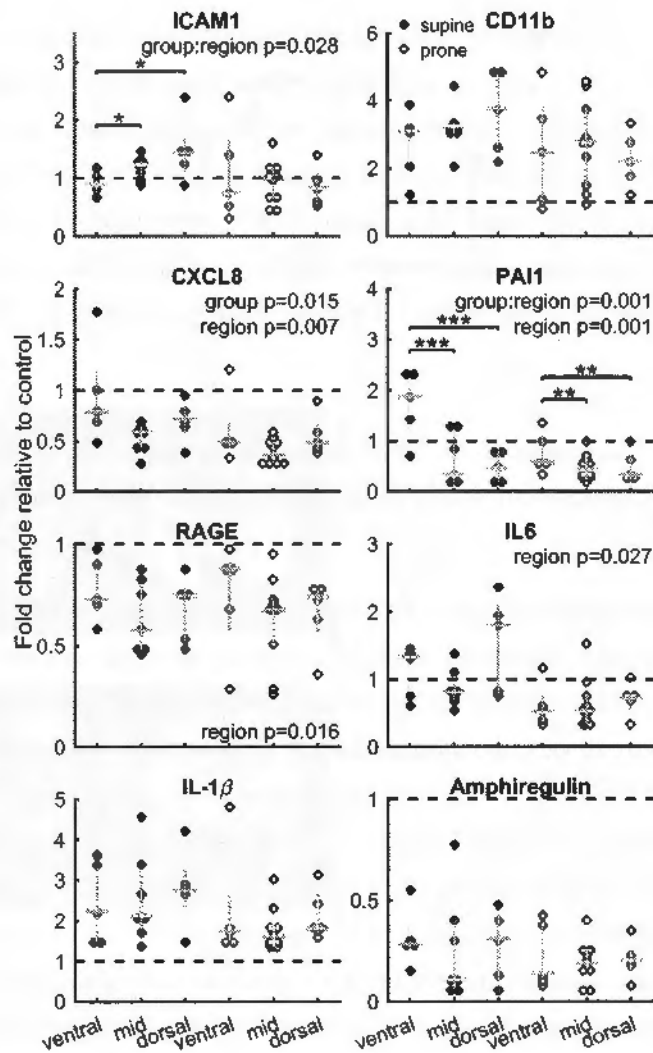
Figure 3.7: Gene expression in three regions with different aeration, blood volume and strain conditions after 24 h of low tidal volume mechanical ventilation and mild endotoxemia. In prone animals, sampled regions were selected to match the three regions along the gravitational axis sampled in the supine animals. Note that mid regions have more samples than dorsal and ventral as tissue was sampled at mid and caudal zones, which showed no difference in a paired Wilcoxon test and were treated as one region. Points are a dotplot representation of fold change relative to β-Actin and a control non-injured animal measured with RT-qPCR, gray lines indicate median (horizontal), first and third quartiles. Comparison between regions in the same group: * p<0.05, ** p<0.01 and *** p<0.001.

Septic Patients Mechanically Ventilated for Less than 96 h Showed Elevated Strain with High Normalized ^{18}F-FDG Uptake in Highest Aeration Regions

A later stage of injury was studied in two septic patients. Both had a bimodal aeration distribution with predominance of high-normal aeration and no-aeration (Appendix A Table A.9 and Fig. A.9). Consistent with the animal experiments, the median of the strain-aeration distribution increased from low toward normal aeration (Fig. 3.8A). Of note, median strain continued to increase with aeration at highly aerated regions including hyperaerated ($F_{GAS}>0.9$) areas (Fig. 3.8A). Such trend matches the increased median strains at higher aeration observed at 24 h in supine animals (Fig. 3.5) indicating a progressive distribution of tidal strains to regions of larger static strains (aeration). Both patients had elevated whole lung ^{18}F-FDG uptake ($0.37 \times 10^{-2}\,\mathrm{min}^{-1}$ and $0.40 \times 10^{-2}\,\mathrm{min}^{-1}$). Regions of higher normal aeration ($F_{GAS}>0.7$) had larger tissue-normalized blood volume (Fig. 3.8C) and uptake than those in the lower half of normal aeration ($F_{GAS}=0.5$ to 0.7, Fig. 3.8B).

3.4 Discussion

In the first 24 h of lung injury produced by mild systemic endotoxemia and mechanical ventilation using typical clinical PEEP and V_T in animals with lung size comparable to that of humans: (1) spatial heterogeneity of tidal strain worsened in supine but not in prone lungs, with increased regions of relative high strain-aeration and of derecruitment; (2) these regions presented biological signs of injury with increased in vivo metabolic activity, representative of inflammation. Derecruited regions showed increased gene expression of adhesion molecules and inflammatory cytokines. In relative high strain-aeration regions, gene expression of endothelial and epithelial stretch markers, and neutrophil chemokine were increased; (3) remarkably, these regions were more frequent in two septic patients in the first 96 h of mechanical ventilation and associated with increased regional inflammation; and (4) regional strain-blood volume interaction and small length-scale strain heterogeneity were associated with neutrophilic inflammation These results indicate that current mechanical ventilation methods do not prevent lung biomechanical deterioration, and support the relevance of interventions preceding ARDS aiming at homogenizing lung aeration to minimize lung injury.

Optimizing mechanical ventilation in patients with normal lungs is greatly important since $\sim$20 % of ventilated patients in intensive care have no primary lung disease [78] and $\sim$230 million patients undergo major surgeries worldwide [79]. While
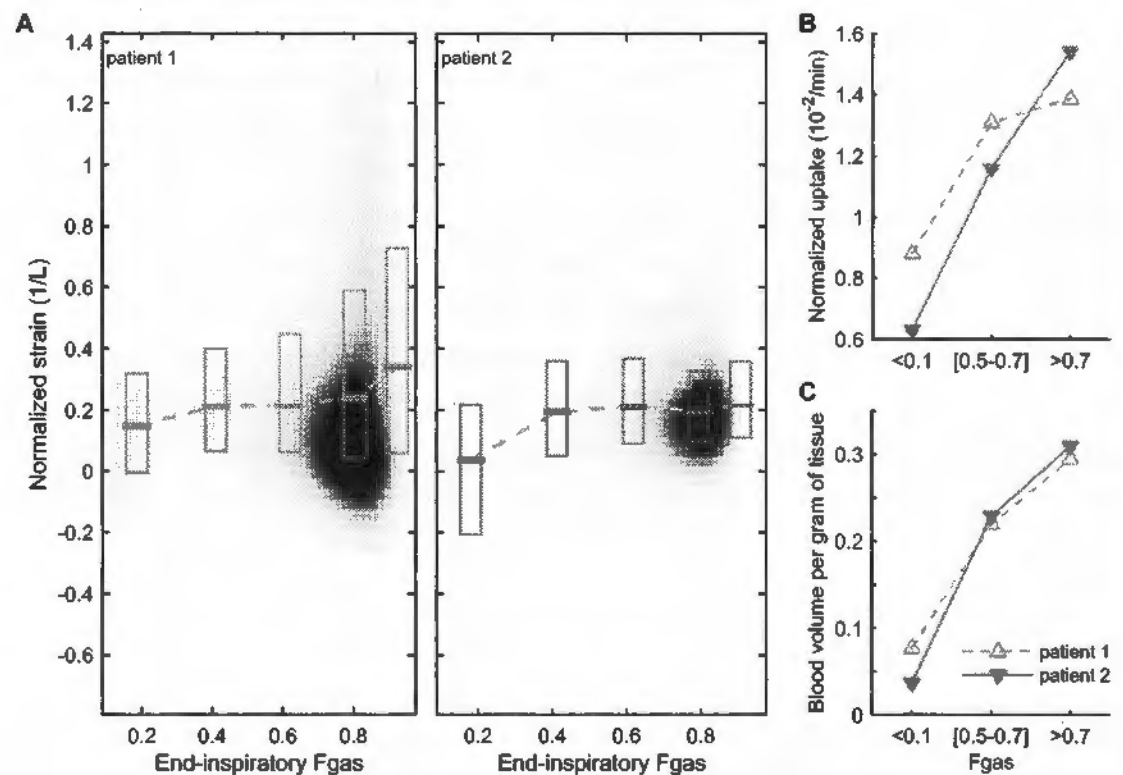
Figure 3.8: Two septic patients at the first 96 h of mechanical ventilation had relationships between voxel level normalized strain and end-inspiratory aeration (fraction of gas, Fgas) consistent with the relationships observed in the animal experiments. Strain increased from lowest aeration toward normal aeration but did not decrease in more aerated regions (3.8A). The boxes represent median and interquartile range of strains for voxels in the aeration intervals: <0.1; 0.1 to 0.3; 0.3 to 0.5; 0.5 to 0.7; 0.7 to 0.9; and >0.9, centered in mean aeration within ranges. Voxels between the 5th and 95th percentiles of strain are depicted in a two-dimensional histogram, with the gray scale representing the fraction of total lung volume in each bin (black is highest). End-inspiratory aeration was chosen to emphasize hyperaerated regions. Inspiratory images were transformed to the expiratory CT references using the same transformation estimated by elastic image registration in order to calculate the voxel level strain. (3.8B) Normalized ^{18}F-FDG uptake and (3.8C) blood volume per gram of tissue in atelectatic (<0.1), normal (0.5 to 0.7) and high aeration (>0.7) regions. In both patients, regions of high aeration and potential hyperinflation have higher normalized uptake and blood volume than normally aerated regions.

there is agreement on the benefit of limiting VT and driving pressures, less is known on interventions aimed at homogenizing lung aeration. In critical care, prone position and evidence for high PEEP benefit are restricted to severe ARDS[126, 127]. Low stretch strategies with low PEEP have actually been defended [121, 128]. In contrast, early prone position has been proposed for comatose [120] and recently for all ARDS patients [119]. In surgical patients, a recent meta-analysis concluded that recruitment maneuvers and PEEP should accompany low V_T [129]. Yet, permissive atelectasis with low PEEP has been defended for open abdominal surgery [118]. Also, despite recommendations in favor of postoperative lung expansion[130], its implementation is poor with important negative consequences [131].

Using CT measurements, we found a markedly different spatial distribution of strains in supine versus prone lungs. Importantly, our assessment of strain was based on voxel level measurements of distances between lung structures in contrast to previous quantifications based on gas volumes and fractions in larger regions-of-interest [67]. In supine, the inverted U-shaped pattern of tidal strain-aeration was consistent with local sigmoid-shaped pressure-volume curves having maximal slope (compliance) and strain at normal aeration $\sim$0.6, and lower compliance and strain at low (derecruitment) and high (hyperinflation) aeration.

Notably, worsening of strain heterogeneity along 24 h was pronounced only in supine lungs. Increased strain heterogeneity was paralleled by increased no- and poor aeration, indicating redistribution of V_T from regions of low to higher aeration. This reveals the inability of PEEP levels prescribed in the utilized protocol, usual in clinical care [44, 121], to protect the lungs against progressive biomechanical deterioration. As a result, at 24 h lungs showed larger atelectatic regions and increased median tidal strains in regions of higher aeration.

Atelectatic regions at 24 h had higher increase in normalized ^{18}F-FDG-uptake and expression of ICAM-1 gene, suggestive of neutrophil infiltration and inflammatory activity, than normally-aerated regions. Such finding implies that a strategy exclusively based on limitation of global cyclic stretch (V_T) does not eliminate lung injury risk, in contrast to a recent meta-analysis [118]. Given that derecruitment and aeration heterogeneity were associated with cellular activation and worsening of strain heterogeneity, early interventions aiming at homogenizing lung aeration are likely important to mitigate injury progress [132, 133]. Importantly, ^{18}F-FDG measurements with PET provide a more comprehensive assessment of inflammation than local measurements from tissue samples or bronchoalveolar lavage.

The two patients had inflamed lungs [100] and large fractions of relative high strain-aeration regions. This was consistent with the progression of those regions along the 24 h in supine sheep. Of note, such regions had larger normalized ^{18}F-FDG-uptake than normally aerated regions in both patients. This suggests local

43

superposition of relative high tidal and static strains as a factor for lung injury, potentially enhanced by the increased blood volume. Indeed, at 24 h sheep had ventral regions with increased gene expression of markers previously associated with injurious mechanical ventilation: PAI-1, RAGE and IL-8 [22, 47, 134–136] implying a biological response to mechanical forces and onset of inflammation with neutrophil recruitment. These findings align with the 20 h inflammatory differential gene expression response of ventral regions in a moderate endotoxemia model [49].

Previous experiments in initially normal lungs pointed to a protective role of prone versus supine [23, 42, 43]. Yet, the applied exaggerated V_T ($\geq 15\,\mathrm{mL\,kg^{-1}}$) and short duration limited their clinical translation. An underlying assumption for those VT is that heterogeneous aeration results in regional strains conductive to mechanical injury despite low global strain. Surprisingly, while 5 % of our supine lungs were submitted to tidal strains above ~ 2.4 times mean values, the absolute magnitudes were below global strains reported as necessary to produce injury exclusively by stretch [41]. Consequently, at the resolution of our CT images (2.5 mm), exaggerated strains do not occur when healthy or mild-endotoxemic lungs are ventilated with typical clinical settings.

Regional metabolic activity was associated with the interaction of strain and blood volume. Blood volume and flow (^{13}N-saline PET [137]) were correlated in 7 studied sheep (r=0.77, p<0.001). Accordingly, both could have contributed to that interaction. High regional blood volume could indicate larger endothelial surface exposed to circulating inflammatory cells, mediators and endotoxin, and high blood flow could enhance their local delivery. These interaction results suggest that during early injury with limited VT and endotoxemia, regional differences in the vascular component magnify the effect of strain on inflammation ("two-hit injury"). Such mechanisms apparently differ from those present during high-VT injury [138]. Therefore, interventions beyond mechanical ventilation could prevent the development of injury. The additional contribution of strain heterogeneity to regional inflammation indicates the potential effect of concentration of mechanical forces and possibly even larger microscopic strain heterogeneity. Finally, because transpulmonary pressures were higher in supine than prone sheep, higher energy delivered to lung tissue could have additionally contributed to injury [139].

Limitations

The imaged lung may have changed from expiration to inspiration. We compensated for this by visually matching the first and last CT slices. Tidal strain computed with breath-holds could misrepresent fast dynamic phenomena. Also, due to a short inspiratory pause, plateau pressures and therefore inspiratory CT lung volume could have been overestimated. Hence, we compared strains per unit of inspired volume

and used measured V_T to calculate absolute strains. Our V_T range was above $6\,\mathrm{mL\,kg^{-1}}$. It was within clinical practice [44], and necessary due to high anatomical dead space in our sheep. Importantly, lower V_T would further decrease regional tidal strains, reinforcing our finding of strains below the proposed injurious limit. Image registration is an ill-posed problem, the required regularization could underestimate heterogeneity. Additionally, the translation from voxel to cell deformation is unknown. ^{18}F-FDG is a glucose analogue and consequently not strictly specific to neutrophilic activation.

In conclusion, during mild-endotoxemic lung injury, a mechanical ventilation strategy that minimizes tidal strain without homogenizing aeration distribution from the beginning of ventilation, before established ARDS, resulted in worsening of levels and spatial distribution of strain and aeration. Atelectatic and relatively high-aeration regions showed increased neutrophilic inflammation. This was dependent on the blood volume-strain interaction and strain heterogeneity. Redistribution of V_T increased strains in those relatively high-aeration regions, which presented gene expression consistent with a stretch response and distinct from atelectatic areas. Those regions were also observed in mechanically ventilated septic patients and associated with increased metabolic activation, indicative of inflammatory activity. Accordingly, provided safe interactions with other organs, strategies that homogenize lung aeration are likely beneficial at the earlier stages of mechanical ventilation in the presence of systemic inflammation.

Chapter 4

Spatial heterogeneity of lung strain and aeration and regional inflammation during early lung injury assessed with PET/CT

4.1 Introduction

Excessive mechanical forces can produce lung injury during mechanical ventilation. Indeed, regional strain (change in lung volume/resting lung volume) has been shown to relate to local lung inflammation particularly in the presence of systemic inflammation [51]. Excessive mechanical forces can occur not only at large lung areas of hyperinflation [140] but also at the microscopic level. Experiments utilizing total lung capacity (TLC) maneuvers in excised dog lobes revealed heterogeneity of regional gas volume changes in relation to gas volume at TLC at length-scales as small as $\sim 2\,mm$ [141]. In fact, pressure-volume relationships determining lung expansion are related to properties that scale down to the microscopic level of collagen and elastin fibers [6]. A theoretical study indicated that alveolar mechanical stress is significantly amplified around collapsed alveoli [142]. Despite the relevance of such small length-scale phenomena, most studies on pulmonary static and dynamic strain are based on whole lung [41, 136] or large regions-of-interest (ROI) [51, 67]. Given that heterogeneity of lung expansion is relevant to lung injury, it is important to understand its topographic basis. Yet, information is scant on the length-scales contributing to strain and aeration heterogeneity during mechanical ventilation. CT imaging and elastic registration allow for estimation of a range of such length-scale contribution by assessment of *in vivo* regional tissue strain and aeration.

Lung injury results from complex interactions among mechanical and biological factors [143]. The inflammatory response to local and global stimuli includes recruitment of cells such as neutrophils and affects pulmonary regional metabolic activity, allowing for its in vivo assessment with the PET tracer ^{18}F-FDG [46, 47, 49, 91, 97, 98]. Recently, we showed that ^{18}F-FDG-PET could provide an early imaging biomarker for ARDS before this condition is clinically established, as well as guide tissue sampling for gene expression analysis [49]. Of note, ^{18}F-FDG-PET kinetics allows for estimation of parameters characterizing tissue phosphorylation rate, associated with tumor aggressiveness and response to therapy in oncological studies [97, 98] and with cytokine gene expression in experimental acute lung injury (ALI) [47]. Accordingly, ^{18}F-FDG-PET kinetics parameters could be a promising tool to guide the analysis of gene expression datasets and identify pathways relevant to the mechanism and treatment of ALI.

We hypothesized that: (1) in normal lungs, small length-scales contribute significantly to heterogeneity of parenchyma expansion and that these contributions differ for aeration versus strain due to their anatomical and functional determinants; (2) contribution of length-scales to total strain and aeration heterogeneity is affected in the early stages of lung injury and depend on body position (supine versus prone); and (3) the distinct regional processes leading to pulmonary inflammation during early lung injury result in regional parameters of ^{18}F-FDG-PET kinetics that signalize of gene expression patterns consistent with pathways relevant to lung injury. We explored these hypotheses in sheep models of mild and moderate endotoxemia during the first 20–24 h of mechanical ventilation with clinically relevant ventilatory settings.

4.2 Materials and Methods

Data derived from two independent sets of sheep models of ALI with systemic inflammation (endotoxemia) and mechanical ventilation. Experimental protocols were approved by the Subcommittee on Research Animal Care and in accordance with the "Guide for the Care and Use of Laboratory Animals" (National Institutes of Health publ. no. 86–23, revised 1996).

4.2.1 Experimental protocol

All animals were anesthetized, paralyzed and ventilated with volume-controlled ventilation and low V_T according to the ARDSNet low PEEP protocol [27]. Initial settings were $V_T = 6 \, \text{mL kg}^{-1}$ (adjusted to reach an alveolar plateau (phase III) at volumetric capnography); PEEP=5 cm H_2O; inspired oxygen fraction=0.3 (ad-

47

justed to maintain arterial oxygen saturation $\geq 90\%$); inspiratory-to-expiratory time ratio=1:2; and respiratory rate aiming at an arterial carbon dioxide partial pressure within 32–45 mmHg. An alveolar recruitment maneuver with application of airway pressure at 40 cm H_2O for 30 s was performed at baseline to expand lung units and standardize lung history. Data were collected at baseline, 6 h and end of the experiment (20 h to 24 h). After baseline measurements, endotoxin was intravenously infused throughout the experiment to model either moderate (10 ng kg^{-1} min^{-1}, Escherichia coli O55:B5, List Biologic Laboratories Inc, Campbell, CA) or mild (2.5 ng kg^{-1} min^{-1}) endotoxemic states.

Moderate endotoxemia

Six sheep were anesthetized with ketamine, propofol and fentanyl, and paralyzed with pancuronium. After 20 h of mechanical ventilation and endotoxemia, animals were euthanized and imaging-guided tissue samples harvested for gene expression analysis. Details on anesthetic and ventilatory management, and tissue sample collection and RNA extraction have been previously described [49].

Imaging protocol and processing. The moderate endotoxemia experiment was exclusively based on PET techniques. The PET camera (Scanditronix PC4096; General Electric, USA) collected 15 transverse slices of 6.5 mm yielding a 9.7-cm-long field-of-view (∼70 % of total lung volume) [55]. Images consisted of an interpolated matrix of $128 \times 128 \times 15$ voxels (2.0 mm $\times$ 2.0 mm $\times$ 6.5 mm). Scans were acquired in stationary mode as:

1. Transmission scans: rotating pin-source (^{68}Ge, 10 min) to correct for attenuation in emission scans, calculate the gas fraction (F_{GAS}) of ROIs from the measured regional density [144] (F_{GAS}=1–regional density), and delineate the lung mask for image analysis. Reconstruction used filtered back projection with a Hanning filter of 11.5 mm width (full width at half maximum, FWHM 13 mm [145]).

2. Emission scans: ^{18}F-FDG tracer used to assess lung metabolic activity [89].20 Tracer dissolved in 8 mL saline (∼40 MBq at 0 h and ∼200 MBq at 6 h and 20 h) was infused at a constant rate through a jugular catheter for 60 s. Starting with ^{18}F-FDG infusion, dynamic PET scan was acquired for 75 min (40 frames: 9 s $\times$ 10 s, 4 s $\times$ 15 s, 1 s $\times$ 30 s, 7 s $\times$ 60 s, 15 s $\times$ 120 s, 1 s $\times$ 300 s and 3 s $\times$ 600 s). Plasma samples of ^{18}F-FDG activity in pulmonary arterial blood were measured at 5.5 min, 9.5 min, 25 min, 37 min and 42.5 min to calibrate an image-derived input function [91]. Metabolic activity was estimated from the regional ^{18}F-FDG net uptake rate (Ki=F_ek$_3$) using a Sokoloff model, which comprises the fractional distribution volume of ^{18}F-FDG available for phos-

phorylation (F_e) and the rate of phosphorylation (k_3). F_e ($=K_1/(k_2+k_3)$) increases with the ^{18}F-FDG that enters tissue from blood at a rate K_1 and decreases when ^{18}F-FDG returns to blood at a rate k_2 or is phosphorylated. In addition, this model provided F_b (ROI's blood fraction), used to calculate regional tissue fraction ($F_{TIS}=1-F_{GAS}-F_b$). The parameter identification method also estimated the blood transit time (t_d) from the heart to studied ROIs [89].20 Emission scans were reconstructed with a filter width of 6.4 mm.

Transcriptome-wide gene expression analysis. Gene expression in tissue samples from dependent (dorsal) and non-dependent (ventral) regions were quantified using species-specific microarray analysis (Agilent Technologies, USA). We used fluorescence quantification, proportional to the amount of RNA hybridized with 15 208 different single-stranded DNA. Genes already identified among that DNA set were selected from a manufacturer's updated list (July 3, 2017) excluding entries classified as predicted. There were 1033 unique genes available. Dorsal/ventral ratio of gene expression was correlated to corresponding ratios of k_3, F_{TIS} and tissue-specific Ki ($Kis=Ki/F_{TIS}$) and F_e ($F_{es}=F_e/F_{TIS}$) estimated at 6 h. For genes measured more than once in the array, the average expression was used.

Mild endotoxemia

Eight female sheep were studied for length-scale analysis of aeration and strain. Animals were sedated with intramuscular ketamine and midazolam, and anesthetized with propofol, ketamine and fentanyl. Paralysis was established with rocuronium. After intubation, lungs were mechanically ventilated with low-PEEP ARDSNet principles [27] for 24 h in supine (N=5) or prone (N=3) position. Sheep were positioned in the NeuroPET/CT scanner (Photo Diagnostic Systems Inc., USA) using CT scans during controlled breathing to maximize lung volume within the field-of-view. Details on anesthesia and mechanical ventilation are provided in *Appendix A*.

Imaging protocol. The mild endotoxemia experiment used PET/CT techniques. CT scans (tube current of 7 mA and voltage of 140 kVp) were acquired during breath holds at end-inspiration (plateau pressure) and end-expiration (PEEP) for strain analysis. Mean lung volume CT images (120 kVp to 140 kVp) were acquired during tidal breathing (2 min) for aeration analysis. Images comprised a matrix of $512 \times 512 \times 82$ voxels (0.49 mm $\times$ 0.49 mm $\times$ 2.5 mm) [146].21 CT images were converted to F_{GAS} considering tissue density equal to 0 Hounsfield units (HU) and air density equal to -1000 HU, $F_{GAS}=HU/-1000$.

Strain estimation. Voxel-level Strain was assessed using elastic image registration to identify the transformation $T(x)$ that mapped each end-inspiratory image back to the corresponding end-expiratory image. Before registration, images were

49

rescaled to achieve within lung parenchyma a minimum of zero and a maximum of one. Each dimension was cropped to the boundaries of the end-inspiratory mask and padded with a margin of 50 voxels at each side. Registration was implemented with diffeomorphic transforms and B-spline spatial regularization in a multistage approach (increasing image resolution and decreasing B-spline knots' distance), using the open source Advanced Normalization Tools (ANTs) [104].22 From T(x) the volumetric deformation of each voxel was quantified by the determinant of the Jacobian (directional derivative) matrix [58, 64–66]. This provides the ratio of the final to the initial volume. Strain is then defined as Jacobian–1 and is referenced to overall volume (tissue+blood+air) at end-expiration.

In the main analysis, the B-spline knots' distance for the first stage was 26 mm and was halved at each one of the three subsequent stages. We tested the influence of that parameter in the contribution of different length-scales to strain heterogeneity (see below, Section 4.2.4) by estimating T(x) with initial knots' distances of 13 mm, 52 mm and 130 mm and the same strategy for distance reduction. Overall accuracy of image registration with each knots' distance was assessed by the standard method of distance between landmarks. In three supine animals (two at baseline and 24 h and one at 6 h) landmarks were automatically defined in the expiratory image and semi-automatically matched in the inspiratory image [110]. A perfect registration would result in a distance equal zero.

Image noise estimation. The level of noise in the mean lung volume CT at full resolution was estimated by two different methods based on histograms of local standard deviations (SD), i.e. estimated in a neighborhood of each voxel, within homogenous ROIs. The first method used the difference between lines and columns to suppress the influence of the image content on the SD [147]. The noise SD was calculated from the parameters of an iterative fitting of the local SD distribution to a chi-square. We implemented it slice-by-slice considering voxels within the lung mask and the following control parameters: histogram limit kmax=number of voxel/200, expansion factor $\alpha = 0.25 \cdot k_{max}/mean$(voxels' value) and fitting gain β=2.12. Global SD was the mean of all slices. The second method calculated the local SD in each slice and designated the global SD as the peak of the histogram in voxels classified as soft-tissue (0<HU<100), considered homogenous [148]. We used a neighborhood of 9 mm for the local SD estimation and a histogram of 200 bins.

4.2.2 Selection of voxels for analysis

Initial lung masks were generated by selecting aerated regions with a fixed threshold. For the moderate endotoxemia experiments, this was combined with perfused regions from ^{13}N-PET scans [149]. For the mild endotoxemia experiments, non-aerated

regions were manually delineated. All masks were manually refined to exclude large bronchi and pulmonary vessels. Within the lung mask, regional ^{18}F-FDG kinetics were computed in three adjacent ROIs of equal height.

4.2.3 Aeration levels

F_{GAS} images were divided into non- ($F_{GAS} < 0.1$), poorly- ($0.1 \leq F_{GAS} < 0.5$), normally- ($0.5 \leq F_{GAS} < 0.85$) and hyper-aerated ($F_{GAS} > 0.85$) compartments expressed as a fraction of lung mass [150].

4.2.4 Length-scale analysis

To quantify the size of sources of heterogeneity contributing to the total variability within the lungs, we applied length-scale analysis [57, 149] to aeration and strain images. In this technique, images are spatially low-pass filtered using a series of pre-determined filter sizes. For each filter size, image heterogeneity is quantified as the variance of the variable being studied (aeration or strain) normalized by the squared mean, equivalent to the squared coefficient of variation. The contribution of each length-scale range to total heterogeneity is calculated as the difference in the normalized variances among consecutive filter sizes. We used a moving average filter with a cylindrical kernel, height equal to the diameter, and sizes of 13 mm to 91 mm (13 mm step) for aeration and 5 mm to 90 mm (5 mm step) for strain (and aeration from CT). Results were expressed relative to the smallest length-scale of each range to eliminate the effects of global heterogeneity changing along the experiment. Linear vertical gradients due to gravity affecting aeration and strain were subtracted from images before filtering [81, 149].

4.2.5 Statistical analysis

Data are expressed as mean±SD or median [25th-75th percentile]. All tests were two-tailed and performed in R 3.3.1 (R Foundation for Statistical Computing, Vienna, Austria), unless otherwise noted.

Aeration and strain analysis: Aeration compartments were compared between time points and experimental conditions, and length-scales relative contributions (aeration and strain) were compared between ranges and time points, using linear mixed-effects models (animal random intercept). Interactions were included when significant. Multiple comparisons p-values were calculated from multivariate t distributions. CT noise was compared between and within methods by repeated measurements ANOVA. Significance was set at $p < 0.05$.

Gene expression analysis: we used Pearson correlation coefficient to determine the association between dorsal/ventral ratios of microarray derived gene expression and ^{18}F-FDG-PET kinetics parameters k_3, F_{es}, and Kis, as well as F_{TIS}. Gene sets for each of these parameters were produced by selecting correlations with significance level $p < 0.1$. Biological pathways derived from these gene sets were identified using DAVID software [151] (National Institute of Allergy and Infectious Diseases, USA) with default settings: at least two genes and EASE<0.1.

4.3 Results

Regional aeration differed among the experimental conditions. Supine mildly endotoxemic animals showed the largest fraction of lung mass regions with $0.1 \leq F_{GAS} < 0.5$ throughout the experiment (Fig. 4.1A). Regions with $F_{GAS} < 0.1$ increased in both supine groups (Fig. 4.1A). Only supine animals presented a vertical gradient of aeration (Fig. 4.1B).
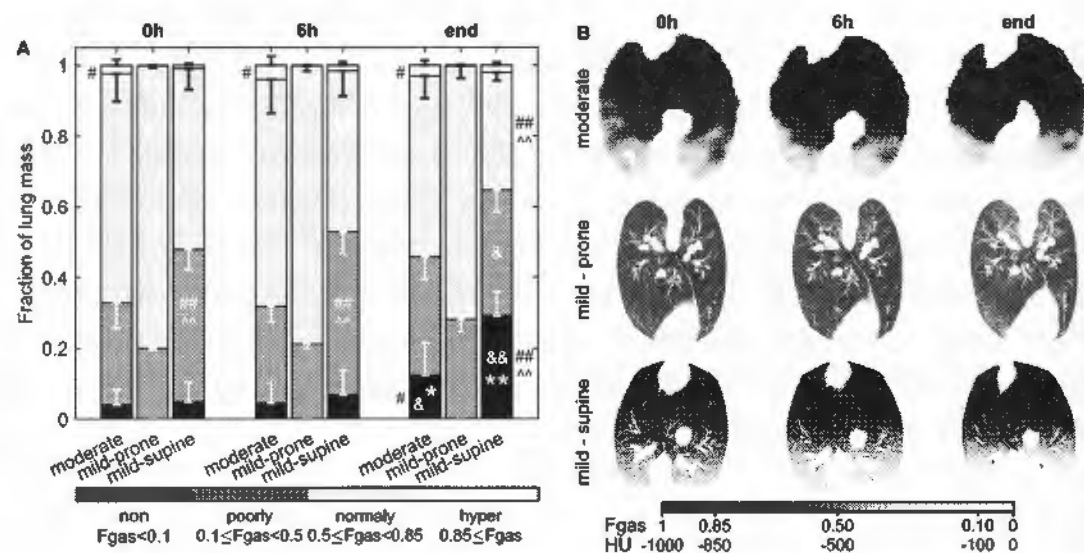
Figure 4.1: Lung aeration in sheep mechanically ventilated with low tidal volume and low to moderate positive and-expiratory pressure for 20–24 h. After the first measurement, intravenous infusion of LPS was started to generate moderate $(10\,\mathrm{ng\,kg^{-1}\,min^{-1}})$ or mild $(2.5\,\mathrm{ng\,kg^{-1}\,min^{-1}})$ systemic endotoxemia. Aeration was quantified as the gas fraction (F_{GAS}) in each voxel of transmission (moderate group) and computed tomography (mild groups) scans during tidal ventilation. (A) Non- (black), poorly- (dark grey), normally- (light grey) and hyper-aerated (white) compartments are expressed as a fraction of total lung mass. Irrespective of the endotoxin dose, non-aerated regions increased after 20 h in supine, but not in prone animals. For supine sheep, the spatial distribution of aeration followed a gravitational gradient decreasing toward dorsal regions (B). Aeration level at 24 h * vs 0 h and & vs 6 h for the same group; ^ vs moderate and # vs mild-prone for the same aeration compartment; one symbol $p < 0.05$, two symbols $p < 0.001$.

4.3.1 Length-scales of aeration heterogeneity

In all cases, aeration heterogeneity at mean lung volume was predominantly present at the 13–26 mm length-scales (Fig. 4.2). The relative contribution of larger length-scales increased as lung injury progressed (Fig. 4.2). Of note, the higher the mean aeration of an animal, the lower was the contribution of larger length-scales (Fig. 4.2D). Mildly endotoxemic supine animals, which presented lowest mean aeration, had the highest contribution of large length-scales, while prone animals had the lowest (Fig. 4.2D).
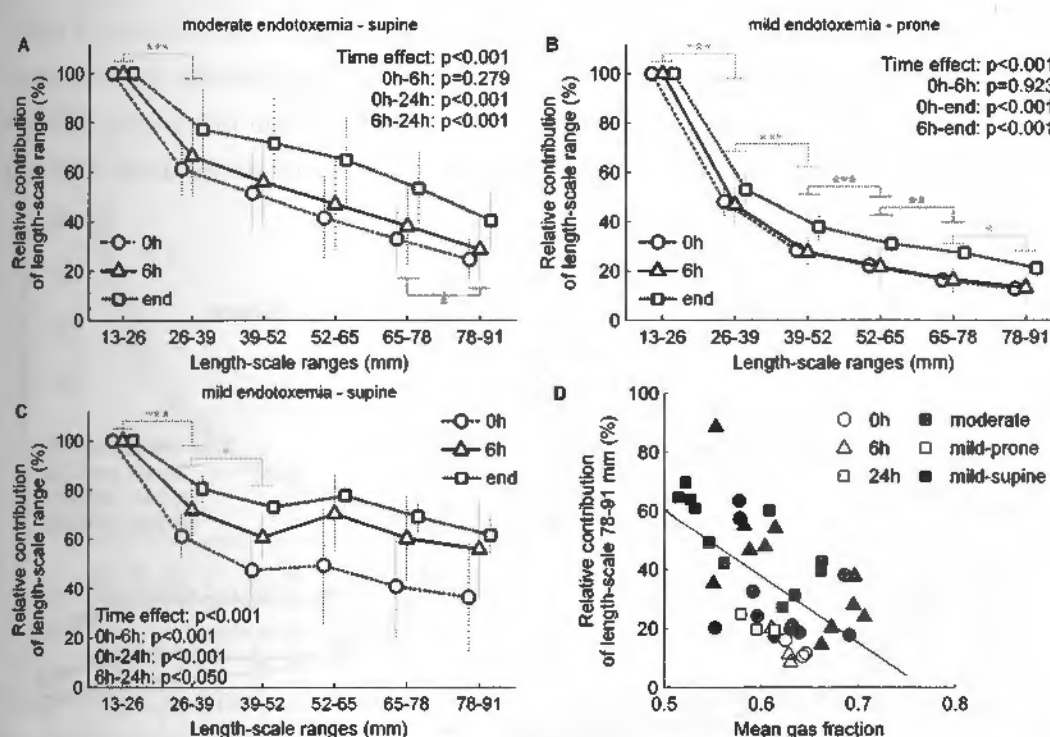
Figure 4.2: Contribution of length-scale ranges to lung aeration heterogeneity. Sheep with moderate (A, $10 \, ng \, kg^{-1} \, min^{-1}$ LPS) or mild (B-C, $2.5 \, ng \, kg^{-1} \, min^{-1}$ LPS) endotoxemia were mechanically ventilated using low tidal volume and low to moderate positive end-expiratory pressure. The contribution of a length-scale range was assessed by the difference between the variances normalized by the square mean in mean lung volume images filtered for effective resolutions from 13 mm to 91 mm. Values were expressed relative to the smallest length-scale (13–26 mm). In both endotoxemia levels and body positions (supine, A and C, prone, B), the largest contribution to heterogeneity was in the length-scale 13–26 mm, with an increase in the contribution of larger length-scales along time. Contribution of larger length-scales decreased with the mean gas fraction (D).* $p<0.05$, ** $p<0.01$ and *** $p<0.001$ for differences between consecutive length-scales.

High resolution CT acquired in the mildly endotoxemic sheep allowed us to analyze length-scales smaller than those obtained with PET transmission scans in moderately endotoxemic sheep, and to calculate voxel-level tidal strains. Increasing

Table 4.1: Noise level estimate in the full resolution mean lung volume CT converted to F_{GAS} and the SD of voxels inside the lung mask after removing the gravitational gradient and filtering with 5 mm kernel.

		0 h	6 h	24 h	p-values
IKEDA *et al.* [147]		0.021 ± 0.002	0.021 ± 0.002	0.021 ± 0.003	Time=0.376
CHRISTIANSON *et al.* [148]		0.027 ± 0.003	0.026 ± 0.003	0.025 ± 0.003	Method<0.001
SD within lung	supine	0.094 ± 0.016	0.095 ± 0.013	0.127 ± 0.019	—
	prone	0.069 ± 0.001	0.066 ± 0.005	0.078 ± 0.009	

the resolution of the length-scale analysis reinforced the predominant contribution of small length-scales to aeration heterogeneity, and the higher contribution of larger length-scales in supine versus prone animals (Fig. 4.3). Importantly, the estimated noise level in the CT images was similar with both estimation procedures, did not change with time and was at least two-fold below the SD of voxels inside the lung mask filtered with the 5 mm kernel (Table 4.1).
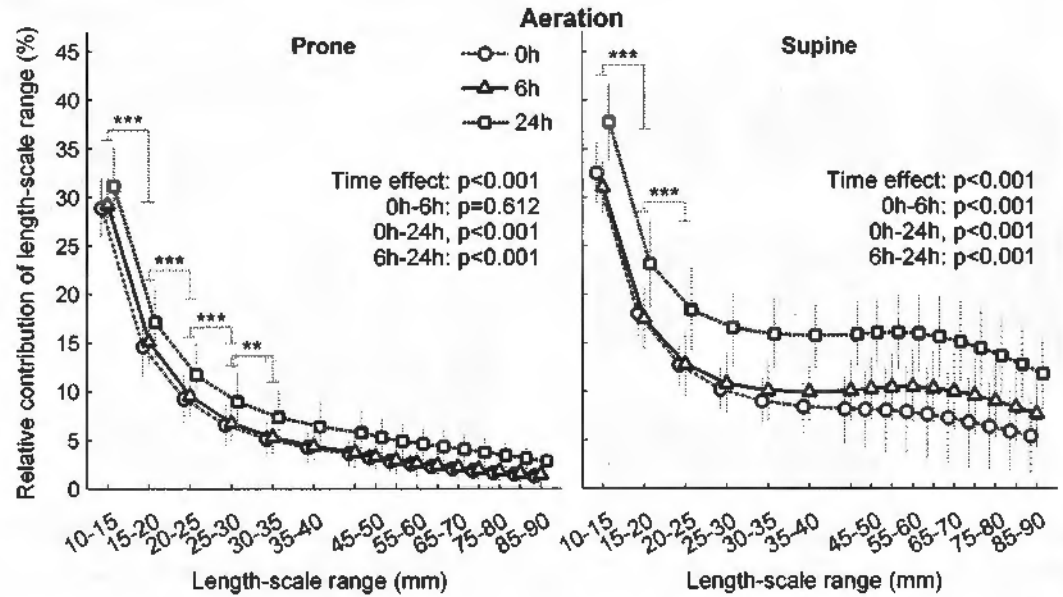
Figure 4.3: Contribution of length-scale ranges to lung aeration heterogeneity for mildly endotoxemic sheep in prone (left) and supine (rigth) positions. Animals were mechanically ventilated with low tidal volume and low positive end-expiratory pressure for 24 h. The contribution of a length-scale range was assessed by the difference between the variances normalized by the square mean in images filtered for effective resolutions from 5 mm to 90 mm. Values were expressed relative to the smallest length-scale (5–10 mm). While both body positions displayed their largest contribution to heterogeneity in length-scale 5–10 mm, supine animals (right) showed substantially higher contribution of larger length-scales than prone (left). ** p<0.01 and *** p<0.001 for differences between consecutive length-scales.

4.3.2 Length-scales of tidal strain heterogeneity

Tidal strain heterogeneity was predominantly present at length-scales of 5–10 mm (Fig. 4.4). Supine animals presented higher relative contributions of larger length-scales than prone animals (Fig. 4.4). The two body positions differed in their time course. The contribution of length-scales to tidal strain heterogeneity did not change with time in prone animals (Fig. 4.4) despite change in their length-scales contribution to aeration heterogeneity (Fig. 4.2B and 4.3). In contrast, an increase of the contribution of larger length-scales to strain heterogeneity was observed already at 6 h in supine animals, and more evident at 24 h (Fig. 4.4).
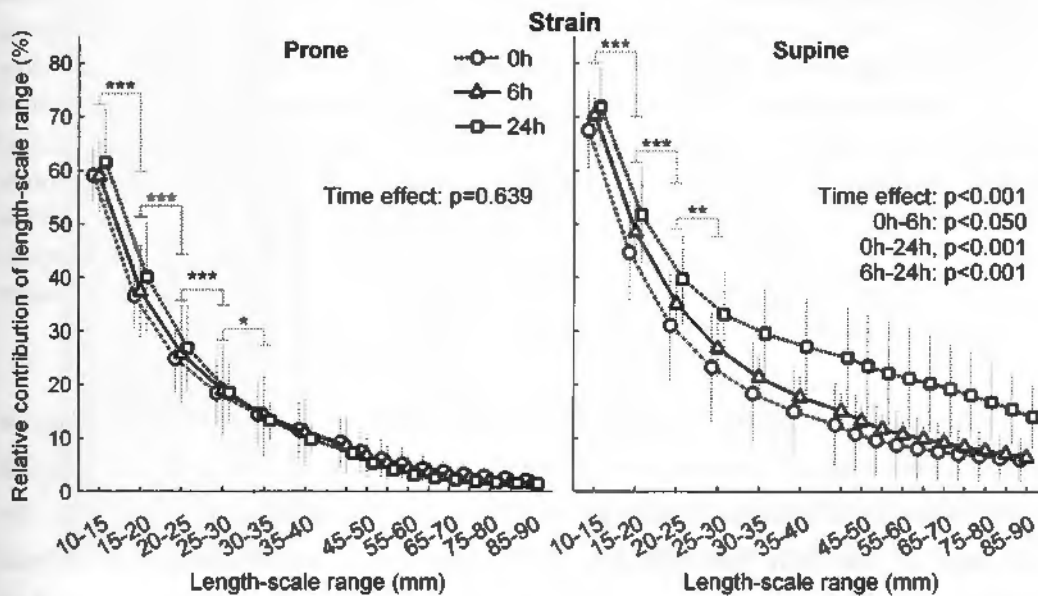
Figure 4.4: Contribution of length-scale ranges to lung tidal strain heterogeneity for mildly endotoxemic sheep in prone (left) or supine (right) positions. Animals were mechanically ventilated with low tidal volume and low positive end-expiratory pressure for 24 h. The contribution of a length-scale was assessed by the difference between the variances normalized by the square mean in images filtered for effective resolutions from 5 mm to 90 mm. Values were expressed relative to the smallest length-scale (5–10 mm). Supine had higher relative contributions of all length-scales and showed significant change at 6 h and 24 h. Prone had no difference between time points. * $p<0.05$, ** $p<0.01$ and ** $p<0.001$ for differences between consecutive length-scales. Strain was calculated with an initial B-spline knot distance of 26 mm.

Before evaluating the effect of varying B-spline knots' distances on the relative contributions of length-scale ranges to strain heterogeneity, we tested the overall accuracy of the different registration results using landmarks. The best agreement was at 0 h (Fig. 4.5) and length-scales were compared only at baseline. Of note, for all knots' distances >13 mm, the 75th percentile of the combined landmarks distances was below the largest dimension of a voxel (2.5 mm).
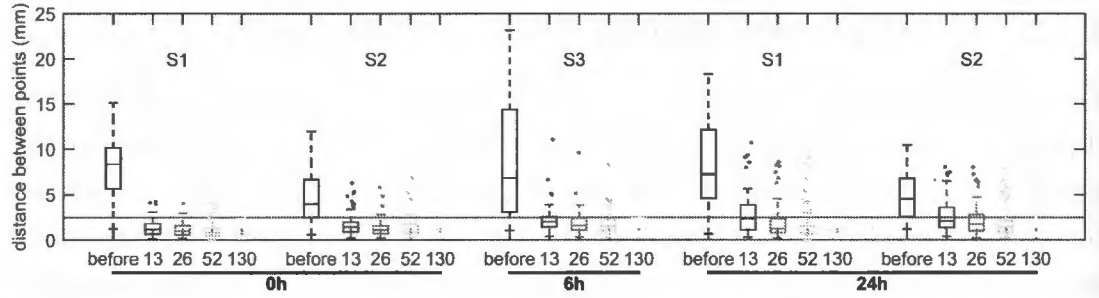
Figure 4.5: Distance between landmark points matched in the expiratory and inspiratory images before and after image registration using different distances for the knots of the B-spline regularization (13 mm, 26 mm, 52 mm and 130 mm). Landmark distance was used as a measure of overall image registration accuracy. Data correspond to two randomly selected supine sheep (S1 and S2) at the beginning (0 h) and end of the experiment (24 h). These time points were chosen because they represent the extremes in aeration and atelectasis. A measurement at 6 h of a third sheep (S3) was added because it represented the study with the largest gas volume difference between inspiratory and expiratory images. An average of 95.8 points [range 74–122] were used for each animal-time point combination. Landmarks were semi-automatically matched in each pair of images by one observer. Dotted line represents the largest dimension of image voxels (2.5 mm). The B-spline knots' distance corresponds to the first stage of registration.

The sizes of the features in strain images increased with the knots' distance, as expected (Fig. 4.6A). However, the relative contribution of length-scales was not affected when initial knots' distances of 13 mm or 52 mm were compared to the 26 mm used in our main analysis (Fig. 4.6B). The initial regularization to 130 mm markedly altered the heterogeneity length-scales, increasing the contributions of all ranges (Fig. 4.6B). With this regularization, after 24 h the increase in contribution was significant for length-scales larger than 30 mm (Fig. 4.6C).

4.3.3 Regional phosphorylation rates and gene-expression

Regional kinetics of ^{18}F-FDG in lung regions of distinct aeration (and likely distinct tidal strain) was significantly different for phosphorylation rate (k_3) and tissue-specific ^{18}F-FDG-uptake rate (Kis) at 6 h (Fig. 4.7). Therefore, while ventral and dorsal regions had similar metabolic activity at 0 h and 24 h, changes in that metabolic activity followed different temporal trajectories.

We tested if these different trajectories resulted from differences in regional biological processes correlating the dorsal/ventral ratio of ^{18}F-FDG kinetics parameters at 6 h and the gene expression from species-specific microarray analysis. The Kis was correlated to 35 genes with an absolute correlation coefficient $|r| = 0.81[0.78 - 0.85]$. Ontology analysis of these genes revealed two pathways linked to metabolism (Table 4.2). The tissue-specific ^{18}F-FDG volume of distribution (F_{es}) showed 106 corre-
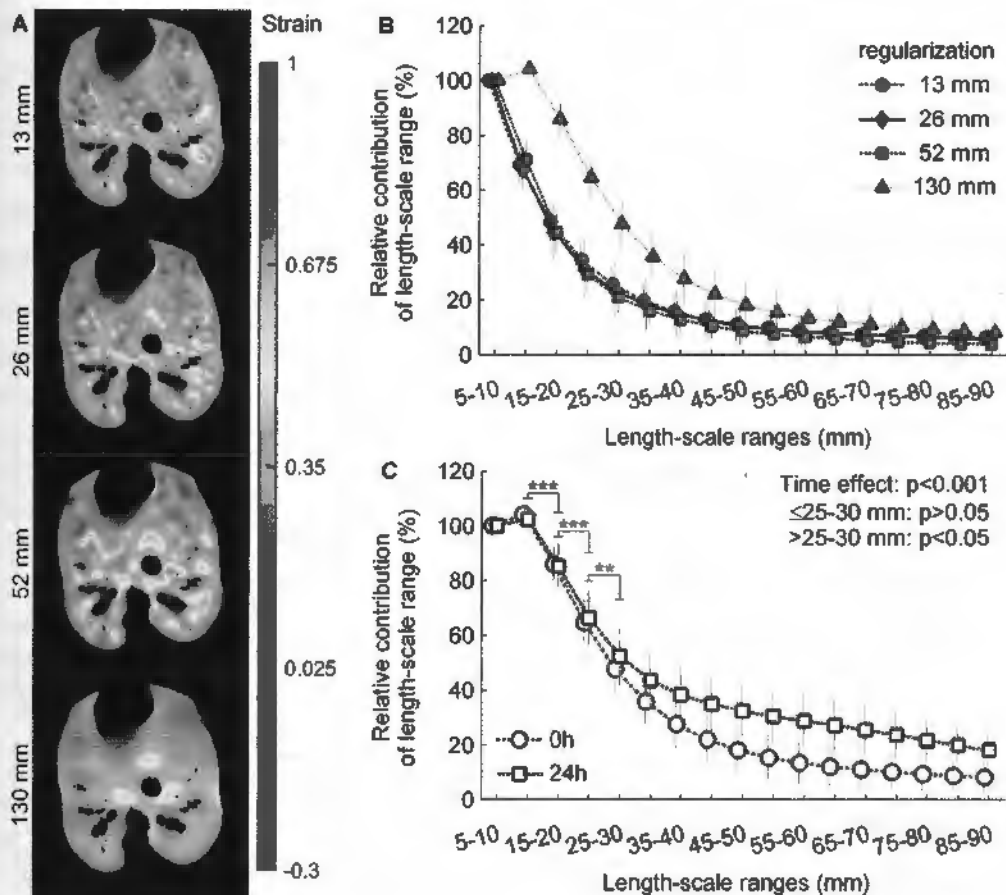
Figure 4.6: Contribution of length-scale ranges to lung tidal strain heterogeneity. Mildly endotoxemic (2.5 ng kg^{-1} min LPS) supine sheep were mechanically ventilated using low tidal volume and low positive end-expiratory pressure. Voxel level strain was estimated using different distances between the knots of the B-spline regularization (13 mm, 26 mm, 52 mm and 130 mm in the first step). The contribution of a length-scale was assessed by the difference between the variances normalized by the squared mean in images filtered for effective resolutions from 5 mm to 35 mm. Values are normalized to the 5–10 mm. Only the baseline data was analyzed, as it was the time point with best agreement in landmarks distance between the four regularization factors. (A) Examples of the spatial distribution of strain estimated with each B-spline knots' distance. Note the increase in size of the regions with similar colors from the upper (13 mm) to the lower (130 mm) images. (B) There was no qualitative difference in contributions of length-scales between 13 mm, 26 mm and 52 mm. (C) Contribution of length-scale ranges at 0 h and 24 h for the largest knots' distance showing a significant increase in contribution of length-scales larger than 30 mm after 24 h. ** $p<0.01$ and *** $p<0.001$ for differences between consecutive length-scales.
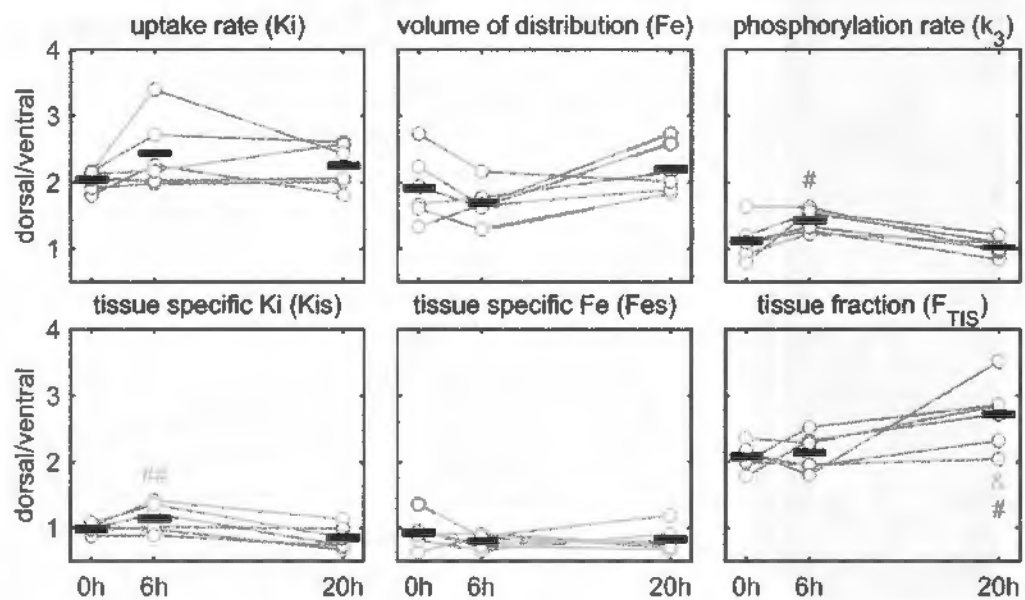
Figure 4.7: Dorsal/ventral ratio of ^{18}F-FDG kinetic parameters and tissue fraction in sheep undergoing low tidal volume and low to moderate positive end-expiratory pressure mechanical ventilation, and moderate endotoxemia ($10\,\mathrm{ng\,kg^{-1}\,min^{-1}}$ LPS). The phosphorylation rate and tissue-specific ^{18}F-FDG uptake rate at 6 h were significantly different from 20 h ($\#$ p$<$0.05 and $\#\#$ p$<$0.01) indicating that dorsal and ventral regions started and ended with similar levels, but followed different temporal trajectories. This could indicate different biological process due to differences in aeration, tidal strain, ventilation and perfusion. Tissue fraction increased at dorsal regions at 20 h compared to both 6 h and 0 h ($\#$ and $\&$ p$<$0.05).

lated genes ($|r| = 0.81[0.78 - 0.85]$) with pathways associated to the immune system and environmental sensing (Tables 4.2 and B.1). The k_3 was correlated to 30 genes ($|r| = 0.84[0.78 - 0.90]$) and a sodium transport pathway. Of note, k_3 was correlated to expression of hexokinase and F_{es} to expression of toll-like receptors TLR2 and TLR4 (Fig. 4.8). Several Kis correlated genes were also correlated with either F_{es} (n=17) or k_3 (n=9). In contrast, there was no gene expressed in simultaneous correlation with F_{es} and k_3. Finally, the regional differences of F_{TIS} were correlated to 59 genes ($|r| = 0.80[0.76 - 0.84]$). The identified pathways overlapped with F_{es} (Tables 4.2 and B.1).

Table 4.2: Significant pathways amongst the genes that were correlated to ^{18}F-FDG kinetics parameters and tissue fraction. A pathway was considered significant if at least two of its' genes were on the analyzed list and had EASE<0.1.

Parameter	Group	Specific pathways
Tissue-specific uptake rate (Kis)	Metabolism	Fructose and mannose metabolism, Biosynthesis of antibiotics
Tissue-specific volume of distribution (F_{es})	Environmental information processing	PI3K-Akt signaling, Calcium signaling, NF-kappa B signaling, Jak-STAT signaling, TNF signaling, Cytokine-cytokine receptor interaction
	Immune system	Toll-like receptor signaling, T cell receptor signaling, Natural killer cell mediated cytotoxicity, Antigen processing and presentation
Phosphorylation rate (k_3)	Excretory system	Aldosterone-regulated sodium reabsorption
Tissue fraction (F_{TIS})	Environmental information processing	Jak-STAT signaling, Neuroactive ligand-receptor interaction
	Immune system	Toll-like receptor signaling, T cell receptor signaling, RIG-I-like receptor signaling, Hematopoietic cell lineage

4.4 Discussion

Our main findings are that in the first 20–24 h of lung injury due to systemic endotoxemia and mechanical ventilation: (1) spatial heterogeneity of lung strain and aeration are predominantly present at small length-scales ($\leq$5–10 mm) in normal and initially injured lungs. Length-scales >5–10 mm contribute more to strain than to aeration heterogeneity suggesting lung regions of size comparable to the secondary pulmonary lobule as the source of strain heterogeneity and regions smaller than that as the source of aeration heterogeneity; (2) acute lung injury and body position importantly affect the relative contribution of length-scales >5–10 mm to strain and aeration heterogeneity, which increase as lung injury progresses and is larger
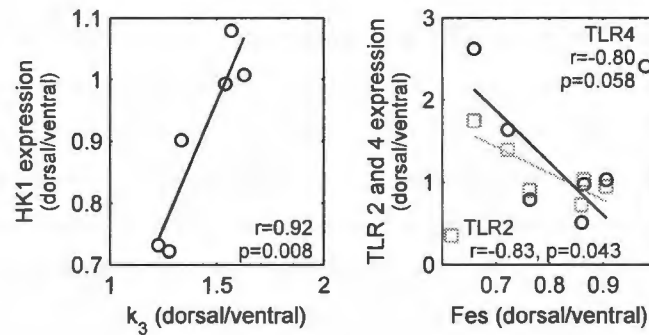
Figure 4.8: Correlations between dorsal to ventral ratios of selected genes expression and ^{18}F-FDG kinetic parameters. The transport rate from the non-metabolized to the metabolized compartment (k_3), which represents the phosphorylation of ^{18}F-FDG, was correlated with gene expression of hexokinase (HK1). The ^{18}F-FDG volume of distribution normalized by tissue fraction (F_{es}) is normally attributed to the number of neutrophils in the analyzed region and was correlated with the expression of toll-like receptors 2 and 4 (TLR2 and TLR4), which are involved in the process of neutrophil migration and bacteria detection.

in heterogeneously (supine) than homogeneously (prone) expanded lungs; and (3) a novel approach to analyze gene expression by using *in vivo* PET-measurement of regional ^{18}F-FDG kinetics reveals pathways consistent with the studied lung injury process, and suggests novel pathways of potential relevance for mechanistical studies and treatment.

4.4.1 Methodological considerations

Decomposing the spatial variability of PET and CT images using length-scale analysis allows characterization of the size of features in the images contributing to total heterogeneity (Fig. B.1). In contrast, global histogram methods characterize the variability among voxels without considering the spatial relation among neighbors. Compared to frequency analysis methods, length-scale analysis does not include assumptions about the periodicity of spatial variations, and does not require an infinite frequency spectrum to represent sharp localized image features. Length-scale analysis is related to methods of fractal analysis such as box counting. However, instead of providing a single number across length-scales (e.g., the global fractal dimension), it provides a set of measures of the contribution of different spatial sizes to total heterogeneity. Importantly, a filter kernel size that is not an integer multiple of the real length-scale generates periodic signals in the frequency domain, resulting in smoother transitions between length-scales (Fig. B.1). On the other hand, due to this smooth characteristic, low-pass filtering is less sensitive to grid misalignment compared to the box counting method [81].

Technical features of the hardware and software utilized for image acquisition and processing affect length-scale analysis. Noise, true resolution, and contrast recovery influence the overall transfer function, which determines how the true variability within the lungs is represented in an image. Accordingly, when analyzing length-scales derived from different imaging systems, factors such as radiation dose, detectors (noise level), modulation transfer function and reconstruction kernel filters must be considered. Image noise affects mostly the small length-scales and would be of particular concern for the 5–10 mm aeration length-scale. Our noise estimation within each image was markedly smaller than the SD for the lung voxels after filtering with a 5 mm kernel. This shows that noise was not the main factor for the length-scale results.

Elastic image registration involves spatial regularization, which smooths the estimated vector field of tissue displacement between two images to suppress effects of imaging noise on the local estimates. This corresponds to a spatial filter, which in our study was determined by the B-spline knots' distance, and could affect the assessment of relative contributions of the different length-scales to total heterogeneity. We tested initial knots' distances of 13 mm, 26 mm, 52 mm and 130 mm resulting in 1.625 mm, 3.25 mm, 6.25 mm and 16.25 mm at the final registration step. If the regularization would affect the relative contribution of length-scales, the contribution of length-scales >5–10 mm should have been lower for the 13 mm knots' distance, and higher for the 52 mm. However, substantial differences were only observed with 130 mm, in which the final knots' distance was between the second and third length-scales. Thus, registration parameters could influence the length-scale analysis, but would not be of sufficient magnitude to affect their biological meaning for smaller knots' distances.

4.4.2 Length-scale analysis of aeration and tidal strain heterogeneity

We found that the largest contribution to aeration and strain heterogeneities was at the 5–10 mm length-scale. The spatial distribution of aeration and strain depend on anatomical and functional factors. Anatomically that observed length-scale ranges from a human acinus (set of alveoli at a terminal airway) [152] to secondary pulmonary lobules (3 to 12 acini marginated by connective tissue [153]). Functionally, local aeration of normal lungs is determined by local parenchyma elastic and resistive properties, and the effect of neighboring units (interdependence). The mechanical properties of parenchyma depend at least on the elements of the extracellular matrix, the alveolar surface tension and the transpulmonary pressure [6]. For strain, different end-expiratory aerations correspond to distinct states of the tissue stress-

61

strain curve leading to different changes in size of alveolar units for the same change in pressure. In addition, local gas flow depends on the impedance of the path from the trachea to the first-order bronchioles at the acini. Previous studies indicate the presence of substantial expansion heterogeneity at the microscopic level [154, 155], while images of aeration and ventilation distribution with different modalities suggest homogeneity at larger length-scales [57, 59]. Thus, our results are consistent with a predominance of the contribution of small length-scales to total heterogeneity in normal lungs.

The relative contribution of length-scales to aeration and tidal strain heterogeneity reveals important differences in their spatial distributions. Length-scales >10 mm contributed significantly more to strain heterogeneity than to aeration heterogeneity. This suggests that substantial strain heterogeneity occurs at lung regions with sizes comparable to or larger than the secondary pulmonary lobule ($\sim$10 mm) [153], while aeration heterogeneity relates predominantly to acinar sizes ($\sim$2.5 mm). This finding is consistent with magnetic resonance measurements of the size of airspaces using the apparent diffusion coefficient of ^{3}He [156]. The greater contribution of larger length-scales to strain heterogeneity may result from a combination of tissue interdependence influencing the expansion of neighboring lung units with the influence of similar gas flow to acini in a secondary pulmonary lobule, supplied by a single small bronchiole [153]. Our findings are also consistent with measurements of fractional lung expansion estimated using parenchymal markers in excised lobes, which indicated that the linear dimension of anatomic units producing expansion variability was $\sim$10 mm [157]. Highly heterogeneous static and dynamic inflation of neighboring small lung units could result in injurious shear stress. Importantly, differences at these length-scales would hardly be seen with previously applied regional strain analysis in large ROIs [51, 67].

While small length-scales contained the largest fraction of aeration heterogeneity, length-scales as large as 78 mm still presented a sizable contribution to heterogeneity at baseline (normal lungs). The contribution of these larger length-scales was markedly different between prone and supine positions. Supine animals had higher relative contributions to total aeration heterogeneity at all length-scales as compared to prone animals, and a lower decrease in these contributions as length-scales increased. Because we removed the gravitational gradient from the spatial distribution of aeration, the quantified heterogeneity cannot be explained merely by dependent lung atelectasis but implies regional differences present at the same vertical level, with aeration heterogeneities up to anatomical sizes compatible with lobes ($\sim$7 cm).

Progress of ALI increased the contribution of larger length-scales not only to aeration, but also to strain heterogeneity. For aeration heterogeneity of supine animals, changes from 0 h to 6 h predominated at length-scales >25–30 mm, and extended to

all length scales at 24 h. This could be due to increase in aeration variability in regions of poor aeration [57] (dorsal areas), and is consistent with growth of such poorly aerated regions. Strain heterogeneity of supine sheep, on the other hand, was affected at the small length-scale range from 0 h to 6 h followed by an increase at all length-scales at 24 h. Such findings agree with previous studies showing increased heterogeneity of specific ventilation at small length-scales within poorly aerated areas (1.75 mm using K-edge CT imaging [59] and <12 mm with ^{13}N-PET [57]). For the homogeneously aerated prone animals, the relative contribution of length-scales to total heterogeneity changed only for aeration at 24 h, with no change observed for strain. Thus, changes in strain length-scale could indicate change in deformations within lung regions before major redistribution of strain between regions of different aeration.

The approximately exponential decrease in the contribution of length-scales to aeration and strain heterogeneity as length-scale increases is consistent with the proposed fractal characteristic of the airway tree [158]. Accordingly, increase in length-scale during mechanical ventilation and endotoxemia could be a marker of lung mechanical conditions conducive to injury. Of note, the change of length-scales contribution at 24 h was almost a parallel shift from baseline suggesting that at early stages of ALI, changes in regional mechanical properties would not overcome other anatomical determinants of aeration and strain spatial distributions.

4.4.3 Gene expression analysis

Supine animals presented differences between ventral and dorsal aeration. Given that regional mean aeration is associated with heterogeneity in aeration and specific ventilation [57], a measurement closely related to strain, we presumed that biological mechanisms would differ between those regions. We previously demonstrated that changes in regional metabolic activation precede changes in regional lung density, clinically used for diagnosis, in the early stages of ARDS [49]. Based on such findings, we now identified pathways derived from genes topographically expressed at magnitudes corresponding to regional metabolic parameters, i.e., correlation between dorsal/ventral ratios of gene expression and ^{18}F-FDG kinetics parameters. This molecular imaging-guided method to identify gene expression differs from previous methods based on whole lung analysis [159, 160]. It aims to advance those by objectively studying lung areas with quantitatively determined distinct metabolic features.

The pathways related to F_{es} revealed the sensing and response to inflammation with toll-like receptors, TNF [161] and NF-kappa B [162] signaling. Such finding reinforces the validity of the proposed method to identify relevant processes and

confirms the expected relevance of those pathways during ALI. F_{es} quantifies the amount of ^{18}F-FDG available to phosphorylation (i.e., the ^{18}F-FDG volume of distribution, F_e) normalized to tissue mass. Correlation of F_{es} with TLR4 suggests the topographical association of F_{es} with lipopolysaccharide recognition [163] and recruitment of neutrophils, consistent with the interpretation of F_e as influenced by the regional number of neutrophils [46]. Tissue fraction had similar pathways to F_{es}, likely due to the spatial distribution of tissue coinciding with higher blood flow (and transport of endotoxin) in dorsal regions [49], lung injury leading to tissue consolidation [106] or to increased F_{TIS} due to more immune system cells.

The ^{18}F-FDG phosphorylation rate (k_3) was correlated to the pathway of aldosterone-regulated sodium reabsorption. This pathway is linked to the epithelial sodium channel (ENaC) that acts to regulate the sodium balance in a cell. In the lungs, it is linked to fluid transport from the alveolar space. Thus, ENaCs are important for clearance of lung edema [31]. Such findings suggest an increased activity of ENaC in regions with high k_3 possibly to overcome increased epithelial permeability. k_3 was also positively correlated with expression of hexokinase, a confirmatory finding for the modeling assumptions of ^{18}F-FDG kinetics, in which k_3 is interpreted as a measure of hexokinase activity.15 This gene was one of the shared genes between k_3 and Kis, and was present in both pathways correlated to Kis. Moreover, the other genes that established the significance of the pathways for Kis were correlated to F_{es}, in line with the composition of the net uptake rate ($Ki = k_3 \cdot F_e$).

4.4.4 Limitations

Length-scale analysis is not limited by precise anatomical boundaries. Consequently, anatomical interpretations were derived from known sizes of structures and not the structures themselves. Tidal strain calculated from breath-hold images may not reflect fast dynamics and regional differences in inflation time constants. Aeration data derived from tidal breathing images, which represent an average of different phases of the breath cycle, and could be partially influenced by time constants. The advantage of having an *in vivo* measurement brings the confounding factor of blood contributing to regional density. Correlations between regional ^{18}F-FDG kinetic parameters and gene expression were performed without corrections for multiple comparisons increasing the probability of false positives. However, for pathway identification, we imposed the additional restriction of having two or more genes that represented a proportion of the correlated genes significantly larger than the proportion of the complete pathway in sheep genome (EASE<0.1). These restrictions increased the power of the analysis.

64

4.5 Conclusion

In normal and initially injured lungs mechanically ventilated with low V_T, small length-scales contribute most to spatial heterogeneity of aeration and tidal strain. Yet, their spatial distributions are not equivalent. Strain heterogeneity length-scales are characterized by larger sizes, comparable to the secondary pulmonary lobule, than those composing aeration heterogeneity. Contributions of length-scales >10 mm to aeration and strain heterogeneity increase with lung injury and with supine position. These changes could represent injurious mechanical conditions, and assessing aeration and strain with large ROIs may delay identification of such conditions. During the initial 20 h of injury, molecular image-guided gene expression analysis reveals a topographically heterogeneous activation of the immune system and fluid regulation in lung parenchyma.

Chapter 5

Generalized estimation of the ventilatory distribution from the multiple-breath nitrogen washout

5.1 Background

The Multiple-Breath Nitrogen Washout (MBN$_2$W) and the Single-Breath Washout are classical pulmonary function tests, based on the measurement of the concentration or fraction of N$_2$ in the breathing gases, to evaluate the ventilation inhomogeneity. Among measures and indices obtainable from the MBN$_2$W, one of the most useful is the Functional Residual Capacity (FRC) or EELV, meaning the relaxed lung functional volume comprising all ventilated alveolar units plus the series dead space. The MBN$_2$W is also able to convey information about ventilation-to-volume (v/V) inhomogeneities, by profiling the rate of expiratory elimination of the tracer gas along many respiratory cycles [74]. Several indexes developed to evaluate the ventilation inhomogeneity are derived from the MBN$_2$W, such as the Lung Clearance Index [164] and the Multiple-breath Alveolar Mixing Inefficiency [71]. However, different patterns of inhomogeneity may be represented by the same values of these indices, which limit their specificity. Despite being relatively benign and non-invasive, the MBN$_2$W needed, when it was being experimentally explored, costly, bulky machinery such as respiratory mass spectrometers (RMS); it could not map anatomy nor the spatial distribution of the quantities it measured, and ultimately it saw a decline of interest as a technique for general, day-to-day clinical application.

Along the time, the instrumentation to measure respiratory gas concentrations underwent evolutions. From the huge RMS to tiny capnometers and oximeters, their price and size shrunk, warranting broader use for them as alternatives to a direct measurement of N$_2$. The presence of such accessible devices suggest revis-

iting techniques such as MBN_2W. Even the usually nontrivial correction of the asynchrony between flow and concentration signals inherent to sidestream gas sampling, which requires high accuracy and is mandatory for adequate measurements of breath-by-breath volumes of gases [70] can be spared, for instance with the available mainstream gas sensors [165] or by simplifications based in taking end-tidal values as representative of mean alveolar concentrations, hence obviating the need for synchronization algorithms [166, 167].

On the other hand, the mathematical models available for the analysis of v/V distribution from the MBN_2W required very stringent maneuvers and circumstances: the fraction of N_2 should decrease in an abrupt step between two respiratory cycles; V_T and, more importantly, the EELV should be kept constant throughout the maneuver, that is, inspiratory and expiratory V_T must be equal. Those requirements may be difficult to meet, especially when the subject breathing spontaneously or in assisted modes of mechanical ventilation (MV) cannot cooperate by keeping a steady respiratory pattern. In order to overcome these limitations, new mathematical models, and model fitting techniques, must be developed. The objective of this work is to present, with simulated signals, a novel, more general mathematical model for the MBN_2W, which accounts for the presence of a series dead space [83] and possibly varying V_T, EELV and inspiratory fraction of N_2, accompanied by candidate data-fitting algorithms aiming at computing the v/V distribution in the lungs.

5.2   Methods

The present mathematical model (Fig. 5.1) comprises a set of N parallel alveolar units with a common series dead space operating as ideal gas mixers. In this model, the sum of the fractions of V_T ventilating the alveolar units is equal to 1, which differs from other approaches [74, 84] that model the anatomical dead space as one of the parallel alveolar units.

The assumptions governing the equations of the present model are the following:

1. Each alveolar unit, as well as the dead space, are ideal gas mixers;

2. All alveolar units are in parallel and they communicate exclusively over the common dead space;

3. Respiratory gases enter and leave all alveolar units synchronously and their volumes are never emptied;

4. All units, including the dead space, are in equilibrium and have the same N_2 concentration prior to the nitrogen washout or washin;

67
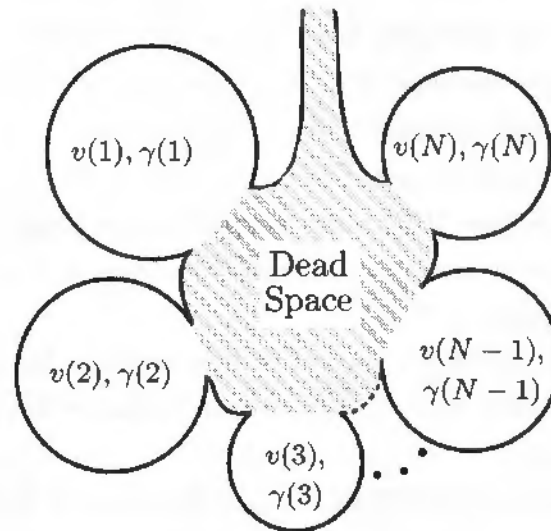
Figure 5.1: Model of the lung. The lung is composed of a common series dead space (hatched area) and a set of N alveolar parallel units. Each alveolar unit has its end-expiratory volume (v) and is ventilated by a fraction of the tidal volume (γ). Units communicate only through the dead space.

5. The common dead space, whose volume is always known, is in series with the set of alveolar units, and includes the anatomical and the instrumental dead spaces;

6. The EELV, representing the sum of the volumes of all ventilated alveolar units plus the common dead space, is also always known ;

7. Gas diffusional phenomena is negligible;

8. The respiratory exchange ratio is always unitary;

9. The N_2 solubility in blood and tissues is negligible;

10. The ventilation-to-volume ratios of the alveolar units are logarithmically distributed.

These assumptions, except that concerning the presence of a series common dead space, although not necessarily as explicit in this form, are the same as in previous works [76, 84].

5.2.1 The model formulation

Considering that a lung alveolar unit (J) is an ideal gas mixer characterized by an end-expiratory volume $v(J)$ and a ventilation fraction of V_T $\gamma(J)$ the specific ventilation is defined as

$$S(J) = \frac{\gamma(J)\,V_T}{v(J)}$$

By assuming an ideal step to a null inspiratory concentration of the tracer gas at the onset of the MBN_2W and a constant EELV during the maneuver, the classical modeling approach calculates the alveolar unit concentration of N_2 at each new breath (k) as

$$F_{N_2}^A (J,k) = \frac{F_{N_2}^A (J,k-1)}{1 + S(J)},$$ (5.1)

a dilution of the previous concentration in the end-inspiratory alveolar unit volume. If the lung is composed by N parallel alveolar units, the end-tidal N_2 concentration measured at the mouth is then a mixture

$$F_{N_2}^{et} (k) = \sum_{J=1}^{N} \gamma (J) F_{N_2}^A (J,k)$$ (5.2)

of the content of each alveolar unit weighted by the corresponding ventilation fraction. For a given distribution of $S(J)$ and a set of initial alveolar units concentrations the model in Eqs. (5.1) and (5.2) can be fitted to real washout data using a linear solver to estimate the corresponding $\gamma (J)$ values.

During MV, the ideal step condition is difficult to achieve without a specially designed circuit and does not hold with usual MV circuits. However, this condition can be disregarded by including the alveolar units inspired N_2 concentration $(F_{N_2}^{I,A}(k))$ to the model. The new equation becomes

$$F_{N_2}^A(J,k) = \frac{F_{N_2}^{I,A}(k)\, S(J) + F_{N_2}^A(J,k-1)}{1 + S(J)}, \tag{5.3}$$

which has the same properties of Eq. (5.1). There is no explicit condition over $F_{N_2}^{I,A}(k)$, so this can be used to incorporate a common series dead space (v_d) to the alveolar units.

At the beginning of inspiration, the concentration of N_2 in v_d is equal to the end-tidal concentration of the previous breath (Eq. (5.2)). The alveolar units inspired gas is a mixture of the ventilator delivered gas ($F_{N_2}^I$) and v_d content, being given by

$$F_{N_2}^{I,A} = \frac{F_{N_2}^{et}(k-1)\, v_d + F_{N_2}^I(k)\,(V_T - v_d)}{V_T} = \left(F_{N_2}^{et}(k-1) - F_{N_2}^I(k)\right) \cdot \frac{v_d}{V_T} + F_{N_2}^I(k). \tag{5.4}$$

During MV, V_T is usually constant but novel modes, markedly the variable ventilation, may provide different volumes for each breath. To extend the model while preserving the constant $S(J)$ distribution, a constant reference value of V_T (V_{T0}) must be incorporated. Redefining the specific ventilation as

$$S(J) = \frac{\gamma(J) \cdot V_{T0}}{v(J)},$$

changes Eq. (5.3) to

$$F_{N_2}^A(J,k) = \frac{F_{N_2}^{I,A}(k) \cdot \frac{S(J)}{V_{T0}} V_T(k) + F_{N_2}^A(J,k-1)}{1 + \frac{S(J)}{V_{T0}} V_T(k)}, \tag{5.5}$$

which is directly dependent on the ratio V_T/V_{T0}. This ratio indicates that different V_T can decrease or increase the dilution rate compared to the reference. In practice, this shifts the $\gamma(J)$ distribution to slower or faster compartment regions while preserving its shape. The reference V_{T0} can be freely chosen and is a way to normalize the distribution to better compare intra and inter subject data. The algorithm was designed to estimate $\gamma(J)$ irrespective of V_T, though, so that we would have the same estimate for $\gamma(J)$ whether V_T is constant or variable. More generally, the intended effect of the algorithm is to factor out any change in V_T in order to have a single curve for $\gamma(J)$, for whatever values of V_T, given a V_{T0}.

In all previous equations the inspiratory (V_T^I) and the expiratory (V_T^E) tidal volumes were considered equal, as expected for a relaxed patient under MV. However, in case of assisted ventilatory modes or during spontaneous ventilation this assumption is no longer valid. As $S(J)$ is related to the (variable) alveolar units volumes, it needs to be defined using a reference value and the washout model must track the changes in EELV and $v(J)$.

The EELV changes are tracked by the ratio of the difference between V_T^I and V_T^E and the current EELV,

$$\beta(k) = 1 + \frac{\left(V_T^I(k) - V_T^E(k)\right)}{EELV(k)}. \tag{5.6}$$

To model the effect of EELV changes in each alveolar unit, in order to keep a unique shape for the distribution of ventilation and prevent alveolar units closures, we hypothesized that all alveolar units reduce or increase volume by the same ratio. Assuming that the reference for $v(J)$ is the volume at the beginning of the washout $(v_0(J))$, at any breath cycle a alveolar unit's volume is known from the relation

$$v(J,k) = \beta(k-1)\,v(J,k-1) = \prod_{i=1}^{k-1}\beta(i)\,v_0(J). \tag{5.7}$$

The alveolar unit N_2 concentration is then calculated defining $S(J)$ in terms of $v_0(J)$. This leads to

$$F_{N_2}^A(J,k) = \frac{F_{N_2}^{I,A}(k)\cdot\frac{S(J)}{V_{T0}}V_T^I(k) + F_{N_2}^A(J,k-1)\prod_{i=1}^{k-1}\beta(i)}{\prod_{i=1}^{k-1}\beta(i) + \frac{S(J)}{V_{T0}}V_T^I(k)}, \tag{5.8}$$

which reduces to Eq. (5.5), if $V_T^E = V_T^I$ for all breath cycles, and to Eq. (5.3), if in addition the V_T is fixed. Considering the assumption that $\beta(k)$ is equal for all alveolar units, the end-tidal expired gas must account for the volume kept or released every breath cycle. Therefore, the end-tidal gas is now

$$F_{N_2}^{et}(k) = \sum_{J=1}^{N}\gamma(J)\frac{\left(V_T^I(k) + (1-\beta(k))\prod_{i=1}^{k-1}\beta(i)\frac{V_{T0}}{S(J)}\right)F_{N_2}^A(J,k)}{V_T^E(k)}, \tag{5.9}$$

with $\gamma(J)\,V_{T0}/S(J)$ expressing $v_0(J)$. Equation (5.9) is simplified to Eq. (5.2) for all the simple cases and then Eqs. (5.8) and (5.9) are a unified model for lung alveolar unit washout. It is important to note that in the most general case, with variable V_T^I and V_T^E, the estimated $\gamma(J)$ distribution is the one at the beginning of the washout maneuver, if $V_T = V_{T0}$ is considered.

For the present numerical results, the MBN_2W was simulated for a human adult under MV. The EELV ranged from $1.0\,L$ to $4.244\,L$ [168, 169] with $N=50$ alveolar units log-distributed on $S(J)$ in the range of 0.01 to 100. Mean V_T was $0.5\,L$ [170] and was kept constant or with a variability of 25 % [171]. The v_d was of $0.125\,L$ [172].

71

5.2.2 Recovering the distributions: inverse problem formulation

To define the inverse problem of finding $\gamma(J)$ knowing $F_{N_2}^{et}$ at each breath cycle of washout, consider the vector form of Eq. (5.9)

$$F_{N_2}^{et}(k) = [a_1 \cdots a_j \cdots a_N] \begin{bmatrix} \gamma(1) \\ \vdots \\ \gamma(N) \end{bmatrix},$$

$$a_j = \frac{\left(V_T^I(k) + (1 - \beta(k)) \prod_{i=1}^{k-1} \beta(i) \frac{V_{T0}}{S(j)}\right) F_{N_2}^A(j, k)}{V_T^E(k)}. \quad (5.10)$$

With Eq. (5.10), it is possible to see that the recovery of the vector γ is the solution of a system of linear equations. It can be noted that even with zero noise the inverse problem is most likely ill-posed when the number of alveolar units is larger than the number of washout breath cycles. To get a unique, smooth solution, the regularization method of Tikhonov [173] can be applied and up to three constraints over γ can be added. The first constraint is the classical nonnegativity condition [74, 84]. The second is the constraint of unitary total ventilation [84]. Finally, the sum of alveolar units volumes is constrained to EELV-v_d.

The problem of finding $\gamma(J)$ becomes equivalent to solve a constrained nonnegative least-square problem

$$\min_{\gamma} \|A\gamma - b\|^2 + \|\lambda L\gamma\|^2, \ s.t. \ \gamma \geq 0; \ C\gamma = c, \quad (5.11)$$

where $A \in R^{MxN}$ is a matrix whose elements a_{ij} are the predicted N_2 concentration of alveolar unit J at breath cycle i and $b \in R^M$ is the measured $F_{N_2}^{et}$ during the washout maneuver. The second term imposes a smoothness condition with a scalar gain λ and a weighting matrix $L \in R^{NxN}$, which can be used to penalize some alveolar units more than others. Matrix C is the constraint matrix.

See Appendix C for a summary of the algorithm to estimate the distribution of ventilation.

Least square solvers

The complete least square problem with three constraints was solved using an active-set algorithm [174], while in the condition requiring only nonnegativity, the Lawson and Hanson algorithm was used [175]. In either cases, the Tikhonov smoothness was applied expanding the matrix A and vector b with λL and a null vector, respectively.

5.2.3 Sensitivity to noise

Sensitivity to noise was assessed by the numerical simulation of uni- and bimodal log-normal distributions with different log-means and log-standard deviation (logSD) [74, 84]. Unimodal shapes are typical of normal young subjects and bimodal shapes are found in normal old as well as in patients with cystic fibrosis or other obstructive lung diseases (1). The simulations included washouts with error-free $F_{N_2}^{et}$ and measurements corrupted by normal distributed noise with zero mean and 3 % or 5 % standard deviation (SD) [84]. The three V_T conditions ($V_T^E = V_T^I = constant$; $V_T^E = V_T^I \neq constant$; and $V_T^E \neq V_T^I$) have been considered with a basal V_T of 500 mL. In presence of noise or with non-constant V_T the simulations were repeated 1000 times. At the beginning of the washout, instead of an ideal step change, the N_2 concentration fell to zero at the 5th breath cycle, simulating the washout of the inspiratory external circuit of the mechanical ventilator. Figure 5.2 depicts a diagram of all simulated conditions.
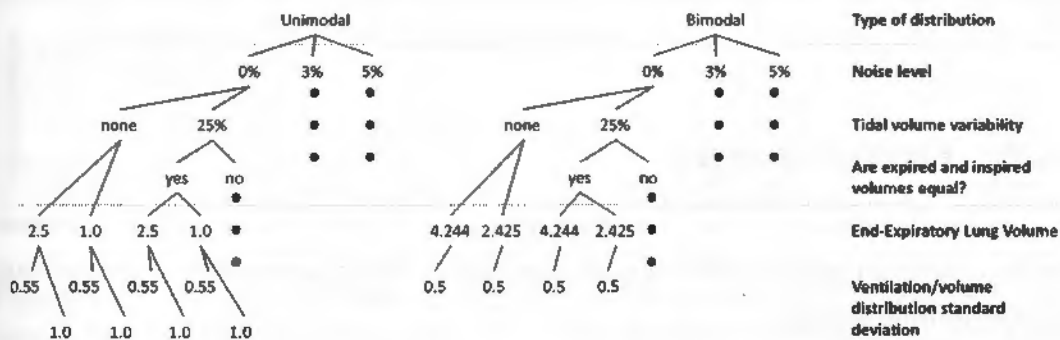
Figure 5.2: Scheme of simulations. Unimodal and bimodal distributions with error-free or noisy data and with tidal volume variability (or not). End-Expiratory Lung Volume as well as distribution standard deviation were selected from 2 options. Black dots indicate that flow chart continuation coincides with the correspondent at the same level.

5.2.4 Reconstruction conditions

To assess the effect of noise on different reconstruction approaches, simulations covered the nonnegative and the full-constrained least square problems, 17 breath cycles [84] or consensus washout (N_2 concentration at the end of the of the washout at 1/40 of the starting concentration [70]) and the use of L equal to identity or the alveolar unit weighting matrix (WM) proposed by LEWIS et al. [74]. Additionally, two Tikhonov gains λ have been used. One gain was constant, independent of noise and equal to 0.033, the other was calculated for each simulated washout as the maximum between this constant value and three values estimated by heuristic

methods (l-curve, Generalized Cross Validation and Normalized Cumulative Periodogram) [176]. Analogously, for noise-free simulations, the constant λwas equal to 0.0008 and the estimate was the maximum among this value and the heuristics. Figure 5.3 shows a diagram of the recovering flow chart.
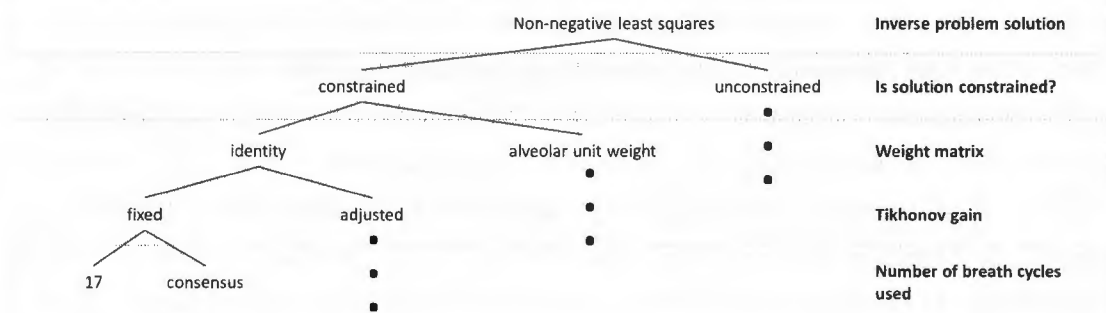
Figure 5.3: Distributions recovery flow chart. Nonnegative least squares are used either unconstrained or constrained (imposed values for tidal volume, end-expiratory lung volume and series dead space) considering a chosen weighting matrix, a Tikhonov gain and different number of breath cycles. Black dots indicate that flow chart continuation coincides with the correspondent at the same level.

5.2.5 Figures of merit

The quality of estimation was assessed by the Sum of Squared Errors (SSE) between the reconstructed and reference distributions and a set of parameters characterizing the distribution shape.

The shape parameters are the first three moments: mean, variance (expressed by the logSD) and skewness, the latter calculated only for unimodal distributions. All moments were estimated considering a continuous probability density function $P(x)$, with $x = log(S)$. The figures of merit are the differences between the parameters calculated for estimated and reference, expressed as a percentage of reference for mean and logSD. Results are calculated as mean and SD of the absolute values of all simulations. Additionally, we established an objective characterization of the reconstructed waveform shape. A unimodal shape was defined as the distribution that has only one peak or, in the presence of two peaks, the smaller to larger peak ratio must be less than 20 % or they must be spaced by less than 5 alveolar units. A bimodal shape was the distribution which has two peaks with smaller to larger peak ratio above 30 % separated by a valley of at most 80 % of smaller peak amplitude. This classification was applied to all tests performed.

For a visualization of the reconstructed curves, they are plotted as boxplot of all repetitions for the best combination of smoothness gain, weighting matrix and least square solver. All software routines were written and run in MatLab (MathWorks, USA).

5.3 Results

Figure 5.4 shows examples of N_2 washouts from ambient air to 100% O_2 for the three V_T conditions. The simulations were accomplished with error-free data. The v/V distributions were identical for the three conditions. Note that for the most general case (variable V_T and EELV), the $F^{et}_{N_2}$ can increase along the washout when $V^E_T > V^I_T$. Recovered $F^{et}_{N_2}$ and v/V distributions were practically coincidental with the simulated.
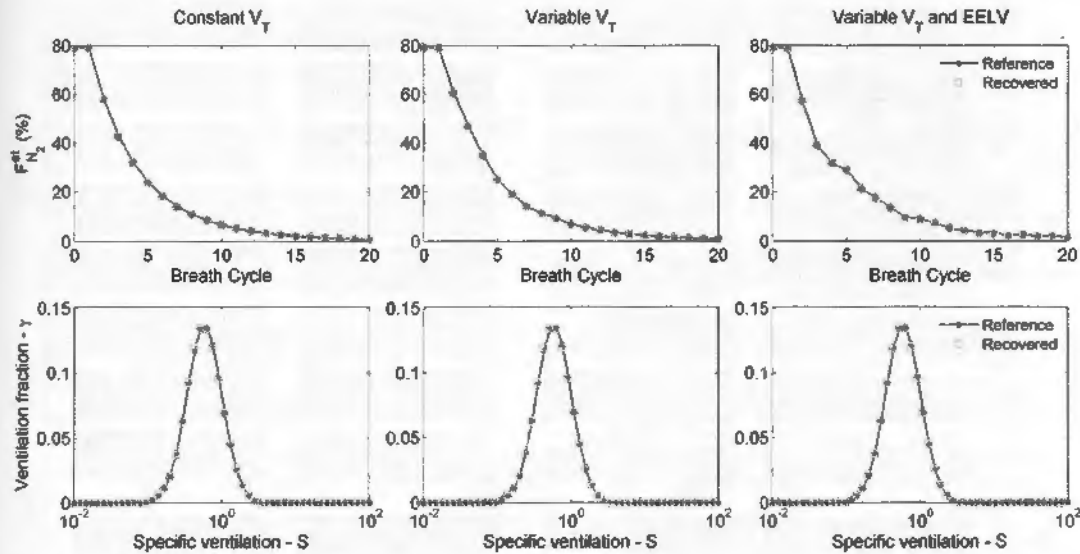
Figure 5.4: Examples of washout for the 3 tidal volume (V_T) conditions. Left panel: V_T is constant; central panel: V_T is variable but End-Expiratory Lung Volume (EELV) is constant; right panel: variables V T and EELV. Closed circles are reference and open circles are recovered values. $F^{et}_{N_2}$ is the N_2 end-tidal fraction.

Figure 5.5 presents the SSE means for the recovered unimodal and bimodal distributions, considering either the first 17 breath cycles or the consensus washout maneuver (see the SD in Fig. C.1). Small values of SSE (colored blue) represent estimated distributions close to the reference with alveolar units outside the simulated $S(J)$ span having a small ventilation fraction. The best result was achieved with fixed λ, and with alveolar unit weight (upper right panel). The constrained and unconstrained solutions gave similar results, slightly better with the former for bimodal distributions. The number of breath cycles used for recovering had minor effect on the results. Regarding the consensus option, the minimum number of breath cycles taken for v/V identification was 15 (unimodal, EELV=1.0 L, logSD=0.55) and the maximum was 50 (bimodal, EELV=4.244 L, logSD=0.50 for both modes).

The averaged absolute values of the relative errors of the means of unimodal and bimodal estimated distributions are shown in Fig. 5.6 (see the SD in Fig. C.2). A positive sign inside the cell indicates a tendency to estimate right shifted distribu-
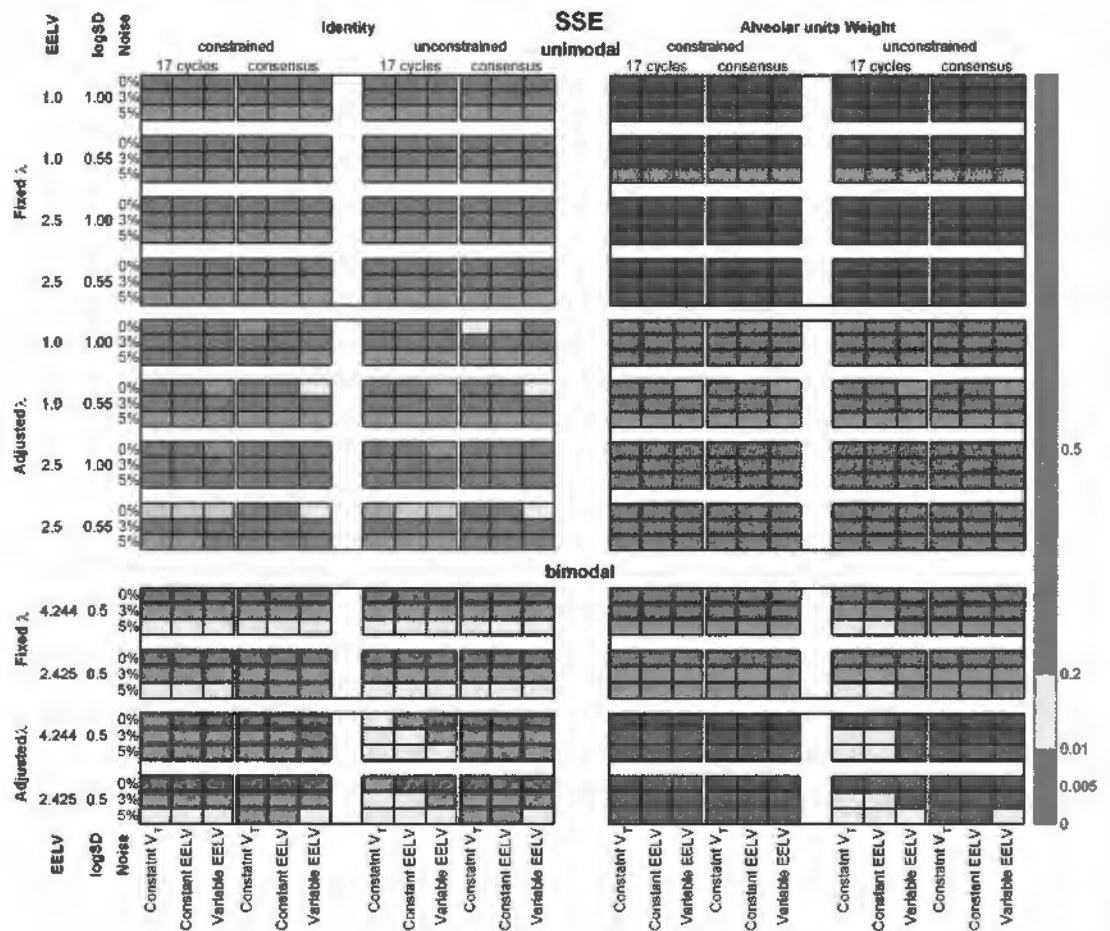
Figure 5.5: Sum of Squared Error (SSE) between estimated and reference ventilation-to-volume distributions. Unimodal (upper panel) and bimodal (lower panel) ventilation-to-volume distributions. All simulation and recovery conditions are depicted and indicated (rows and columns of the matrices). Colors coded on the right side of the figure indicate intervals of values of the mean SSE; EELV=End-expiratory Lung Volume; V_T = Tidal Volume.

tions, while a negative sign indicates a left shift. Analogously to the SSE evaluation, the best solution was found with fixed λ, with WM and constrained (up-right panel).
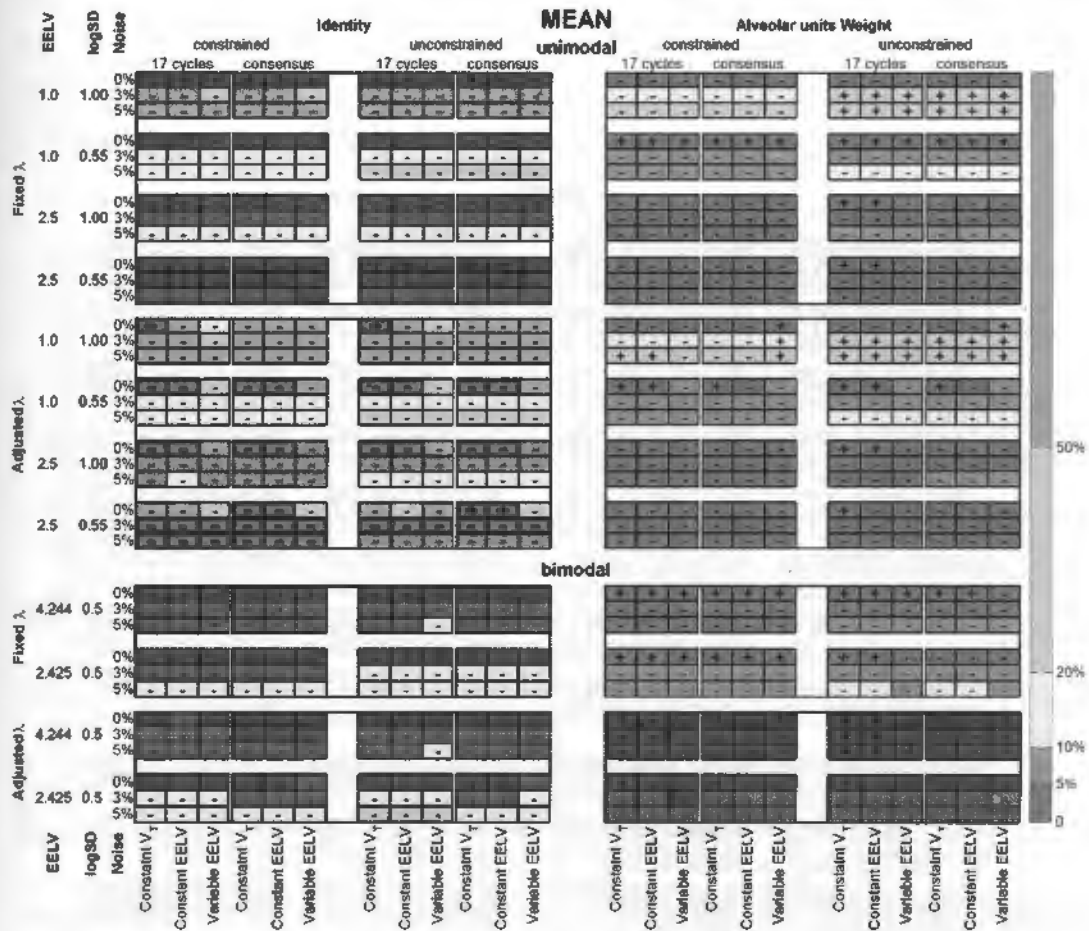
Figure 5.6: Averaged absolute values of the relative difference between means of estimated and reference ventilation-to-volume distributions. Unimodal (upper panel) and bimodal (lower panel) distributions. All simulation and recovery conditions are depicted and indicated (rows and columns of the matrices). Colors coded on the right side indicate intervals of the relative difference; sign inside each cell indicate if the recovered distribution is right (+) or left (-) shifted. EELV=End-expiratory Lung Volume; V_T = Tidal Volume.

Besides displacement of the mean value, the distribution can be narrowed or broadened. This characteristic was measured with the relative errors of logSD, shown in Fig. 5.7 (see the SD in Fig. C.3). Positive signs indicate broadened and negative signs, narrowed distributions. Signs, except for a few error-free data distributions, were positive (broadened). Analogously to the precedent evaluations, the best results were found with fixed λ, WM and constrained (up-right panel). The errors increased for small logSD distributions.

For a unimodal distribution, a shift in the mean can be a consequence of displacement of the entire distribution or a loss in symmetry. This was assessed with the
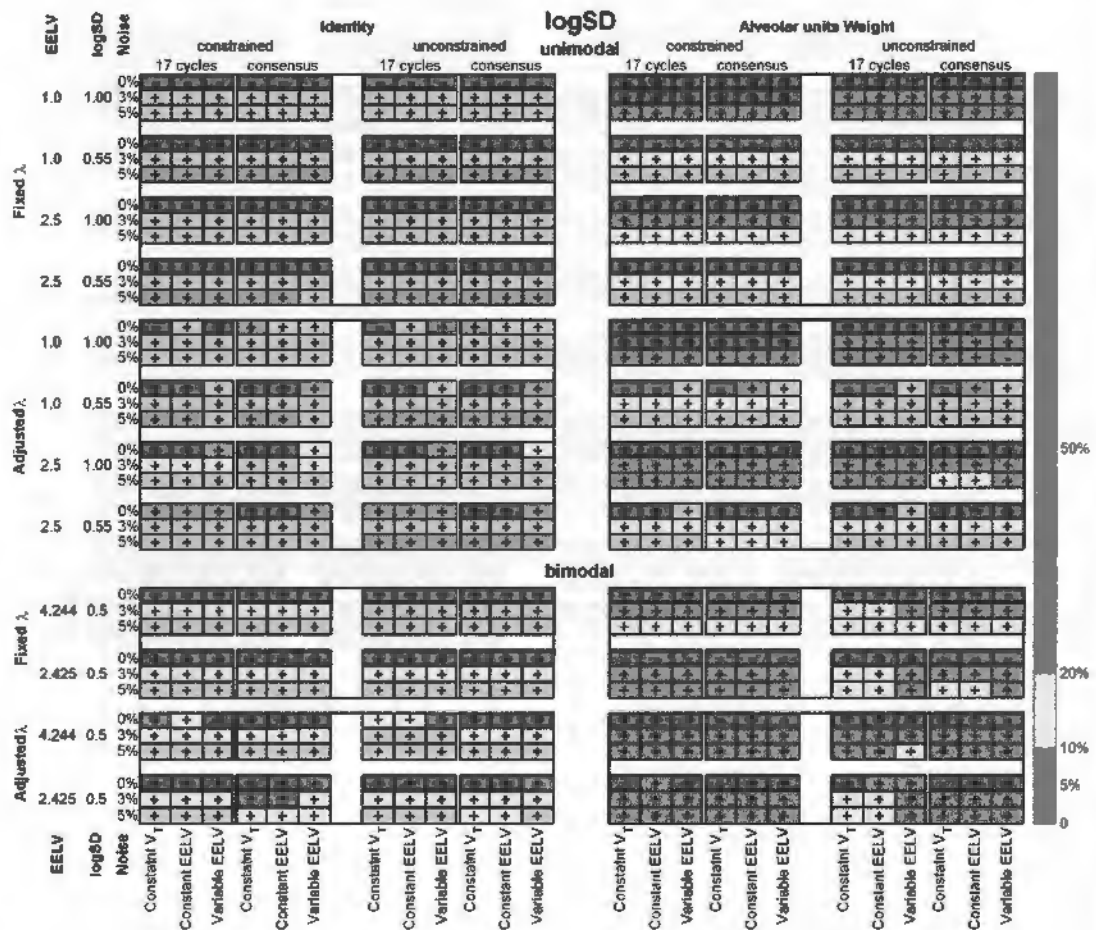
Figure 5.7: Averaged absolute values of the relative difference between logSD of estimated and reference ventilation-to-volume distributions. Unimodal (upper panel) and bimodal (lower panel). All simulation and recovery conditions are depicted and indicated (rows and columns of the matrices). Colors coded on the right side of the figure indicate intervals of the relative difference. Sign inside each cell indicate if the recovered distribution is broadened (+) or narrowed (-); EELV=End-expiratory Lung Volume; V_T = Tidal Volume

difference of skewness in estimated and reference distribution, as shown in Fig. 5.8 (see the SD in Fig. C.4). A positive (negative) sign inside the rectangle indicates a tail to the right (left). Note that the skewness sign was positive in most cases and opposed to the mean difference, which means an asymmetry of the estimated distribution. The errors were smaller than 0.05 only for error-free data, and increased 10-fold when noise was added to the data.
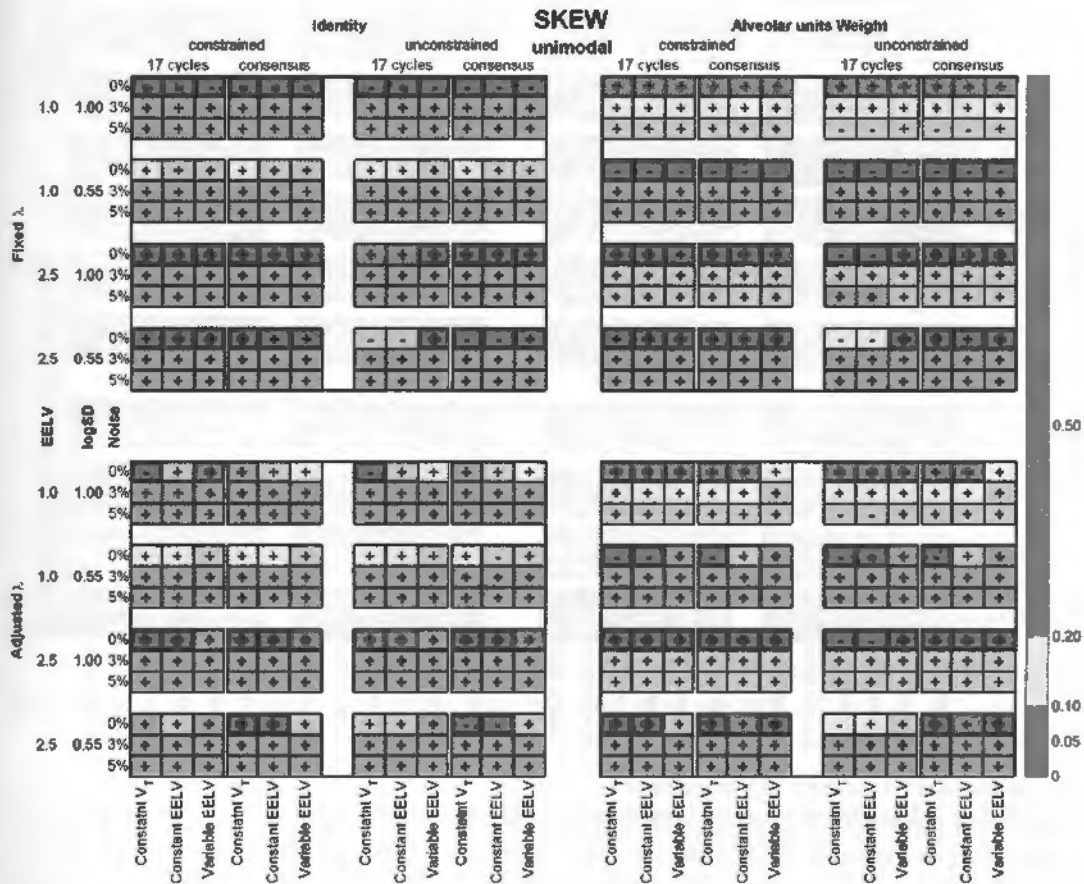
Figure 5.8: Averaged absolute values of the difference between skewness of estimated and reference unimodal ventilation-to-volume distributions. All simulation and recovery conditions are depicted and indicated (rows and columns of the matrices).Colors coded on the right side indicate intervals of the skewness error mean value; sign inside each cell indicate if the recovered distribution is tailed to the right (+) or left (-).EELV=End-expiratory Lung Volume; V_T = Tidal Volume

The waveform shape classification is shown in Fig. 5.9 for both unimodal and bimodal distributions. The results were calculated in percentage of agreements after 1000 tests for each case. For unimodal distributions, a high agreement was found for all recovering combinations. Considering 5 % of noise, the overall maximum agreement averaged 97.2 % (constrained, WM, adjusted lambda, 17 breath cycles) and the minimum was 84.0 % (constrained, identity, fixed lambda, consensus washout). For bimodal distributions the results spread from high to very low agreement. The

maximum was 90.0 % (constrained, identity, fixed lambda, 17 breath cycles) and the minimum was 17.8 % (unconstrained, identity, adjusted lambda, 17 breath cycles).
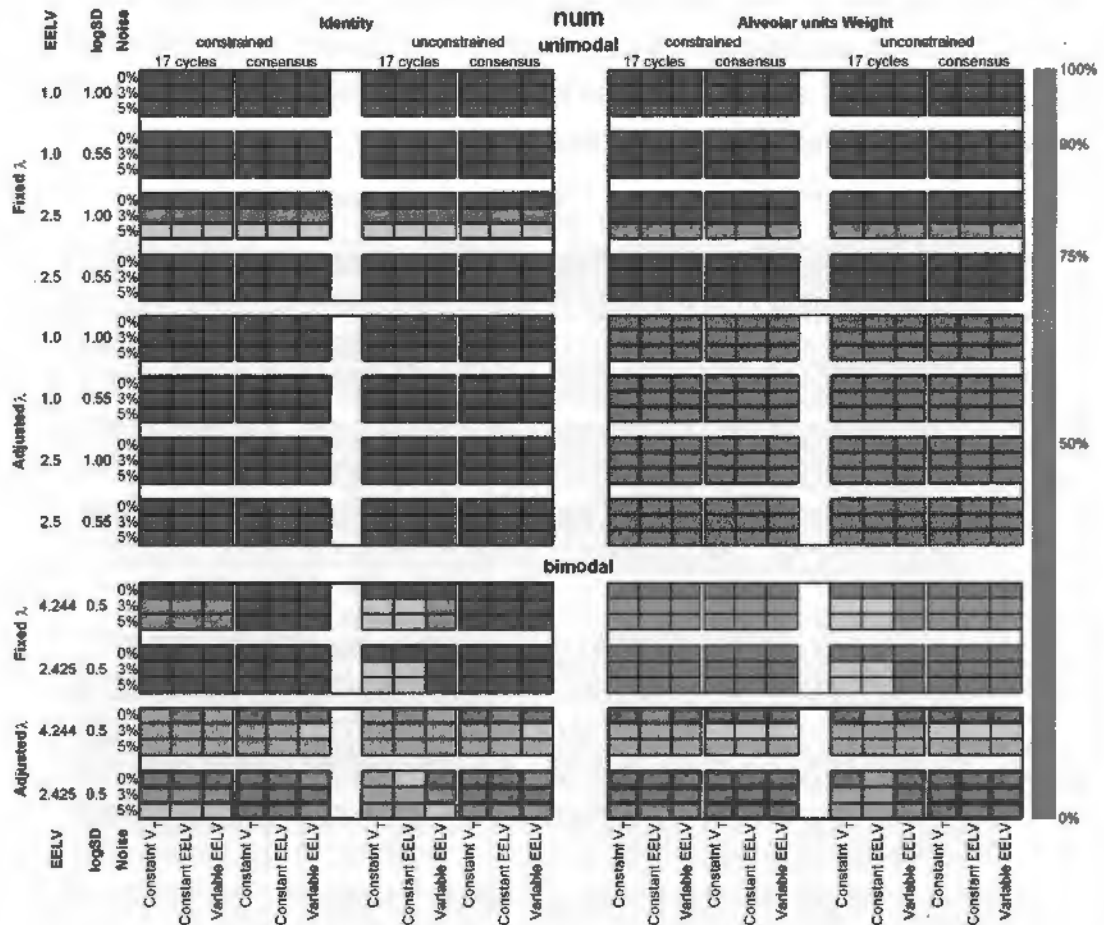
Figure 5.9: Waveform shape classification for unimodal (upper) and bimodal (lower) ventilation-to-volume distributions. All simulation and recovery conditions are depicted and indicated (rows and columns of the matrices). Colors coded on the right side indicate intervals of distribution shape agreements in percentage. EELV=End-expiratory Lung Volume; V_T = Tidal Volume

In order to depict the summary statistics and get a qualitative view of estimations, Figs. 5.10 and 5.11 show the boxplot of estimated unimodal and bimodal distributions, respectively. The plots represented the alternative of using WM, fixed Tikhonov gain, consensus washout estimation applied to data with 5 % of noise. In general, for unimodal distributions (Fig. 5.10) the median of the estimated alveolar unit fraction of ventilation was close to the reference, with higher agreement for the broad distributions (upper panels). For narrow distributions (lower panels), the estimated distribution has a small right skew, which leads to the negative difference of mean and positive skewness (Figs. 5.6 and 5.8, respectively). There are also some outliers outside the simulated alveolar units span, which increase the estimated logSD (Fig. 5.7). Most of these outliers are in the fast region (high v/V), as an effect

of noise, but do not reach the end of $S(J)$ range, penalized by the WM matrix. For bimodal distributions (Fig. 5.11), the estimated medians presented modes close to the reference with a higher agreement to the mode at low v/V. The high v/V mode was shifted to the left with a tail to the right.
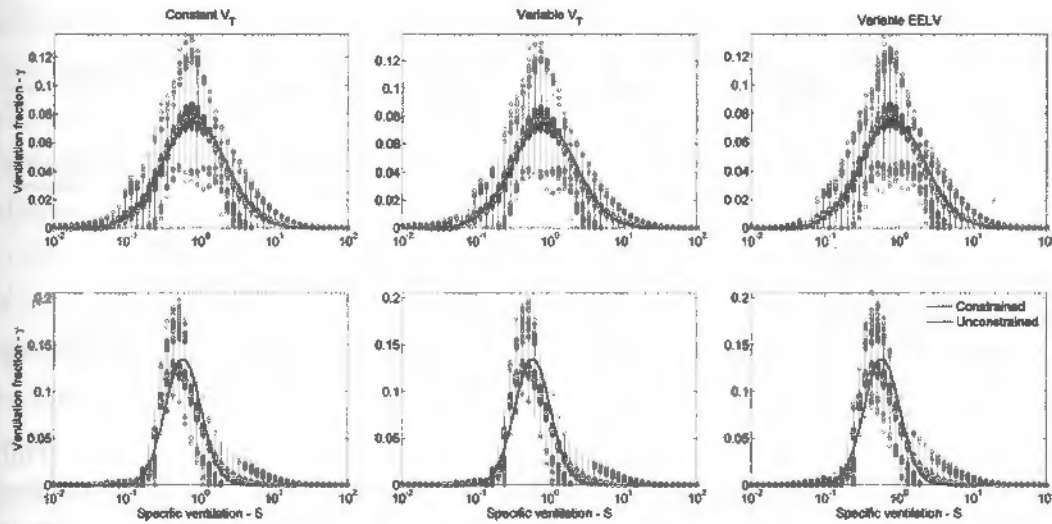
Figure 5.10: Boxplot of all estimated unimodal distributions with EELV = 1.0 L and 5 % of noise. Only the alternative with alveolar unit weight, fixed Tikhonov gain and consensus washout is represented. Both constrained (blue) and unconstrained (green) linear solvers are shown. logSD = 1.00 (upper panels); logSD = 0.55 (lower panels). Black dots = median values; wide bars = first and third quartiles; thin lines extend to extreme values that are not outliers; colored circles = outliers.

To assess the influence of errors of v_d measurement on the estimated distribution, Fig. 5.12 shows the boxplot of a 3 % noisy unimodal distribution with EELV = 1.0 L and logSD=0.55 estimated with +5 % and −5 % of error on the simulated v_d. When compared with the estimated error-free v_d (red line), an over/underestimated v_d lead to a small right/left shift on the distribution, respectively.

5.4 Discussion

A brief summary of the results ensues. A generalized equation has been demonstrated and tested which allows for the identification of v/V distributions for a lung with a common series dead space and variable V_T and EELV. As seen in Figs. 5.2 and 5.3, a rather large set of combinations of v/V distributions and strategies for the recovery algorithms was tested, mostly with results that support the proposed approach. Considering all V_T conditions and all figures of merit in ensemble (errors in SSE, mean, logSD, and skewness) the best combination for unimodal distributions was obtained with the joint use of WM, constrained solver, and fixed λ. The
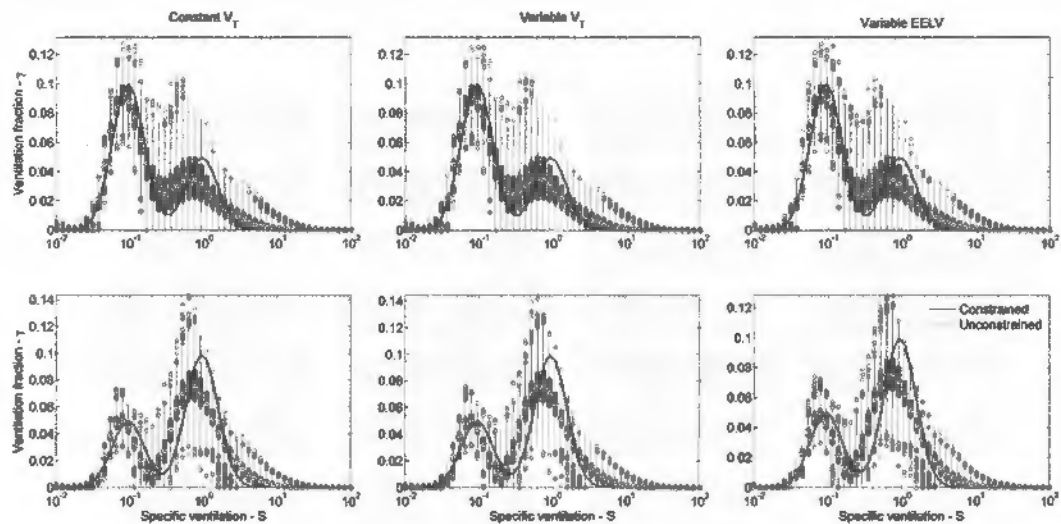
Figure 5.11: Boxplot of all estimated bimodal distributions with 5 % of noise. Only the alternative with alveolar unit weight, fixed Tikhonov gain and consensus washout is represented. Both constrained (blue) and unconstrained (green) linear solvers are shown. End-expiratory Lung Volume (EELV) of 4.244 L (upper panels) and 2.425 L (lower panels). Black dots = median values; wide bars = first and third quartiles; thin lines extend to extreme values that are not outliers; colored circles = outliers.
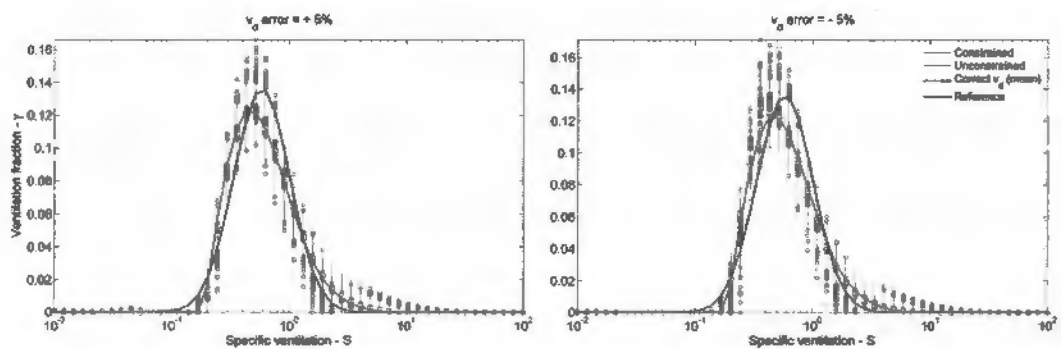
Figure 5.12: Influence of errors of dead space on the estimated distribution. Boxplot of all estimated unimodal distributions with EELV = 1 L, logSD=0.55, 3 % of noise on N_2 concentration and 5 % of error in dead space (v_d) volume estimation. Only the case with alveolar unit weight, fixed Tikhonov gain and consensus washout is represented. Both constrained (blue) and unconstrained (green) linear solvers are shown. Reference distribution (black) and estimated without v d error (red). Black dots = median values; wide bars = first and third quartiles; thin lines extend to extreme values that are not outliers; colored circles = outliers.

number of cycles used for recovery, 17 or consensus washout, produced similar outcomes. The best classification for unimodal distributions was achieved with WM, constrained solver, 17 cycles and adjusted (instead of fixed) λand resulted in 97.2 % of agreement, higher than the best combination for moments' estimates (91.6 %). For bimodal distributions, the best result for the figures of merit was obtained with WM, the constrained solver and adjusted (instead of fixed) λ, and the technique was insensitive to the number of breath cycles. The best classification was achieved with the identity matrix (instead of WM), the constrained solver and the fixed λ(90.0 %), much higher than using the best combination used for the moments' estimates (63.9 %).

The use of Tikhonov regularization spans several fields of applied sciences, as an effective tool to enforce smoothness when a curve with such a characteristic is expected, as in the present case. Nevertheless, it requires choosing the shape of the corresponding matrix and its values; here, only two regularization matrices were tested, the identity matrix and the WM proposed by LEWIS et al. [74] and applied as described by WHITELEY et al. [84], which penalizes the non-zero solutions found close to the upper and lower limits of the specific ventilation. Albeit we have tested a numerous set of distributions and recovering combinations, this is far from exhaustive. Moreover, the v/V distributions were also chosen, in the present case, to represent both normal and abnormal lungs of adults [74], with 50 alveolar units as in almost all previous works on this subject. We used specific ventilation ranging from 0.01 up to 100, as did WAGNER [72] and KAPITAN [177], differently from WHITELEY et al. [84]. Different choices may be required to model other patients e.g. infants.

As expected, all estimates were sensitive to measurement noise. The simulated experimental errors limit the recovery of v/V distributions with MBN_2W, and that would be expected with real signals. It remains a challenge to increase the accuracy of measurements in order to identify, with a single test, whether the distribution is uni- or bimodal, skewed to right or left, narrow or broad and apply this to assess or to control therapeutic procedures. The classical experimental setup requires an RMS and the use of mean expired gas demands the synchronization of signals, which are additional sources of errors [178]. The current technology allows the indirect monitoring of $F_{N_2}^{et}$ as the complement of O_2 and CO_2 gas fractions measured by the sensors available in mechanical ventilators [68] or other instruments [167, 179], which may also involve errors. Moreover, the MBN_2W, if performed with small amplitude changes of O_2, for instance with critically-ill patients [69], may see a reduction in the signal-to-noise-ratio; however, since with the present model the N_2 washout may be followed by a series of washin-washout maneuvers, perhaps the increased number of breath cycles may compensate for increased relative measurement errors.

The effect of experimental errors on recovering v/V distributions was studied by LEWIS *et al.* [74], KAPITAN [177] and WHITELEY *et al.* [84] with noise levels of 1 %, 0.1 %, 3 %–5 %, respectively. We consider the highest error limits more realistic, since other sources of errors such as that in flow rate and V_T must be considered. Their recovering algorithms were comparable to those applied in the present work [74, 84]. A direct comparison of results is difficult, however, since the modeled distributions, as well as the criteria to quantify the recovering estimates accuracy, are different. However, the present study used the same error amplitudes as tested by WHITELEY *et al.* [84] and also evaluated the first moments and the agreement in curve shapes for both unimodal and bimodal distributions. In particular, our results of shape agreement were higher than reported by WHITELEY *et al.* [84]. Nevertheless, these authors did not specify their criteria; our model allowed, for example, for the presence of a small second mode in order not to reject the identification of a unimodal distribution. Differently, our best classification result was found without the use of the WM of LEWIS *et al.* [74].

The present model includes most of the assumptions proposed in previous works addressing the recovery of v/V distributions from the MBN_2W LEWIS *et al.* [74], WHITELEY *et al.* [84]. A key difference here is the use of a common series dead space, instead of a parallel dead space (all-parallel model). There is a correspondence between both models, already demonstrated by EVANS *et al.* [180]. Nevertheless, if the washout comes from a lung with a common series dead space and the v/V reconstruction is based on the all-parallel topology, the distributions will not be identical. One first obvious difference is the amplitudes of the fractional ventilations, which add up to 1 in our model, but to $(1-v_d/V_T)$ in the all-parallel model. This amplitude reduction will imply a shift to the left and a warped shape in the classical graphical representation of the v/V distribution. Actually, the all-parallel model is a representation of the fractional alveolar ventilation instead of the total ventilation (which includes dead space rebreathing). It is a matter of choice: the all-parallel model follows the gas exchange terminology, whereas our model quantifies the real volume change of each alveolar unit, comparable to image estimates of ventilation distribution [181]. The v_d can be measured with the Fowler's technique [182] and preferentially by capnography instead of N_2 monitoring, because N_2 fraction amplitudes fall quickly along the washout and the early N_2 emptying of fast alveolar units tends to apparently increase the magnitude of v_d [76].

It should be noted that some of the assumptions involved in the assembly of the present general equation are rather restrictive and some are opposed to evidence, for instance the synchronous filling and emptying of alveolar units, and homogeneous N_2 concentrations in all units before the beginning of washout. Also, a simple model was used for v_d, a single airway connecting all alveolar units to the outside

environment, disregarding the several ramifications of the airways and the inherent presence of personal dead space [77]. Some of the assumptions are needed because the information obtainable from the MBN$_2$W is limited and simplification is mandatory.

The nonnegative least squares solution was obtained either with or without two additional constraints: 1- the V$_T$ fractions add up to 1; 2- the sum of the alveolar units volumes is equal to (EELV-v$_d$). Obviously, the effect on results of using these constraints depends on the accurate measurements of V$_T$, EELV and v$_d$. Measuring EELV and V$_T$ is inherent to the MBN$_2$W. Regarding EELV, its accuracy depends on both the N$_2$ analyzer and the flow rate sensor from which the V$_T$ is calculated. Moreover, a time delay correction to synchronize both signals may be necessary and this is a critical step [70, 178]. During washout, an aliquot of N$_2$ comes from blood and tissues and must be subtracted from the total eliminated amount of N$_2$ for the correct EELV evaluation [183]. However, the absence of reliable data has induced the recommendation not to correct for this effect [70]. Additionally, it was shown that the N$_2$ diffusion from outside the lungs causes only a small effect on v/V distributions recovering [184]. It must be noted that the present technique is not limited to the use of N$_2$ as the test gas. Other inert gases such as SF$_6$ or He [70] can be used and with obvious advantages because of their lower solubility in water and body tissues. Another potential confounder arises from the fact that, during washout, the composition of gases changes breath-by-breath and usual flowmeters are not immune to dependencies on physical properties of the gas mixture such as viscosity, density or thermal conductivity, depending on the operating principle of the transducer.

5.5   Conclusion

In conclusion, we demonstrated a generalized equation that allows the identification of v/V distributions without V$_T$ and EELV restrictions, for a lung model with a common series dead space. Moreover, nonidealities such as the departure from a step change in N$_2$ concentration are allowed by the model, which supports the applicability in spontaneously as well as in mechanically ventilated patients. We identified the best combinations of processing tools applied to minimize estimation errors, and showed the limitations of applying such a technique in presence of experimental noise.

Chapter 6

Generalized estimation of the ventilatory distribution from the multiple-breath washout: a bench evaluation

6.1   Background

The estimation of the pulmonary ventilation-to-volume (v/V) distribution may provide clinically useful information on intrapulmonary gas-mixing but is an underused byproduct of the end-expiratory lung volume (EELV) measurements during mechanical ventilation. The v/V can be calculated with the multiple-breath washout test, especially using N_2 as the inert and low solubility gas (MBN$_2$W). The classical method [72, 74, 84] models the lungs as a set of all-parallel units, including a dead space, whose contributions to the total lung ventilation are the unknowns. This approach has some limitations. For instance, it disregards the effects of the series dead space (v_d), whose volume may be estimated via the Fowler's method [182] throughout the washout; not only the EELV but also the tidal volume (V_T) must remain constant during the MBN$_2$W; the inspired fraction of tracer gas should decrease instantaneously to zero. Recently, we [82][1] proposed a generalized multicompartmental model for MBN$_2$W that includes a series dead space and copes with a non-ideal step change in gas concentration, variable V_T during the maneuver, and changes in EELV, as long as no compartment is completely emptied. Computational simulations showed that this model, together with an algorithm to estimate its parameters from measurements taken at the airway opening during MBN$_2$W, usually retrieved more correct estimations of the v/V distribution than previous propos-

---

[1]This is the paper presented in Chapter 5

als [82]. Furthermore, the alternative to impose *a priori* constraints determined along the MBN$_2$W limits the set of the v/V parameters estimates. However, since this same novel model drove the simulated MBN$_2$W, the results could have favored the algorithm in some form. It is arguable, hence, that bench tests with well-known physical models would allow for a better, less biased assessment of the effects of modelling the series dead space in the estimates of v/V distributions.

The present work intends to compare the v/V distributions estimated by both the classical and generalized approaches employing experimental data obtained from physical models, under the conditions (constant V_T and EELV) required by the assumptions of the classical model. Similar estimation procedures were used for both models, employing non-negative least squares and Tikhonov regularization plus a weighting matrix. The generalized approach adds a constrained least squares solver with imposed EELV, V_T and v_d. The results previously obtained by us [82], with numerically simulated experimental noise, directed the choice of the weighting matrix.

6.2 Methods

6.2.1 Mathematical model of the MBN$_2$W

The generalized mathematical model of the MBN$_2$W is as follows. The respiratory system comprises N parallel compartments, all connected through a single duct whereby the gases are exchanged with the ambient air. Each compartment J, whose volume is Vol$_J$, is an ideal mixer characterized by the fraction γ of V_T that enters and leaves it at each cycle, and its specific ventilation ($S(J)=\gamma V_T/Vol_J$), the sum of all compartmental volumes being equal to EELV-v_d. A series dead space is incorporated, considering that a compartment inspires a mixture of fresh gas from the inspiratory circuit and the content of the common duct. This also allows the model to be driven by a non-ideal step in inspiratory concentration of the tracer gas. Variable V_T is admitted by defining $S(J)$ with respect to a reference V_T, and variable EELV is achieved by tracking the differences between inspired and expired volumes, returning the distribution corresponding to EELV at the onset of maneuver [82].

In the experimental setup, where V_T and EELV were constant, the end-tidal N$_2$ concentration ($F_{N_2}^{et}$) at the k-th cycle is modeled by

$$F_{N_2}^{et}(k) = \sum_{J=1}^{N} \gamma(J) F_{N_2}^A(J,k), \tag{6.1}$$

87

with the compartmental concentrations given by

$$F_{N_2}^A(J,k) = \frac{\left(F_{N_2}^{et}(k-1)\alpha + F_{N_2}^I(k)(1-\alpha)\right) S(J) + F_{N_2}^A(J,k-1)}{1 + S(J)} \qquad (6.2)$$

where α is the dead space to tidal volume ratio (v_d/V_T).

The classical approach to model multiple compartment MBN$_2$W considers an ideal step change of the inspired tracer gas at the onset of washout with the dead space as an additional parallel compartment. Under these assumptions, Eq. (6.2) simplifies to

$$F_{N_2}^A(J,k) = \frac{F_{N_2}^A(J,k-1)}{1 + S(J)} \qquad (6.3)$$

and the combined compartmental concentrations are fitted to the measured mean expiratory N$_2$, by adjusting the respective weights. For a single compartment with a series dead space, it can be demonstrated, by using Eqs. (6.2) and (6.3), that this classical parallel model estimates a compartment with ventilation (1-α) shifted leftwards (lower specific ventilation) from the real compartment. The estimated specific ventilation (S') depends on the actual specific ventilation (S'=(1-α)S/(αS+1)), causing larger differences for faster compartments. Accordingly, the estimated compartmental volume is equal to EELV.

In case of a non-ideal step at onset of washout, a further shift depending on the ratio of inspired to expired concentrations occurs. To distinguish partially between this effect of a non-ideal step and the presence of a series dead space, an alternative classical model was tested. This is modeled by Eq. (6.2) with α=0.

6.2.2 Experimental setup

To test the effect of a series dead space in the washout maneuver under controlled conditions, two physical models were assembled: one with four compartments of equal γ and different Vol$_J$ (4C); and one with a single compartment (1C). The 4C allowed to examine the recovery of location, and the spread/breadth of the distribution, while with 1C the classical model distribution shift could be analytically predicted. Both models were ventilated by an Evita XL (Draeger Medical, Lübeck, Germany) and N$_2$, O$_2$ and CO$_2$ concentrations were measured by a fast mass spectrometer (AMIS 2000, Innovision, Glamsbjerg, Denmark). Pressure and flow signals were acquired directly from the ventilator and with a proximal pneumotachograph plus a pressure transducer. In order to synchronize the signals of gas concentration and flow, an uncalibrated flow signal was recorded from a pneumotachograph connected to the mass spectrometer, and the mainstream capnometer from the ventila-

tor was placed close to the gas sampling port. All data were recorded simultaneously with a program written in LabView (National Instruments, Austin, USA).

The ventilated compartments were 1-L anesthetic bags (VBM Medizintechnik GmbH, Sulz am Neckar, Germany) with end-expiratory volume maintained by application of a PEEP. A super-syringe inflation determined that at PEEP of $10\,\mathrm{cm}\,H_2O$ the volume of the bag was 1 L. CO_2 production was simulated by a constant low flow of this gas into the compartment with the smallest v/V ratio. CO_2 flow was titrated to achieve end-tidal concentration between 0.5 % and 1 % to reduce effects in expired volume.

The series dead space comprised an anatomical and an instrumental dead space. The anatomical dead space was represented by a resistive piece and standard connectors used in mechanical ventilation, such as 22-to-15 mm reductions and Y-pieces. The instrumental dead space was the connector for sidestream gas sampling and the pneumotachograph of the mass spectrometer, the mainstream capnometer of the ventilator, the proximal pneumotachograph and pressure outlet, a 90-degree connector to the resistance, and an HME filter (BB25, Pall Medical, Port Washington, USA) (Fig. 6.1). The total dead space volume (v_d), calculated from the geometry, were of 92 mL for 1C and of 152 mL for 4C.
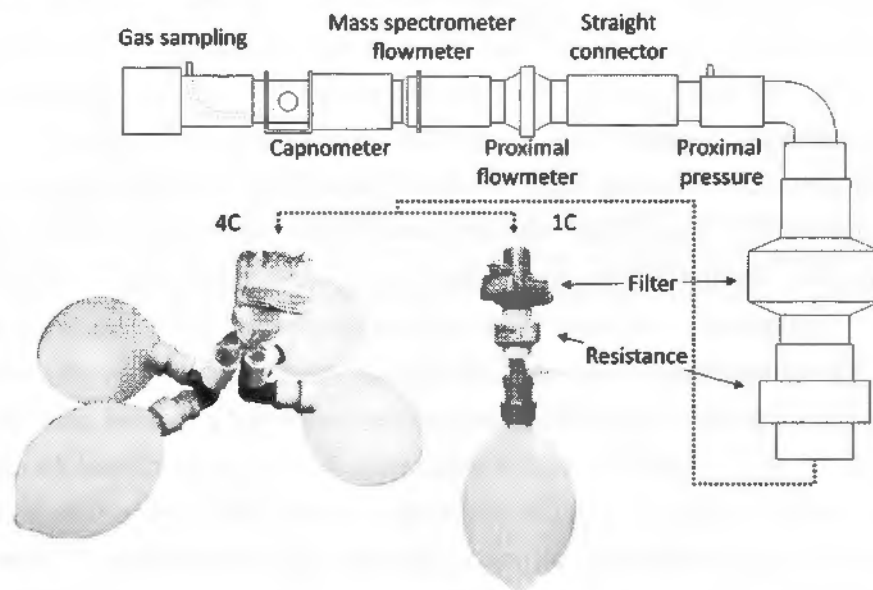
Figure 6.1: Representation of the experimental setup. The physical models are shown as photos with the anesthetic balloons at end-expiration. The components of the series dead space are represented by schematic drawings. The Y-piece of the ventilatory circuit was connected directly to the gas sampling piece. Note that the gas is sampled close to the capnometer chamber to avoid inspiratory/expiratory delay changes.

Tidal volume and end-expiratory volume of compartments were selected to match, as nearly as possible, specific compartments from a logarithmic distribution

of N=50 ventilation-to-volume ratios ranging from 0.01 to 100. The 1C model was ventilated with V_T=250 mL, representing a compartment with S=0.25. The respiratory frequency was of 15 breaths/min. A total of 5 washouts were performed with a N_2 step change from 50 % to zero. The 4C model compartments had 1.00 L, 0.83 L, 0.69 L and 0.57 L and were ventilated with V_T=560 mL, or 140 mL per compartment (S = 0.14, 0.83, 0.69 and 0.57, respectively). Where applicable, the compartmental end-expiratory volumes available for gas washout were reduced by inserting closed, impermeable plastic containers (Profissimo Gefrierbeutel, Germany) into the anesthetic bags, filled with appropriate volumes of air. The respiratory frequency was of 12 breaths/min (7 tests), 10 breaths/min (3 tests) or 15 breaths/min (2 tests). A total of 12 washouts were performed. In 9 tests, the N_2 step change was from 50 % to zero and in 3 tests the step change was limited from 10 % to zero. Experiments were performed in ATPD[2] conditions, disabling the ventilator's BTPS[3] compensation.

6.2.3 Signal processing

Before the data analysis, gas concentrations and flow were synchronized with a two-step procedure. First, flow curves from the ventilator and the mass spectrometer were aligned by maximizing their cross-correlation. Second, the delay from gas sampling was compensated breath-by-breath using the cross-correlation between the CO_2 signals from the mass spectrometer and the ventilator mainstream sensor.

The synchronized signals were processed to estimate v_d, EELV and the γvalues of the compartments. The v_d was calculated from CO_2 and volume curves using Fowler's method [4]. The EELV was estimated from inspired and expired N_2 volume during the washout (from onset until a N_2 concentration $\leq 1/40^{th}$ of initial value)[70]. Analogously, the distributions were estimated using the same number of cycles. The parameters of the multiple compartment model were estimated with nonnegative least squares and Tikhonov regularization with a fixed gain (4×10^{-3} for 1C and 3.3×10^{-2} for 4C) and a weighting matrix proportional to the compartmental washout ratio [84]. The generalized model was also estimated with a constrained least squares solver, imposing the sum of compartmental volume equal to the EELV-v_d and unitary total ventilation [82]. Overall resistance and elastance were calculated from pressure and flow signals to ensure similar mechanical behaviors of the compartments. Data were analyzed in MatLab (Mathworks, USA).

---

[2]*Ambient Temperature and Pressure Dry*
[3]*Body Temperature and Pressure Saturated*

6.3 Results

The time profile of inspiratory N_2 was not that of an ideal step and, as expected, the washout of 4C was slower than that of 1C (Fig. 6.2-A). EELV was estimated, from the MBN_2W inspired and expired N_2 volumes, as (1.13 ± 0.01) L for 1C and (3.24 ± 0.07) L for 4C. Typical expiratory capnogram curves were observed, despite the difference in magnitude (Fig. 6.2-B). The estimated v_d were (73.8 ± 6.4) mL for 1C and (185.7 ± 4.5) mL for 4C (see the Appendix D, Tables D.1 and D.2, for individual estimates of each experiment). The calculated overall resistance and elastance were R=(16.6 ± 0.3) cm H_2O L^{-1} s^{-1} and E=(78.5 ± 1.2) cm H_2O L^{-1} for 1C and R=(16.1 ± 0.6) cm H_2O L^{-1} s^{-1} and E=(20.8 ± 0.3) cm H_2O L^{-1} for 4C.
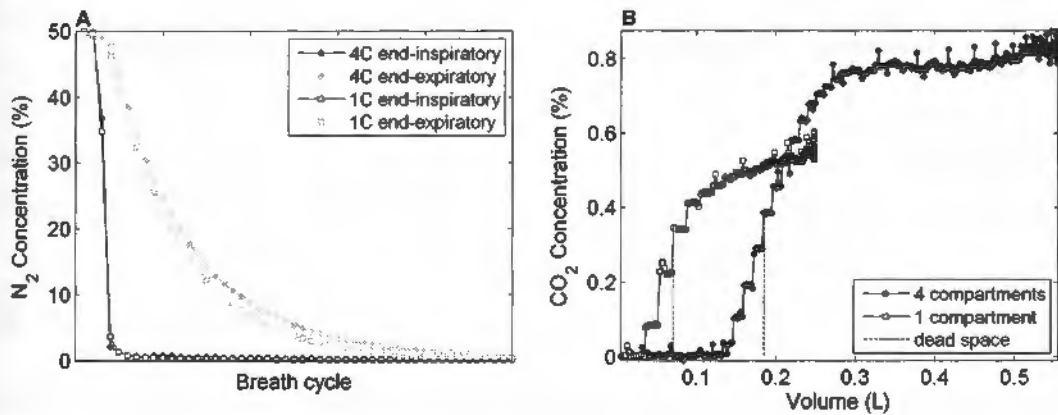
Figure 6.2: Examples of N_2 washout and CO_2 versus volume curves for the single (hollow square) and four compartment (filled square) physical models. 2-A) Inspiratory (black) and expiratory (gray) end-tidal N_2 fractions during one washout maneuver of each model. 2-B) Expired CO_2 versus volume, the dashed line represents the dead space volume as calculated by Fowler's technique.

The distribution retrieved by the constrained generalized model for physical model 1C was located at the correct compartment, with a small contribution of an adjacent compartment, and corresponded to the smallest sum of squared errors between estimates and the real distribution of v/V (Fig. 6.3-A and Table 6.1). In the case without constraints, the sum of compartmental volumes plus v_d underestimated EELV by 3 %, and the total ventilation was overestimated by 5 % (Fig. 6.3-B). The classical model retrieved two or three compartments, located, however, leftwards from the actual compartment, as theoretically predicted (Fig. 6.3-C). EELV was overestimated by 24 %, and v_d (complement of total ventilation) was underestimated by 10 %. The inclusion of the inspired N_2 concentration partially corrected EELV estimations (mean error of 18 %), but the distribution almost did not change (Fig. 6.3-D). The estimated distribution of each test with each model is shown in the Appendix D, Figs. D.1 to D.4.

91

Table 6.1: Sums of the squared errors between the estimated and true ventilation-to-volume ratio distributions.

	Single compartment (1C) 50 % N$_2$ step	Four compartments (4C) 50 % N$_2$ step	Four compartments (4C) 10 % N$_2$ step
Generalized Constrained	0.19 ± 0.15	0.07 ± 0.03	0.08 ± 0.01
Generalized Unconstrained	0.55 ± 0.15	0.12 ± 0.01	0.120 ± 0.004
Classical	1.21 ± 0.03	0.16 ± 0.01	0.160 ± 0.003
Classical + Inspired Fraction	1.20 ± 0.02	0.15 ± 0.02	0.160 ± 0.002
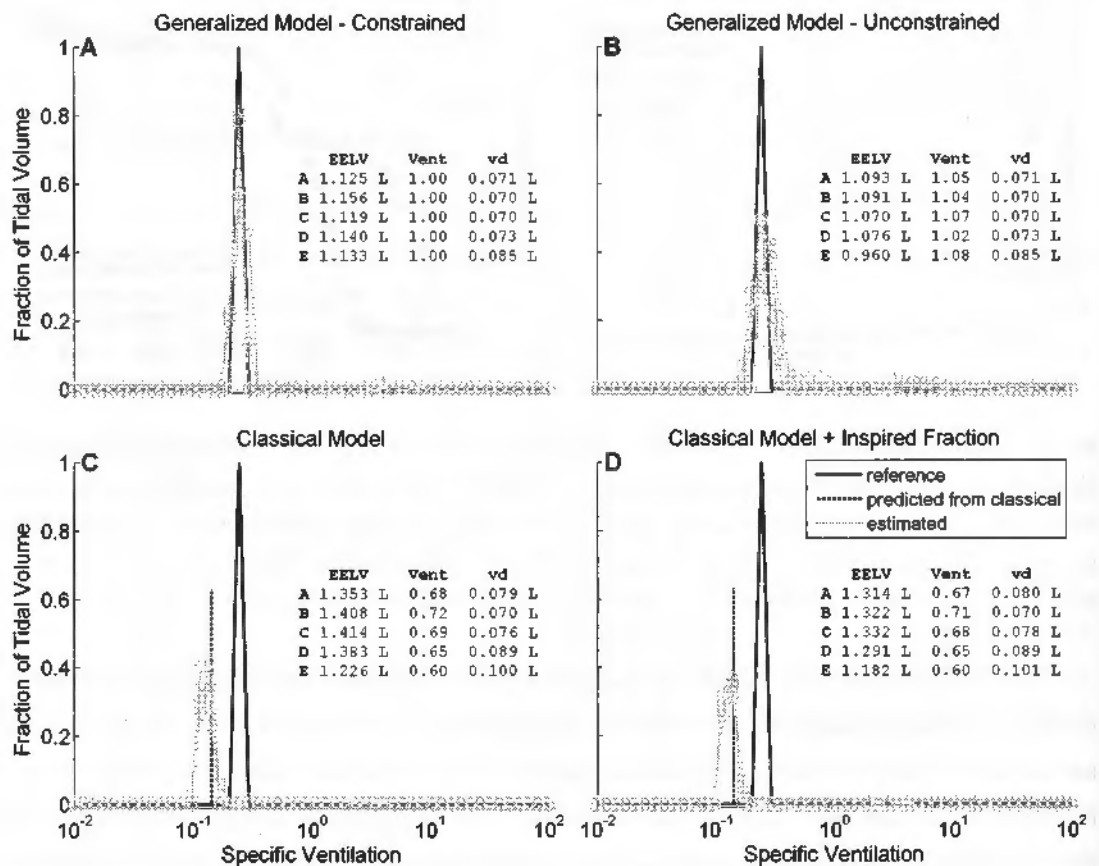
Figure 6.3: Distribution of specific ventilation estimated from the N$_2$ washout of a single compartment physical model. Results from each of five (A to E) repetitions are represented in gray with different symbols. The reference distribution is shown in black. The vertical dashed line (panels C and D) represents the theoretical distribution predicted for the compartment estimated by the classical model (ideal step washout). EELV is the End-Expiratory Lung Volume; Vent is the sum of the fractional compartmental ventilations ($\sum \gamma$); and v$_d$ is the dead space volume estimated by: Fowler's technique (for the generalized model) or the complement of total ventilation (for the classical model).

For large N_2 step changes (9 washouts, corresponding to cases A to I), the results for the model 4C were analogous to those for 1C. The constrained generalized model estimated v/V matching the expected specific ventilation, although narrower (Fig. 6.4-A); the unconstrained generalized model underestimated EELV and overestimated the total ventilation by 13 %, causing a rightward-shifted and broadened estimated v/V (Fig. 6.4-B). The distribution estimated with the classical model was broader than expected and shifted leftwards from the actual distribution (Fig. 6.4-C and Fig. 6.4-D); the EELV was overestimated by 15 % and v_d was underestimated by 6 %. Again, including the measured inspired N_2 in the classical model partially corrected EELV estimation reducing the errors to 7 %. For N_2 step changes limited to 10 % (3 washouts, Fig. 6.4, corresponding to the cases J to L), all estimated distributions with the generalized as well as the classical approach resulted broadened (Fig. 6.4) and with larger sums of squared errors relative to the real distribution (Table 6.1), indicating the deleterious effect of a decreased signal-to-noise ratio on the estimates. All individual estimated distributions are shown in the Appendix D, Figs. D.5 to D.8.

6.4 Discussion

We proposed a bench comparison between a novel generalized mathematical model for the MBN$_2$W [82] and a classical all-parallel model [72]. The tests were performed with a commercial intensive care unit ventilator and physical models mimicking lungs with one or four parallel compartments and a common series dead space. The main results are: (1) the retrieved v/V distribution with the constrained generalized approach was practically coincidental with the actual v/V distribution for both physical models for high N_2 step changes; the unconstrained solution did not represent the expected distributions, missing the true values of EELV and V_T;; and (2) the v/V distribution retrieved with the classical approach was leftward shifted and broader, as compared to the actual, and its corresponding estimates of EELV were slightly favored when the non-ideal step change of N_2 at the washout onset was taken into account.

We used estimates of respiratory mechanics to provide a first assessment of the reproducibility of the tests and of the assumption of equal ventilation to each of the compartments in 4C. The small spread shows that the physical properties of the models may be considered constant along the washout repetitions, while the four-fold decrease in elastance in 4C compared to 1C suggests that all four anesthetic bags have similar compliances and, consequently, similar ventilations.

The anatomy of the airways consists of a network of ramifications where a strictly common dead space is restricted only to the trachea [185]. The set of subdivisions

Generalized Model - Constrained

	EELV		Vent	vd	
A	3.268	L	1.00	0.185	L
B	3.269	L	1.00	0.187	L
C	3.321	L	1.00	0.186	L
D	3.254	L	1.00	0.189	L
E	3.113	L	1.00	0.185	L
F	3.249	L	1.00	0.172	L
G	3.208	L	1.00	0.188	L
H	3.350	L	1.00	0.186	L
I	3.150	L	1.00	0.186	L
J	3.295	L	1.00	0.188	L
K	3.260	L	1.00	0.188	L
L	3.202	L	1.00	0.188	L

Generalized Model - Unconstrained

	EELV		Vent	vd	
A	2.874	L	1.13	0.185	L
B	2.878	L	1.13	0.187	L
C	2.953	L	1.14	0.186	L
D	2.828	L	1.15	0.189	L
E	2.700	L	1.15	0.185	L
F	3.032	L	1.11	0.172	L
G	2.672	L	1.10	0.188	L
H	2.658	L	1.10	0.186	L
I	2.696	L	1.09	0.186	L
J	2.954	L	1.15	0.188	L
K	2.892	L	1.15	0.188	L
L	2.904	L	1.13	0.188	L

Classical Model

	EELV		Vent	vd	
A	3.644	L	0.75	0.137	L
B	3.627	L	0.72	0.152	L
C	3.689	L	0.74	0.142	L
D	3.606	L	0.74	0.144	L
E	3.499	L	0.74	0.142	L
F	3.568	L	0.70	0.166	L
G	3.639	L	0.74	0.145	L
H	3.660	L	0.76	0.137	L
I	3.592	L	0.74	0.146	L
J	4.257	L	0.79	0.115	L
K	4.074	L	0.76	0.134	L
L	4.044	L	0.74	0.146	L

Classical Model + Inspired Fraction

— reference
··· estimated, $F^I_{N_2}$ 0.5→0.0
— estimated, $F^I_{N_2}$ 0.1→0.0

	EELV		Vent	vd	
A	3.485	L	0.75	0.138	L
B	3.492	L	0.72	0.153	L
C	3.506	L	0.74	0.142	L
D	3.480	L	0.74	0.145	L
E	3.373	L	0.74	0.142	L
F	3.434	L	0.70	0.166	L
G	3.219	L	0.74	0.146	L
H	3.252	L	0.75	0.139	L
I	3.184	L	0.74	0.148	L
J	3.864	L	0.78	0.120	L
K	3.743	L	0.75	0.136	L
L	3.725	L	0.73	0.147	L

Figure 6.4: Distribution of specific ventilation estimated from the N_2 washout of a four compartments physical model. Results from each of twelve repetitions are represented (A to I, in light gray, with $F^I_{N_2}$ step from 0.5 to 0, and J to L, in dark gray, with $F^I_{N_2}$ step from 0.1 to 0), with different symbols for each test. The reference distributions are shown in black. EELV is the End-Expiratory Lung Volume; vent is the sum of the fractional compartmental ventilations $(\sum \gamma)$; and v_d is the dead space volume estimated by: Fowler's technique (for the generalized model) or the complement of total ventilation (for the classical model).

from the main bronchi to the deeper bronchioles results, during the expiration, in a mixture of alveolar gases originated from their respective airways. Thus, assuming the totality of the anatomical dead space simply as a common series duct is a considerable simplification, even though, as reported by FORTUNE e WAGNER [77], most of the dead space lies proximal to the carina. Nevertheless, the lungs, as represented by the classical model (alveoli connected to the airways opening and the airways as one additional parallel compartment), is less corresponding to the reality. In the present experiments, the physical models agreed very well to the proposed mathematical model, since most of the tubings comprise the common dead space.

Because of the lack of correspondence between the classical model and the actual anatomy, two features arise: the retrieved distribution is shifted to the left as previously reported [77] and broadened as compared to the expected. The specific ventilation of the estimated 1C compartment was close to the theoretically predicted specific ventilation (see Fig. 6.3-C). The spread of the distribution is influenced by factors inherent to the model, such as the difference in sensitivity to the common dead space for slow and fast compartments and the mixing of the contents of the compartments, which decreases the differences between the compartmental washout curves. The distribution curve is also sensitive to choices in data processing, for example the regularization gain used for the estimation of the parameters. The present gains were chosen on the basis of previously simulated experiments [82]. This may be a critical parameter in what concerns the shape of the estimated curve of v/V distribution, particularly its breadth and smoothness. Nevertheless, a tradeoff between accuracy and sensitivity to noise and artifacts is expected, hence this choice should be subjected to further investigations.

The distribution recovering technique applied to the classical model is essentially unconstrained. The solution includes the estimates of EELV and the parallel dead space of the distribution. This dead space does not necessarily correspond to v_d, representing the ventilation of a compartment with an infinite specific ventilation [74]. Regarding the EELV estimates, they were always overestimated with the classical model. EELV alone has been increasingly regarded as a useful parameter to evaluate the overall lung aeration [68], and it may be straightforwardly calculated by the breath-by-breath summation of the net N_2 (or other inert gas) volumes expired during the washout.

For the generalized model of MBN_2W, the EELV that serves as input to the constrained least squares estimation was calculated as above. The EELV estimates resulted accurate for both physical models. Gas exchange calculations based on measurements of gas concentrations and flow rate are very sensitive to the correction of the time delay between these signals [178]. A mainstream capnometer, currently a usual instrument in mechanical ventilation, was used as the time refer-

ence to synchronize the mass spectrometer measurements with the flow rate. This time correction, using just the maximal cross-correlation between the CO_2 concentration signals from the capnometer and the mass spectrometer, revealed feasible and reliable (EELV error $<5\%$ and variability between repetitions $<10\%$ [70]). Alternatively, an ultrasound flowmeter monitoring the washout of sulfur hexafluoride (SF_6), an inert and insoluble gas with a high molecular mass compared to the ambient air components, may be used. This device allows simultaneous and synchronous measures of flow rate and SF_6 concentration and has been used for the estimation of ventilatory inhomogeneity [186, 187].

Breath-by-breath estimates of the series dead space is a requirement for both the constrained and the unconstrained generalized v/V distribution. Instead of using prediction formulae, a direct measurement of that dead space is recommended, for example by applying Fowler's technique [182] to the capnogram [82] as in the present work. Prediction formulae are scarce and inaccurate, especially for some conditions such as during mechanical ventilation, in which body position varies and EELV depends on the applied PEEP. For instance, there are conflicting reports as to the effect of the dead space on a vastly employed index to quantify ventilatory inhomogeneity, the lung clearance index (LCI). Despite HAIDOPOULOU *et al.* [186] concluded that LCI is minimally affected by airway dead space, NEUMANN *et al.* [187] found an association between LCI and v_d/V_T. The LCI is an overall index of ventilatory inhomogeneity; in theory the increase of v_d/V_T should increase the magnitude of LCI. As an alternative, the alveolar lung clearance index (aLCI) [186] was proposed by considering the alveolar ventilation instead of the total ventilation as the bulk flow washing the alveolar units. The present generalized approach is based on the same assumption. Notably, an error in v_d estimation will result in a shifted distribution [82], as demonstrated with the extreme case of the classical model. Likewise, if v_d is overestimated the shift will be to the right (Appendix D, Fig. D.9) due to slower washout (increased rebreathing) for each modeled v/V.

The v/V distribution of the respiratory system may be modeled by a continuous curve within a finite interval. The recovery of this distribution from the limited information present in a MBN_2W is an ill-posed problem and requires simplifying assumptions. The three assumptions relevant to the estimation method are smoothness, known bounds and discrete representativity. The first assumption was discussed above. The bounds used here are the same from [72, 177], and clearly will lead to wrong estimates if they don't encompass all the v/V ratios of the real compartments. The *a priori* choice of 50 compartments is usual in the literature [72, 74, 76, 177]. In this study we tried to match every physical compartment to values present in the chosen 50 v/V ratios, favoring estimation: mismatch(es) between the physical v/V ratios and the set of chosen v/V ratios in the mathematical model will, in general,

cause the true ratio to be represented by a combination of modeled compartments. This should affect mainly the amplitude and breadth of the distribution, and less its location. An example of the effects of such mismatch can be seen in Appendix D (Fig. D.10).

Some limitations are addressed hereupon. To our best knowledge, this is the first report on multiple-breath washout of a multicompartmental physical model. Hence, we could not discuss our results against the literature as to possible comparative improvements. The physical models were limited to up to 4 units and this is far from the number of units found in experimental works with humans [73–76]. Considering that the v/V is distributed on a log scale, a simulation with many more units would be difficult to perform in view of the present method of construction of v/V units. For the estimation of v/V distribution we used the same cycles selected for calculating the EELV [70]. For our combination of V_T and compartments' volumes, this choice lead to a larger number of cycles than the commonly used of 17 [72, 84], which could have favored our results. Numerical simulations showed that, for the generalized model, both choices of cycles have similar estimations, although 17 cycles respected more the number of modes [82]. In the Appendix D, we show that this equivalence holds true in our experimental condition, including for the classical model (Figs. D.1 to D.8). Lastly, one of the features of the generalized approach to estimate v/V distributions is that V_T and EELV are not necessarily constrained to be constant, as in the classical method. The present results did not include tests with variable ventilation [171] feasible at the laboratory since commercial mechanical ventilators currently feature this choice of strategy.

6.5   Conclusion

In conclusion, the present work compared the v/V distributions estimated by both the classical and generalized approaches employing experimental data obtained with in vitro models. The method that resulted in better coincidence with the actual distribution was the generalized approach with a constrained least squares solver with imposed EELV and V_T.

Chapter 7

Discussion and Conclusion

Lung cells sense mechanical stimuli and generate chemical signals that regulate different biological processes. This mechanotransduction is important during lung development and for the healthy function of lungs [15]. However, excessive cell deformation stimulates the production of inflammatory mediators [19] and can disrupt cellular function, for example, surfactant properties and production [20, 188]. The expansion of human lungs is spatially heterogeneous and excessive regional deformation may be present even with limited global values. This thesis studied lung expansion heterogeneity in an animal model of the early phase of VILI in initially normal lungs, and in a mathematical model of the MBN$_2$W maneuver. The animal experiments investigated the effects of local mechanotransduction to lung injury during mechanical ventilation with clinically relevant settings (ARDSNet protocol, i.e. low V$_T$ and PEEP) and time frames (24 h). The MBN$_2$W may provide a bedside estimation of lung expansion heterogeneity, and the proposed model extended previously published models to account for variation in the ventilatory parameters and inspired gas concentration likely present in clinical application of the maneuver.

The main findings of the thesis are: (1) for mechanical ventilation of normal lungs, starting from a more heterogeneous aeration distribution (supine position) results in faster deterioration of the spatial heterogeneity of aeration and tidal strain, when compared to a more homogenous initial aeration distribution (prone position). However, regional strains were clearly below the proposed injurious threshold of 1.5 [41]; (2) independent of body position, the main contribution to the spatial heterogeneity of aeration and strain comes from small length-scales (5–10 mm), with tidal strain presenting larger contributions of length-scales of 10–15 mm, indicating influence of larger anatomical units to this variable; (3) the overall increase in heterogeneity of tidal strain and aeration in supine position was followed by an increase in the contribution of larger length-scales. Interestingly, this change in length-scale was also observed, in a smaller magnitude, for aeration distribution of prone animals; (4) whole lung phosphorylation rate (k$_3$) increased similarly in supine and prone

positions in a mild endotoxemia model. However, in supine animals, the regional differences in aeration and tidal strain resulted in spatially heterogeneous inflammatory processes. The effect of tidal strain on inflammation was dependent of the interaction of strain with blood volume and directly related to regional tidal strain heterogeneity; (5) the proposed generalized mathematical model (parallel lung units + series dead space, with variable V_T, EELV and inspired N_2) of the gas mixing compartments in the lungs during a MBN_2W performed better in the estimation of uni- and bimodal distributions of specific ventilation when compared with previous reports of the classical model (parallel lung units and dead space, with constant V_T and instantaneous change in inspired N_2); and (6) positioning the dead space in series with the ventilated compartments allowed for a better estimation of the location and spread of the specific ventilation distribution. Imposing constraints during the solution of the inverse problem further improved the estimations.

In the animal experiment, the initially more heterogeneous lung in supine position showed a marked mechanical deterioration when compared with prone position. At 24 h the overall inflammation, quantified as increase in ^{18}F-FDG uptake and phosphorylation rates, was similar in both groups. This may be attributed to the systemic inflammatory stimulus associated to the prolonged mechanical ventilation. In fact, at the end of the experiment the uptake rate in the supine group was comparable to a previous experiment with 16 h of mechanical stimulus alone (which may have been more aggressive due to the absence of PEEP, i.e. higher heterogeneity) [189], and was lower than found with a similar ventilation strategy, but higher endotoxemia than present in this thesis [49]. However, the moderate difference between supine and prone in tidal strain heterogeneity at baseline was marked at 24 h following the increase in aeration heterogeneity of the supine animals. Their dependent (dorsal) regions derecruited with a consequent redistribution of strain to the non-dependent (ventral) regions. This redistribution could act as a positive feedback mechanism with the under-ventilated areas becoming stiffer due to reduced stimuli for surfactant production. Because of airway parenchyma interdependence, the dorsal regions may also present a reduction in airway diameter (or airway closure), which adds to the reduction of ventilation. The mechanical impairment was also observed in the increase of the contribution of larger length-scales to the heterogeneity of aeration and tidal strain in supine lungs. Thus, while the level of inflammation and the mild histological injury could be considered acceptable when mechanical ventilation is essential for patient support, the gradual mechanical deterioration in supine indicates a progressively higher risk of more serious injury.

A strategy focused in reduction of the global strain (low V_T) and following just gas exchange goals (PEEP/F_IO_2 table driven by oxygenation) is not appropriate to hold impairment of lung mechanics in initially normal lungs. The mechanical

ventilation protocol adopted in the animal experiments is the hallmark of protective strategies for ARDS lungs proposed in the ARDSNet clinical trial [27]. In this protocol, lung expansion is achieved following step changes in PEEP accordingly to a pre-defined table that alternates between changes in end-expiratory pressure and F_IO_2. The adjustments of these variables are triggered to comply with a target oxygenation range (P_aO_2=55 mmHg to 80 mmHg or P_pO_2=88 % to 95 %). From the present results, it is clear that this type of goal results in delayed action in the case of mechanical ventilation of uninjured lungs. This finding is in agreement with a previous study showing that gas exchange (especially F_IO_2) does not fully reflect lung tissue conditions [190]. Therefore, it is necessary to design ventilatory protocols specific for those patients with normal lungs, which will probably involve a different parameter to be monitored, or at least a higher oxygenation threshold.

According our experimental findings, a preventive (halting the development of *de novo* injury) mechanical ventilation should: a) homogenize the spatial distribution of aeration and tidal strain; and, secondarily, b) minimize global strain and stress. One direct strategy could be to adopt prone position at the beginning of ventilation, extending to patients with normal lungs the recent push for this intervention in ARDS [119]. However, prone positioning is not universally applicable. In the surgical scenario, the patient position is generally dictated by the surgical procedure. In the intensive care unit, there are concerns with more complicated routine care of the patient and contraindications to proning exist [191, 192]. A possible alternative for homogenization of aeration in supine position is the open lung approach (OLA), i.e. to temporally apply high airway pressure in order to open all lung units (recruitment maneuver) and then set a PEEP that keep them open [193]. The ultimate goal to the OLA-PEEP should be to homogenize lung expansion, what is optimally assessed by CT. However, for clinical management simpler parameters directly measured at bedside are necessary and surrogates for this homogenization goal should be pursued. From the literature, some bedside strategies could be suggested for further detailed animal studies.

Different methods were proposed for how to choose the adequate PEEP for OLA [194]. While increasing PEEP to achieve an end-inspiratory pressure close to the pressure measured at total lung capacity in normal individuals seems to open ventral and dorsal lungs[195, 196], different lung regions will open at distinct airway pressures and at different rates [197, 198]. Thus, instead of just expanding poorly- and non-aerated regions, a high airway pressure could harmfully overdistend regions that are already aerated. One PEEP adjustment method that tries to avoid the harmful effects of a blind high-PEEP, is non-invasive and simple to apply at the bedside is the minimization of respiratory system elastance. CT scans in pigs with healthy lungs indicate that at a pressure slight above (usually $2\,cm\,H_2O$) the

PEEP of minimal elastance there is a balance between the amount of end-expiratory derrecruitment and end-inspiratory overdistension [199]. Experimental data of the effect of minimizing elastance on the distribution of strain and ventilation is absent. Though, PEEP has an effect in the ventro-dorsal distribution of strain measured in large ROIs [67] and high PEEP ($(17 \pm 3)\,cm\,H_2O$) lead to lower small length-scale heterogeneity of specific ventilation when compared with expiration to $0\,cm\,H_2O$ [51].

In our experiments, which adopted mechanical ventilation settings in accordance with current clinical practice, the measured tidal strains at voxel level were markedly below the proposed threshold for lung injury generated by mechanical stimuli [41]. This limited tidal strain agrees with findings in larger ROIs in pigs [67], and seems compatible with global strain measurements in patients [136]. A consequence of not having extreme regional strains in a heterogeneous normal lung is that for patients without lung injury a V_T less restrictive than the recommended for ARDS can be tolerated. This is important because lower V_T requires larger respiratory rate to maintain adequate minute ventilation and CO_2 clearance. High respiratory rate may have a contribution to lung injury by itself via mechanotransduction [21], and contribute to increase the power applied to the lungs during mechanical ventilation [139]. The bedside tool to balance the setting of V_T may also be the elastance. Because the pressure-volume relationship of the respiratory system can be characterized by a sigmoidal [200], the (bell-shaped) respiratory system elastance can be approximated by a second order polynomial. Thus, the contribution of the volume depended elastance (second order term) to the total elastance reflects the lung "point of operation" in the overall pressure-volume curve, indicating the presence of hyperdistention when it is positive [201, 202]. A naïve method applicable with the current parameters calculated by the mechanical ventilator is to observe the change in elastance (or driving pressure) after changing V_T. An increase in elastance or increase in driving pressure disproportional to the V_T step indicates presence of hyperdistention. For these measurements, using an esophageal balloon to separate the contributions of chest wall and lung to elastance/driving pressure may be more sensitive [203, 204]. Because tissue overdistension is a combination of initial inflation level and tidal expansion, the best PEEP (as defined in a titration maneuver) may change when V_T is increased. In general, a change in either PEEP of V_T should lead to consideration of readjusting the other parameter.

Importantly, for optimal management of mechanical ventilation, it must be noted that lung injury develops progressively, as reinforced by the current results. The homogeneously aerated prone animals did not develop atelectasis, but had a decrease in aeration. This indicates an increase in risk for prolonged ventilation. In both supine and prone position, together with the impairment in aeration quantified with CT, there was an increase in respiratory system and lung elastances. Experimental

data show that progressive impairment of lung mechanics is also present when using a titrated PEEP [205, 206]. Therefore, for the best care of mechanically ventilated patients, the temporal trend of lung mechanics should be periodically assessed as an indicative of regional mechanics deterioration, allowing for early adjustment in ventilator settings. Ultimately, it could be necessary to perform a new recruitment maneuver and PEEP titration. A ventilatory strategy that may delay or avoid the repetition of recruitment, and its hemodynamic repercussions, is the variable ventilation [206, 207]. In this strategy, the V_T varies at each breath. Because the lung expansion is heterogeneous, the hypothesis behind variable ventilation is that cycles with high V_T will recruit units that have an opening pressure above the range covered by the mean V_T [208]. Meanwhile, cycles with lowest V_T would relax overstretched areas. Indeed, in animal studies, variable ventilation is shown to improve respiratory mechanics in injured lungs [209–211], slow or halt the impairment of elastance in normal unrecruited lungs [206, 212], increase surfactant release [213] and improve gas exchange [214]. Although, the few results in patients with normal lungs are not conclusive [215, 216]. Also addressing the lung heterogeneity, a multi-frequency ventilatory strategy was recently proposed and may be considered in the future depending on the experimental data obtained [217, 218].

Finally, the present results suggest a vascular contribution to VILI. Others have proposed this effect is due to mechanical factors [123, 138, 219], and there is evidence that blood delivered inflammatory mediators potentiate mechanical injury of lung tissue tyler, altemeir. Therefore, the effect of a chosen combination of PEEP and V_T on the distribution of blood (flow or volume) within the lungs must be considered. The pulmonary vessels are classified in two categories, the alveolar capillaries (located at the alveoli edges) and the corner vessels. Alveolar expansion compresses the first and expands the second group, with the inverse occurring for low alveolar volumes. The net effect is that global pulmonary vascular resistance presents a flat minimum close to FRC [220]. This U-shaped behavior of vascular resistance is preserved regionally with the heterogeneous tissue density [221]. The PEEP effect over regional blood content depends then on its capacity of homogenization of lung aeration. Experimental studies using injected microspheres showed that in supine position, without a recruitment maneuver, PEEP=5 cm H_2O redistributes blood from ventral do dorsal regions, and this effect is exacerbated when PEEP=20 cm H_2O [222, 223]. In prone (homogeneously aerated) position, no vertical gradient of blood flow was observed and there was almost no flow redistribution with PEEP [224]. The differences between prone and supine positions may be explained by extra pulmonary and structural factors [224], but support the further investigation of the effect of a titrated PEEP on blood flow distribution in supine normal lungs. Large V_T add to vascular impairment with possible cyclic occlusion

of vessels at end-inspiration [138, 219], but there is no regional assessment of this occlusion in clinically used V_T. The interaction of strain and other inflammatory stimuli and the inflammation caused by ventilation itself suggest that a pharmacological therapy might complement protective ventilation [225]. Besides neuromuscular blockade [226], no large clinical trial has demonstrated a benefit for pharmacological intervention in VILI [225, 227]. One reason may be the large variability in comorbidities in patients that develop lung injury with a large number of underling biological processes. Considering the observed regional variability in these processes, methods for targeted tissue sampling [49] and pathway analysis (as proposed here) using functional imaging could help in finding specific pathways for intervention. Additionally, they may provide image aided patient screening for treatment.

Further improvements on individualization of ventilatory settings may come from bedside technologies that represent better surrogates of tidal strain (or, at least, aeration) heterogeneity than the single compartment global parameters. Two currently available of such technologies are the EIT and ultrasound. EIT is demonstrating increased number of clinical applications [228], including spatial information of both ventilation and perfusion distributions [62]. However, not without its limitations on which patients can be monitored, e.g. excludes cases of unstable spinal lesions, rib fracture or presence of thoracic wounding dresses [229]. Lung ultrasound is also an expanding image modality. It requires operator direct action and training, but provides identification of lung pathologies (including atelectasis and edema) [230], and could help in ventilator management by, for example, identifying lung recruitment [231]. The MBN_2W explored in this thesis could become a complementary tool that allow automatic unsupervised measurements and could be embedded in mechanical ventilators for use in virtually all patients.

The heterogeneity of specific ventilation quantified by the variance of the distribution is related to the heterogeneity of tidal strain. While the tidal strain measured in this thesis represents the deformation of the whole parenchyma and the specific ventilation represents variation in concentration of one gas, it is reasonable to assume that in ventilated regions the determinants of tidal variation in gas concentration are almost the same as of lung tissue expansion. Indeed, image measurements of tidal strain by image registration and specific ventilation by xenon washout are correlated [58]. Because it is possible that different distributions of specific ventilation (e.g. bimodal or unimodal with large standard deviation) will result in similar inhomogeneity indexes, but have distinct clinical implications, estimating the shape of the distribution is more interesting than assess just the spread. In spontaneously breathing critical care patients, sedation and lung disease may hinder establishment of a steady ventilation with constant V_T required by the classical MBN_2W mathematical model. In addition, in mechanically ventilated patients, the

current recommendation to avoid muscle paralysis and deep sedation [232] allows for spontaneous breathing efforts, which may result in differences in EELV during the MBN_2W. The multiple-compartments model proposed here addresses these conditions and could recover the application of estimation of specific ventilation distribution from MBN_2W, helping to monitor changes in heterogeneity of strain. The current simulation and bench results show the repeatability of the estimated specific ventilation distributions from noisy data and the advantage in modeling the series dead space. However, for translation to clinical application some challenges are still present.

In the physical model experiments the gases concentrations were measured with a mass spectrometer that has characteristics hardly find in more clinical equipment. For example, in anesthesia ventilators where gas monitoring in mandatory, normally, just O_2, CO_2 and the anesthetic agents are measured and the temporal resolution is poor [233]. Therefore, the N_2 concentration must be derived from the Dalton's law of partial pressure under the assumption of the presence of only the measured gases and N_2. Because each gas is measured with different sensors, integrating the measurements, to calculate FRC for example, may lead to an increased error. Additionally, the estimation errors for N_2 may increase for low concentrations. Yet, measurement of FRC in a physical model using this technique showed a worst case $(0.1$ step in F_IO_2 starting from $1.0)$ precision of $(3 \pm 7)\%$ [166], compatible with the recommendation for washout systems [70]. The indirect N_2 measurement also provided LCI values with the same characteristics of the standard SF_6 measurement with mass spectrometer [179]. The low sampling frequency could affect the synchronization between gas concentration and flow, and the determination of the series dead space. Though, as addressed in the simulation and in the analysis of the bench study, those errors have an impact in the estimation of the specific ventilation distribution, the generalized model still seems to perform better than the classical. Of note, a recent technology for measurement of gas concentration using laser spectroscopy can provide a mainstream O_2 and CO_2 (and water vapor) sensor with high temporal resolution and accuracy [234]. It is even suggested that this new sensor could provide information about ventilation-perfusion from only ventilatory maneuvers [235]. With the generalized model, in addition to the gas concentration, it is required to measure the inspired and expired volumes. Because in the physical model study these values came from flows measured by the mechanical ventilator, they should represent a realistic scenario.

The effect of two additional assumptions needed in the generalized model in comparison to the classical: all compartments have the same ratio of change in end-expiratory volume, and are connected directly to the series dead space, should be addressed. Experimental data using the parenchymal mark technique shows that the

change in total volume (tissue+gas) is different for tetrahedra in the dependent and non-dependent (supine) regions after decremental steps from TLC [236]. However, the gas volume distribution is also heterogeneous with a vertical gradient. Because this is the reference for the specific ventilation it is unclear what is the consequence of that regional difference in volume change. Moreover, one compartment in the MBN$_2$W model represents multiple real lung units that could be distributed in different spatial locations. Thus, the equal ratio assumption may be a sufficient approximation. The direct connection of ventilation units and dead space is an oversimplification of the lung structure [185], and the personal dead space (the conducing airways from a compartment until the common airway) may decrease the performance of the generalized model. Still, the bulk of the dead space volume is enclosed in the main airways [77] making a single series dead space better than none as considered before. Beyond the important result of improving the representation of the real ventilation distribution, modeling the dead space may approximate the numerical values of specific ventilation and tidal strain.

7.1   Conclusion

This thesis studied the heterogeneity of lung expansion in an experimental model of the early phase of VILI and in a theoretical model of the MBN$_2$W. The results advance the knowledge of the pathophysiology of lung injury in initially normal lungs and show the feasibility of a generalized model of the distribution of specific ventilation potentially applicable to mechanically ventilated patients. Therefore, they have the potential to improve clinical practice.

The animal experiments used advanced PET/CT image analysis to undercover the regional distributions of the static and dynamic expansion of lungs and its consequence to lung injury, during mechanical ventilation with currently recommended ventilator settings. The proposed method for defining regions-of-interest for PET kinetics analysis allowed for the determination of different aspects of regional inflammation in higher resolution than previous studies.

This combination of techniques helped to link the important results about regional mechanical deterioration during early VILI with local inflammation, suggesting mechanisms (strain redistribution and positive interaction with blood volume) for the development of lung injury in patients without injury at the onset of ventilation (e.g. surgical or septic patients).

Targets for further study of VILI biological pathways were pointed by the results of the image guided analysis. This, by itself may add to the field through better functional characterization of samples used for measurement of gene expression.

For the MBN_2W, the new ventilation model proposed does not have some of the hypothesis that limited the use of previous models in patients requiring mechanical ventilation. Computer simulations and controlled bench experiments showed the improved performance of the new model supporting investigations with human data.

However, more studies are necessary to address the effects in the results obtained when gas concentrations are measured with the limited devices available in clinical care. In the future, measurement of distribution of specific ventilation, and MBN_2W in general, may complement monitoring techniques already available for clinical use such as EIT and lung ultrasound, allowing for better characterization of lung expansion heterogeneity.

The tools used and proposed in this thesis can be employed for the study of new ventilatory strategies specifically designed for patients with normal lungs, as well as for advanced monitoring of lung conditions at the bedside.

Bibliography

[1] MILIC-EMILI, J. "Static Distribution of Lung Volumes". In: *Comprehensive Physiology*, pp. 561–574, American Cancer Society, 2011. ISBN: 9780470650714. Disponível em: <https://onlinelibrary.wiley.com/doi/abs/10.1002/cphy.cp030331>. First published in print 1986.

[2] D'ANGELO, E., AGOSTONI, E. "Distribution of transpulmonary pressure and chest wall shape", *Respir Physiol*, v. 22, n. 3, pp. 335–344, Dec 1974.

[3] TAWHAI, M. H., NASH, M. P., LIN, C.-L., et al. "Supine and prone differences in regional lung density and pleural pressure gradients in the human lung with constant shape", *Journal of Applied Physiology*, v. 107, n. 3, pp. 912–920, 2009. Disponível em: <https://doi.org/10.1152/japplphysiol.00324.2009>.

[4] VAWTER, D. L., MATTHEWS, F. L., WEST, J. B. "Effect of shape and size of lung and chest wall on stresses in the lung", *Journal of Applied Physiology*, v. 39, n. 1, pp. 9–17, 1975. Disponível em: <https://doi.org/10.1152/jappl.1975.39.1.9>.

[5] WEST, J. B., MATTHEWS, F. L. "Stresses, strains, and surface pressures in the lung caused by its weight", *Journal of Applied Physiology*, v. 32, n. 3, pp. 332–345, 1972. Disponível em: <https://doi.org/10.1152/jappl.1972.32.3.332>.

[6] SUKI, B., STAMENOVIĆ, D., HUBMAYR, R. "Lung parenchymal mechanics", *Compr Physiol*, v. 1, n. 3, pp. 1317–1351, Jul 2011.

[7] SALAZAR, E., KNOWLES, J. H. "An analysis of pressure-volume characteristics of the lungs", *Journal of Applied Physiology*, v. 19, n. 1, pp. 97–104, 1964. Disponível em: <https://doi.org/10.1152/jappl.1964.19.1.97>.

[8] GLENNY, R. W., ROBERTSON, H. T. "Spatial Distribution of Ventilation and Perfusion: Mechanisms and Regulation". In: *Comprehensive Physiology*, pp. 373–395, American Cancer Society, 2011. ISBN:

9780470650714. Disponível em: <https://onlinelibrary.wiley.com/doi/abs/10.1002/cphy.c100002>.

[9] PARÉ, P. D., MITZNER, W. "Airway-Parenchymal Interdependence". In: *Comprehensive Physiology*, pp. 1921–1935, American Cancer Society, 2012. ISBN: 9780470650714. Disponível em: <https://onlinelibrary.wiley.com/doi/abs/10.1002/cphy.c110039>.

[10] FROESE, A., BRYAN, A. "Effects of Anesthesia and Paralysis on Diaphragmatic Mechanics in Man", *Anesthesiology*, v. 41, n. 3, pp. 242–255, 1974. Disponível em: <http://anesthesiology.pubs.asahq.org/article.aspx?articleid=1962091>.

[11] ALBERT, R., HUBMAYR, R. "The Prone Position Eliminates Compression of the Lungs by the Heart", *American Journal of Respiratory and Critical Care Medicine*, v. 161, n. 5, pp. 1660–1665, 2000. Disponível em: <https://doi.org/10.1164/ajrccm.161.5.9901037>.

[12] HEDENSTIERNA, G., EDMARK, L. "Effects of anesthesia on the respiratory system", *Best Practice & Research Clinical Anaesthesiology*, v. 29, n. 3, pp. 273 – 284, 2015. ISSN: 1521-6896. Disponível em: <https://doi.org/10.1016/j.bpa.2015.08.008>.

[13] HEDENSTIERNA, G., MCCARTHY, G., BERGSTRÖM, M. "Airway Closure during Mechanical Ventilation", *Anesthesiology*, v. 44, n. 2, pp. 114–123, 1976. Disponível em: <http://anesthesiology.pubs.asahq.org/article.aspx?articleid=1961324>.

[14] PALUCH, E. K., NELSON, C. M., BIAIS, N., et al. "Mechanotransduction: use the force(s)", *BMC Biology*, v. 13, n. 1, pp. 47, Jul 2015. ISSN: 1741-7007. Disponível em: <https://doi.org/10.1186/s12915-015-0150-4>.

[15] WIRTZ, H. R., DOBBS, L. G. "The effects of mechanical forces on lung functions", *Respiration Physiology*, v. 119, n. 1, pp. 1 – 17, 2000. ISSN: 0034-5687. Disponível em: <https://doi.org/10.1016/S0034-5687(99)00092-4>.

[16] EDWARDS, Y. S. "Stretch stimulation: its effects on alveolar type II cell function in the lung", *Comparative Biochemistry and Physiology Part A: Molecular & Integrative Physiology*, v. 129, n. 1, pp. 245 – 260, 2001. ISSN: 1095-6433. Disponível em: <https://doi.org/10.1016/S1095-6433(01)00321-X>. Surfactant, Lungs and the Evolution of Air Breathing - Tribute to R.E. Pattle.

[17] SPIETH, P. M., BLUTH, T., GAMA DE ABREU, M., et al. "Mechanotrans-duction in the lungs", *Minerva Anestesiol*, v. 80, n. 8, pp. 933–941, Aug 2014.

[18] WIRTZ, H., DOBBS, L. "Calcium mobilization and exocytosis after one mechanical stretch of lung epithelial cells", *Science*, v. 250, n. 4985, pp. 1266–1269, 1990. Disponível em: <https://doi.org/10.1126/science.2173861>.

[19] VLAHAKIS, N. E., SCHROEDER, M. A., LIMPER, A. H., et al. "Stretch induces cytokine release by alveolar epithelial cells in vitro", *American Journal of Physiology-Lung Cellular and Molecular Physiology*, v. 277, n. 1, pp. L167–L173, 1999. Disponível em: <https://doi.org/10.1152/ajplung.1999.277.1.L167>.

[20] AMIN, S. D., MAJUMDAR, A., ALKANA, P., et al. "Modeling the effects of stretch-dependent surfactant secretion on lung recruitment during variable ventilation", *Journal of Biomedical Science and Engineering*, v. 06, n. 12, pp. 61–70, 2013. Disponível em: <https://doi.org/10.4236/jbise.2013.612a008>.

[21] TSCHUMPERLIN, D. J., OSWARI, J., MARGULIES, A. S. "Deformation-induced injury of alveolar epithelial cells. Effect of frequency, duration, and amplitude", *Am. J. Respir. Crit. Care Med.*, v. 162, n. 2 Pt 1, pp. 357–362, Aug 2000.

[22] ALTEMEIER, W. A., MATUTE-BELLO, G., FREVERT, C. W., et al. "Mechanical ventilation with moderate tidal volumes synergistically increases lung cytokine response to systemic endotoxin", *American journal of physiology.Lung cellular and molecular physiology*, v. 287, n. 3, pp. L533–42, Sep 2004.

[23] NAKOS, G., BATISTATOU, A., GALIATSOU, E., et al. "Lung and 'end organ' injury due to mechanical ventilation in animals: comparison between the prone and supine positions", *Critical Care*, v. 10, n. 1, pp. R38, 02/28 2006. Disponível em: <https://doi.org/10.1186/cc4840>.

[24] DE CAMPOS, T., DEREE, J., COIMBRA, R. "From acute pancreatitis to end-organ injury: mechanisms of acute lung injury", *Surg Infect (Larchmt)*, v. 8, n. 1, pp. 107–120, Feb 2007.

[25] WIENHOLD, S.-M., MACRI, M., NOUAILLES, G., et al. "Ventilator-induced lung injury is aggravated by intestinal microbiome disruption in mice", *European Respiratory Journal*, v. 50, pp. PA350, 2017.

[26] AMATO, M. B. P., BARBAS, C. S. V., MEDEIROS, D. M., et al. "Effect of a Protective-Ventilation Strategy on Mortality in the Acute Respiratory Distress Syndrome", *New England Journal of Medicine*, v. 338, n. 6, pp. 347–354, 1998. Disponível em: <http://dx.doi.org/10.1056/NEJM199802053380602>.

[27] ARDS NETWORK. "Ventilation with lower tidal volumes as compared with traditional tidal volumes for acute lung injury and the acute respiratory distress syndrome. The Acute Respiratory Distress Syndrome Network", *The New England journal of medicine*, v. 342, n. 18, pp. 1301–1308, May 4 2000.

[28] GAJIC, O., DARA, S. I., MENDEZ, J. L., et al. "Ventilator-associated lung injury in patients without acute lung injury at the onset of mechanical ventilation", *Critical Care Medicine*, v. 32, n. 9, pp. 1817–1824, Sep 2004.

[29] CHOI, G., WOLTHUIS, E. K., BRESSER, P., et al. "Mechanical ventilation with lower tidal volumes and positive end-expiratory pressure prevents alveolar coagulation in patients without lung injury", *Anesthesiology*, v. 105, n. 4, pp. 689–695, Oct 2006.

[30] DETERMANN, R. M., ROYAKKERS, A., WOLTHUIS, E. K., et al. "Ventilation with lower tidal volumes as compared with conventional tidal volumes for patients without acute lung injury: a preventive randomized controlled trial", *Critical Care (London, England)*, v. 14, n. 1, pp. R1, Jan 7 2010.

[31] DE OLIVEIRA, R. P., HETZEL, M. P., DOS ANJOS SILVA, M., et al. "Mechanical ventilation with high tidal volume induces inflammation in patients without lung disease", *Critical Care (London, England)*, v. 14, n. 2, pp. R39, 2010.

[32] FUTIER, E., CONSTANTIN, J. M., PAUGAM-BURTZ, C., et al. "A trial of intraoperative low-tidal-volume ventilation in abdominal surgery", *The New England journal of medicine*, v. 369, n. 5, pp. 428–437, Aug 1 2013.

[33] SEVERGNINI, P., SELMO, G., LANZA, C., et al. "Protective Mechanical Ventilation during General Anesthesia for Open Abdominal Surgery Improves Postoperative Pulmonary Function", *Anesthesiology*, v. 118, n. 6, pp. 1307–1321, Jun 2013.

[34] LADHA, K., MELO, M. F. V., MCLEAN, D. J., et al. "Intraoperative protective mechanical ventilation and risk of postoperative respiratory complications: hospital based registry study", *BMJ (Clinical research ed.)*, v. 351, pp. h3646, Jul 14 2015.

[35] GATTINONI, L., PESENTI, A. "The concept of "baby lung"", *Intensive Care Med*, v. 31, n. 6, pp. 776–784, Jun 2005.

[36] GATTINONI, L., CARLESSO, E., CAIRONI, P. "Stress and strain within the lung", *Curr Opin Crit Care*, v. 18, n. 1, pp. 42–47, Feb 2012.

[37] WEBB, H. H., TIERNEY, D. F. "Experimental pulmonary edema due to intermittent positive pressure ventilation with high inflation pressures. Protection by positive end-expiratory pressure", *Am. Rev. Respir. Dis.*, v. 110, n. 5, pp. 556–565, Nov 1974.

[38] AMATO, M. B., MEADE, M. O., SLUTSKY, A. S., et al. "Driving Pressure and Survival in the Acute Respiratory Distress Syndrome", *New England Journal of Medicine*, v. 372, n. 8, pp. 747–755, 2015. Disponível em: <http://dx.doi.org/10.1056/NEJMsa1410639>.

[39] GATTINONI, L., PESENTI, A., AVALLI, L., et al. "Pressure-volume curve of total respiratory system in acute respiratory failure. Computed tomographic scan study", *Am. Rev. Respir. Dis.*, v. 136, n. 3, pp. 730–736, Sep 1987.

[40] HEDENSTIERNA, G., EDMARK, L. "Protective Ventilation during Anesthesia: Is It Meaningful?" *Anesthesiology*, v. 125, n. 6, pp. 1079–1082, Dec 2016.

[41] PROTTI, A., CRESSONI, M., SANTINI, A., et al. "Lung Stress and Strain during Mechanical Ventilation: Any Safe Threshold?" *American Journal of Respiratory and Critical Care Medicine*, v. 183, n. 10, pp. 1354–1362, 2011. Disponível em: <https://doi.org/10.1164/rccm.201010-1757OC>.

[42] BROCCARD, A., SHAPIRO, R. S., SCHMITZ, L. L., et al. "Prone positioning attenuates and redistributes ventilator-induced lung injury in dogs", *Critical Care Medicine*, v. 28, n. 2, pp. 295–303, Feb 2000.

[43] VALENZA, F., GUGLIELMI, M., MAFFIOLETTI, M., et al. "Prone position delays the progression of ventilator-induced lung injury in rats: does lung strain distribution play a role?" *Critical Care Medicine*, v. 33, n. 2, pp. 361–367, Feb 2005.

[44] NETO, A. S., BARBAS, C. S., SIMONIS, F. D., et al. "Epidemiological characteristics, practice of ventilation, and clinical outcome in patients at risk of acute respiratory distress syndrome in intensive care units from 16 countries (PRoVENT): an international, multicentre, prospective study", *The Lancet. Respiratory medicine*, v. 4, n. 11, pp. 882–893, Nov 2016.

[45] CHEN, D. L., SCHUSTER, D. P. "Positron emission tomography with [18F]fluorodeoxyglucose to evaluate neutrophil kinetics during acute lung injury", *American journal of physiology.Lung cellular and molecular physiology*, v. 286, n. 4, pp. L834–40, Apr 2004.

[46] SCHROEDER, T., VIDAL MELO, M. F., MUSCH, G., et al. "Modeling pulmonary kinetics of 2-deoxy-2-[18F]fluoro-D-glucose during acute lung injury", *Acad Radiol*, v. 15, n. 6, pp. 763–775, Jun 2008.

[47] DE PROST, N., FENG, Y., WELLMAN, T., et al. "18F-FDG kinetics parameters depend on the mechanism of injury in early experimental acute respiratory distress syndrome", *Journal of nuclear medicine : official publication, Society of Nuclear Medicine*, v. 55, n. 11, pp. 1871–1877, Nov 2014.

[48] RODRIGUES, R. S., BOZZA, F. A., HANRAHAN, C. J., et al. "18F-fluoro-2-deoxyglucose PET informs neutrophil accumulation and activation in lipopolysaccharide-induced acute lung injury", *Nuclear medicine and biology*, v. 48, pp. 52–62, Jan 17 2017.

[49] WELLMAN, T. J., DE PROST, N., TUCCI, M., et al. "Lung Metabolic Activation as an Early Biomarker of Acute Respiratory Distress Syndrome and Local Gene Expression Heterogeneity", *Anesthesiology*, v. 125, n. 5, pp. 992–1004, Nov 2016.

[50] COSTA, E. L., MUSCH, G., WINKLER, T., et al. "Mild endotoxemia during mechanical ventilation produces spatially heterogeneous pulmonary neutrophilic inflammation in sheep", *Anesthesiology*, v. 112, n. 3, pp. 658–669, Mar 2010.

[51] WELLMAN, T. J., WINKLER, T., COSTA, E. L., et al. "Effect of local tidal lung strain on inflammation in normal and lipopolysaccharide-exposed sheep", *Critical Care Medicine*, v. 42, n. 7, pp. e491–500, Jul 2014.

[52] NETO, A. S., HEMMES, S. N. T., BARBAS, C. S. V., et al. "Association between driving pressure and development of postoperative pulmonary complications in patients undergoing mechanical ventilation for general

anaesthesia: a meta-analysis of individual patient data", *The Lancet Respiratory Medicine*, v. 4, n. 4, pp. 272–280, apr 2016. Disponível em: <https://doi.org/10.1016/s2213-2600(16)00057-6>.

[53] "Epidemiology, practice of ventilation and outcome for patients at increased risk of postoperative pulmonary complications", *European Journal of Anaesthesiology*, v. 34, n. 8, pp. 492–507, aug 2017. Disponível em: <https://doi.org/10.1097/eja.0000000000000646>.

[54] CAIRONI, P., LANGER, T., CARLESSO, E., et al. "Time to generate ventilator-induced lung injury among mammals with healthy lungs: a unifying hypothesis", *Intensive Care Medicine*, v. 37, n. 12, pp. 1913–1920, Dec 2011. ISSN: 1432-1238. Disponível em: <https://doi.org/10.1007/s00134-011-2388-9>.

[55] VIDAL MELO, M. F., LAYFIELD, D., HARRIS, R. S., et al. "Quantification of regional ventilation-perfusion ratios with PET", *J. Nucl. Med.*, v. 44, n. 12, pp. 1982–1991, Dec 2003.

[56] RICHARD, J. C., JANIER, M., LAVENNE, F., et al. "Quantitative assessment of regional alveolar ventilation and gas volume using 13N-N2 washout and PET", *J. Nucl. Med.*, v. 46, n. 8, pp. 1375–1383, Aug 2005.

[57] WELLMAN, T. J., WINKLER, T., COSTA, E. L., et al. "Effect of regional lung inflation on ventilation heterogeneity at different length scales during mechanical ventilation of normal sheep lungs", *J. Appl. Physiol.*, v. 113, n. 6, pp. 947–957, Sep 2012.

[58] REINHARDT, J. M., DING, K., CAO, K., et al. "Registration-based estimates of local lung tissue expansion compared to xenon CT measures of specific ventilation", *Medical image analysis*, v. 12, n. 6, pp. 752–763, Dec 2008.

[59] BAYAT, S., PORRA, L., ALBU, G., et al. "Effect of positive end-expiratory pressure on regional ventilation distribution during mechanical ventilation after surfactant depletion", *Anesthesiology*, v. 119, n. 1, pp. 89–100, Jul 2013.

[60] SÁ, R. C., ASADI, A. K., THEILMANN, R. J., et al. "Validating the distribution of specific ventilation in healthy humans measured using proton MR imaging", *J. Appl. Physiol.*, v. 116, n. 8, pp. 1048–1056, Apr 2014.

[61] HORN, F. C., DEPPE, M. H., MARSHALL, H., et al. "Quantification of regional fractional ventilation in human subjects by measurement of hyper-

polarized 3He washout with 2D and 3D MRI", *J. Appl. Physiol.*, v. 116, n. 2, pp. 129–139, Jan 2014.

[62] FRERICHS, I., AMATO, M. B., VAN KAAM, A. H., et al. "Chest electrical impedance tomography examination, data analysis, terminology, clinical use and recommendations: consensus statement of the TRanslational EIT developmeNt stuDy group", *Thorax*, v. 72, n. 1, pp. 83–93, Jan 2017.

[63] WELLMAN, T. J., WINKLER, T., COSTA, E. L., et al. "Measurement of regional specific lung volume change using respiratory-gated PET of inhaled 13N-nitrogen", *J. Nucl. Med.*, v. 51, n. 4, pp. 646–653, Apr 2010.

[64] KACZKA, D. W., CAO, K., CHRISTENSEN, G. E., et al. "Analysis of regional mechanics in canine lung injury using forced oscillations and 3D image registration", *Annals of Biomedical Engineering*, v. 39, n. 3, pp. 1112–1124, 2011.

[65] CHOI, S., HOFFMAN, E. A., WENZEL, S. E., et al. "Registration-based assessment of regional lung function via volumetric CT images of normal subjects vs. severe asthmatics", *Journal of applied physiology (Bethesda, Md.: 1985)*, v. 115, n. 5, pp. 730–742, Sep 1 2013.

[66] DU, K., BAYOUTH, J. E., CAO, K., et al. "Reproducibility of registration-based measures of lung tissue expansion", *Medical physics*, v. 39, n. 3, pp. 1595–1608, Mar 2012.

[67] PAULA, L. F., WELLMAN, T. J., WINKLER, T., et al. "Regional Tidal Lung Strain in Mechanically Ventilated Normal Lungs", *Journal of applied physiology (Bethesda, Md.: 1985)*, p. jap.00861.2015, Jul 21 2016.

[68] CHIUMELLO, D., CRESSONI, M., CHIERICHETTI, M., et al. "Nitrogen washout/washin, helium dilution and computed tomography in the assessment of end expiratory lung volume", *Crit Care*, v. 12, 2008. Disponível em: <https://doi.org/10.1186/cc7139>.

[69] DELLAMONICA, J., LEROLLE, N., SARGENTINI, C., et al. "Accuracy and precision of end-expiratory lung-volume measurements by automated nitrogen washout/washin technique in patients with acute respiratory distress syndrome", *Crit Care*, v. 15, 2011. Disponível em: <https://doi.org/10.1186/cc10587>.

[70] ROBINSON, P. D., LATZIN, P., VERBANCK, S., et al. "Consensus statement for inert gas washout measurement using multiple- and single- breath

v. 0, n. ja, pp. null, 0. Disponível em: <https://doi.org/10.1164/rccm.201710-2038OC>. ahead of print.

[81] VENEGAS, J. G., GALLETTI, G. G. "Low-pass filtering, a new method of fractal analysis: application to PET images of pulmonary blood flow", *J. Appl. Physiol.*, v. 88, n. 4, pp. 1365–1373, Apr 2000.

[82] MOTTA-RIBEIRO, G. C., JANDRE, F. C., WRIGGE, H., et al. "Generalized estimation of the ventilatory distribution from the multiple-breath nitrogen washout", *BioMedical Engineering OnLine*, v. 15, n. 1, pp. 89, Aug 2016. ISSN: 1475-925X. Disponível em: <https://doi.org/10.1186/s12938-016-0213-y>.

[83] JANDRE, F. C., GIANNELLA-NETO, A. "A disturbance-enabled method for retrieving lung ventilation distributions from multibreath N2 washout". In: *In: Engineering in medicine and biology society, 2000 proc. 22nd annual int. conf. IEEE*, pp. 2968–71, 2000.

[84] WHITELEY, J. P., GAVAGHAN, D. J., HAHN, C. E. W. "A mathematical evaluation of the multiple breath nitrogen washout (MBNW) technique and the multiple inert gas elimination technique (MIGET)", *J Theor Biol*, v. 194, 1998. Disponível em: <https://doi.org/10.1006/jtbi.1998.0772>.

[85] MOTTA-RIBEIRO, G. C., JANDRE, F. C., WRIGGE, H., et al. "Generalized estimation of the ventilatory distribution from the multiple-breath washout: a bench evaluation study", *BioMedical Engineering OnLine*, v. 17, n. 1, pp. 3, Jan 2018. ISSN: 1475-925X. Disponível em: <https://doi.org/10.1186/s12938-018-0442-3>.

[86] JADVAR, H., PARKER, J. "Clinical PET and PET/CT". cap. PET Radiotracers, pp. 45–67, Springer-Verlag, 2005. Disponível em: <https://doi.org/10.1007/b138777>.

[87] COX, B. L., MACKIE, T. R., ELICEIRI, K. W. "The sweet spot: FDG and other 2-carbon glucose analogs for multi-modal metabolic imaging of tumor metabolism", *American journal of nuclear medicine and molecular imaging*, v. 5, n. 1, pp. 1–13, 2015. ISSN: 2160-8407. Disponível em: <http://europepmc.org/articles/PMC4299774>.

[88] SOKOLOFF, L., REIVICH, M., KENNEDY, C., et al. "THE [14C]DEOXYGLUCOSE METHOD FOR THE MEASUREMENT OF

LOCAL CEREBRAL GLUCOSE UTILIZATION: THEORY, PROCEDURE, AND NORMAL VALUES IN THE CONSCIOUS AND ANESTHETIZED ALBINO RAT", *Journal of Neurochemistry*, v. 28, n. 5. Disponível em: <https://doi.org/10.1111/j.1471-4159.1977.tb10649.x>.

[89] WELLMAN, T. J., WINKLER, T., VIDAL MELO, M. F. "Modeling of Tracer Transport Delays for Improved Quantification of Regional Pulmonary ¹⁸F-FDG Kinetics, Vascular Transit Times, and Perfusion", *Ann Biomed Eng*, v. 43, n. 11, pp. 2722–2734, Nov 2015.

[90] POUZOT, C., RICHARD, J.-C., GROS, A., et al. "Noninvasive Quantitative Assessment of Pulmonary Blood Flow with 18F-FDG PET", *Journal of Nuclear Medicine*, v. 54, n. 9, pp. 1653–1660, 2013. Disponível em: <https://doi.org/10.2967/jnumed.112.116699>.

[91] SCHROEDER, T., VIDAL MELO, M. F., MUSCH, G., et al. "Image-derived input function for assessment of 18F-FDG uptake by the inflamed lung", *J. Nucl. Med.*, v. 48, n. 11, pp. 1889–1896, Nov 2007.

[92] CROTEAU, E., LAVALLÉE, É., LABBE, S. M., et al. "Image-derived input function in dynamic human PET/CT: methodology and validation with 11C-acetate and 18F-fluorothioheptadecanoic acid in muscle and 18F-fluorodeoxyglucose in brain", *European Journal of Nuclear Medicine and Molecular Imaging*, v. 37, n. 8, pp. 1539–1550, Aug 2010. ISSN: 1619-7089. Disponível em: <https://doi.org/10.1007/s00259-010-1443-z>.

[93] BOL, A., MELIN, J. A., VANOVERSCHELDE, J. L., et al. "Direct comparison of [13N]ammonia and [15O]water estimates of perfusion with quantification of regional myocardial blood flow by microspheres." *Circulation*, v. 87, n. 2, pp. 512–525, 1993. ISSN: 0009-7322. Disponível em: <http://circ.ahajournals.org/content/87/2/512>.

[94] TSENG, J., DUNNWALD, L. K., SCHUBERT, E. K., et al. "18F-FDG Kinetics in Locally Advanced Breast Cancer: Correlation with Tumor Blood Flow and Changes in Response to Neoadjuvant Chemotherapy", *Journal of Nuclear Medicine*, v. 45, n. 11, pp. 1829–1837, 2004. Disponível em: <http://jnm.snmjournals.org/content/45/11/1829.abstract>.

[95] ZASADNY, K., TATSUMI, M., WAHL, R. "FDG metabolism and uptake versus blood flow in women with untreated primary breast cancers", *European Journal of Nuclear Medicine and Molecular Imaging*, v. 30, n. 2, pp. 274–280, 2 2003. ISSN: 1619-7070.

[96] STRAUSS, L. G., KOCZAN, D., KLIPPEL, S., et al. "Dynamic PET with (18)F-Deoxyglucose (FDG) and quantitative assessment with a two-tissue compartment model reflect the activity of glucose transporters and hexokinases in patients with colorectal tumors", *American journal of nuclear medicine and molecular imaging*, v. 3, n. 5, pp. 417–424, 2013. ISSN: 2160-8407. Disponível em: <http://europepmc.org/articles/PMC3784805>.

[97] OKAZUMI, S., ISONO, K., ENOMOTO, K., et al. "Evaluation of liver tumors using fluorine-18-fluorodeoxyglucose PET: characterization of tumor and assessment of effect of treatment", *J. Nucl. Med.*, v. 33, n. 3, pp. 333–339, Mar 1992.

[98] DIMITRAKOPOULOU-STRAUSS, A., STRAUSS, L. G., BURGER, C., et al. "Prognostic aspects of 18F-FDG PET kinetics in patients with metastatic colorectal carcinoma receiving FOLFOX chemotherapy", *J. Nucl. Med.*, v. 45, n. 9, pp. 1480–1487, Sep 2004.

[99] RODRIGUES, R. S., MILLER, P. R., BOZZA, F. A., et al. "FDG-PET in patients at risk for acute respiratory distress syndrome: a preliminary report", *Intensive Care Medicine*, v. 34, n. 12, pp. 2273, Aug 2008. ISSN: 1432-1238. Disponível em: <https://doi.org/10.1007/s00134-008-1220-7>.

[100] BELLANI, G., MESSA, C., GUERRA, L., et al. "Lungs of patients with acute respiratory distress syndrome show diffuse inflammation in normally aerated regions: a [18F]-fluoro-2-deoxy-D-glucose PET/CT study", *Critical Care Medicine*, v. 37, n. 7, pp. 2216–2222, Jul 2009.

[101] CHEN, D. L., FERKOL, T. W., MINTUN, M. A., et al. "Quantifying Pulmonary Inflammation in Cystic Fibrosis with Positron Emission Tomography", *American Journal of Respiratory and Critical Care Medicine*, v. 173, n. 12, pp. 1363–1369, 2006. Disponível em: <https://doi.org/10.1164/rccm.200506-9340C>.

[102] ZAMBELLI, V., DI GRIGOLI, G., SCANZIANI, M., et al. "Time course of metabolic activity and cellular infiltration in a murine model of acid-induced lung injury", *Intensive Care Medicine*, v. 38, n. 4, pp. 694–701, Apr 2012. ISSN: 1432-1238. Disponível em: <https://doi.org/10.1007/s00134-011-2456-1>.

[103] SAHA, D., TAKAHASHI, K., DE PROST, N., et al. "Micro-Autoradiographic Assessment of Cell Types Contributing to 2-Deoxy-2-[18F]Fluoro-d-

Glucose Uptake During Ventilator-Induced and Endotoxemic Lung Injury", *Molecular Imaging and Biology*, v. 15, n. 1, pp. 19–27, Feb 2013. ISSN: 1860-2002. Disponível em: <https://doi.org/10.1007/s11307-012-0575-x>.

[104] TUSTISON, N. J., AVANTS, B. B. "Explicit B-spline regularization in diffeomorphic image registration", *Front Neuroinform*, v. 7, pp. 39, 2013.

[105] GALBÁN, C. J., HAN, M. K., BOES, J. L., et al. "Computed tomography–based biomarker provides unique signature for diagnosis of COPD phenotypes and disease progression", *Nature Medicine*, v. 18, n. 11, pp. 1711–1715, oct 2012. Disponível em: <https://doi.org/10.1038/nm.2971>.

[106] CEREDA, M., XIN, Y., HAMEDANI, H., et al. "Tidal changes on CT and progression of ARDS", *Thorax*, v. 72, n. 11, pp. 981–989, Nov 2017.

[107] KAIFANG, D., E., B. J., KAI, D., et al. "Reproducibility of intensity-based estimates of lung ventilation", *Medical Physics*, v. 40, pp. 063504. Disponível em: <https://aapm.onlinelibrary.wiley.com/doi/abs/10.1118/1.4805106>.

[108] MURPHY, K., VAN GINNEKEN, B., REINHARDT, J. M., et al. "Evaluation of Registration Methods on Thoracic CT: The EMPIRE10 Challenge", *IEEE Transactions on Medical Imaging*, v. 30, n. 11, pp. 1901–1920, nov 2011. Disponível em: <https://doi.org/10.1109/tmi.2011.2158349>.

[109] NIELSEN, M. S., ØSTERGAARD, L. R., CARL, J. "A new method to validate thoracic CT-CT deformable image registration using auto-segmented 3D anatomical landmarks", *Acta Oncologica*, v. 54, n. 9, pp. 1515–1520, jul 2015. doi: 10.3109/0284186x.2015.1061215. Disponível em: <https://doi.org/10.3109/0284186x.2015.1061215>.

[110] MURPHY, K., VAN GINNEKEN, B., PLUIM, J. P. W., et al. "Semi-automatic Reference Standard Construction for Quantitative Evaluation of Lung CT Registration". In: Metaxas, D., Axel, L., Fichtinger, G., et al. (Eds.), *Medical Image Computing and Computer-Assisted Intervention – MICCAI 2008*, pp. 1006–1013, Berlin, Heidelberg, 2008. Springer Berlin Heidelberg. ISBN: 978-3-540-85990-1.

[111] RUDYANTO, R. D., KERKSTRA, S., VAN RIKXOORT, E. M., et al. "Comparing algorithms for automated vessel segmentation in computed tomog-

raphy scans of the lung: the VESSEL12 study", *Medical Image Analysis*, v. 18, n. 7, pp. 1217–1232, oct 2014. Disponível em: <https://doi.org/10.1016/j.media.2014.07.003>.

[112] PAN, Y., KUMAR, D., HOFFMAN, E. A., et al. "Estimation of regional lung expansion via 3D image registration". v. 5746, pp. 5746 – 5746 – 12, 2005. Disponível em: <http://dx.doi.org/10.1117/12.596617>.

[113] CAO, K. *Local lung tissue expansion analysis based on inverse consistent image registration*. Tese de Mestrado, University of Iowa, 2008. Disponível em: <http://ir.uiowa.edu/etd/19/>.

[114] LEE, P. C., HELSMOORTEL, C. M., COHN, S. M., et al. "Are low tidal volumes safe?" *Chest*, v. 97, n. 2, pp. 430–434, Feb 1990.

[115] NETO, A. S., NAGTZAAM, L., SCHULTZ, M. J. "Ventilation with lower tidal volumes for critically ill patients without the acute respiratory distress syndrome: a systematic translational review and meta-analysis", *Current opinion in critical care*, v. 20, n. 1, pp. 25–32, Feb 2014.

[116] MASLOW, A. D., STAFFORD, T. S., DAVIGNON, K. R., et al. "A randomized comparison of different ventilator strategies during thoracotomy for pulmonary resection", *The Journal of thoracic and cardiovascular surgery*, v. 146, n. 1, pp. 38–44, Jul 2013.

[117] NETO, A. S., CARDOSO, S. O., MANETTA, J. A., et al. "Association between use of lung-protective ventilation with lower tidal volumes and clinical outcomes among patients without acute respiratory distress syndrome: a meta-analysis", *JAMA : the journal of the American Medical Association*, v. 308, n. 16, pp. 1651–1659, Oct 24 2012.

[118] GULDNER, A., KISS, T., NETO, A. S., et al. "Intraoperative protective mechanical ventilation for prevention of postoperative pulmonary complications: a comprehensive review of the role of tidal volume, positive end-expiratory pressure, and lung recruitment maneuvers", *Anesthesiology*, v. 123, n. 3, pp. 692–713, Sep 2015.

[119] MARINI, J. J., JOSEPHS, S. A., MECHLIN, M., et al. "Should Early Prone Positioning Be a Standard of Care in ARDS With Refractory Hypoxemia?" *Respiratory care*, v. 61, n. 6, pp. 818–829, American Association for Respiratory Care 2016.

[120] BEURET, P., CARTON, M.-J., NOURDINE, K., et al. "Prone position as prevention of lung injury in comatose patients: a prospective, randomized, controlled study", *Intensive care medicine*, v. 28, n. 5, pp. 564–569, 05/01 2002. Disponível em: <https://doi.org/10.1007/s00134-002-1266-x>.

[121] CAVALCANTI, A. B., SUZUMURA, E. A., LARANJEIRA, L. N., et al. "Effect of Lung Recruitment and Titrated Positive End-Expiratory Pressure (PEEP) vs Low PEEP on Mortality in Patients With Acute Respiratory Distress Syndrome: A Randomized Clinical Trial", *JAMA*, v. 318, n. 14, pp. 1335–1345, 10 2017. Disponível em: <http://dx.doi.org/10.1001/jama.2017.14171>.

[122] JONG, M. A. C. D., LADHA, K., MELO, M. F. V., et al. "Differential effects of intra-operative positive end-expiratory pressure (PEEP) on respiratory outcome in major abdominal surgery versus craniotomy", *Ann.Surg.*, v. 264, pp. 362–369, 2016.

[123] BROCCARD, A., HOTCHKISS, J., KUWAYAMA, N., et al. "Consequences of Vascular Flow on Lung Injury Induced by Mechanical Ventilation", *Am J Respir Crit Care Med*, v. 157, n. 6, pp. 1935–1942, 1998. Disponível em: <https://doi.org/10.1164/ajrccm.157.6.9612006>.

[124] DE PROST, N., TUCCI, M. R., MELO, M. F. V. "Assessment of Lung Inflammation With 18F-FDG PET During Acute Lung Injury", *American Journal of Roentgenology*, v. 195, n. 2, pp. 292–300, 2010.

[125] MATUTE-BELLO, G., DOWNEY, G., MOORE, B. B., et al. "An official American Thoracic Society workshop report: features and measurements of experimental acute lung injury in animals", *American journal of respiratory cell and molecular biology*, v. 44, n. 5, pp. 725–738, May 2011.

[126] BRIEL, M., MEADE, M., MERCAT, A., et al. "Higher vs lower positive end-expiratory pressure in patients with acute lung injury and acute respiratory distress syndrome: systematic review and meta-analysis", *JAMA : the journal of the American Medical Association*, v. 303, n. 9, pp. 865–873, Mar 3 2010.

[127] GATTINONI, L., TACCONE, P., CARLESSO, E., et al. "Prone position in acute respiratory distress syndrome. Rationale, indications, and limits", *American journal of respiratory and critical care medicine*, v. 188, n. 11, pp. 1286–1293, Dec 1 2013.

[128] PAGE, B., VIEILLARD-BARON, A., BEAUCHET, A., et al. "Low stretch ventilation strategy in acute respiratory distress syndrome: eight years of clinical experience in a single center", *Critical Care Medicine*, v. 31, n. 3, pp. 765–769, Mar 2003.

[129] YANG, D., GRANT, M. C., STONE, A., et al. "A Meta-analysis of Intra-operative Ventilation Strategies to Prevent Pulmonary Complications: Is Low Tidal Volume Alone Sufficient to Protect Healthy Lungs?" *Annals of Surgery*, v. 263, n. 5, pp. 881–887, May 2016.

[130] QASEEM, A., SNOW, V., FITTERMAN, N., et al. "Risk assessment for and strategies to reduce perioperative pulmonary complications for patients undergoing noncardiothoracic surgery: A guideline from the american college of physicians", *Annals of Internal Medicine*, v. 144, n. 8, pp. 575–580, 2006. Disponível em: <http://dx.doi.org/10.7326/0003-4819-144-8-200604180-00008>.

[131] HEDENSTIERNA, G. "Oxygen and anesthesia: what lung do we deliver to the post-operative ward?" *Acta Anaesthesiologica Scandinavica*, v. 56, n. 6, pp. 675–685, 2012. Disponível em: <https://onlinelibrary.wiley.com/doi/abs/10.1111/j.1399-6576.2012.02689.x>.

[132] BROCHARD, L., SLUTSKY, A., PESENTI, A. "Mechanical Ventilation to Minimize Progression of Lung Injury in Acute Respiratory Failure", *American Journal of Respiratory and Critical Care Medicine*, v. 195, n. 4, pp. 438–442, 2017. Disponível em: <https://doi.org/10.1164/rccm.201605-1081CP>.

[133] ALBERT, R. K. "The Role of Ventilation-induced Surfactant Dysfunction and Atelectasis in Causing Acute Respiratory Distress Syndrome", *American Journal of Respiratory and Critical Care Medicine*, v. 185, n. 7, pp. 702–708, 2012. Disponível em: <https://doi.org/10.1164/rccm.201109-1667PP>.

[134] DOS SANTOS, C. C., OKUTANI, D., HU, P., et al. "Differential gene profiling in acute lung injury identifies injury-specific gene expression", *Critical Care Medicine*, v. 36, n. 3, pp. 855–865, Mar 2008.

[135] CALFEE, C. S., WARE, L. B., EISNER, M. D., et al. "Plasma receptor for advanced glycation end products and clinical outcomes in acute lung injury", *Thorax*, v. 63, n. 12, pp. 1083–1089, Dec 2008.

[136] GONZALEZ-LOPEZ, A., GARCIA-PRIETO, E., BATALLA-SOLIS, E., et al. "Lung strain and biological response in mechanically ventilated patients", *Intensive care medicine*, v. 38, n. 2, pp. 240–247, Feb 2012.

[137] TREPPO, S., MIJAILOVICH, S. M., VENEGAS, J. G. "Contributions of pulmonary perfusion and ventilation to heterogeneity in V(A)/Q measured by PET", *Journal of applied physiology (Bethesda, Md.: 1985)*, v. 82, n. 4, pp. 1163–1176, Apr 1997.

[138] KATIRA, B. H., GIESINGER, R. E., ENGELBERTS, D., et al. "Adverse Heart–Lung Interactions in Ventilator-induced Lung Injury", *American Journal of Respiratory and Critical Care Medicine*, v. 196, n. 11, pp. 1411–1421, 2017. Disponível em: <https://doi.org/10.1164/rccm.201611-2268OC>.

[139] CRESSONI, M., GOTTI, M., CHIURAZZI, C., et al. "Mechanical Power and Development of Ventilator-induced Lung Injury", *Anesthesiology*, v. 124, n. 5, pp. 1100–1108, May 2016.

[140] GRASSO, S., TERRAGNI, P., MASCIA, L., et al. "Airway pressure-time curve profile (stress index) detects tidal recruitment/hyperinflation in experimental acute lung injury", *Crit. Care Med.*, v. 32, n. 4, pp. 1018–1027, Apr 2004.

[141] RODARTE, J. R., CHANIOTAKIS, M., WILSON, T. A. "Variability of parenchymal expansion measured by computed tomography", *J. Appl. Physiol.*, v. 67, n. 1, pp. 226–231, Jul 1989.

[142] MEAD, J., TAKISHIMA, T., LEITH, D. "Stress distribution in lungs: a model of pulmonary elasticity", *J Appl Physiol*, v. 28, n. 5, pp. 596–608, May 1970.

[143] GATTINONI, L., CARLESSO, E., CADRINGHER, P., et al. "Physical and biological triggers of ventilator-induced lung injury and its prevention", *Eur Respir J Suppl*, v. 47, pp. 15s–25s, Nov 2003.

[144] HARRIS, R. S., WILLEY-COURAND, D. B., HEAD, C. A., et al. "Regional VA, Q, and VA/Q during PLV: effects of nitroprusside and inhaled nitric oxide", *J. Appl. Physiol.*, v. 92, n. 1, pp. 297–312, Jan 2002.

[145] ROTA KOPS, E., HERZOG, H., SCHMID, A., et al. "Performance characteristics of an eight-ring whole body PET scanner", *J Comput Assist Tomogr*, v. 14, n. 3, pp. 437–445, 1990.

[146] GROGG, K. S., TOOLE, T., OUYANG, J., et al. "National Electrical Manufacturers Association and Clinical Evaluation of a Novel Brain PET/CT Scanner", *J. Nucl. Med.*, v. 57, n. 4, pp. 646–652, Apr 2016.

[147] IKEDA, M., MAKINO, R., IMAI, K., et al. "A method for estimating noise variance of CT image", *Comput Med Imaging Graph*, v. 34, n. 8, pp. 642–650, Dec 2010.

[148] CHRISTIANSON, O., WINSLOW, J., FRUSH, D. P., et al. "Automated Technique to Measure Noise in Clinical CT Examinations", *AJR Am J Roentgenol*, v. 205, n. 1, pp. W93–99, Jul 2015.

[149] VIDAL MELO, M. F., WINKLER, T., HARRIS, R. S., et al. "Spatial heterogeneity of lung perfusion assessed with (13)N PET as a vascular biomarker in chronic obstructive pulmonary disease", *J. Nucl. Med.*, v. 51, n. 1, pp. 57–65, Jan 2010.

[150] BORGES, J. B., OKAMOTO, V. N., MATOS, G. F. J., et al. "Reversibility of Lung Collapse and Hypoxemia in Early Acute Respiratory Distress Syndrome", *American Journal of Respiratory and Critical Care Medicine*, v. 174, n. 3, pp. 268–278, 2006. Disponível em: <https://doi.org/10.1164/rccm.200506-976OC>.

[151] HUANG, D. A. W., SHERMAN, B. T., LEMPICKI, R. A. "Systematic and integrative analysis of large gene lists using DAVID bioinformatics resources", *Nat Protoc*, v. 4, n. 1, pp. 44–57, 2009.

[152] SAPOVAL, B., FILOCHE, M., WEIBEL, E. R. "Smaller is better–but not too small: a physical scale for the design of the mammalian pulmonary acinus", *Proc. Natl. Acad. Sci. U.S.A.*, v. 99, n. 16, pp. 10411–10416, Aug 2002.

[153] WEBB, W. R. "Thin-section CT of the secondary pulmonary lobule: anatomy and the image–the 2004 Fleischner lecture", *Radiology*, v. 239, n. 2, pp. 322–338, May 2006.

[154] PERLMAN, C. E., BHATTACHARYA, J. "Alveolar expansion imaged by optical sectioning microscopy", *J. Appl. Physiol.*, v. 103, n. 3, pp. 1037–1044, Sep 2007.

[155] MERTENS, M., TABUCHI, A., MEISSNER, S., et al. "Alveolar dynamics in acute lung injury: heterogeneous distension rather than cyclic opening and collapse", *Crit. Care Med.*, v. 37, n. 9, pp. 2604–2611, Sep 2009.

[156] CEREDA, M., EMAMI, K., XIN, Y., et al. "Imaging the interaction of atelectasis and overdistension in surfactant-depleted lungs", *Crit. Care Med.*, v. 41, n. 2, pp. 527–535, Feb 2013.

[157] OLSON, L. E., RODARTE, J. R. "Regional differences in expansion in excised dog lung lobes", *J Appl Physiol Respir Environ Exerc Physiol*, v. 57, n. 6, pp. 1710–1714, Dec 1984.

[158] GLENNY, R. W. "Emergence of matched airway and vascular trees from fractal rules", *J. Appl. Physiol.*, v. 110, n. 4, pp. 1119–1129, Apr 2011.

[159] COPLAND, I. B., KAVANAGH, B. P., ENGELBERTS, D., et al. "Early changes in lung gene expression due to high tidal volume", *Am. J. Respir. Crit. Care Med.*, v. 168, n. 9, pp. 1051–1059, Nov 2003.

[160] DOLINAY, T., KAMINSKI, N., FELGENDREHER, M., et al. "Gene expression profiling of target genes in ventilator-induced lung injury", *Physiol. Genomics*, v. 26, n. 1, pp. 68–75, Jun 2006.

[161] SPOONER, C. E., MARKOWITZ, N. P., SARAVOLATZ, L. D. "The role of tumor necrosis factor in sepsis", *Clin. Immunol. Immunopathol.*, v. 62, n. 1 Pt 2, pp. S11–17, Jan 1992.

[162] LIU, S. F., MALIK, A. B. "NF-kappa B activation as a pathological mechanism of septic shock and inflammation", *Am. J. Physiol. Lung Cell Mol. Physiol.*, v. 290, n. 4, pp. L622–L645, Apr 2006.

[163] BRUBAKER, S. W., BONHAM, K. S., ZANONI, I., et al. "Innate immune pattern recognition: a cell biological perspective", *Annu. Rev. Immunol.*, v. 33, pp. 257–290, 2015.

[164] BOUHUYS, A., LICHTNECKERT, S., LUNDGREN, C., et al. "Voluntary changes in breathing pattern and N2 clearance from lungs", *J Appl Physiol*, v. 16, 1961.

[165] SCHIBLER, A., HENNING, R. "Measurement of functional residual capacity in rabbits and children using an ultrasonic flow meter", *Pediatr Res*, v. 49, 2001. Disponível em: <https://doi.org/10.1203/00006450-200104000-00022>.

[166] OLEGARD, C., SONDERGAARD, S., HOULTZ, E., et al. "Estimation of functional residual capacity at the bedside using standard monitoring equipment: a modified nitrogen washout/washin technique requiring a small change of the inspired oxygen fraction", *Anesth Analg*,

v. 101, 2005. Disponível em: <https://doi.org/10.1213/01.ANE.0000165823.90368.55>.

[167] BREWER, L. M., ORR, J. A., SHERMAN, M. R., et al. "Measurement of functional residual capacity by modified multiple breath nitrogen washout for spontaneously breathing and mechanically ventilated patients", *Br J Anaesth*, v. 107, 2011. Disponível em: <https://doi.org/10.1093/bja/aer220>.

[168] BIKKER, I. G., BOMMEL, J., REIS MIRANDA, D., et al. "End-expiratory lung volume during mechanical ventilation: a comparison with reference values and the effect of positive end-expiratory pressure in intensive care unit patients with different lung conditions", *Crit Care*, v. 12, 2008. Disponível em: <https://doi.org/10.1186/cc7125>.

[169] HEINZE, H., SEDEMUND-ADIB, B., HERINGLAKE, M., et al. "Relationship between functional residual capacity, respiratory compliance, and oxygenation in patients ventilated after cardiac surgery", *Respir Care*, v. 55, 2010.

[170] FERNANDEZ-BUSTAMANTE, A., KLAWITTER, J., REPINE, J. E., et al. "Early effect of tidal volume on lung injury biomarkers in surgical patients with healthy lungs", *Anesthesiology*, v. 121, 2014. Disponível em: <https://doi.org/10.1097/ALN.0000000000000301>.

[171] HUHLE, R., PELOSI, P., ABREU, M. G. "Variable ventilation from bench to bedside", *Crit Care*, v. 20, 2016. Disponível em: <https://doi.org/10.1186/s13054-016-1216-6>.

[172] HART, M. C., ORZALESI, M. M., COOK, C. D. "Relation between anatomic respiratory dead space and body size and lung volume", *J Appl Physiol*, v. 18, 1963.

[173] CHIANG, Y. . W., BORBAT, P. P., FREED, J. H. "The determination of pair distance distributions by pulsed ESR using Tikhonov regularization", *J Magn Reson*, v. 172, 2005. Disponível em: <https://doi.org/10.1016/j.jmr.2004.10.012>.

[174] GILL, P. E., MURRAY, W., WRIGHT, M. H. *Practical optimization*. New York, Emerald Group Publishing Limited, 1982.

[175] LAWSON, C. L., HANSON, R. J. *Solving least squares problems*. Philadelphia, Society for Industrial and Applied Mathematics, 1987.

[176] HANSEN, P. C. "Regularization tools version 4.0 for Matlab 7.3", *Numer Algorithms*, v. 46, 2007. Disponível em: <https://doi.org/10.1007/s11075-007-9136-9>.

[177] KAPITAN, K. S. "Information content of the multibreath nitrogen washout: effects of experimental error", *J Appl Physiol*, v. 68, 1990.

[178] BRUNNER, J. X., WOLFF, G., CUMMING, G., et al. "Accurate measurement of N2 volumes during N2 washout requires dynamic adjustment of delay time", *J Appl Physiol*, v. 59, 1985.

[179] JENSEN, R., STANOJEVIC, S., GIBNEY, K., et al. "Multiple breath nitrogen washout: a feasible alternative to mass spectrometry", *PLoS One*, v. 8, 2013. Disponível em: <https://doi.org/10.1371/journal.pone.0056868>.

[180] EVANS, J. W., CANTOR, D. G., NORMAN, J. R. "The dead space in a compartmental lung model", *Bull Math Biophys*, v. 29, 1967. Disponível em: <https://doi.org/10.1007/BF02476922>.

[181] VIEIRA, S. R., PUYBASSET, L., RICHECOEUR, J., et al. "A lung computed tomographic assessment of positive end-expiratory pressure-induced lung overdistension", *Am J Respir Crit Care Med*, v. 158, 1998. Disponível em: <https://doi.org/10.1164/ajrccm.158.5.9802101>.

[182] FOWLER, W. S. "Lung function studies. II. The respiratory dead space", *Am J Physiol*, v. 154, 1948.

[183] WRIGGE, H., SYDOW, M., ZINSERLING, J., et al. "Determination of functional residual capacity (FRC) by multibreath nitrogen washout in a lung model and in mechanically ventilated patients. Accuracy depends on continuous dynamic compensation for changes of gas sampling delay time", *Intensiv Care Med*, v. 24, 1998. Disponível em: <https://doi.org/10.1007/s001340050601>.

[184] HARRIS, E. A., WHITLOCK, R. M. "Correction of inert gas washin or washout for gas solubility in blood", *J Appl Physiol*, v. 65, 1988.

[185] WEIBEL, E. R. "What makes a good lung?" *Swiss Med Wkly*, v. 139, n. 27-28, pp. 375–386, Jul 2009.

[186] HAIDOPOULOU, K., LUM, S., TURCU, S., et al. "Alveolar LCI vs. standard LCI in detecting early CF lung disease", *Respir Physiol Neurobiol*, v. 180, n. 2-3, pp. 247–251, Mar 2012.

[187] NEUMANN, R. P., PILLOW, J. J., THAMRIN, C., et al. "Influence of respiratory dead space on lung clearance index in preterm infants", *Respir Physiol Neurobiol*, v. 223, pp. 43–48, Mar 2016.

[188] VELDHUIZEN, R. A. W., WELK, B., HARBOTTLE, R., et al. "Mechanical ventilation of isolated rat lungs changes the structure and biophysical properties of surfactant", *Journal of Applied Physiology*, v. 92, n. 3, pp. 1169–1175, 2002. Disponível em: <https://doi.org/10.1152/japplphysiol.00697.2001>.

[189] TUCCI, M. R., COSTA, E. L. V., WELLMAN, T. J., et al. "Regional Lung Derecruitment and Inflammation during 16 Hours of Mechanical Ventilation in Supine Healthy Sheep", *Anesthesiology*, v. 119, n. 1, pp. 156–165, 2013. Disponível em: <http://dx.doi.org/10.1097/ALN.0b013e31829083b8>.

[190] CRESSONI, M., CHIURAZZI, C., GOTTI, M., et al. "Lung Inhomogeneities and Time Course of Ventilator-induced Mechanical Injuries", *Anesthesiology*, v. 123, n. 3, pp. 618–627, 2015. Disponível em: <http://dx.doi.org/10.1097/ALN.0000000000000727>.

[191] MESSEROLE, E., PEINE, P., WITTKOPP, S., et al. "The Pragmatics of Prone Positioning", *American Journal of Respiratory and Critical Care Medicine*, v. 165, n. 10, pp. 1359–1363, 2002. Disponível em: <https://doi.org/10.1164/rccm.2107005>.

[192] GUERIN, C., REIGNIER, J., RICHARD, J.-C., et al. "Prone Positioning in Severe Acute Respiratory Distress Syndrome", *New England Journal of Medicine*, v. 368, n. 23, pp. 2159–2168, 2013. Disponível em: <https://doi.org/10.1056/NEJMoa1214103>.

[193] LACHMANN, B. "Open up the lung and keep the lung open", *Intensive Care Med*, v. 18, n. 6, pp. 319–321, 1992.

[194] CARAMEZ, M. P., KACMAREK, R. M., HELMY, M., et al. "A comparison of methods to identify open-lung PEEP", *Intensive Care Medicine*, v. 35, n. 4, pp. 740–747, Apr 2009. ISSN: 1432-1238. Disponível em: <https://doi.org/10.1007/s00134-009-1412-9>.

[195] MERCAT, A., RICHARD, J.-C. M., VIELLE, B., et al. "Positive End-Expiratory Pressure Setting in Adults With Acute Lung Injury and Acute Respiratory Distress Syndrome", *JAMA*, v. 299, n. 6, pp. 646, feb 2008. Disponível em: <https://doi.org/10.1001/jama.299.6.646>.

[196] STAFFIERI, F., STRIPOLI, T., MONTE, V. D., et al. "Physiological effects of an open lung ventilatory strategy titrated on elastance-derived end-inspiratory transpulmonary pressure", *Critical Care Medicine*, v. 40, n. 7, pp. 2124–2131, jul 2012. Disponível em: <https://doi.org/10.1097/ccm.0b013e31824e1b65>.

[197] BATES, J. H. T., IRVIN, C. G. "Time dependence of recruitment and derecruitment in the lung: a theoretical model", *Journal of Applied Physiology*, v. 93, n. 2, pp. 705–713, 2002. Disponível em: <https://doi.org/10.1152/japplphysiol.01274.2001>.

[198] CROTTI, S., MASCHERONI, D., CAIRONI, P., et al. "Recruitment and Derecruitment during Acute Respiratory Failure", *American Journal of Respiratory and Critical Care Medicine*, v. 164, n. 1, pp. 131–140, 2001. Disponível em: <https://doi.org/10.1164/ajrccm.164.1.2007011>.

[199] CARVALHO, A. R., JANDRE, F. C., PINO, A. V., et al. "Effects of descending positive end-expiratory pressure on lung mechanics and aeration in healthy anaesthetized piglets", *Crit Care*, v. 10, n. 4, pp. R122, 2006.

[200] SCOTT?HARRIS, R., HESS, D., VENEGAS, J. "An Objective Analysis of the Pressure-Volume Curve in the Acute Respiratory Distress Syndrome", *American Journal of Respiratory and Critical Care Medicine*, v. 161, n. 2, pp. 432–439, 2000. Disponível em: <https://doi.org/10.1164/ajrccm.161.2.9901061>.

[201] CARVALHO, A. R., SPIETH, P. M., PELOSI, P., et al. "Ability of dynamic airway pressure curve profile and elastance for positive end-expiratory pressure titration", *Intensive Care Medicine*, v. 34, n. 12, pp. 2291, Sep 2008. ISSN: 1432-1238. Disponível em: <https://doi.org/10.1007/s00134-008-1301-7>.

[202] KANO, S., LANTERI, C. J., DUNCAN, A. W., et al. "Influence of nonlinearities on estimates of respiratory mechanics using multilinear regression analysis", *Journal of Applied Physiology*, v. 77, n. 3, pp. 1185–1197, 1994. Disponível em: <https://doi.org/10.1152/jappl.1994.77.3.1185>.

[203] BAEDORF-KASSIS, E., LORING, S. H., TALMOR, D. "Recruitment maneuvers: using transpulmonary pressure to help Goldilocks", *Intensive Care Medicine*, v. 43, n. 8, pp. 1162–1163, Aug 2017. ISSN: 1432-1238. doi: 10.1007/s00134-017-4784-2. Disponível em: <https://doi.org/10.1007/s00134-017-4784-2>.

[204] BUGEDO, G., RETAMAL, J., BRUHN, A. "Driving pressure: a marker of severity, a safety limit, or a goal for mechanical ventilation?" *Critical Care*, v. 21, n. 1, pp. 199, Aug 2017. ISSN: 1364-8535. doi: 10.1186/s13054-017-1779-x. Disponível em: <https://doi.org/10.1186/s13054-017-1779-x>.

[205] SOARES, J. H. N., CARVALHO, A. R., BERGAMINI, B. C., et al. "Alveolar Tidal recruitment/derecruitment and Overdistension During Four Levels of End-Expiratory Pressure with Protective Tidal Volume During Anesthesia in a Murine Lung-Healthy Model", *Lung*, v. 196, n. 3, pp. 335–342, Jun 2018. ISSN: 1432-1750. doi: 10.1007/s00408-018-0096-8. Disponível em: <https://doi.org/10.1007/s00408-018-0096-8>.

[206] CAMILO, L. M., ÁVILA, M. B., CRUZ, L. F. S., et al. "Positive End-Expiratory Pressure and Variable Ventilation in Lung-Healthy Rats under General Anesthesia", *PLOS ONE*, v. 9, n. 11, pp. 1–10, 11 2014. Disponível em: <https://doi.org/10.1371/journal.pone.0110817>.

[207] CAMILO, L. M., MOTTA-RIBEIRO, G. C., DE ÁVILA, M. B., et al. "Variable Ventilation Associated With Recruitment Maneuver Minimizes Tissue Damage and Pulmonary Inflammation in Anesthetized Lung-Healthy Rats", *Anesthesia & Analgesia*, p. 1, jun 2018. Disponível em: <https://doi.org/10.1213/ane.0000000000003582>.

[208] MA, B., SUKI, B., BATES, J. H. T. "Effects of recruitment/derecruitment dynamics on the efficacy of variable ventilation", *Journal of Applied Physiology*, v. 110, n. 5, pp. 1319–1326, 2011. Disponível em: <https://doi.org/10.1152/japplphysiol.01364.2010>.

[209] SOLURI-MARTINS, A., MORAES, L., SANTOS, R. S., et al. "Variable Ventilation Improved Respiratory System Mechanics and Ameliorated Pulmonary Damage in a Rat Model of Lung Ischemia-Reperfusion", *Frontiers in Physiology*, v. 8, pp. 257, 2017. ISSN: 1664-042X. Disponível em: <https://doi.org/10.3389/fphys.2017.00257>.

[210] HENRIQUES, I., PADILHA, G. A., HUHLE, R., et al. "Comparison between Variable and Conventional Volume-Controlled Ventilation on Cardiorespiratory Parameters in Experimental Emphysema", *Frontiers in Physiology*, v. 7, pp. 277, 2016. ISSN: 1664-042X. Disponível em: <https://doi.org/10.3389/fphys.2016.00277>.

[211] DE MAGALHÃES, R. F., SAMARY, C. S., SANTOS, R. S., et al. "Variable ventilation improves pulmonary function and reduces lung dam-

age without increasing bacterial translocation in a rat model of experimental pneumonia", *Respiratory Research*, v. 17, n. 1, pp. 158, Nov 2016. ISSN: 1465-993X. doi: 10.1186/s12931-016-0476-7. Disponível em: <https://doi.org/10.1186/s12931-016-0476-7>.

[212] THAMMANOMAI, A., HUESER, L. E., MAJUMDAR, A., et al. "Design of a new variable-ventilation method optimized for lung recruitment in mice", *Journal of Applied Physiology*, v. 104, n. 5, pp. 1329–1340, 2008. Disponível em: <https://doi.org/10.1152/japplphysiol.01002.2007>.

[213] AROLD, S. P., SUKI, B., ALENCAR, A. M., et al. "Variable ventilation induces endogenous surfactant release in normal guinea pigs", *American Journal of Physiology-Lung Cellular and Molecular Physiology*, v. 285, n. 2, pp. L370–L375, 2003. Disponível em: <https://doi.org/10.1152/ajplung.00036.2003>.

[214] MUTCH, W. A., ESCHUN, G. M., KOWALSKI, S. E., et al. "Biologically variable ventilation prevents deterioration of gas exchange during prolonged anaesthesia", *British Journal of Anaesthesia*, v. 84, n. 2, pp. 197 – 203, 2000. ISSN: 0007-0912. Disponível em: <https://doi.org/10.1093/oxfordjournals.bja.a013403>.

[215] BOKER, A., HABERMAN, C. J., GIRLING, L., et al. "Variable ventilation improves perioperative lung function in patients undergoing abdominal aortic aneurysmectomy", *Anesthesiology*, v. 100, n. 3, pp. 608–616, Mar 2004.

[216] SPIETH, P., GÜLDNER, A., UHLIG, C., et al. "Variable versus conventional lung protective mechanical ventilation during open abdominal surgery (PROVAR): a randomised controlled trial", *British Journal of Anaesthesia*, v. 120, n. 3, pp. 581–591, mar 2018. Disponível em: <https://doi.org/10.1016/j.bja.2017.11.078>.

[217] KACZKA, D. W., HERRMANN, J., ZONNEVELD, C. E., et al. "Multi-frequency Oscillatory Ventilation in the Premature Lung", *Anesthesiology*, v. 123, n. 6, pp. 1394–1403, dec 2015. Disponível em: <https://doi.org/10.1097/aln.0000000000000898>.

[218] HERRMANN, J., TAWHAI, M. H., KACZKA, D. W. "Parenchymal strain heterogeneity during oscillatory ventilation: why two frequencies are better than one", *Journal of Applied Physiology*, v. 124, n. 3, pp. 653–

663, 2018. Disponível em: <https://doi.org/10.1152/japplphysiol.00615.2017>.

[219] BROCCARD, A. F., VANNAY, C., FEIHL, F., et al. "Impact of low pulmonary vascular pressure on ventilator-induced lung injury", *Crit. Care Med.*, v. 30, n. 10, pp. 2183–2190, Oct 2002.

[220] SIMMONS, D. H., LINDE, L. M., MILLER, J. H., et al. "Relation Between Lung Volume and Pulmonary Vascular Resistance", *Circulation Research*, v. 9, n. 2, pp. 465–471, 1961. ISSN: 0009-7330. doi: 10.1161/01.RES.9.2.465. Disponível em: <http://doi.org/10.1161/01.RES.9.2.465>.

[221] BAILE, E. M., PARE, P. D., BROOKS, L. A., et al. "Relationship between regional lung volume and regional pulmonary vascular resistance", *Journal of Applied Physiology*, v. 52, n. 4, pp. 914–920, 1982. doi: 10.1152/jappl.1982.52.4.914. Disponível em: <https://doi.org/10.1152/jappl.1982.52.4.914>.

[222] KALLAS, H. J., DOMINO, K. B., GLENNY, R. W., et al. "Pulmonary blood flow redistribution with low levels of positive end-expiratory pressure", *Anesthesiology*, v. 88, n. 5, pp. 1291–1299, May 1998.

[223] HEDENSTIERNA, G., WHITE, F. C., MAZZONE, R., et al. "Redistribution of pulmonary blood flow in the dog with PEEP ventilation", *Journal of Applied Physiology*, v. 46, n. 2, pp. 278–287, 1979. Disponível em: <https://doi.org/10.1152/jappl.1979.46.2.278>.

[224] WALTHER, S. M., JOHANSSON, M. J., FLATEBO, T., et al. "Marked differences between prone and supine sheep in effect of PEEP on perfusion distribution in zone II lung", *Journal of Applied Physiology*, v. 99, n. 3, pp. 909–914, 2005. Disponível em: <https://doi.org/10.1152/japplphysiol.01388.2004>.

[225] UHLIG, S., UHLIG, U. "Pharmacological interventions in ventilator-induced lung injury", *Trends in Pharmacological Sciences*, v. 25, n. 11, pp. 592 – 600, 2004. ISSN: 0165-6147. Disponível em: <https://doi.org/10.1016/j.tips.2004.09.002>.

[226] PAPAZIAN, L., FOREL, J.-M., GACOUIN, A., et al. "Neuromuscular Blockers in Early Acute Respiratory Distress Syndrome", *New England Journal of Medicine*, v. 363, n. 12, pp. 1107–1116, 2010. Disponível em: <https://doi.org/10.1056/NEJMoa1005372>.

[227] MAC SWEENEY, R., MCAULEY, D. F. "Pharmacological therapy for acute lung injury", *Open Crit Care Med J*, v. 3, pp. 7–19, 2010.

[228] BODENSTEIN, M., DAVID, M., MARKSTALLER, K. "Principles of electrical impedance tomography and its clinical application", *Crit. Care Med.*, v. 37, n. 2, pp. 713–724, Feb 2009.

[229] TESCHNER, E., IMHOFF, M., LEONHARDT, S. *Electrical Impedance Tomography: The realisation of regional ventilation monitoring.* 2 ed. Lübeck, Drägerwerk AG & Co. KGaA, Jan 2015.

[230] SARAOGI, A. "Lung ultrasound: Present and future", *Lung India*, v. 32, n. 3, pp. 250, 2015. Disponível em: <https://doi.org/10.4103/0970-2113.156245>.

[231] BOUHEMAD, B., BRISSON, H., LE-GUEN, M., et al. "Bedside Ultrasound Assessment of Positive End-Expiratory Pressure-induced Lung Recruitment", *American Journal of Respiratory and Critical Care Medicine*, v. 183, n. 3, pp. 341–347, 2011. Disponível em: <https://doi.org/10.1164/rccm.201003-0369OC>.

[232] READE, M. C., FINFER, S. "Sedation and Delirium in the Intensive Care Unit", *New England Journal of Medicine*, v. 370, n. 5, pp. 444–454, 2014. Disponível em: <http://dx.doi.org/10.1056/NEJMra1208705>.

[233] LANGTON, J. A., HUTTON, A. "Respiratory gas analysis", *Continuing Education in Anaesthesia Critical Care & Pain*, v. 9, n. 1, pp. 19–23, 2009. Disponível em: <http://dx.doi.org/10.1093/bjaceaccp/mkn048>.

[234] CIAFFONI, L., O'NEILL, D. P., COUPER, J. H., et al. "In-airway molecular flow sensing: A new technology for continuous, noninvasive monitoring of oxygen consumption in critical care", *Science Advances*, v. 2, n. 8, 2016. Disponível em: <http://advances.sciencemag.org/content/2/8/e1600560>.

[235] MOUNTAIN, J. E., SANTER, P., O'NEILL, D. P., et al. "Potential for noninvasive assessment of lung inhomogeneity using highly precise, highly time-resolved measurements of gas exchange", *Journal of Applied Physiology*, v. 124, n. 3, pp. 615–631, 2018. Disponível em: <https://doi.org/10.1152/japplphysiol.00745.2017>.

[236] HUBMAYR, R. D., WALTERS, B. J., CHEVALIER, P. A., et al. "Topographical distribution of regional lung volume in anesthetized dogs", *Journal*

of Applied Physiology, v. 54, n. 4, pp. 1048–1056, 1983. Disponível em: <https://doi.org/10.1152/jappl.1983.54.4.1048>.

[237] AKOUMIANAKI, E., MAGGIORE, S. M., VALENZA, F., et al. "The Application of Esophageal Pressure Measurement in Patients with Respiratory Failure", *American Journal of Respiratory and Critical Care Medicine*, v. 189, n. 5, pp. 520–531, 2014. Disponível em: <https://doi.org/10.1164/rccm.201312-2193CI>.

[238] CARVALHO, A. R., ZIN, W. A. "Respiratory system dynamical mechanical properties: modeling in time and frequency domain", *Biophysical Reviews*, v. 3, n. 2, pp. 71, May 2011. ISSN: 1867-2469. doi: 10.1007/s12551-011-0048-5. Disponível em: <https://doi.org/10.1007/s12551-011-0048-5>.

[239] WOBBROCK, J. O., FINDLATER, L., GERGLE, D., et al. "The Aligned Rank Transform for Nonparametric Factorial Analyses Using Only Anova Procedures". In: *Proceedings of the SIGCHI Conference on Human Factors in Computing Systems*, CHI '11, pp. 143–146, New York, NY, USA, 2011. ACM. ISBN: 978-1-4503-0228-9. Disponível em: <http://doi.acm.org/10.1145/1978942.1978963>.

[240] BENJAMINI, Y., HOCHBERG, Y. "Controlling the False Discovery Rate: A Practical and Powerful Approach to Multiple Testing", *Journal of the Royal Statistical Society. Series B (Methodological)*, v. 57, n. 1, pp. 289–300, 1995. ISSN: 00359246. Disponível em: <http://www.jstor.org/stable/2346101>.

Appendix A

Supplementary Data for Chapter 3

A.1 Extended Methods

Animal experiments were performed in compliance with institutional guidelines approved by the Subcommittee on Research Animal Care at the Massachusetts General Hospital (protocol 2006N000129) and in accordance with the "Guide for the Care and Use of Laboratory Animals" published by the National Institutes of Health (publ. no. 86–23, revised 1996).

A.1.1 Protocol

Ten female sheep ($(15.7 \pm 2.6)\,$kg) were studied. Animals were sedated with intramuscular ketamine ($3\,\mathrm{mg\,kg^{-1}}$–$8\,\mathrm{mg\,kg^{-1}}$) and midazolam ($1\,\mathrm{mg\,kg^{-1}}$). General anesthesia was induced with propofol ($2\,\mathrm{mg\,kg^{-1}}$–$4\,\mathrm{mg\,kg^{-1}}$) or ketamine ($3\,\mathrm{mg\,kg^{-1}}$–$4\,\mathrm{mg\,kg^{-1}}$) and maintained with a continuous infusion of propofol ($45\,\mathrm{mg\,h^{-1}}$) and fentanyl ($50\,\mathrm{\mu g\,h^{-1}}$) titrated to hemodynamics. Muscle relaxation was achieved with rocuronium (bolus dose of $1\,\mathrm{mg\,kg^{-1}}$–$2\,\mathrm{mg\,kg^{-1}}$) at induction and continuously infused at a rate of $10\,\mathrm{mg\,h^{-1}}$ during the experiment. For monitoring and collection of blood samples, we percutaneously cannulated a femoral artery and introduced a pulmonary artery catheter via the jugular vein using sterile techniques. After intubation, sheep were positioned prone and lungs were recruited ($40\,\mathrm{cm\,H_2O}$ for $30\,\mathrm{s}$). We aimed to investigate the effect of lung aeration heterogeneity on the spatial distribution and time progression of tidal strain. Thus, following lung recruitment, animals were divided in two groups according to the expected distribution of lung aeration with body position. For heterogenous aeration animals were positioned supine (N=5), while for homogeneous condition animals were kept prone (N=5).

All animals underwent mechanical ventilation for 24 hour using volume controlled mode with a protective strategy: $V_T=8\,\mathrm{mL\,kg^{-1}}$ adjusted to anatomical dead-space

measured with volumetric capnography to reach an alveolar plateau (phase III), positive end-expiratory pressure (PEEP) $=5\,\mathrm{cm}\,H_2O$, F_IO_2=0.3, inspiration to expiration ratio of 1:2 and respiratory rate adjusted to normocapnia. Sheep were positioned in the PET/CT scanner (NeuroPET/CT, Photo Diagnostic Systems Inc., Boxboro, MA) using CT scans during controlled breathing to maximize the lung volume within the scanner's field of view.

After a period of stabilization, baseline physiological variables, arterial and central venous blood samples, CT and PET images were acquired (baseline, 0 h). After these, a continuous intravenous infusion of endotoxin $2.5\,\mathrm{ng}\,\mathrm{kg}^{-1}\,\mathrm{min}^{-1}$ (Escherichia coli O55:B5, List Biological Laboratories Inc, Campbell, CA) was started, and similar image acquisition was performed at 6 h and 24 h. Respiratory mechanics and hemodynamic parameters were continuously monitored and $PEEP/F_IO_2$ were adjusted, if needed, following the low-PEEP ARDS network table [27]. At the end of the study, animals were euthanized under deep general anesthesia.

A.1.2 Physiological parameters

At each measurement point, respiratory flow, expired CO_2 (NICO, Respironics), and airway, esophageal, arterial and central venous pressures (Solar 8000, GE Healthcare) were recorded using a purpose-built program in Labview (National Instruments, Austin, TX) with sampling rate of 200 Hz. Esophageal pressure was measured with a nasogastric balloon catheter (SmartCath, Bicore, Riverside, CA), positioned using the occlusion method with chest compression [237]. Transpulmonary pressure was measured as the difference between airway and esophageal pressures (presumed to estimate pleural pressures). Respiratory signals were filtered offline with a low-pass 20 Hz cutoff frequency. Filtered flow was numerically integrated to compute volume.

Airway peak pressure and PEEP were continuously monitored during the experiment using the NICO monitor and are reported for baseline, 6 h and 24 h. Respiratory mechanics were assessed by respiratory system, chest wall and lung resistance and elastance (E_{RS}, E_{CW} and E_L) estimated at each respiratory cycle using the single compartment equation of motion [238]. For each time point the reported value is the average over 40 s–60 s. The same cycles were used to calculate driving pressure ($E_{RS} \cdot V_T$), and delta transpulmonary pressure ($E_L \cdot V_T$). This assessment of driving and delta transpulmonary pressures was used to increase accuracy by allowing for dynamic measurement, i.e., during mechanical ventilation, and reducing the effect of noise (e.g., random and cardiogenic oscillations) given that those estimates based on the motion equation characterize better the airway and esophageal

pressures and flow signals during the 40 s–60 s sampling period than isolated manual measurements.

Hemodynamics was evaluated as systolic, diastolic, mean systemic arterial, pulmonary arterial and wedge pressures. Cardiac output was considered as the mean of three repetitions with the usual thermodilution method.

A.1.3 Image acquisition

CT images (tube current of 7 mA and voltage of 140 kVp) were acquired at end-inspiratory and end-expiratory conditions for lung aeration and strain analysis using breath holds at plateau and PEEP pressures, respectively. An additional mean lung volume CT image for PET attenuation correction and delineation of regions-of-interest (ROI) was acquired during tidal breathing (2 min). Reconstructed CT images consisted of a matrix of $512 \times 512 \times 82$ voxels of $0.49 \, \text{mm} \times 0.49 \, \text{mm} \times 2.5 \, \text{mm}$ each [146].

Dynamic PET scans to assess pulmonary inflammation distribution were acquired at baseline and after 24 hour of endotoxin infusion. The PET field of view has a diameter of 25 cm, an axial length of 22 cm, and spatial resolution measured as full-width at half maximum (FWHM) of 3.5 mm in the center [146]. PET scan acquisition in 3D list mode started 30 s before the injection of ^{18}F-FDG ($\sim$2 mCi) as a bolus ($<$2 s) through the jugular vein catheter, and continued for 90 min. Pulmonary arterial blood was sampled at 3.0 min, 5.5 min, 7.5 min, 9.5 min, 25 min, 37 min and 42.5 min to calibrate the image-derived input function [91]. Images were reconstructed using filtered back projection algorithm in sequential frames (20 s, 10 s, 6 s × 5 s, 6 s × 10 s, 6 s × 30 s, 9 s × 60 s, 5 s × 120 s, 5 s × 300 s and 4 s × 600 s) composed by 92 slices with thickness of 2.3 mm and in plane resolution of 2 mm.

A.1.4 Image processing

Computed Tomography

Aeration:

Lung aeration was expressed as fraction of gas quantified considering air Hounsfield units (HU)$= -1000$ and tissue HU$=0$ as $F_{GAS}=$voxel HU$/-1000$. The sizes of hyperaerated (-1000 to -901 HU, $F_{GAS}>0.9$), normally aerated (-900 to -501 HU, $0.5 < F_{GAS} < 0.9$), poorly- (-500 to -101 HU, $0.1 < F_{GAS} < 0.5$) and non-aerated (-100 to 0 HU, $F_{GAS} < 0.1$) regions were expressed as percentage of the total lung volume (number of voxels inside the mask).

Strain:

Strain analysis was performed at the voxel level using image registration to calculate the transformation T(x) ($\Re^3 \rightarrow \Re^3$) that mapped each end-inspiratory image back to the corresponding end-expiratory image. Before registration, images were rescaled to have, inside the parenchyma, the maximum equal to zero and the minimum equal to one. Then, each dimension was cropped to the bounding box of the end-inspiratory mask and padded with a margin of 50 voxels at each side. Registration was implemented with diffeomorphic transforms and B-Spline regularization in a multistage approach (increasing image resolution and decreasing B-Spline knots distance), using the open source Advanced Normalization Tools 2.1.0 (ANTs) [104]. The cost function used cross-correlation inside a radius of four voxels and the B-spline knots were initialized with 26 mm, and halved in each of the subsequent three steps.

From T(x) the volumetric deformation of each voxel was quantified by the determinant of the Jacobian (directional derivative) matrix, normally referred to as just Jacobian [58, 64–66]. The Jacobian matrix

$$\begin{bmatrix} \frac{\delta f_x}{\delta x} & \frac{\delta f_x}{\delta y} & \frac{\delta f_x}{\delta z} \\ \frac{\delta f_y}{\delta x} & \frac{\delta f_y}{\delta y} & \frac{\delta f_y}{\delta z} \\ \frac{\delta f_z}{\delta x} & \frac{\delta f_z}{\delta y} & \frac{\delta f_z}{\delta z} \end{bmatrix}$$

is composed by the first order partial derivatives of a vector function value (the transformation T(x)). This matrix represents how the function varies in each direction at a given point, similar to how the derivative approximates a scalar function. Its determinant measures the ratio of the final to the initial volume. Strain is then defined as *Jacobian–1* and is referred to total lung volume (tissue + air) at end-expiration. Due to possible variations in VT between time points and imprecision of CT estimated lung volumes during breath hold images to represent V_T, strains were normalized by CT measured inspired air volume.

Anatomical accuracy of image registration was validated by the landmark distance method in two supine and one prone sheep at baseline and 24 hour (extremes of aeration) and one supine at 6 h (maximum difference between inspiratory and expiratory volume). Landmarks were automatically identified in the expiratory image and semi-automatically matched in the inspiratory image by one observer [110].

Spatial Heterogeneity:

The spatial heterogeneity of aeration and strain were assessed by the normalized variance in the end-expiratory image. The normalization factors were the squared mean voxel level aeration and the global strain (considered equal the mean of all voxel). This measure is then equivalent to the squared coefficient of variation. The overall heterogeneity was computed in an image filtered to an effective in plane

resolution equal to the slice thickness (2.5 mm). The component due to gravity was estimated from a linear regression of all voxels against their height.

Positron Emission Tomography

^{18}F-FDG parameters were determined using a three compartment model with a delay in the input function [89]. Briefly, the model consists of an intravascular compartment, a precursor compartment representing the concentration of ^{18}F-FDG available for phosphorylation (i.e., the concentration of ^{18}F-FDG that can serve as a substrate for hexokinase), and a metabolized compartment accounting for the concentration of ^{18}F-FDG that has been phosphorylated by hexokinase [124]. In this analysis, the ^{18}F-FDG net uptake rate (Ki), a measure of cellular metabolic activity, is expressed as: $Ki = F_e \cdot k_3$. The constant k_3 is the rate of ^{18}F-FDG phosphorylation, proportional to hexokinase activity, and F_e (volume of distribution) is the fraction of the ROI occupied by the precursor compartment [124]. The intravascular compartment of the model is characterized by the volume of blood in the ROI expressed as a fraction (F_b) of the ROI's volume. The delay in the input function models transit time from the right heart to each ROI [89].

The time activity of the input function was calibrated to the tracer activity measured in the plasma drawn during the image acquisition using an one compartment model [91]. For each ^{18}F-FDG image, at least three plasma activity measurement points were used for calibration with at least one point at the early (<10 min) and one at the late phase of the ^{18}F-FDG activity curve. The points were chosen in order to minimize the weighted sum of squared error for the three compartments plus delay model fitted to the whole lung.

A.1.5 Voxel selection

CT masks of lung parenchyma were created using a threshold of -200 HU and manually refined to include atelectatic regions and exclude major vessels and airways. CT masks for mean lung volume were converted to PET image resolution, and once again refined to reduce areas with partial volume effects due to heart motion, large blood vessels and bronchi.

Tidal lung expansion and loss in aeration could change the amount of lung inside the field of view from end-expiration to end-inspiration, as well as between timepoints. For this reason, for the strain analyses, the first and last slices of each image were visually matched using identifiable anatomical features.

CT image analyses were performed at voxel level within lung parenchyma. ^{18}F-FDG kinetics were evaluated for the whole lung and in approximately cylindrical ROIs with ~1.4 mL ($9 \times 9 \times 2$ voxels, excluding the corners). These last used to

define the significance of regional blood volume, aeration and strain as predictors of metabolic activity. Importantly, in order to match the small ROIs between baseline and 24 hour, they were defined in the baseline and image registration derived transformations were used to obtain the ROIs at 24 hour.

For the image derived ^{18}F-FDG input function, a blood pool mask corresponding to right heart and the main pulmonary artery was drawn using the frame with the peak of plasma ^{18}F-FDG activity.

A.1.6 Tissue sample

After euthanasia, lungs were excised en block. Tissue samples were collected from four regions of the right lung for gene expression analysis, wet-to-dry ratio and protein quantification. In supine animals, regions were selected as: 1) highly aerated (ventral, middle from apex to base); 2-a) normally aerated (middle in ventro-dorsal and cephalo-caudal axes); 2-b) normally aerated (middle in ventro-dorsal axis, caudal); and 3) non-aerated (dorsal regions). In prone animals, regions followed the same anatomical zones, i.e. in reverse according to gravity. After lung harvest, tissue samples were snap frozen in liquid nitrogen and stored at $-80\,°C$.

After sampling, the remaining left lung was filled from the trachea with Trump's fixative to approximately $27\,cm\,H_2O$. A block of lung tissue was sampled from same regions described above and embedded in paraffin. Sections of 5-μm thickness were cut, mounted, and stained with hematoxylin-eosin for light microscopy. Lung injury score was assessed in 60 high-power (400X) fields per animal (20 per region, just 2-a for middle) by one investigator who was blinded to the group assignment. The continuous score (0 to 1) consisted in the weighted mean of semi-quantitative scale assigned to neutrophils in alveolar space, neutrophils in interstitial space, hyaline membranes, proteinaceous debris filling the airspace and alveolar septal thickening [125].

A.1.7 Gene expression and inflammatory markers

Total RNA was extracted from sheep lung tissues using RNeasy Mini Kit (Qiagen, Valencia, CA) according to the manufacturer's instructions. RNA was quantified by Nanodrop ND-1000. 1 μg of RNA was reverse-transcribed to cDNA using random hexamers with SuperScript III (Life Technologies, Carlsbad, CA). Using reverse transcription quantitative real-time PCR (RT-qPCR), we measured regional lung expression of genes related to inflammatory cytokines (Interleukin 1 beta [IL-1β], Interleukin 6 [IL-6], Interleukin 8 [CXCL-8]), neutrophilic inflammation (Intercellular Adhesion Molecule 1 [ICAM-1], Cluster of Differentiation molecule 11B [CD11B]), and epithelial cell injury (Receptor for Advanced Glycation Endproducts [RAGE]),

as well as genes previously found by us as regionally expressed in early lung injury (amphiregulin, Plasminogen Activator Inhibitor-1 [PAI-1]) and associated with endothelial injury. For each target gene, we used custom-designed TaqMan® primers and probes (Table A.1). RT-qPCR reactions were run in an assay containing $12.5\,\mu L$ of TaqMan® Gene Expression Master Mix, $0.9\,\mu mol$ each primer, $0.25\,\mu mol$ each probe and $11.25\,\mu L$ of 10-fold diluted cDNA, made up to $25\,\mu L$ with deionized water. The cycling conditions for all genes were as follows: 10 min at 95 °C, 40 cycles of 15 s at 95 °C and 1 min at 60 °C. Copy numbers were determined from the Ct values of each sample. Final quantitation was performed by comparison with the internal standard β-actin reference gene and controlled with the gene expression of lung tissue collected from a healthy sheep not used in this study (2-ΔΔCt). Two prone animals were studied after the first set of experiments to increase the power of the analysis. Gene expressions of these animals were adjusted to the previous measurements by the ratio of control measurements.

A.1.8 Wet-to-dry weight ratios

Tissue samples were weighed directly after collection to record the wet weight and then were dried in an incubator for 3 days at 80 °C to obtain the dry weight. Wet to dry ratios, as an indicator of lung water content, were calculated as the average of the ratio of wet weight to dry weight of two samples in each region.

A.1.9 Human image data

A similar set of CT and PET images from the animal experiments were acquired in two septic patients (height=1.65/1.68 m, BMI=22.6/18.3 $kg\,m^{-2}$, male, Pneumonia-Sepsis, P_aO_2/F_IO_2=194/330 mmHg) after obtaining informed consent from their surrogates (IRB 2008P000561). Both patients were mechanically ventilated (V_T=5/7 mL kg^{-1}, PEEP=13/8 cm H_2O, RR=30/24 min^{-1}, F_IO_2=0.5/0.4) for less than 96 h in one critical care unit of Massachusetts General Hospital.

CT and PET images were acquired on a Biograph 64 TruePoint (Siemens, Germany). The CT used low dose (tube current-time product of 30 mA s) with voxel size 0.73 mm × 0.73 mm × 0.75 mm and superposition of 0.25 mm. PET images were reconstructed with filtered backprojection in voxels of 5.3 mm × 5.3 mm × 2.0 mm.

The following differences in acquisition protocol and data processing were necessary: mean lung volume CT was acquired during a breath hold at mean lung pressure; PET acquisition total time was 53 min (frames reconstructed as 9 s × 10 s, 3 s × 15 s, 1 s × 30 s, 7 s × 60 s, 14 s × 120 s, 1 s × 300 s and 1 s × 600 s); and only five blood samples were collected for input function calibration.

141

Table A.1: Primer and probe sequences for quantitative real-time PCR

Target	Sequence	
	forward	5'-GCTCTCCACCTCCTCTCACA-3'
IL-1β	reverse	5'-CCTCTCCTTGTACGAAGCTCATG-3'
	probe	CAGAACACCACTTCTCG-3'
	forward	5'-GTGACCATGTATAGCTTCCCACTTC-3'
ICAM-1	reverse	5'-ACGGTCACAGTAGTCCATTCTGA-3'
	probe	5'-CCCTGACCCTGAGCCC-3'
	forward	5'-CGGATCACAGGCTCACAGAT-3'
CD11b	reverse	5'-AAGTCTACCAGTCCATCCATTGTG-3'
	probe	5'-ACTGCCCAAAATACTG-3'
	forward	5'-TGGCCAGGATTCACGAGTTC-3'
CXCL8	reverse	5'-TCTGTGAGGTAGAAAGATGACTGAGATATT-3'
	probe	5'-ACTGTGCCTCGATTTC-3'
	forward	5'-CTGAAGGAAAAGATCGCAGGTCTAA-3'
IL-6	reverse	5'-GACTGCATCTTCTCCAGCATGT-3'
	probe	5'-CCAGCCACACACACTG-3'
	forward	5'-GAAAACTCTGATTCCTGATGGCAAA-3'
RAGE	reverse	5'-CGGGTGTCTCTTGGTCTCTT-3'
	probe	5'-CCTTCACGGACACTCC-3'
	forward	5'-GCATGGTCGACAGTGATTTATCAAAA-3'
Amphiregulin	reverse	5'-GTATCGTCTTCGAAGCAGGATTGTA-3'
	probe	5'-CTCCGCCATGACCTTC-3'
	forward	5'-GCATGATCAGCGACTTACTTGGT-3'
PAI-1	reverse	5'-GCCGTTGAAGTAGAGGGCATTTA-3'
	probe	5'-ACGCGCCTGGTCCTG-3'
	forward	5'-CCAGCACGATGAAGATCAAGATCA-3'
β-actin	reverse	5'-AGGATGGAGCCGCCAATC-3'
	probe	5'-CCTGAGCGCAAGTACT-3'

A.1.10 Statistical analysis

Sample sizes were determined from our group previous experimental observations, taking into account the more homogeneous distribution of aeration, ventilation and perfusion in the prone position. We considered a power of 0.8, significance of 0.05 and paired tests. For the supine group an effect size for variation of aeration heterogeneity of 1.8 was determined from an experiment with sheep ventilated in supine with zero end-expiratory pressure and low V_T for 16 h [189]. We estimated that half of the sample size would be sufficient for prone because it was showed in dogs that specific ventilation heterogeneity is approximately the double in supine [137], however we used the same number of animals to increase the power. Animals were selected by the vendor without knowledge of the protocol or group assignment, restricted only to a weight range.

Respiratory mechanics, hemodynamic, lung CT derived and ^{18}F-FDG kinetics parameters were compared between groups and time points using repeated measures ANOVA (2 groups by 3 or 2 times, accordingly to the measurement time points available). To account for multiple comparisons, p-values were calculated from a multivariate t distribution (lsmeans package, version 2.25). Values were expressed as mean and standard deviation.

For gene expression, statistical analysis used repeated measures ANOVA (2 groups by 3 regions) after rank transformation with aligned rank transform [239]. Multiple comparisons p-values were corrected by Benjamini & Hochberg [240] (each gene was considered as independent). Samples from mid lung regions (2-a and 2-b) were combined into one group after confirmation of no difference with a paired Wilcoxon test. Values were expressed as median, first and third quartiles ([Q1-Q3]). All statistical tests were two-tailed and performed in R 3.3.1 (R Foundation for Statistical Computing, Vienna, Austria). Significance was set at $p < 0.05$.

A.2 Determinants of inflammation

To assess the determinants of change in regional phosphorylation rate from baseline to 24 h in regions continuously aerated ($F_{GAS} > 0.1$), the aeration, blood volume per unit of non-gas volume ($1 - F_{GAS}$) and tidal strain within the small ROIs were included in a mixed-effects linear regression as an average of both time points. A categorical variable for group was included and each animal was given a random intercept. We started with a model containing the three paired interactions and selected the significant ones using Akaike information criterion (AIC) in backward elimination. The final model was composed of group, aeration, blood volume, tidal

strain and the interaction between strain and blood volume. These last two terms were identified as presenting significant effects (Table A.2).

Of note, the significance of the blood volumexstrain interaction term is consistent with the two-hit concept: the higher the regional blood volume (i.e., more exposure to intravenous endotoxin, inflammatory cells and mediators) the higher the sensitivity to strain. An interaction between tidal strain and blood volume should be interpreted as a slope for the strain-phosprorylation relationship that varies with the local amount of blood per tissue (Fig. A.1). For example, a tidal strain of 0.25 would contribute to increase phosphorylation rate by $0.42 \times 10^{-2} \, \mathrm{min}^{-1}$ above the intercept ($[-2.8 + 14.9 \cdot 0.3] \cdot 0.25$), while the same tidal strain in a region with blood fraction of 0.4 would contribute with $0.79 \times 10^{-2} \, \mathrm{min}^{-1}$ above the intercept ($[-2.8 + 14.9 \cdot 0.4] \cdot 0.25$). Thus, in our experimental conditions (mild endotoxemia and limited regional strains) the effect that strain has over inflammation is modulated by the regional blood volume.

After defining this regression model with the main cofactors for change in phosphorylation rate we included the information of small length-scale heterogeneity of strain quantified as the standard deviation of the voxel level tidal strains within each small ROI (SD_{strain}). The addition of this new variable improved the fitting of the model (AIC=3695.4 vs. 3735.8), and SD_{strain} was an additional significant variable related to the phosphorylation rate change (Table A.2). This dependence of inflammation to small length-scale heterogeneity could be a surrogate for higher heterogeneity in sub-voxel resolution or a marker of concentrations of mechanical forces.

Table A.2: Mixed-effects linear regression for predictors of variation in phosphorylation rate. Only regions that were aerated both at baseline and 24 h were considered. The continuous variables are an average from both time points.

|	Coefficient	Upper limit	Lower limit	t-value	p-value
Intercept	0.3	-0.5	1.1	0.807	0.432
Group	0.2	-0.7	1.2	0.649	0.650
Aeration	0.2	-0.1	0.6	1.234	0.217
Blood volume	-0.2	-2.0	1.7	-0.173	0.863
Tidal strain	-2.8	-5.2	-0.3	-2.207	0.028
Blood volume x strain	14.9	1.9	27.8	2.244	0.025
After inclusion of Tidal strain heterogeneity (SD_{strain})					
Intercept	0.1	-0.6	0.9	0.327	0.748
Group	0.2	-0.7	1.1	0.420	0.656
Aeration	0.3	-0.04	0.6	1.721	0.086
Blood volume	-0.7	-2.5	1.2	-0.708	0.479
Tidal strain	-4.6	-7.1	-2.1	-3.622	<0.001
Blood volume x strain	16.9	4.0	29.6	2.575	0.010
SD_{strain}	9.4	6.6	12.3	6.527	<0.001
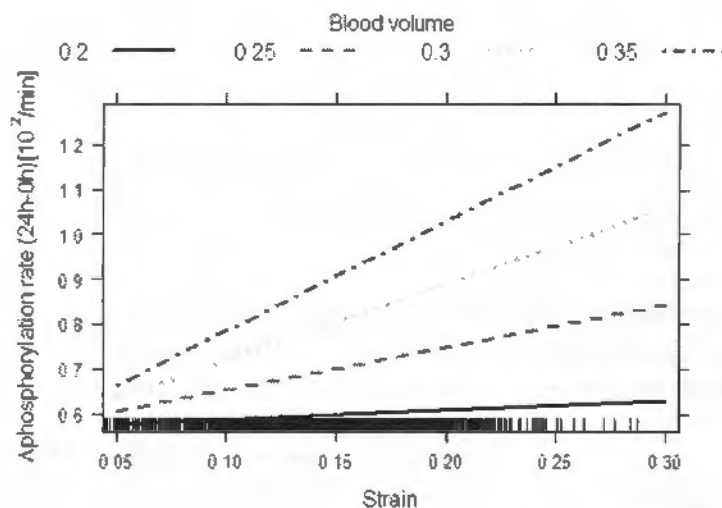
Figure A.1: Effect of blood volume per gram of tissue and strain interaction in a mixed-effects linear regression on predictors of change in phosphorylation rate from baseline to 24 h. Note that the strain has more influence in inflammation in regions with higher blood volume. The vertical marks in the bottom of the figure represent the strain data points used as input for the regression.

A.3   Additional tables

Table A.3: Ventilatory settings at baseline, 6 h and 24 h of low tidal volume mechanical ventilation and mild endotoxemia. Data are mean±SD. † difference between groups at specific time point and (xx) difference to xx time point in the same group.

		Baseline	6 hours	24 hours	ANOVA
PEEP	Prone	$5.0\pm0.4^{(24)}$	5.0 ± 0.1	4.9 ± 0.1	time p=0.006
(cm H_2O)	Supine	$5.3\pm0.2^{(24)}$	5.0 ± 0.2	4.9 ± 0.2	group p=0.189
					group:time p=0.253
Respiratory Rate	Prone	$33\pm2^{(24)}$	$34\pm2^{(24)}$	29 ± 5	time p=0.01
(min^{-1})	Supine	33 ± 1	34 ± 3	34 ± 4	group p=0.349
					group:time p=0.032
Tidal Volume	Prone	8.1 ± 0.6	8.4 ± 0.9	8.4 ± 0.9	time p=0.116
(mL kg^{-1})	Supine	$9.3\pm1.7^{(24)}$	8.8 ± 2.3	8.0 ± 1.2	group p=0.598
					group:time p=0.014
F_IO_2	Prone	0.30 ± 0.00	0.30 ± 0.00	0.30 ± 0.00	time p=0.001
	Supine	$0.30\pm0.00^{(24)}$	$0.32\pm0.04^{(24)}$	$0.38\pm0.05^{\dagger}$	group p=0.005
					group:time p=0.001

Table A.4: Gas exchange variables at baseline, 6 h and 24 h of low tidal volume mechanical ventilation and mild endotoxemia. Data are mean±SD. [†] difference between groups at specific time point and (xx) difference to xx time point in the same group.

		Baseline	6 hours	24 hours	ANOVA
VD/VT	Prone	0.77 ± 0.08	0.79 ± 0.05	0.72 ± 0.08	time p=0.065
	Supine	0.66 ± 0.06	0.72 ± 0.04	0.67 ± 0.07	group=0.018
					group:time p=0.491
P_aO_2/F_IO_2	Prone	$415\pm63^{†,(24)}$	343 ± 54	$411\pm74^{†}$	time p=0.001
(mmHg)	Supine	$316\pm55^{(24)}$	268 ± 22	214 ± 30	group p<0.001
					group:time p=0.002
Alveolar − arterial	Prone	33 ± 17	54 ± 15	$43\pm19^{†}$	time p<0.001
O_2 gradient	Supine	$64\pm14^{(24)}$	$81\pm21^{(24)}$	138 ± 26	group p<0.001
					group:time p<0.001
Arterial pH	Prone	$7.34\pm0.09^{(24)}$	7.30 ± 0.07	7.22 ± 0.09	time p=0.006
	Supine	$7.36\pm0.06^{(24)}$	7.31 ± 0.09	7.27 ± 0.03	group p=0.235
					group:time p=0.676
Arterial pCO2	Prone	43 ± 6	$44\pm9^{(24)}$	37 ± 3	time p=0.009
(mmHg)	Supine	42 ± 5	$48\pm7^{(24)}$	41 ± 5	group p=0.427
					group:time p=0.395
Arterial pO2	Prone	$125\pm19^{(6)}$	103 ± 16	123 ± 22	time p=0.032
(mmHg)	Supine	$95\pm17^{(6)}$	85 ± 6	81 ± 12	group p=0.001
					group:time p=0.104
Mixed venous pH	Prone	$7.31\pm0.08^{(24)}$	7.28 ± 0.06	7.20 ± 0.10	time p=0.014
	Supine	$7.33\pm0.06^{(24)}$	7.29 ± 0.09	7.26 ± 0.03	group p=0.213
					group:time p=0.653
Mixed venous pCO_2	Prone	$50\pm6^{(24)}$	$49\pm8^{(24)}$	41 ± 4	time p=0.004
mmHg)	Supine	$48\pm6^{(24)}$	$51\pm7^{(24)}$	43 ± 6	group p=0.594
					group:time p=0.627
Mixed venous pO_2	Prone	$52\pm8^{(24)}$	53 ± 7	59 ± 9	time p=0.017
(mmHg)	Supine	$50\pm7^{(24)}$	53 ± 8	54 ± 11	group p=0.574
					group:time p=0.501
Mixed venous O_2	Prone	69 ± 7	72 ± 4	77 ± 4	time p=0.079
saturation	Supine	66 ± 8	68 ± 8	68 ± 9	group p=0.132
					group:time p=0.247

Table A.5: Hemodynamics variables at baseline, 6 h and 24 h of low tidal volume mechanical ventilation and mild endotoxemia. Data are mean±SD. [†] difference between groups at specific time point and (xx) difference to xx time point in the same group.

		Baseline	6 hours	24 hours	ANOVA
Cardiac output	Prone	4.0±1.9	4.3±1.8	3.0±0.8	time p=0.144
(L min^{-1})	Supine	6.5±1.4	5.6±1.8	5.3±1.0	group p=0.005
					group:time p=0.477
Heart rate	Prone	137±51	159±44$^{(24)}$	119±29	time p=0.042
(min^{-1})	Supine	178±39	157±15	154±32	group p=0.203
					group:time p=0.048
Blood pressure (mmHg)					
Mean systemic	Prone	100±12	106±10†	92±20	time p=0.011
	Supine	102±7$^{(6),(24)}$	84±11	84±9	group p=0.127
					group:time p=0.022
Mean pulmonary	Prone	21±3$^{(6)}$	26±5$^{(24)}$	20±2	time p=0.007
	Supine	21±3$^{(6)}$	23±3$^{(24)}$	21±1	group p=0.775
					group:time p=0.164
Pulmonary wedge	Prone	10±1	11±4	9±2	time p=0.524
	Supine	11±2	10±3	10±1	group p=0.822
					group:time p=0.301
Central venous	Prone	8±5	8±5	8±2	time p=0.696
	Supine	10±3	10±3	9±1	group p=0.353
					group:time p=0.986

Table A.6: Categories of histological lung injury score (presence of neutrophils in airspace, neutrophils in interstitium, Hyaline membrane and proteinaceous and alveolar thickening). For it category one region is represented by the mean of the 20 fields classified as 0, 1 and 2. Data are mean±SD. [†] difference between groups at specific region. * difference to ventral region in the same group.

		ventral	middle	dorsal	ANOVA
Neutrophils	Prone	0.8±0.3	0.9±0.1	1.1±0.4*	region p=0.002
in airspace	Supine	0.8±0.4	1.3±0.5	1.3±0.4*	group p=0.271
					group:region p=0.449
Neutrophils	Prone	1.2±0.3	1.3±0.3	1.4±0.4	region p=0.164
in interstitium	Supine	1.4±0.4	1.7±0.4	1.7±0.4	group p=0.088
					group:region p=0.647
Hyaline membrane	Prone	0.2±0.2	0.2±0.2	0.2±0.2	region p<0.001
	Supine	0.1±0.1	0.5±0.2*	0.6±0.2*,†	group p=0.029
					group:region p<0.001
Proteinaceous	Prone	2.0±0.1	2.0±0.0	2.0±0.0	region p=0.413
	Supine	2.0±0.0	2.0±0.0	2.0±0.1	group p=0.564
					group:region p=0.596
Septal thickening	Prone	1.3±0.3	1.4±0.3	1.4±0.3*	region p=0.010
	Supine	1.3±0.3	1.5±0.2	1.7±0.3*	group p=0.487
					group:region p=0.126

Table A.7: Respiratory mechanics at baseline, 6 h and 24 h of low tidal volume mechanical ventilation and mild endotoxemia. Data are mean±SD. [†] difference between groups at specific time point and (xx) difference to xx time point in the same group.

		Baseline	6 hours	24 hours	ANOVA
Peak pressure	Prone	$15.2\pm1.1^{(6),(24)}$	$18.4\pm1.7^{(24)}$	20.4 ± 0.6	time p<0.001
(cm H$_2$O)	Supine	$17.7\pm1.7^{(24),\dagger}$	$18.5\pm1.0^{(24)}$	20.6 ± 1.2	group p=0.112
					group:time p=0.019

Elastance (cm H$_2$O L^{-1})

		Baseline	6 hours	24 hours	ANOVA
Lung	Prone	$31.8\pm16.1^{(24)}$	$48.7\pm24.8^{(24)}$	63.3 ± 16.9	time p<0.001
	Supine	$44.2\pm7.9^{(24)}$	$49.6\pm14.5^{(24)}$	76.9 ± 17.8	group p=0.262
					group:time p=0.418
Chest wall	Prone	37.3 ± 6.5	45.6 ± 5.6	43.9 ± 10.3	time p=0.076
	Supine	27.8 ± 6.8	33.8 ± 8.9	27.6 ± 3.9	group p<0.001
					group:time p=0.504
Respiratory system	Prone	$69.1\pm14.3^{(6),(24)}$	97.3 ± 19.2	107.2 ± 17.8	time p<0.001
	Supine	$71.9\pm9.9^{(24)}$	$83.4\pm18.7^{(24)}$	104.4 ± 19.2	group p=0.612
					group:time p=0.042

Resistance (cm H$_2$O L^{-1} s^{-1})

		Baseline	6 hours	24 hours	ANOVA
Lung	Prone	$5.3\pm1.5^{(24)}$	$5.4\pm2.0^{(24)}$	10.7 ± 3.4	time p<0.001
	Supine	$5.7\pm3.3^{(24)}$	$5.6\pm3.1^{(24)}$	9.8 ± 2.8	group p=0.877
					group:time p=0.792
Chest wall	Prone	1.2 ± 0.4	1.2 ± 0.4	1.5 ± 1.2	time p=0.691
	Supine	1.3 ± 0.2	1.2 ± 0.3	0.9 ± 0.2	group=0.371
					group:time p=0.105
Respiratory system	Prone	$6.5\pm1.7^{(24)}$	$7.0\pm1.8^{(24)}$	12.2 ± 4.4	time p<0.001
	Supine	$7.0\pm3.3^{(24)}$	$6.8\pm2.9^{(24)}$	10.7 ± 3.0	group p=0.759
					group:time p=0.582

Table A.8: Total lung mass (TLM), air volume and aeration compartments (relative to total lung volume, TLV) measured from computed tomography images acquired during end-inspiratory breath hold at baseline, 6 h and 24 h of low tidal volume mechanical ventilation and mild endotoxemia. Data are mean±SD. [†] difference between groups at specific time point and (xx) difference to xx time point in the same group.

		Baseline	6 hours	24 hours	ANOVA
Total Lung mass	Prone	$340\pm51^{(6)}$	315 ± 37	320 ± 37	time p=0.009
(g)	Supine	$406\pm53^{(6)}$	390 ± 60	410 ± 74	group p=0.026
					group:time p=0.188
Air volume	Prone	$701\pm113^{(24)}$	602 ± 78	581 ± 53	time p=0.002
(mL)	Supine	$744\pm127^{(24)}$	691 ± 164	596 ± 110	group p=0.376
					group:time p=0.514
Hyperaerated	Prone	0.11 ± 0.07	0.11 ± 0.08	0.14 ± 0.11	time p=0.003
(%TLV)	Supine	$0.41\pm0.18^{(24)}$	$0.82\pm0.47^{(24),†}$	$1.4\pm0.78^{†}$	group p=0.001
					group:time p=0.006
Normally aerated	Prone	90 ± 1	88 ± 2	86 ± 1	time p<0.001
(%TLV)	Supine	$82\pm3^{(24)}$	$77\pm8^{(24)}$	69 ± 2	group p<0.001
					group:time p=0.013
Poorly aerated	Prone	10 ± 1	12 ± 2	13 ± 2	time p=0.099
(%TLV)	Supine	17 ± 3	20 ± 7	21 ± 4	group p<0.001
					group:time p=0.935
Nonaerated	Prone	0 ± 0	0 ± 0	0 ± 0	time p<0.001
(%TLV)	Supine	$0.5\pm0.6^{(24)}$	$2\pm3^{(24)}$	$8\pm3^{†}$	group p<0.001
					group:time p<0.001

Table A.9: Total lung mass, air volume and aeration compartments (relative to total lung volume, TLV) measured from computed tomography images acquired during end-expiratory breath hold in two septic patients with early ARDS.

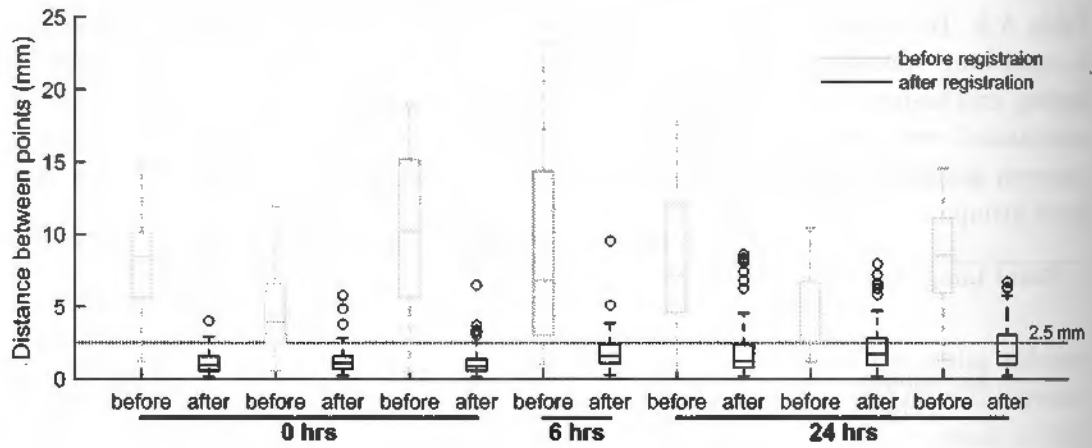|		Expiratory CT	Inspiratory CT
Total Lung mass	Patient 1	1115	1036
(g)	Patient 2	2502	2169
Air volume	Patient 1	1474	1895
(mL)	Patient 2	1843	2446
Hyperaerated	Patient 1	8.6	14
(%TLV)	Patient 2	1.3	4.2
Normally aerated	Patient 1	59	63
(%TLV)	Patient 2	49	60
Poorly aerated	Patient 1	17	12
(%TLV)	Patient 2	21	15
Nonaerated	Patient 1	15	11
(%TLV)	Patient 2	29	21

149

A.4 Additional figures

Figure A.2: Evaluation of image registration anatomical accuracy using paired landmarks. Landmarks were automatically defined in the expiratory image and semi-automatically matched in the inspiratory image by one observer. For comparison, the distance between paired landmarks were shown as boxplots before (grey) and after image registration (black). Data correspond to randomly selected supine (n=2) and prone (n=1) sheep at the beginning and end of the experiment. These time points were chosen because in the supine position they represent the extremes in aeration and atelectasis. The measurement at 6 h (supine sheep) corresponds to the largest gas volume difference between inspiratory and expiratory images. An average of 98.5 points [range 74-122] were used for each animal-time point combinations Dotted line represents the largest dimension of image voxel 2.5 mm.
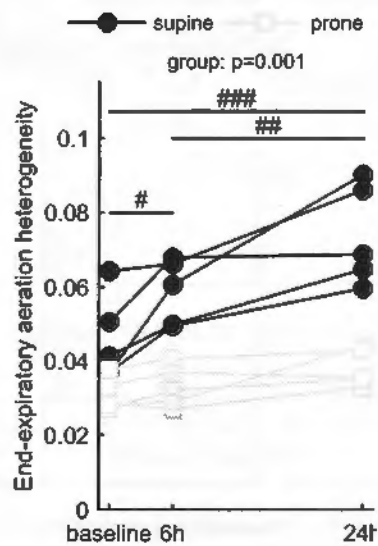
Figure A.3: Heterogeneity of aeration without contriubution of the vertical gradient. Heterogeneity was measured as the variance normalized by the squared mean in an image filtered to in plane resolution of 2.5 mm. The vertical gradient was estimated by a linear regression of voxel aeration versus height. Heterogeneity increased significantly only in the initially more heterogeneous supine position. Group effect is indicated in the figure. # represents comparison among time points, # $p<0.05$, ## $p<0.01$ and ### $p<0.001$. Prone animals had no difference between time points. Gray squares = prone; black circles = supine. All data refer to the whole lung.
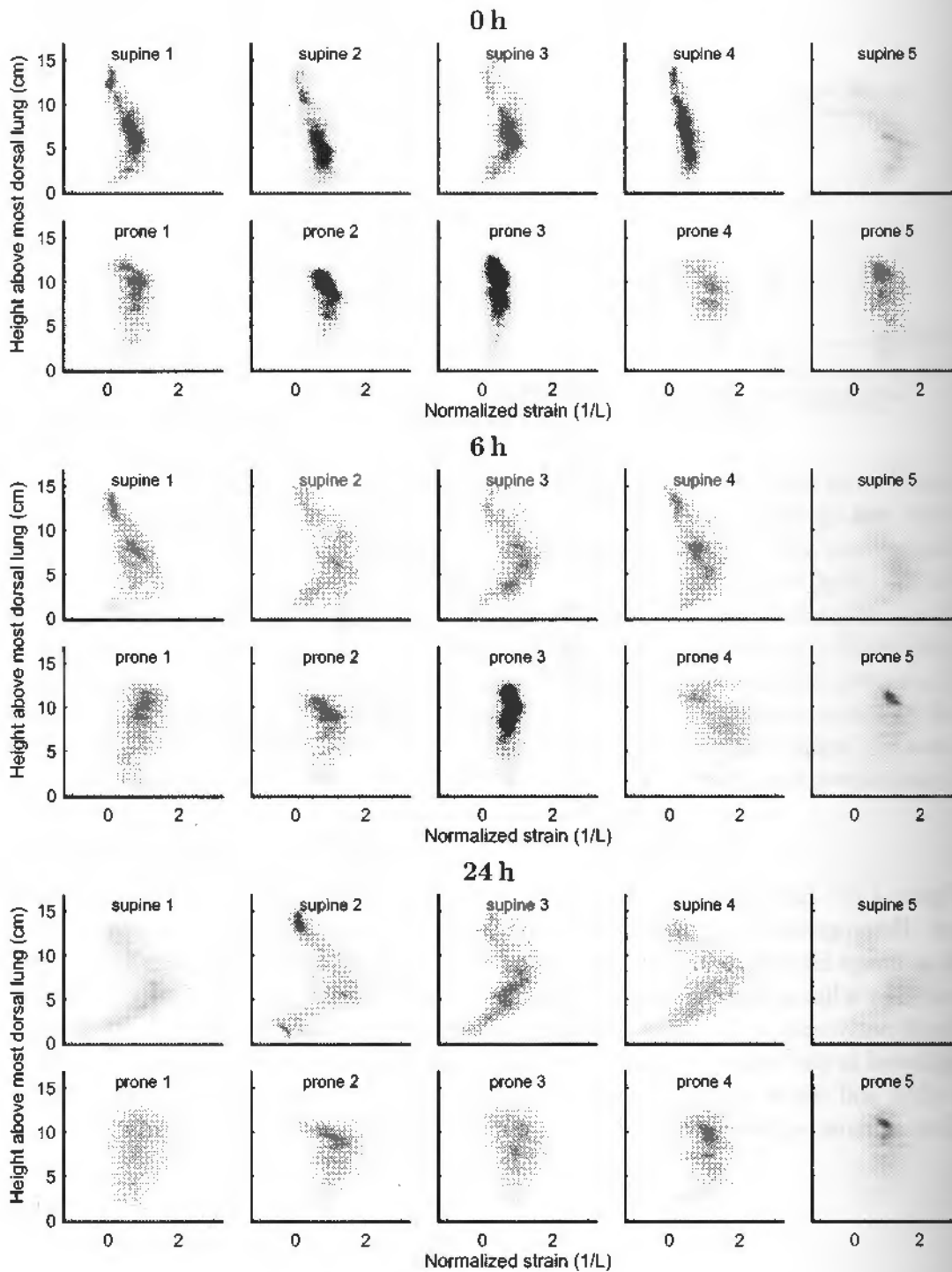
Figure A.4: Normalized strain spatial distribution along the ventro-dorsal axis. Each panel represents one animal at one time point. The grey scale represents the frequency of a given strain at each height and is the same in all panels. Note that the supine animals had a progressively more heterogeneous distribution of strain between ventral and dorsal regions. All animals show variability of strain for regions with the same height.
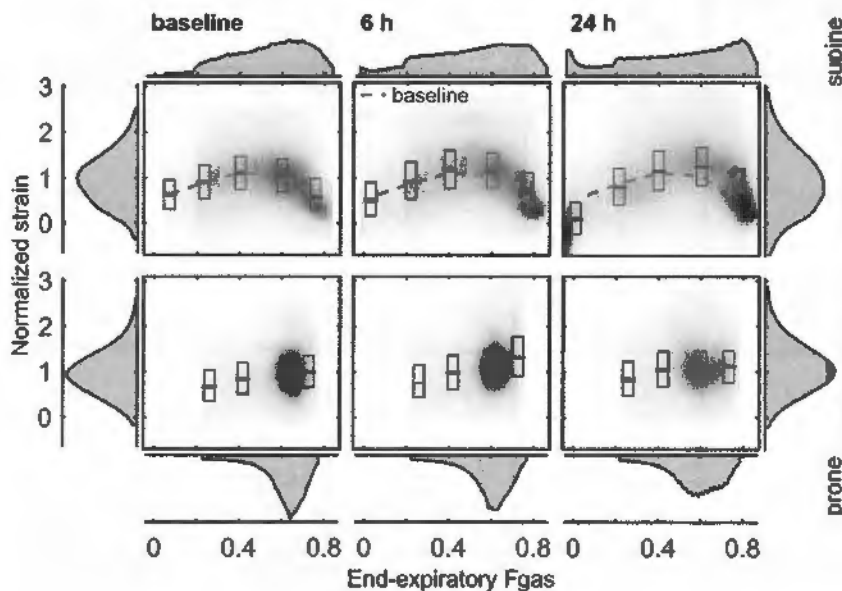
Figure A.5: Relationship of normalized strain and end-expiratory aeration (fraction of gas, F_{GAS}) at the voxel level at baseline and after 6 h and 24 h of low tidal volume mechanical ventilation and mild endotoxemia. Data is relative to all animals in supine (upper panels) and prone (lower panels). The boxes represent median and interquartile range of strains for voxels in the aeration intervals: ¡0.1; 0.1 to 0.3; 0.3 to 0.5; 0.5 to 0.7; and 0.7 to 0.9, centered in mean aeration within ranges. Voxels between the 5th and 95th strain percentiles are depicted in a two-dimensional histogram, with the gray scale representing the fraction of total lung volume (black is highest). Color scale is the same within groups. In the supine group (upper panels), strain increased with aeration until approximately 0.5, then decreased again. This pattern is consistent across time points, although compared to baseline (green dashed line) at 24 h median strain is lower in low aeration and higher in the high end. The decrease in grayscale for prone (lower panels) at 24 h indicate a slight spread of the distribution

153
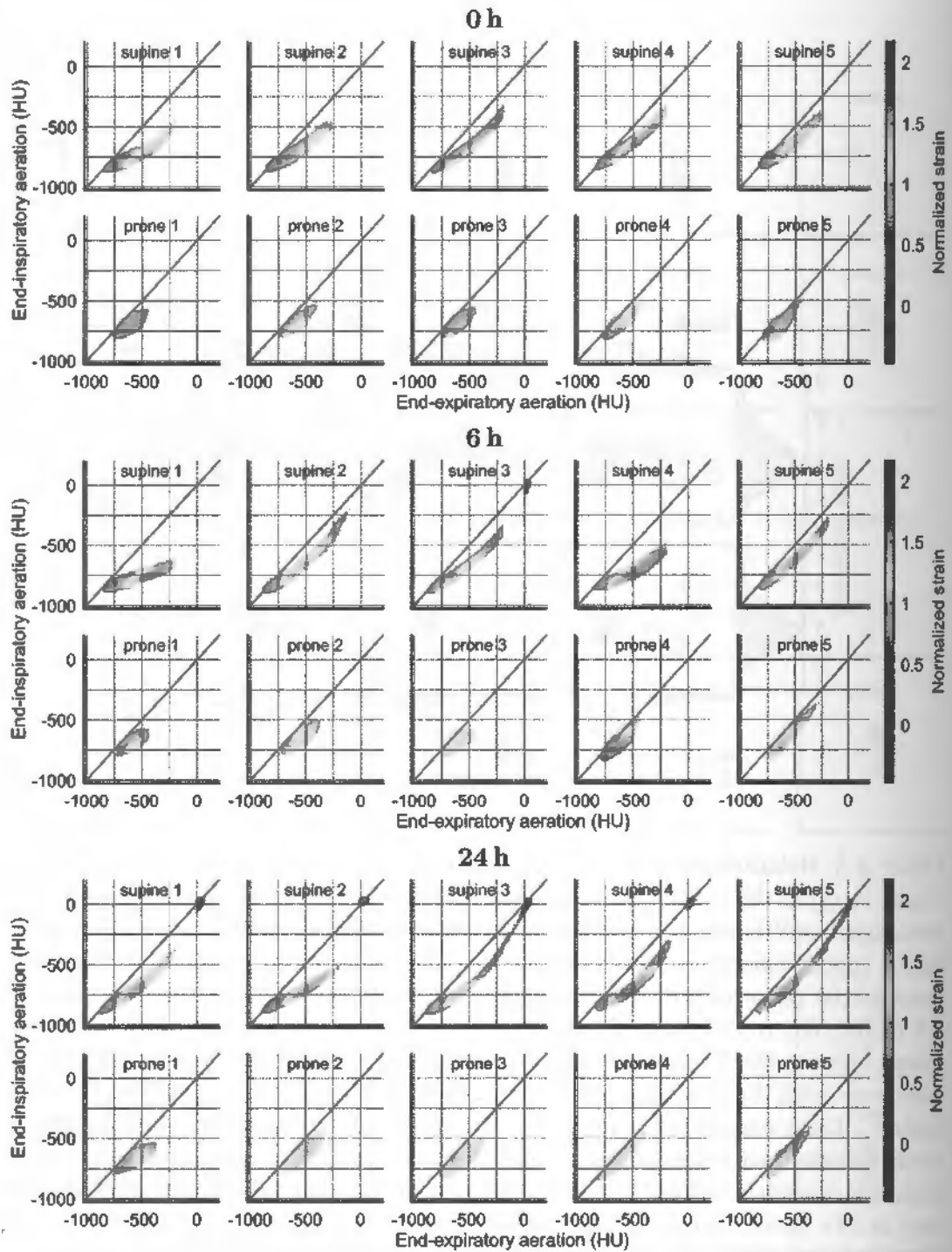
Figure A.6: Parametric response maps of each animal at each time point representing end-expiratory and end-inspiratory density, and average normalized strain (color scale) in a grid of 100 bins between −1024 HU and −200 HU. The red line is identity. End-inspiratory image was transformed to the end-expiratory reference using the same transformation computed with elastic image registration for strain analysis. Note that the supine animals had the largest dispersion in aeration and showed a concave relationship between inspiratory and expiratory aeration. This shape indicates that areas of normal aeration had the largest changes in density, which coincided with the regions of relative high strain. All data refer to the whole lung, but only bins corresponding to 0.05 % of the lung are represented.

154
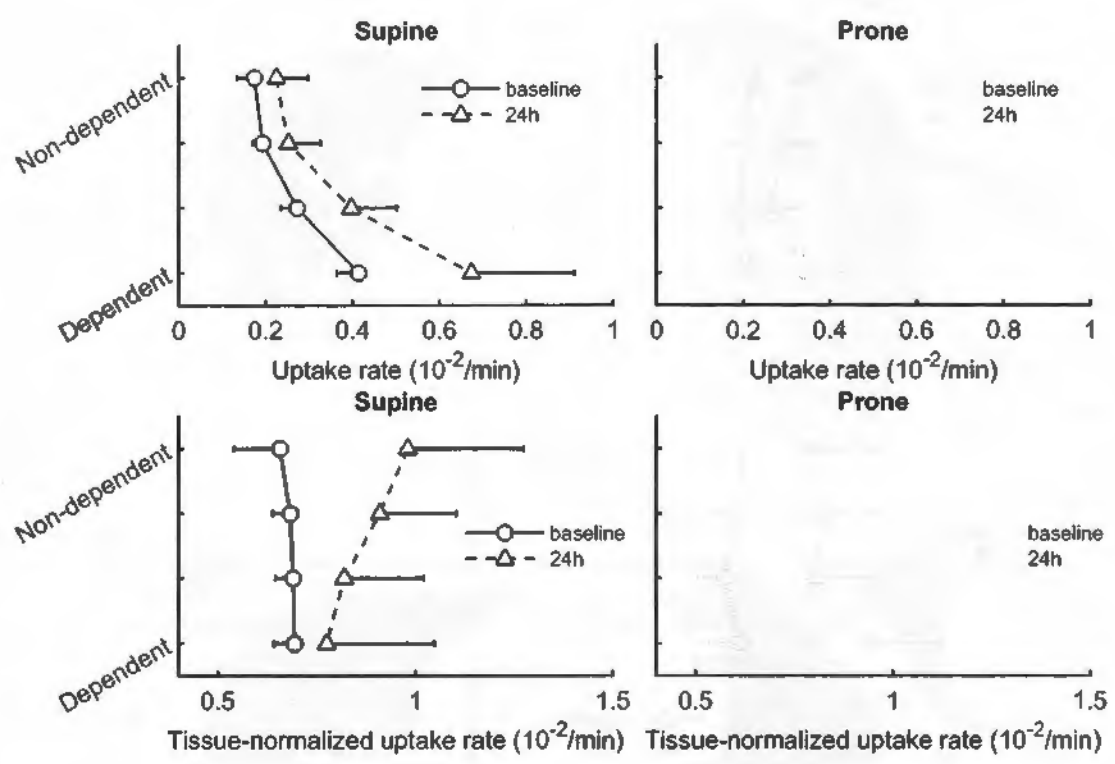
Figure A.7: ^{18}F-FDG uptake rate in 4 isogravitational regions-of-interest at baseline and after 24 h of mild endotoxemia and mechanical ventilation. Sheep were mechanically ventilated with low tidal volume and positive end-expiratory pressure according to the ARDSNet protocol. ^{18}F-FDG kinetics was modeled by a Sokoloff model including a time delay from the heart to each region-of-interest. In this compartmental model uptake rate is the product of phosphorylation rate (k_3) and the ^{18}F-FDG volume of distribution (F_e). Tissue-normalized uptake rate is the uptake rate divided by the tissue content of a region-of-interest (1-gas fraction-blood fraction). Both supine and prone animals had an increase in uptake after 24 h, with supine showing an increase in regional differences beyond aeration.
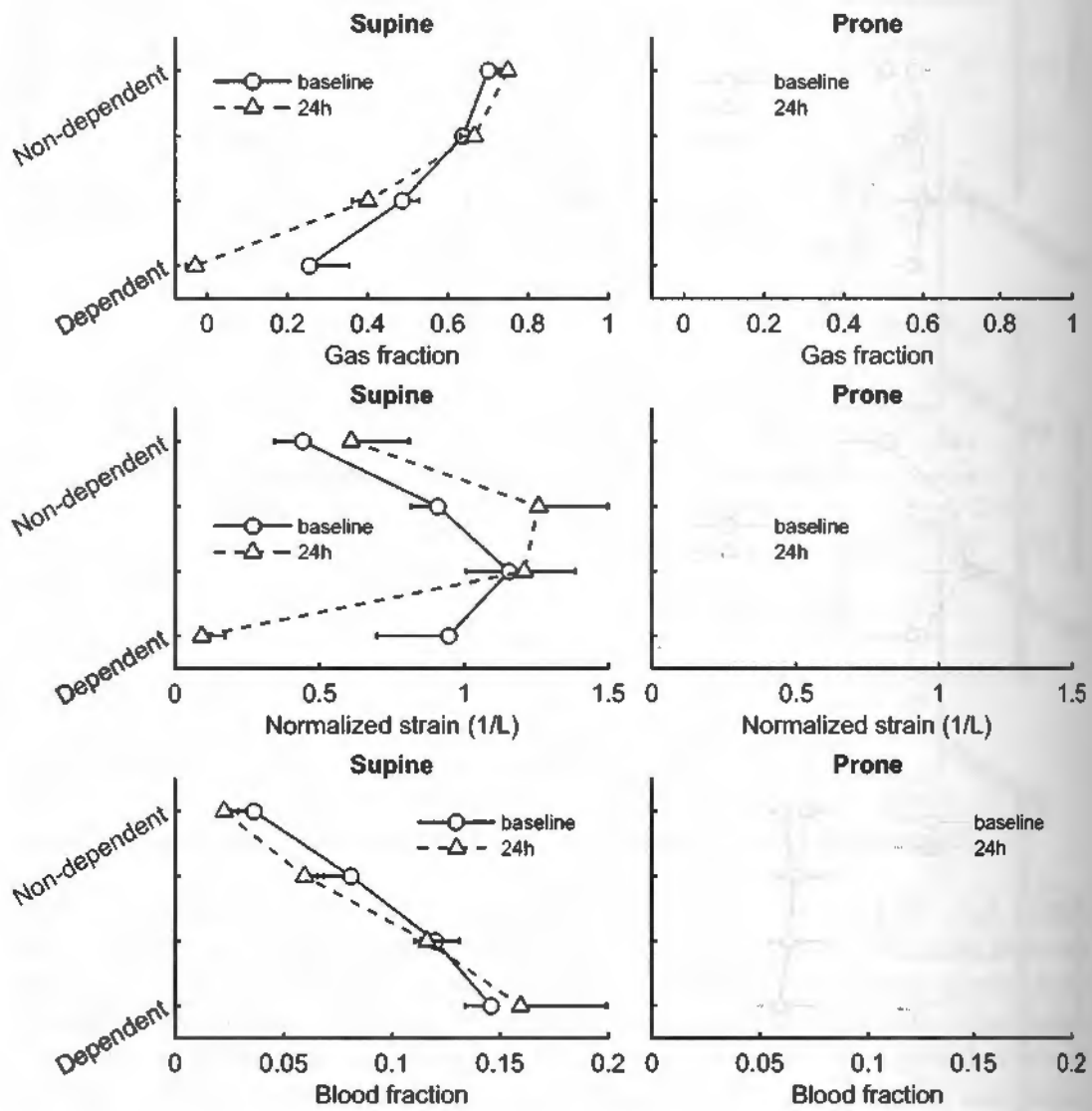
Figure A.8: Fraction of gas at mean lung volume, normalized strain and fraction of blood in 4 isogravitational regions-of-interest at baseline and after 24 h of mild endotoxemia and mechanical ventilation. For each animal strain is the mean of voxel level strain obtained with image registration. Blood fraction derived from ^{18}F-FDG kinetics. Note that prone animals showed a more homogeneous spatial distribution of all three variables.
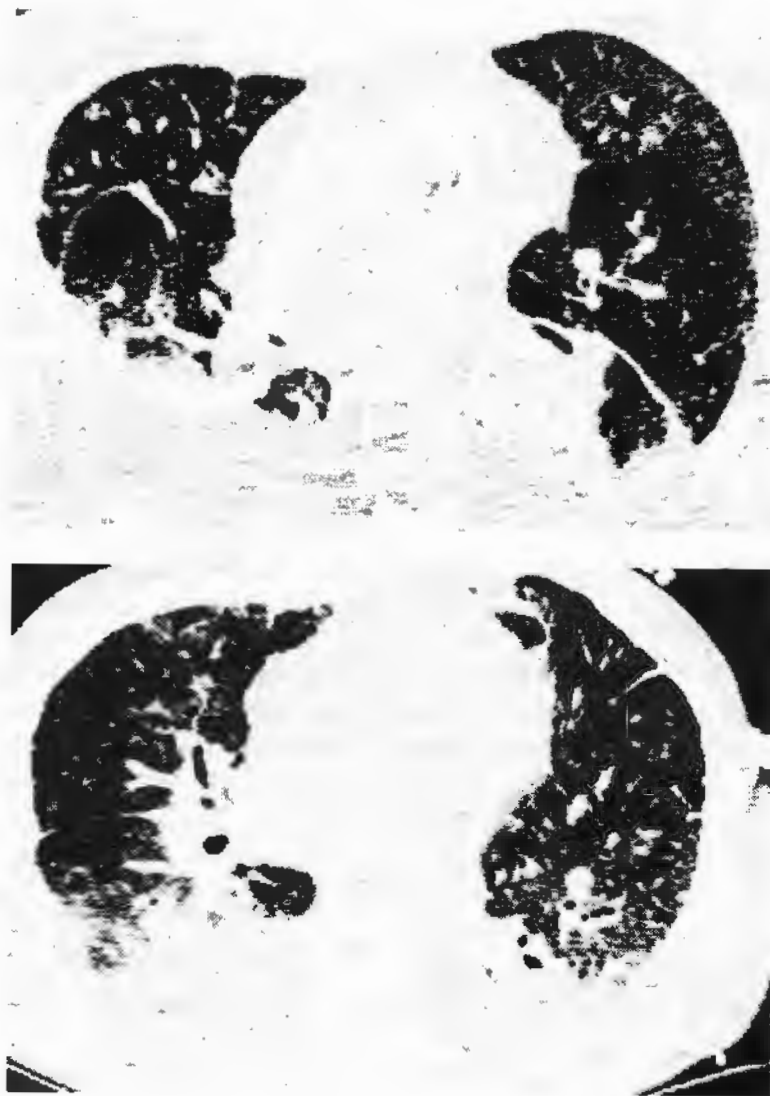
Figure A.9: Example of computed tomography slices at end-expiration in patient 1
(left) and patient 2 (right).

Appendix B

Supplementary Data for Chapter 4

Table B.1: Complementary significant pathways amongst the genes that were correlated to the tissue-specific ^{18}F-FDG volume of distribution and the tissue fraction. A pathway was considered significant if at least two of its' genes were on the analyzed list and had a EASE<0.1.

Parameter	Group	Specific pathways
Tissue-specific volume of distribution (F_{es})	Diseases	Alzheimer's disease, Huntington's disease, Salmonella infection, Pertussis, Legionellosis, Leishmaniasis, Chagas' disease, African trypanosomiasis, Malaria, Toxoplasmosis, Amoebiasis, Tuberculosis, Hepatitis B, Measles, Influenza A, HTLV-1 infection, Herpes simplex infection, Proteoglycans cancer, Asthma, Inflammatory bowel disease, Rheumatoid arthritis, Allograft rejection, Graft-versus-host disease, Type I diabetes mellitus, Non-alcoholic fatty liver disease
	Other systems	Prolactin signaling, Osteoclast differentiation
Tissue fraction (F_{TIS})	Diseases	Salmonella infection, Pertussis, Leishmaniasis, Chagas' disease, Influenza A, Pathways in cancer
	Nervous system	Long-term depression

B.1 Simulated example of length-scales

As a visual support of the concept of length-scale and the low-pass filtering analysis consider Fig. B.1 where the same global heterogeneity is represented with different black and white check board patterns. The different sizes for the squares (5, 15 and 30 units) are presented with the respective relative contributions of length-scales from 5 mm to 35 mm.
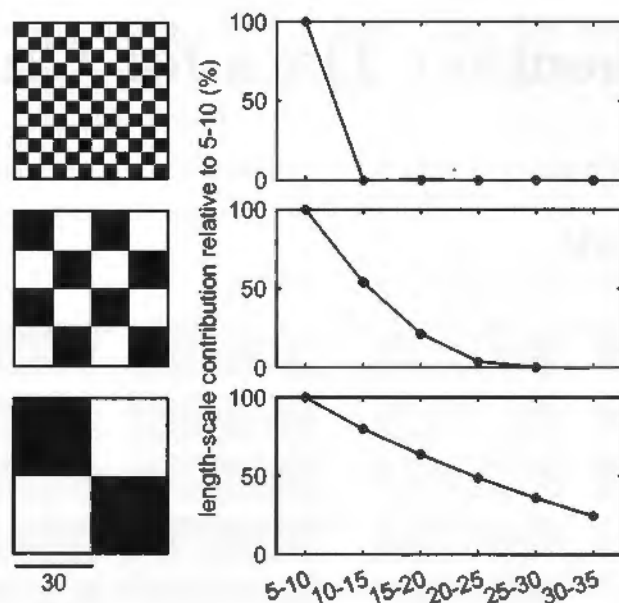

Figure B.1: Example of length-scale analysis with the multiple low-pass filter technique applied to check board patterns. All check boards have the same dimensions and total heterogeneity with size of white and black squares increasing from top to bottom.

Appendix C

Supplementary Data for Chapter 5

C.1 Methods

The algorithm to estimate the distribution of ventilation is summarized as follows:

Input

- N alveolar units log distributed on S(J);
- $F_{N_2}^{et}$, V_T^I, V_T^E, v_d and $F_{N_2}^I$ at each breath cycle;
- Reference volume V_{T0} and the EELV at the onset of washout.

Steps

1. Initialize alveolar units and v_d N_2 concentration with the $F_{N_2}^{et}$ measured at baseline.

2. For each breath cycle, calculate each alveolar unit's N_2 concentration using Eq. (5.8).

3. Generate a matrix with rows being breath cycles and columns alveolar units' concentration corrected to the EELV change, like in Eq. (5.10).

4. The ventilation fractions vector (γ) is estimated solving the least square problem in Eq. (5.11), with (or not) the desired constraints (nonnegativity, unitary sum of ventilation fractions and sum of alveolar units' volumes equal to EELV-v_d).

Output

- $\gamma(J)$ for each alveolar unit with respect to a reference tidal volume V_{T0} and the EELV at the onset of washout.

C.2 Results

Figures C.1 to C.4 show the color-coded standard deviation (SD) values of the sum of squared errors (SSE) and the SD from the difference between estimated and reference first three moments (mean, SD and skewness) as a supplementary information to Figs. 5.5 to 5.8.

The SD of the SSE values depicted in Fig. C.1 shows that the use of a weighting matrix (WM) has a stabilizing effect on the solutions. The presence of noise generates fast compartments near the limit of the specific ventilation (S) distribution, which are penalized by the WM. As in Fig. 5.5, the smallest SD were obtained with WM and fixed Tikhonov gain (λ) (upper right panel), with minimum effects of using constraints and changing the number of cycles.
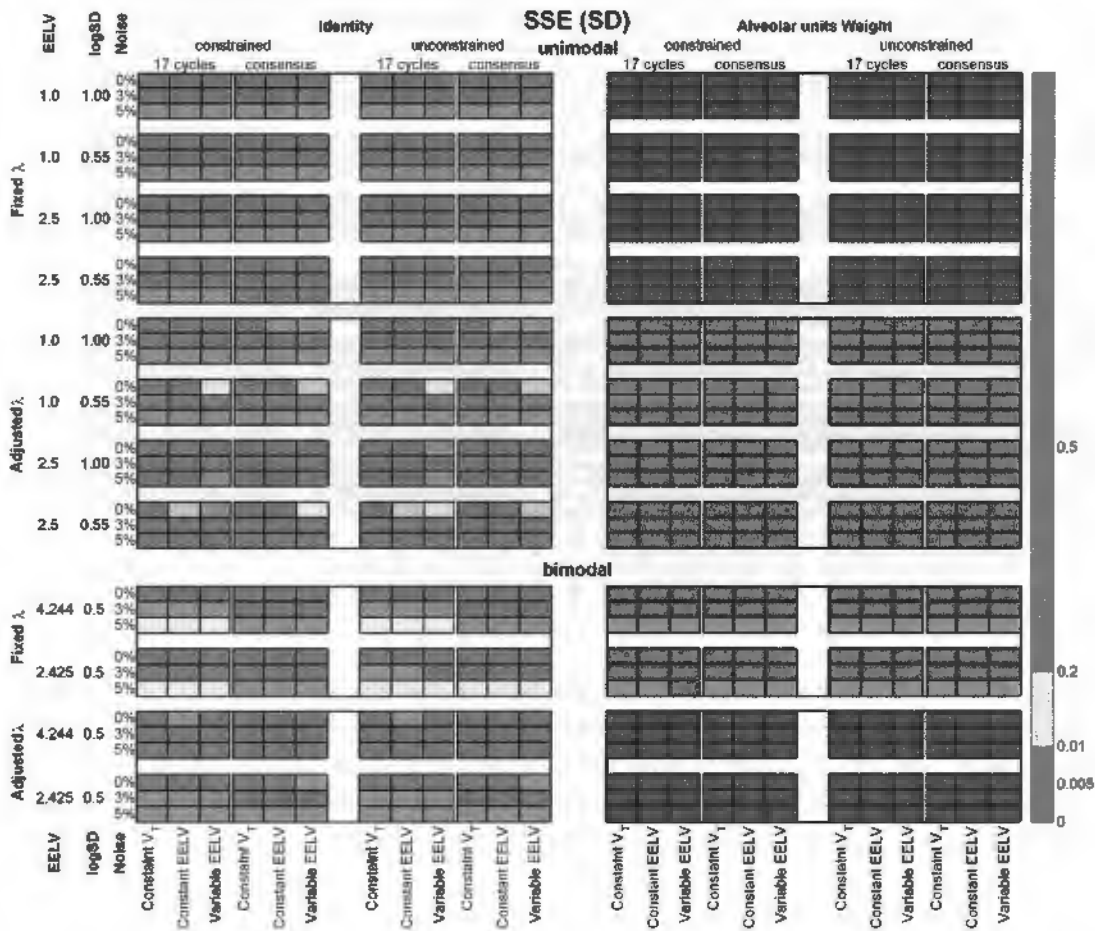
Figure C.1: Standard deviation (SD) of sum of squared errors (SSE) between estimated and reference unimodal and bimodal distributions. All simulation and recovery conditions are depicted and indicated (lines and rows of the matrices). Colors coded on the right side of the figure indicate intervals of values of the SD of SSE; EELV=End-expiratory Lung Volume; V_T = Tidal Volume

Figure C.2 presents the SD of the differences between absolute means of estimated and reference unimodal and bimodal distributions. Note the similarity with Fig. 5.6. The most varying solutions are coincident with higher mean differences. Again the best solution was reached with fixed λ and WM. For bimodal distributions, the use of adjusted λ presents a small advantage.
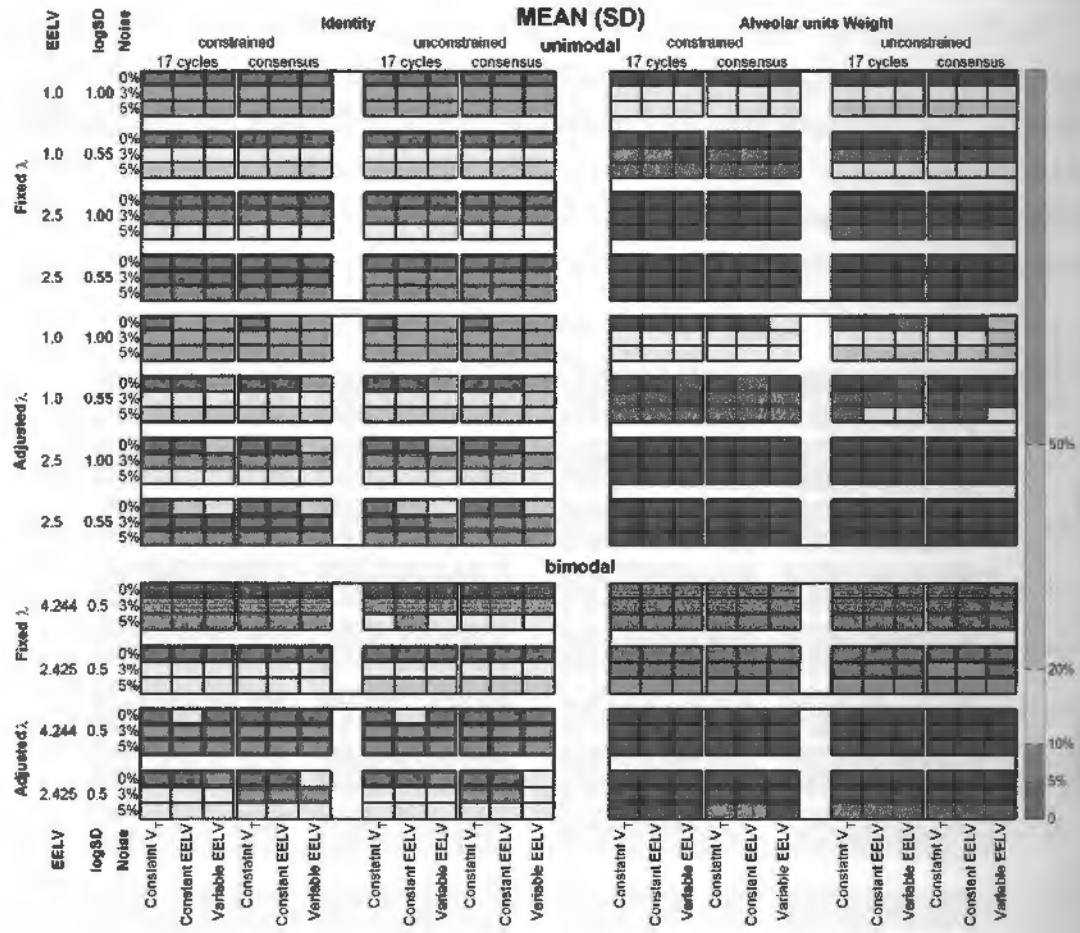

Figure C.2: Standard deviation (SD) of absolute values of the relative differences between means of estimated and reference unimodal and bimodal distributions. All simulations and recovery conditions are depicted and indicated (lines and rows of the matrices). Colors coded on the right side indicate intervals of the SD value. EELV=End-expiratory Lung Volume; V_T = Tidal Volume

As for the mean values of the differences between estimated and reference logSD (Fig. 5.7), their SD are higher when Tikhonov is applied using an identity matrix (see Fig. C.3). Note that in presence of noise, the use of an adjusted λ leads to less varying solution for both uni- and bimodal distributions. In these cases λ becomes higher, imposing a smoother solution.
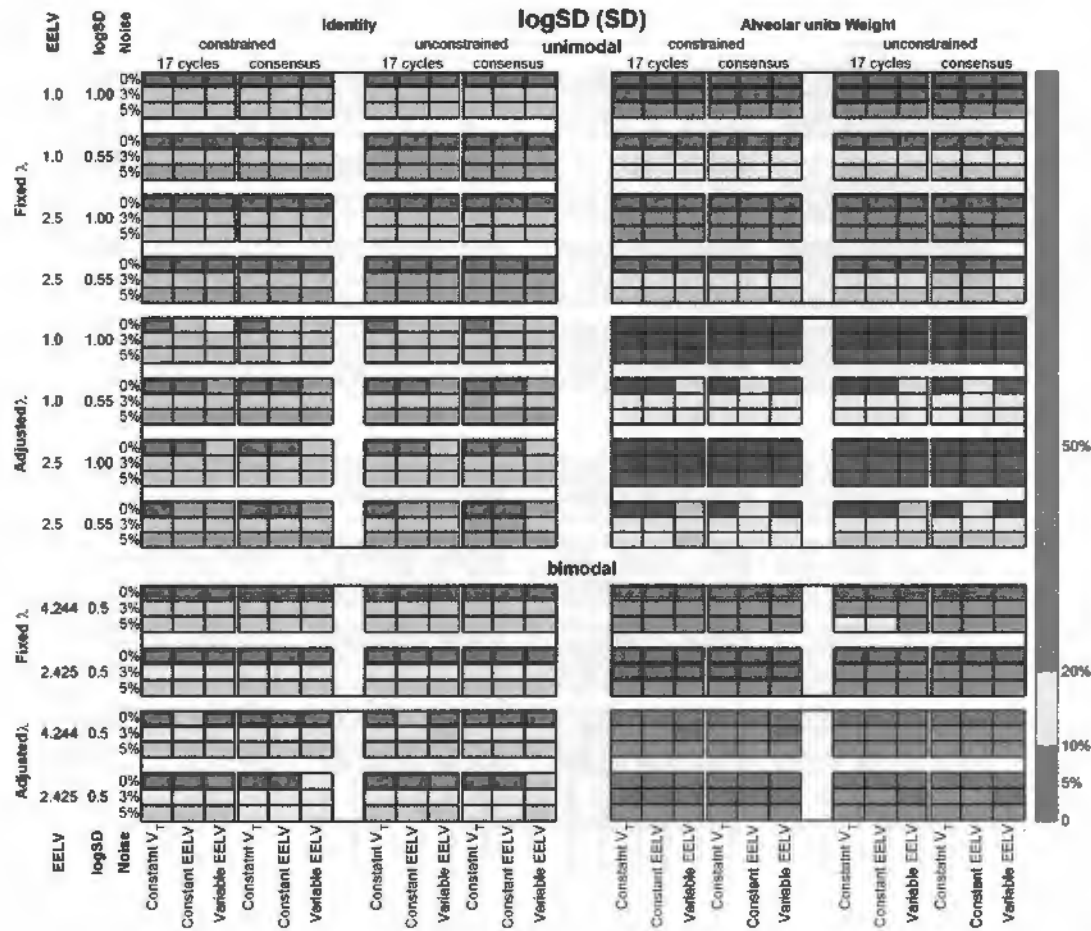

Figure C.3: Standard deviation (SD) of absolute values of the relative differences between logSD of estimated and reference unimodal and bimodal distributions. All simulation and recovery conditions are depicted and indicated (lines and rows of the matrices). Colors coded on the right side of the figure indicate intervals of the SD values. EELV=End-expiratory Lung Volume; V_T = Tidal Volume.

For unimodal distributions, similar to the first two moments, the SD of the difference between estimated and reference skewness are higher for the solutions without the WM (Fig. C.4). Once more, the smoothed solutions with adjusted λ leads to a less varying skewness estimation. However, the use of a fixed λ gives better error-free solutions and appears to be the best choice.
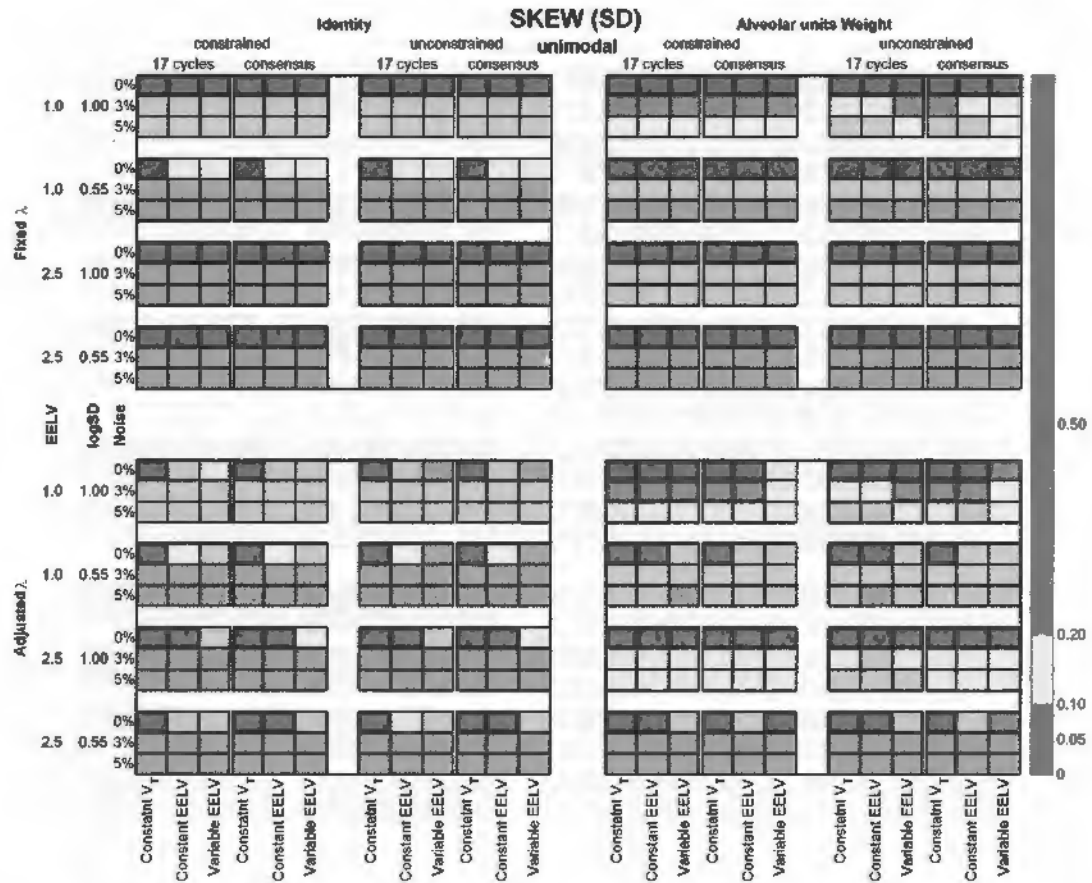

Figure C.4: Standard deviation (SD) of the differences between skewness of estimated and reference unimodal distributions. All simulation and recovery conditions are depicted and indicated (lines and rows of the matrices). Colors coded on the right side indicate intervals of the SD values. EELV=End-expiratory Lung Volume; V_T = Tidal Volume.

Appendix D

Supplementary Data for Chapter 6

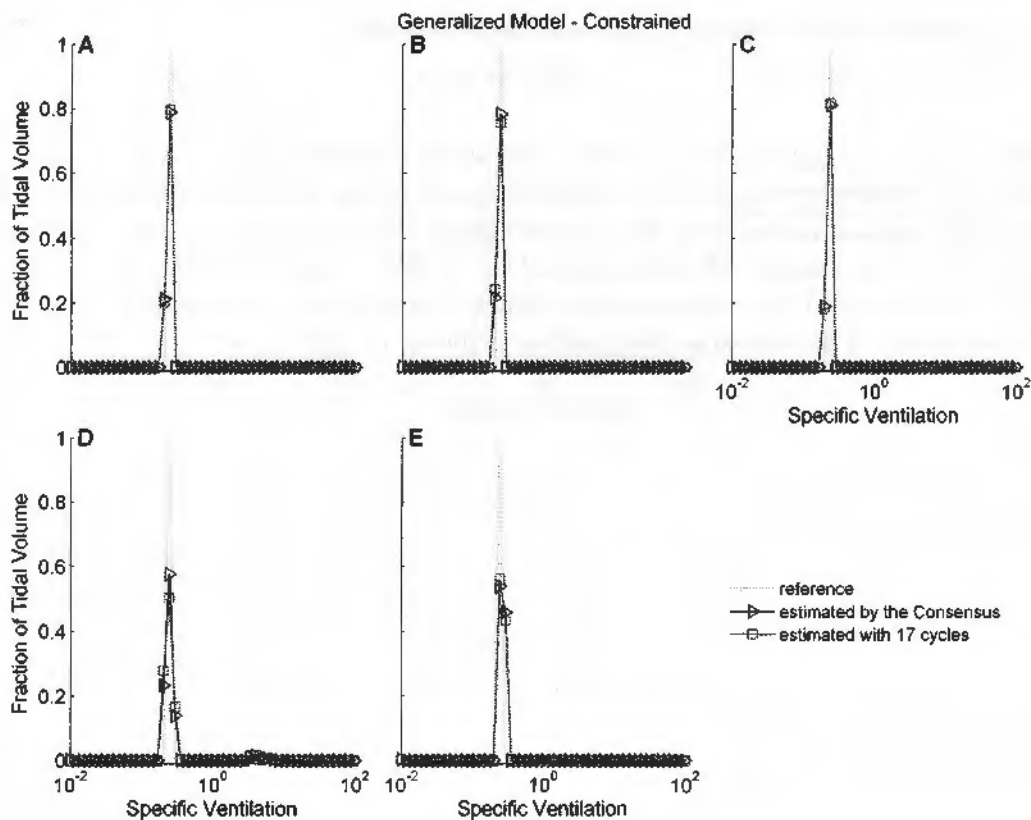## D.1 Individual results for the single-compartment model (1C)

Figure D.1: Distribution of specific ventilation estimated from each of five N_2 washouts of a single-compartment physical model using the constrained generalized mathematical model with 50 compartments. The distributions were estimated using either the number of cycles according to the Consensus [70], that is, until $1/40^{th}$ of the initial N_2 concentration (black triangles) or alternatively 17 cycles (gray squares). The reference distribution is shown in light gray.
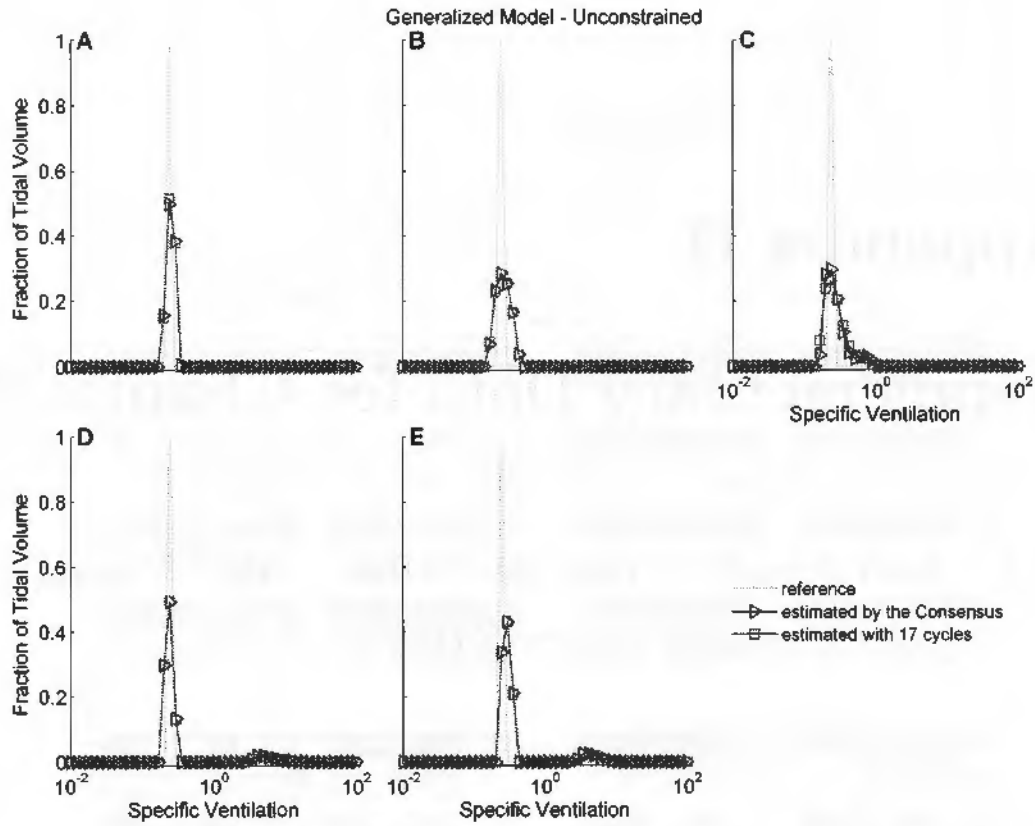
Figure D.2: Distribution of specific ventilation estimated from each of five N_2 washouts of a single-compartment physical model using the unconstrained generalized mathematical model with 50 compartments. The distributions were estimated using either the number of cycles according to the Consensus [70], that is, until $1/40^{th}$ of the initial N_2 concentration (black triangles) or alternatively 17 cycles (gray squares). The reference distribution is shown in light gray.
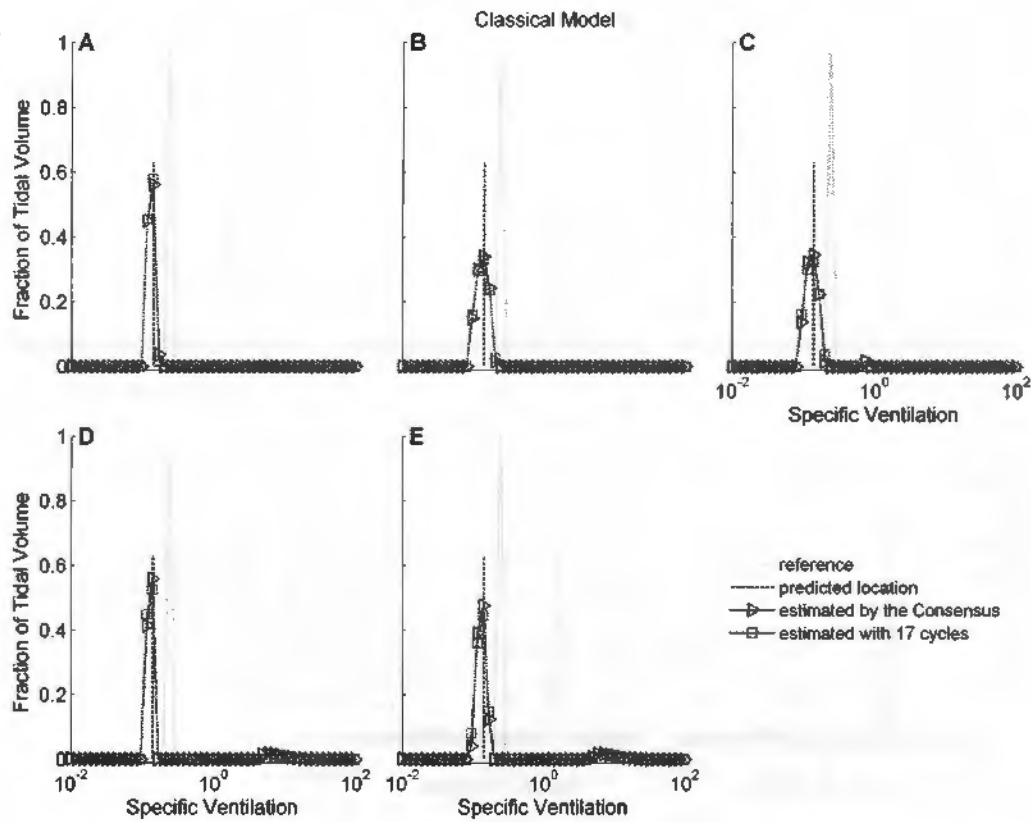
Figure D.3: Distribution of specific ventilation estimated from each of five N_2 washouts of a single-compartment physical model using the classical all parallel mathematical model with 50 compartments. The distributions were estimated using either the number of cycles according to the Consensus [70], that is, until $1/40^{th}$ of the initial N_2 concentration (black triangles) or alternatively 17 cycles (gray squares). The reference distribution is shown in light gray. The dashed vertical line represents the theoretical prediction for the compartment estimated with the classical model if there is a series dead space in the actual system.
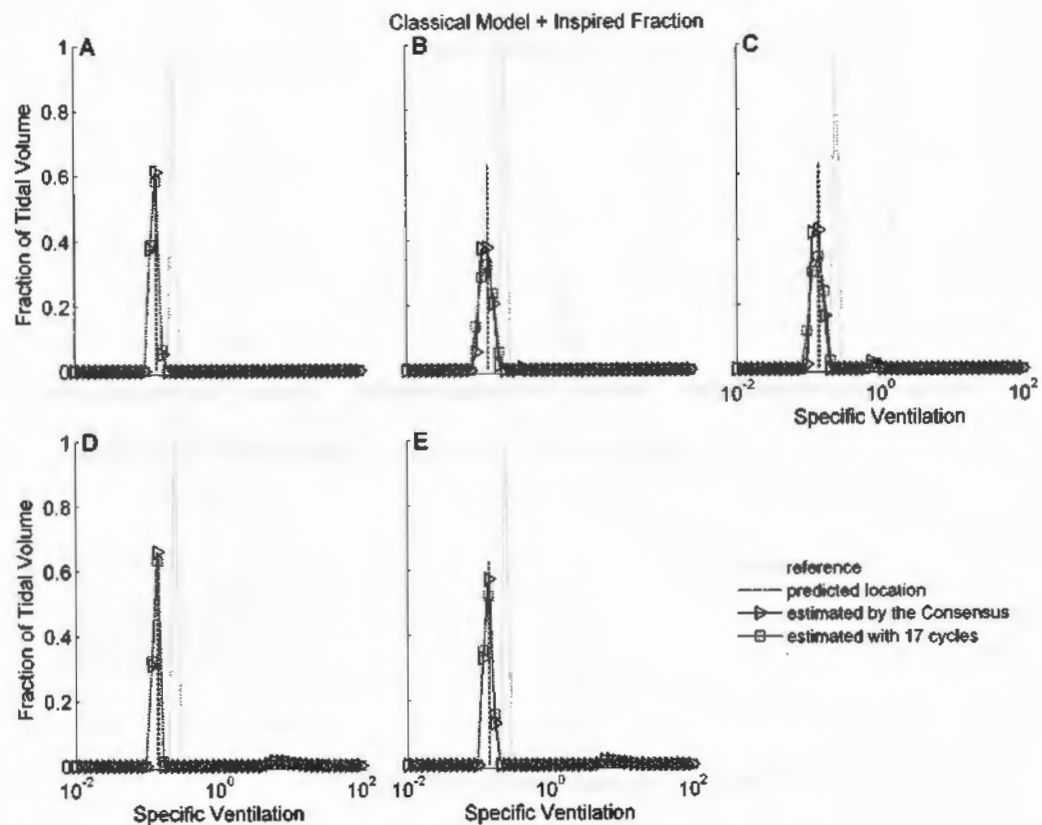
Figure D.4: Distribution of specific ventilation estimated from each of five N_2 washouts of a single-compartment physical model using the classical all parallel mathematical model with 50 compartments, and considering the measurements of the inspired N_2 concentration. The distributions were estimated using either the number of cycles according to the Consensus [70], that is, until $1/40^{\text{th}}$ of the initial N_2 concentration (black triangles) or alternatively 17 cycles (gray squares). The reference distribution is shown in light gray. The dashed vertical line represents the theoretical prediction for the compartment estimated with the classical model if there is a series dead space in the actual system.

Table D.1: End expiratory volume, total ventilation and dead space for each washout model in all five experiments with the single-compartment physical model. End expiratory volume is the sum of the estimated compartmental volumes; total ventilation is the sum of the estimated compartmental fractions of ventilation (unitary, in the constrained case); and dead space is estimated from the capnograms using Fowler's method (constrained and unconstrained cases) or from the complement to the total ventilation and the measured tidal volume (classical and classical + inspired fraction cases). Reference values are the expected from the geometry of the physical model.

| | | Experiments | | | | | Reference |
		A	B	C	D	E	
End expiratory volume (L)	Constrained	1.125	1.156	1.119	1.140	1.133	1.092
	Unconstrained	1.093	1.091	1.07	1.077	0.96	
	Classical	1.353	1.408	1.414	1.383	1.226	
	Classical + inspired fraction	1.314	1.322	1.333	1.291	1.182	
Total ventilation	Constrained	1.00	1.00	1.00	1.00	1.00	1.00
	Unconstrained	1.05	1.04	1.07	1.02	1.08	
	Classical	0.68	0.72	0.69	0.65	0.60	
	Classical + inspired fraction	0.67	0.72	0.68	0.65	0.60	
Dead space (mL)	Constrained	71	70	69	73	85	92
	Unconstrained	71	70	69	73	85	
	Classical	79	70	76	89	100	
	Classical + inspired fraction	80	70	78	89	101	

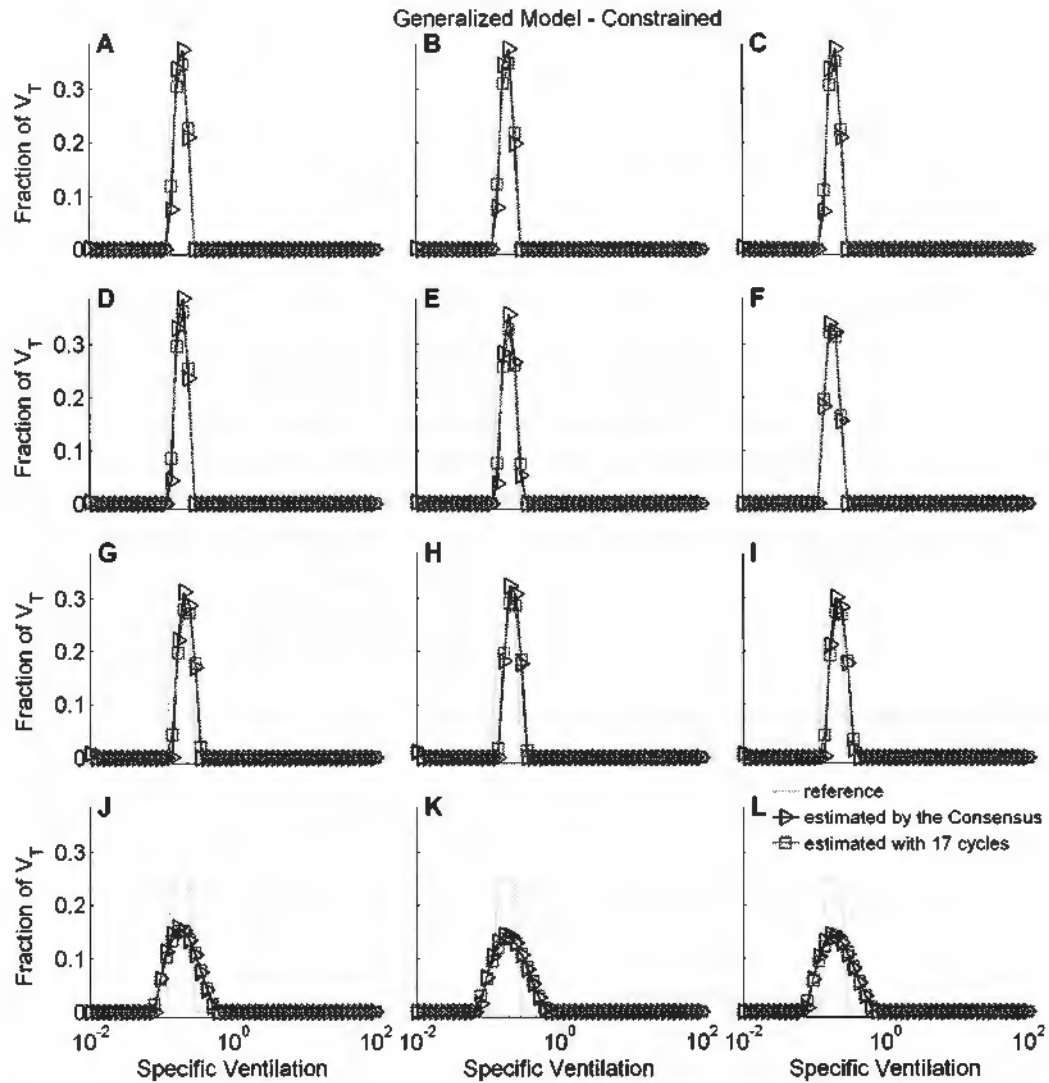# D.2 Individual results for the four-compartments model (4C)

Figure D.5: Distribution of specific ventilation estimated from each of twelve N_2 washouts of the four-compartment physical model using the constrained generalized mathematical model with 50 compartments. The distributions were estimated using either the number of cycles according to the Consensus [70], that is, until $1/40^{th}$ of the initial N_2 concentration (black triangles) or alternatively 17 cycles (gray squares). The reference distribution is shown in light gray.
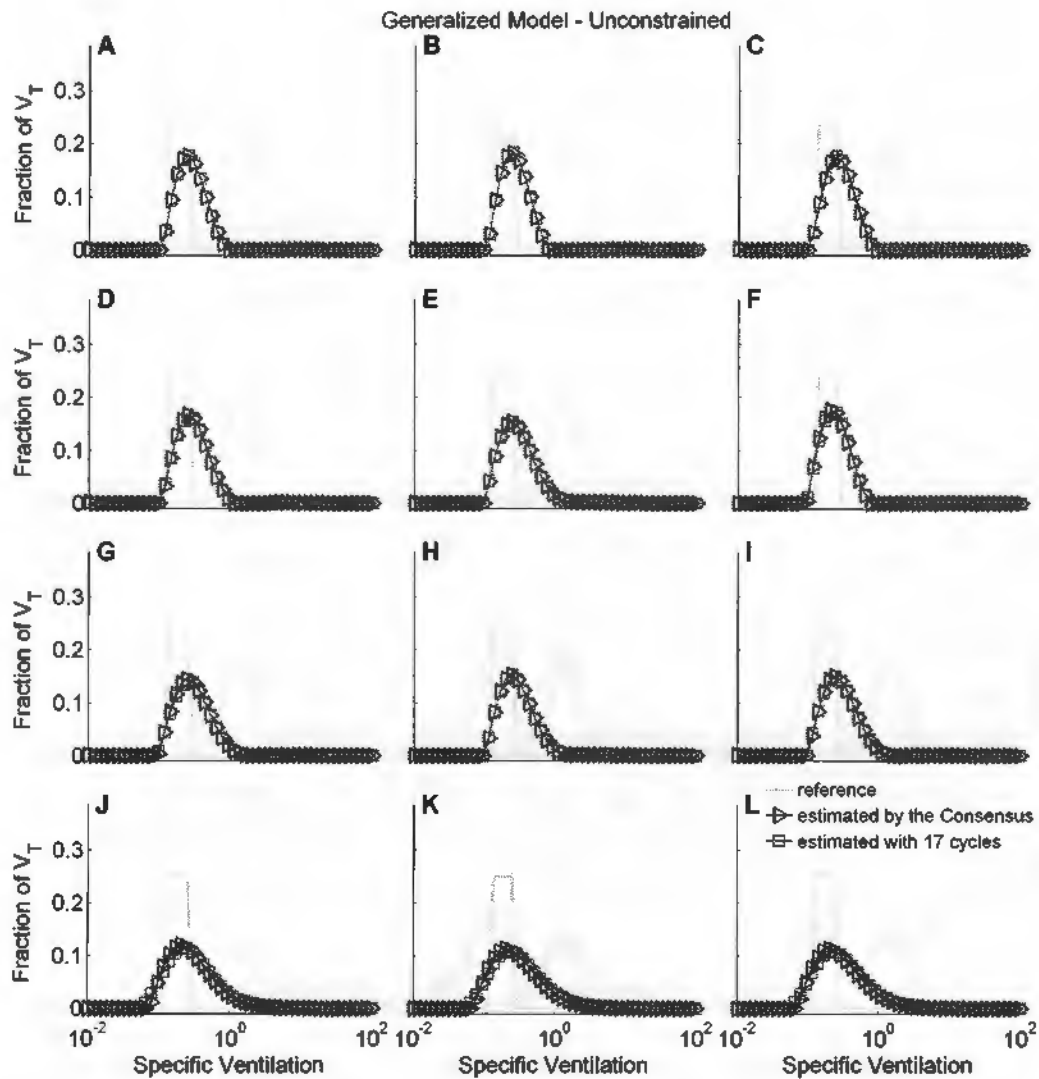
Figure D.6: Distribution of specific ventilation estimated from each of twelve N_2 washouts of the four-compartment physical model using the unconstrained generalized mathematical model with 50 compartments. The distributions were estimated using either the number of cycles according to the Consensus [70], that is, until $1/40^{th}$ of the initial N_2 concentration (black triangles) or alternatively 17 cycles (gray squares). The reference distribution is shown in light gray.
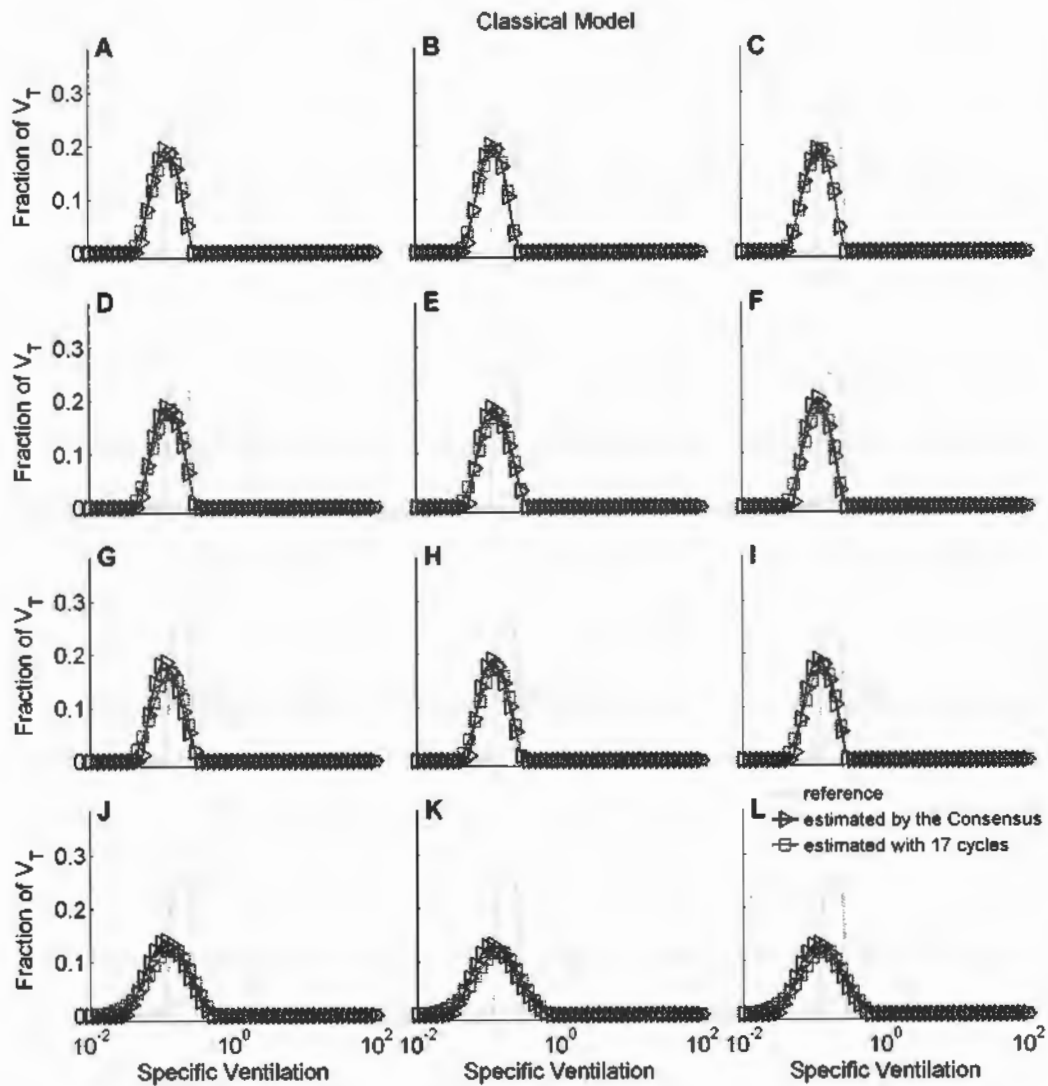
Figure D.7: Distribution of specific ventilation estimated from each of twelve N_2 washouts of the four-compartment physical model using the classical all-parallel mathematical model with 50 compartments. The distributions were estimated using either the number of cycles according to the Consensus [70], that is, until $1/40^{th}$ of the initial N_2 concentration (black triangles) or alternatively 17 cycles (gray squares). The reference distribution is shown in light gray.
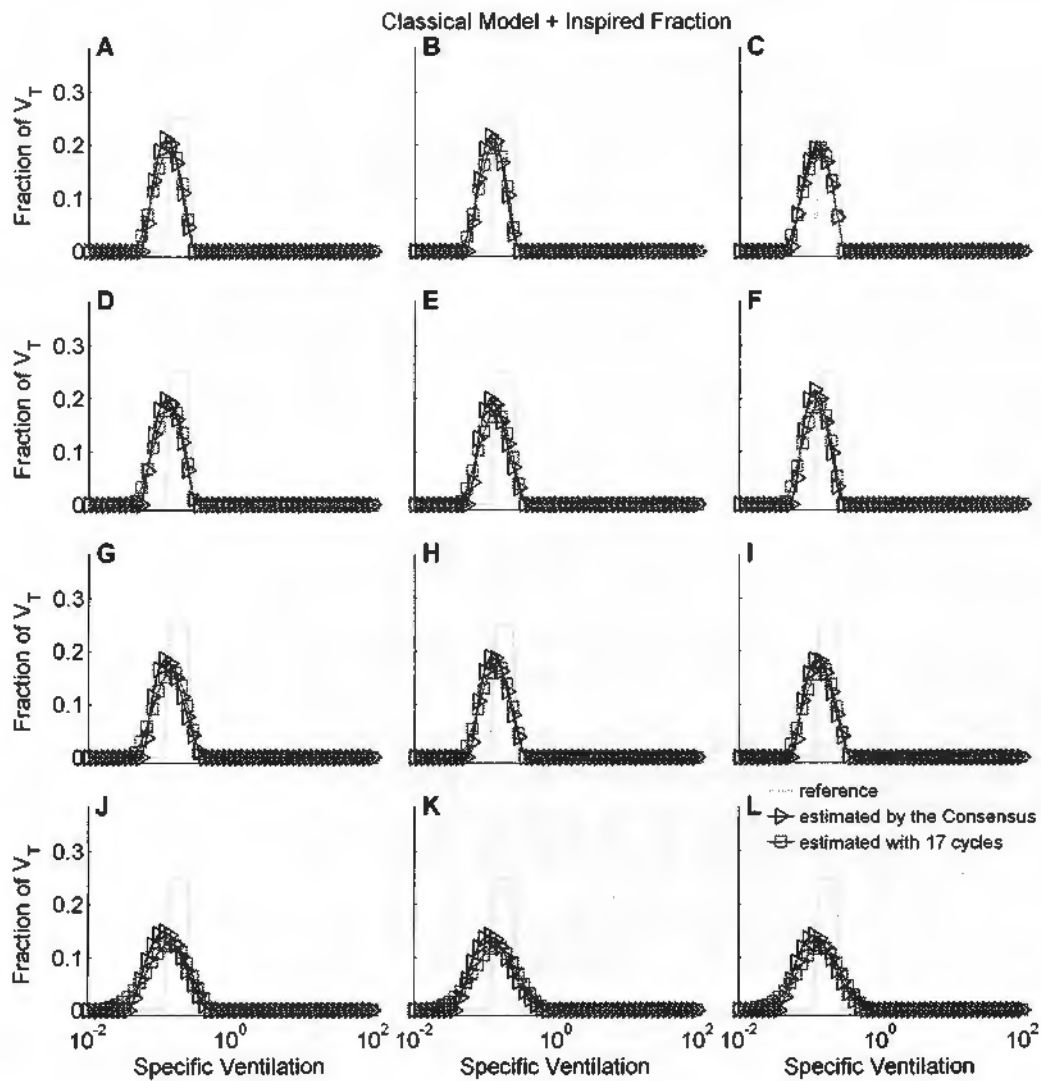
172

Figure D.8: Distribution of specific ventilation estimated from each of twelve N_2 washouts of the four-compartment physical model using the classical all-parallel mathematical model with 50 compartments, accounting for the measured inspired concentration of N_2. The distributions were estimated using either the number of cycles according to the Consensus [70], that is, until $1/40^{th}$ of the initial N_2 concentration (black triangles) or alternatively 17 cycles (gray squares). The reference distribution is shown in light gray.

Table D.2: End expiratory volume, total ventilation and dead space for each washout model in all twelve experiments with the four-compartment physical model. End expiratory volume is the sum of the estimated compartmental volumes; total ventilation is the sum of the estimated compartmental fraction of ventilation (unitary, in the constrained case); and dead space is estimated from the capnograms using Fowler's method (constrained and unconstrained cases) or from the complement to the total ventilation and the measured tidal volume (classical and classical + inspired fraction cases). Reference values are the expected from the geometry of the physical model.

174

| | | Experiments | | | | | | | | | | | | Reference |
		A	B	C	D	E	F	G	H	I	J	K	L	
End expiratory volume (L)	Constrained	3.268	3.269	3.321	3.254	3.113	3.249	3.208	3.350	3.150	3.295	3.260	3.202	
	Unconstrained	2.874	2.878	2.953	2.828	2.700	3.032	2.672	2.658	2.696	2.954	2.892	2.904	3.242
	Classical	3.644	3.627	3.689	3.606	3.499	3.568	3.639	3.660	3.592	4.257	4.074	4.044	
	Classical + inspired fraction	3.485	3.492	3.506	3.480	3.373	3.434	3.219	3.252	3.184	3.864	3.743	3.725	
Total ventilation	Constrained	1.00	1.00	1.00	1.00	1.00	1.00	1.00	1.00	1.00	1.00	1.00	1.00	
	Unconstrained	1.13	1.13	1.14	1.15	1.15	1.11	1.10	1.10	1.09	1.15	1.15	1.13	1.00
	Classical	0.75	0.72	0.74	0.74	0.74	0.70	0.74	0.76	0.74	0.79	0.76	0.74	
	Classical + inspired fraction	0.75	0.72	0.74	0.74	0.74	0.70	0.74	0.75	0.74	0.78	0.75	0.73	
Dead space (mL)	Constrained	185	187	186	189	185	172	188	186	186	188	188	188	
	Unconstrained	185	187	186	189	185	172	188	186	186	188	188	188	152
	Classical	137	152	142	144	142	166	145	137	146	115	134	146	
	Classical + inspired fraction	138	153	142	145	142	166	146	139	148	120	136	147	

D.3 Sensitivity to error in estimated series dead space (v_d)
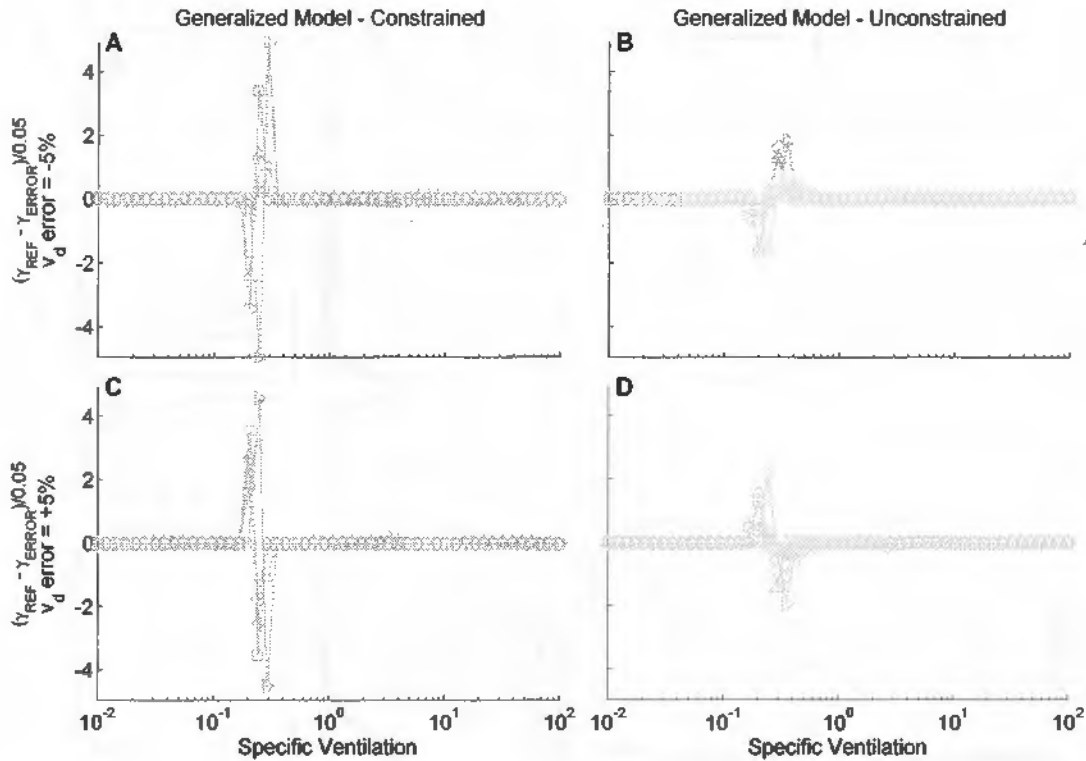

Figure D.9: Sensitivity of estimated specific ventilation distribution to the error in series dead space estimation. The graphs show the difference between the fractions of tidal volume estimated with the measured v_d (γ_{REF}, distributions shown in the main paper and in Figures S1-S2) and those estimated with -5% and $+5\%$ deviation in v_d (γ_{ERROR}) (respectively, A and B, and C and D), divided by 5%. For both constrained and unconstrained estimates, an overestimation in v_d shifts the distribution toward fast compartments (right side), and vice-versa.

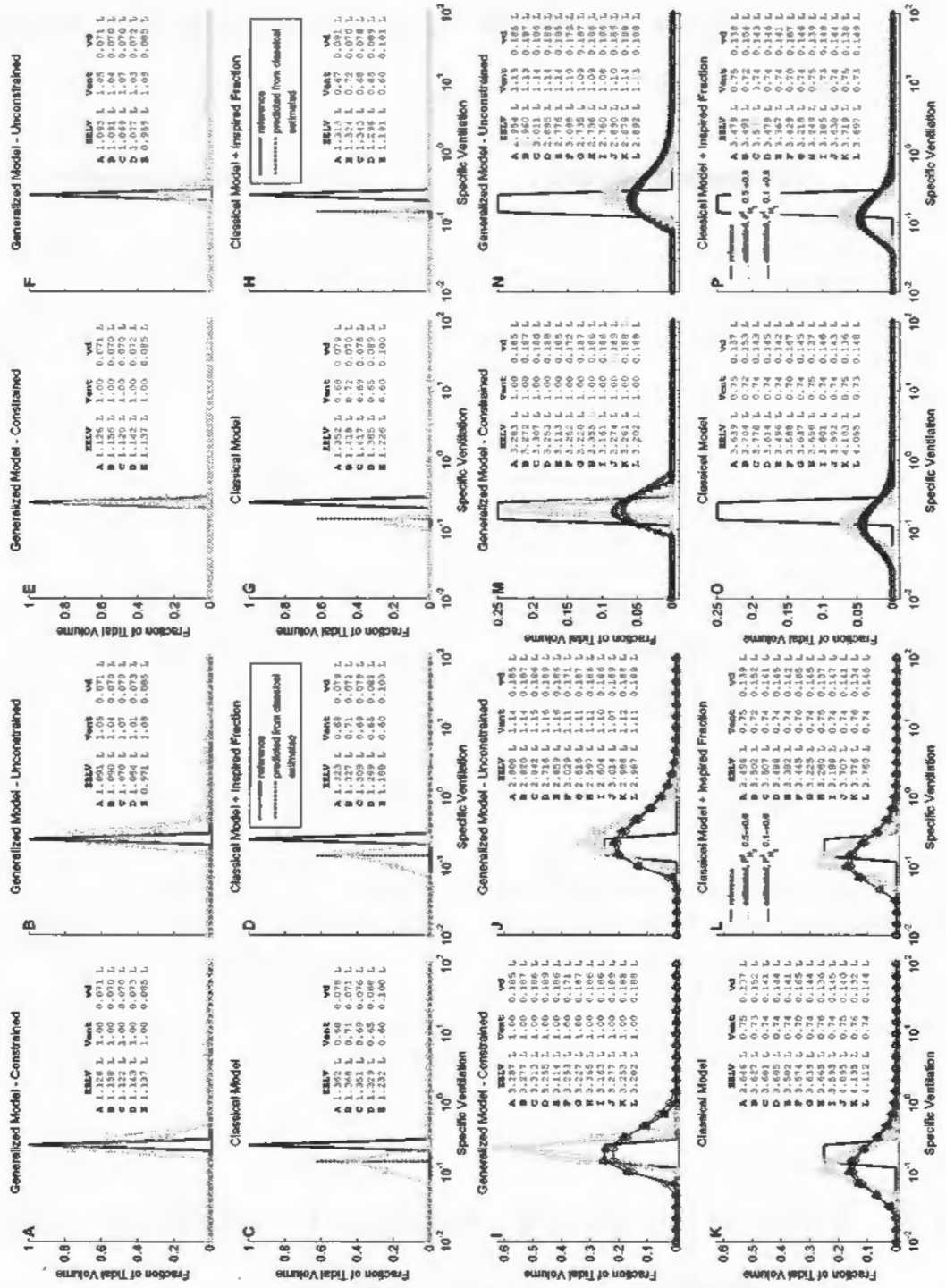# D.4 Sensitivity to the number of modeled compartments (N) for 1C and 4C

Figure D.10: Distribution of v/V estimated from N_2 washouts of a single- (upper panels) or four- (lower panels) compartment physical model. The distributions were estimated using the classical all-parallel model or the novel generalized model with series v_d. The constrained version of the last model imposes a solution with the measured v_d and EELV, and a unitary total ventilation (Vent). Reconstruction with 25 (panels A,B,C,D,I,J,K,L) or 100 (panels E,F,G,H,M,N,O,P) compartments. For the four-compartment model, inspired N_2 ($F_{N_2}^I$) varied by 50 % (light gray) or 10 % (dark gray). In all cases, the number of cycles used for estimation was determined according to the Consensus [70], that is, until $1/40^{th}$ of the initial N_2 concentration. The reference distribution, expected from the geometries of the physical models, is shown in black.